

Novel Synthetic Biomaterials for Kidney-Derived Progenitor / Stem Cell Differentiation

Thesis submitted in accordance with the requirements of the University of
Liverpool for the degree of Doctor in Philosophy

By

Isabel Hopp

October 2016

Acknowledgements

I would like to thank the following people for their contributions to this work:

Prof. Patricia Murray, Prof. Rachel Williams and Simon Dixon for all of their guidance and patience through this process in their role as my advisors

Ass. Prof. Krasimir Vasilev and Dr. Melanie Ramiasa for preparation and supply of plasma coated substrates

Prof. Chris Sanderson and Dr. Diana Moss for their guidance while serving on my committee

The stem cell lab and the Nephrotools research group for their support, help and advice

Dr. Paul Unsworth for the collection of XPS spectra

Dr. Riaz Akhtar and Zhuola Chang for their help with AFM measurements and image analysis

Dr. Heike Arnolds for her help with Raman Spectroscopy

Prof. Paul Winyard and Chiara Mari for providing human fetal kidney-derived cell lines

Dr. Bettina Wilm and Ilaria Santeramo for providing human infant kidney-derived cell lines

Prof. Moin Saleem for providing human conditionally immortalised podocytes

Prof. Roos Masereeuw for providing human conditionally immortalised proximal tubule cells

Claire Fielding and Stephanie Reed for helping me to complete this project

My mother, brother, friends and Shahed for their continuous support and encouragement.

This research was funded by:

This work has been supported by Marie Curie Actions, Initial Training Networks Grant EC contract number 289754, with support from the Institute of Translational Medicine, University of Liverpool.

Abstract

End-stage kidney disease is increasing in prevalence and is associated with high levels of morbidity and mortality. At present, the only treatment options are dialysis or renal transplantation. However, dialysis is very costly and is associated with high levels of morbidity, whereas the problem with transplantation is that there is a shortage of organ donors. For these reasons, over recent years, there has been an increasing interest in developing novel therapies in the field of regenerative medicine including stem cell based therapies and tissue engineering. Stem cells could be used in a number of ways to develop new therapies for kidney disease. Firstly, they could be administered as cell therapies to patients with kidney disease, and secondly, they could be used to generate specific types of renal cells *in vitro* that could be used for understanding disease mechanisms and for drug discovery programmes.

The barriers to the development of novel stem cell therapies include the difficulties in expanding kidney-derived stem cells in culture without altering their phenotype, and directing their differentiation to specific types of renal cells. These issues could be addressed by developing biomaterial substrates that provide an appropriate microenvironment for the successful culture and differentiation of stem cells.

Within this study we interrogated a wide range of biomaterial substrates for their capability to direct the differentiation of kidney derived progenitor / stem cells. These materials were thoroughly characterised in terms of their physicochemical properties, such as surface chemistry, nanotopography and wettability by employing a wide range of analytic techniques, including X-Ray Photoelectron Spectroscopy (XPS), Atomic Force Microscopy (AFM), colorimetry and contact angle measurements.

We firstly investigated a range of polyacrylates. These substrates were novel in that, they were precisely designed to mimic cell binding motifs of the extracellular matrix stereochemically by using monomeric precursors that display particular chemical functional group chemistries, namely amine, hydroxyl, carboxyl groups or aliphatic spacer groups. We found that these materials differed strongly in the presence and distribution of surface functional group chemistries and topographical features, including the distribution of surface artefacts on a macroscale. Moreover, some of these materials were able to direct the differentiation into specialised renal cell lines. Two substrates, namely ESP 003 and ESP 004, directed the differentiation of kidney derived stem cells into podocytes and two further

substrates, namely ESP 007 and BTL 15, directed differentiation into functional proximal tubule cells. These four substrates stimulated cell differentiation to an extent of about 40 to 50% after only 96 h in cell culture. We were moreover able to identify surface physicochemical cues, including surface micro- and nanoscale topography and surface functional group chemistries that are important to stimulate the differentiation process.

In addition, we investigated a range of plasma polymer coatings composed of allylamine and octadiene that were provided as homo-or copolymers and in form of chemical gradients, the latter one differing in the amount of nitrogen functional group chemistries across the surfaces. We found that substrates with higher allylamine content displayed a greater amount of nitrogen functional groups and therefore increased in wettability. Moreover, those plasma polymer substrates with higher amine functionality directed kidney progenitor cell differentiation into podocytes, whereas substrates with higher octadiene concentration directed cell differentiation into functional proximal tubule cells, both to an extent of 35 to 45% after only 96 h in culture. To further study cell differentiation, we then incorporated gold nanoparticles underneath these plasma coatings, either in form of homogeneous coatings or in form of a nanoparticle density gradient. We found that surface topographic gradients increased cell differentiation into podocytes 3- to 4-fold, whereas differentiation into proximal tubule cells was only dependent on surface chemistry. Our studies on plasma polymer substrates highlighted not only the great potential of plasma polymers to modify surface functionality of a wide range of surfaces, but also emphasized the great capabilities of surface gradients, whether chemical or topographical in nature, to effect cellular fate.

In summary, the results of this study include the identification of biomaterial substrates that have the potential to differentiate kidney-derived progenitor/stem cells *in vitro* and of the cues that are necessary to assist in the differentiation process. In the future, these biomaterials could be useful for directing the differentiation of pluripotent stem cell-derived renal progenitors to specific types of renal cells that could be used for applications in regenerative medicine and drug discovery programmes.

Table of Contents

Acknowledgements	I
Abstract.....	II
Table of Contents	V
List of Figures	VIII
List of Tables.....	XVIII
List of Equations	XIX
List of Abbreviations	XX
1 Introduction	1
1.1 Biomaterials as stem cell regulators	2
1.1.1 Mimicking extracellular matrices and the stem cell niche	3
1.1.2 Biomaterial-cell interface and cellular regulation	4
1.2 Stem and progenitor cells	10
1.2.1 Background	10
1.2.2 Embryonic stem cells and their progeny.....	10
1.2.3 Adult stem cells and the stem cell niche.....	11
1.2.4 Progenitor cells	12
1.2.5 Induced pluripotent stem cells	12
1.2.6 Stem cells in regenerative medicine	13
1.3 Kidney disease and kidney stem cells	15
1.3.1 Background	15
1.3.2 Podocytes.....	18
1.3.3 Proximal tubule cells.....	20
1.3.4 Stem cells in the kidney	22
1.3.5 Potential of kidney-derived stem/progenitor cells for renal therapies and drug discovery	24
1.4 Motivation and aim of this work	25
2 Materials and Methods	28
2.1 Biomaterial coatings	28
2.1.1 Polyacrylates	28
2.1.2 Plasma polymer coatings	31
2.2 Physicochemical substrate characterisation	33
2.2.1 Surface wettability analyses	33
2.2.2 Atomic Force Microscopy	35
2.2.3 Characterisation of surface chemistry	37
2.3 Cell culture	42
2.3.1 Cell lines	42
2.3.2 Routine cell culture	43
2.3.3 Cell culture on biomaterial substrates.....	44
2.3.4 Cryopreservation.....	44
2.3.5 Cell recovery.....	45

2.4	Evaluation of the cell response.....	45
2.4.1	Morphological assessment using methylene blue.....	45
2.4.2	Cell viability	45
2.4.3	Cell proliferation, population doubling time and cell spread.....	46
2.4.4	Immunostaining.....	47
2.4.5	Alkaline phosphatase staining	48
2.4.6	Live cell imaging.....	48
2.4.7	Podocyte quantification.....	49
2.4.8	Fluorescence activated cell sorting.....	49
2.4.9	Reverse transcription quantitative real-time polymerase chain reaction.....	51
2.5	Statistical analyses.....	55
3	Physicochemical characterisation of polyacrylates.....	56
3.1	Introduction.....	56
3.2	Results.....	62
3.2.1	Surface characterisation using X-Ray Photoelectron Spectroscopy	62
3.2.2	Surface wettability analyses	67
3.2.3	Substrate characterisation using Atomic Force Microscopy	73
3.3	Discussion.....	76
3.3.1	Surface characterisation using X-Ray Photoelectron Spectroscopy	76
3.3.2	Surface wettability analyses	80
3.3.3	Surface characterisation using Atomic Force Microscopy.....	86
3.4	Conclusions.....	91
4	Effect of polyacrylates on kidney progenitor / stem cells	92
4.1	Introduction.....	92
4.2	Results.....	94
4.2.1	Polyacrylate biocompatibility.....	94
4.2.2	Effect of polyacrylates on mouse kidney-derived stem cells.....	102
4.2.3	Effect of polyacrylates on conditionally immortalised kidney cell lines.....	113
4.2.4	Effect of polyacrylates on putative human kidney progenitor cells	124
4.3	Discussion.....	135
4.3.1	Polyacrylate biocompatibility.....	135
4.3.2	Effect of polyacrylates on mouse kidney-derived stem cells.....	137
4.3.3	Effect of polyacrylates on conditionally immortalised renal cell lines	142
4.3.4	Effect of polyacrylates on putative human kidney progenitor cells	145
4.4	Conclusions.....	148
4.5	Supplementary information	149
5	Physicochemical characterisation of plasma polymer coatings.....	151
5.1	Introduction.....	151
5.2	Results.....	154
5.2.1	Characterisation of surface chemistry	154
5.2.2	Surface wettability analyses	161

5.2.3	Substrate characterisation using Atomic Force Microscopy	165
5.3	Discussion.....	167
5.3.1	Characterisation of surface chemistry	167
5.3.2	Surface wettability analyses	170
5.3.3	Substrate characterisation using Atomic Force Microscopy	172
5.4	Conclusions.....	172
6	Effect of plasma polymer coatings on mouse kidney-derived stem cells	174
6.1	Introduction.....	174
6.2	Results.....	176
6.2.1	Effect of surface chemistry on mouse kidney-derived stem cells	176
6.2.2	Effect of surface nanotopography on mouse kidney-derived stem cells	187
6.3	Discussion.....	196
6.3.1	Effect of surface chemistry on mouse kidney-derived stem cells	196
6.3.2	Effect of surface topography on mouse kidney-derived stem cells.....	200
6.4	Conclusions.....	202
7	Concluding remarks and future work	204
7.1	Polyacrylates	205
7.1.1	Key findings	205
7.1.2	Applications and future work.....	207
7.2	Plasma polymer coatings	209
7.2.1	Key findings	209
7.2.2	Applications and future work.....	210
7.3	Final Remarks	211
8	References	213
Appendix I	Cell culture.....	239
Appendix II	Immunofluorescence and cell staining.....	241
Appendix III	Buffers and solutions	242
Appendix IV	Molecular biology	243
Appendix V	Polymer analyses	245

List of Figures

- Figure 1.1:** The extracellular matrix consists of a complex network of macromolecules: structural proteins, proteoglycans and adhesive glycoproteins that support the attachment of cells to the matrix. 4
- Figure 1.2:** Cells adhere to a substrate (i.e. ECM or biomaterial) through focal adhesions and sense its physicochemical cues, including topography, elasticity, wettability and chemistry. Cells then adapt their properties in response. 5
- Figure 1.3:** Within the stem cell niche, stem cells are kept in a quiescent state and stem cells are continuously interacting with their environment that includes the extracellular matrix, other stem cells, progenitors and differentiated cells. The combination of all signals that derive from the stem cell environment cause self-renewal and the maintenance of a stem cell pool. Once injurious signals arise (i.e. inflammatory cytokines) stem cells self-renew, proliferate and differentiate into functional cells..... 13
- Figure 1.4:** The fusion of sperm and egg results in the formation of a zygote, the ultimate, totipotent stem cell. Through cell division these cells will further differentiate to create a blastocyst with an outer and an inner cell mass, the latter one being the source of embryonic stem cells. Embryonic stem cells can continuously self-renew, but also further differentiate into all three germ layers (endoderm, mesoderm and ectoderm). These will then further develop to form an entire organism. Adult stem cells are present in tissue niches. They can also self-renew, but have a rather limited, more committed, differentiation potential. Moreover, specialised cells can be reprogrammed to become pluripotent again. All three cell types, embryonic, adult and induced pluripotent stem cells are known to be able to differentiate *in vitro* under the appropriate cell culture conditions. Adapted from Connor *et al.* [202]. 15
- Figure 1.5:** Simplified schematic of a nephron, the functional units of the kidney. Each nephron consist of a renal corpuscle which is associated with a renal tubule. The renal corpuscle is the place where blood plasma is filtered and urine formation begins. It consists of an epithelial cup, the Bowman's capsule that encloses a network of capillaries, the glomerulus. Podocytes (visceral epithelial cells) wrap around these capillaries. The current view assumes the presence of renal progenitors at the urinary pole of the Bowman's capsule, tubular progenitors are scattered along the tubules and podocyte precursors localise along the Bowman's capsule. The renal corpuscle is associated with the renal tubule that is comprised of several segments, one of them being the proximal convoluted tubule with the proximal tubule cells. It is responsible for the reabsorption of solutes from the filtrate (tubular fluid). At the fluid side, the proximal tubule cells have microvilli and the entire apical membrane contains a network composed of different receptors, coated pits and endosomes, whereas the basolateral membrane has multiple infoldings to increase surface area. Here most transport processes are driven by Na-K-ATPases. 17
- Figure 1.6:** Phase contrast image (left) and F-actin and DAPI labelled (right) image of a podocyte. Scale bar is 100 μm 19
- Figure 2.1:** Polymer dipcoating procedure. Step 1: A glass coverslip was immersed halfway through into the polymeric solution (polymer diluted in organic solvent) and subsequently dried in an oven at 85°C for 15 min to evaporate the solvent. Step 2: The half coated coverslip was then inverted and the other, uncoated half was immersed into the polymeric solution. The polymer coated coverslip was then taken back to the oven and heated another 15 min at 85°C to evaporate the solvent. Samples were stored in sealed tissue culture plates. 29
- Figure 2.2:** Experimental setup of cytotoxicity experiments on polyacrylate substrates using mL929 cells. 31
- Figure 2.3:** Simple schematic of the sessile drop technique. (A) Schematic diagram of a drop contour where the CA is measured at the interface (Y) between solid-gas (SG), solid-liquid (SL) and liquid-gas (LG) and (B) change of drop shape with increasing surface wettability. 33

Figure 2.4: Schematic set up of the contact angle measurements using the CB method.	34
Figure 2.5: Simple schematic of the Wilhelmy plate method to assess substrate DCA. (A) Experimental setup. The substrate is immersed into the liquid downwards and subsequently taken out upwards. (B) Simultaneously advancing and receding curves are acquired using the associated software.	35
Figure 2.6: Atomic Force Microscopy. (A) Simple illustration of the AFM setup. A tip attached to a cantilever raster scans a sample that is attached to a piezo element. An optical laser beam is focussed on the cantilever and the deflection is transferred onto a Photodiode. From here the detector analyses the deflection signal and gives a 3D image. (B) Schematic of a typical force curve measurement. The tip is in distance from the surface, no force (1). Once the tip approaches the surface, attractive forces (deflection downwards) occur and the tip contacts the surface (deflection upwards) (2). When the tip is retracted from the surface, adhesion forces maintain a certain distance between tip and sample (3 → 4) until the spring force allows to overcome adhesion forces (5) and the tip returns to position (1).	36
Figure 2.7: X-Ray Photoelectron Spectroscopy. (A) Simplified schematic of the instrumental XPS set up. An X-Ray source is focused on the substrate and excites core electrons in the upper layers of a substrate surface (B and C). These photoelectrons are ejected from an atomic level or valence band of the sample surface. Photoelectron energy is determined using a concentric hemispherical analyser. The signal then becomes transferred to a detector, resulting in a spectrum with a series of photoelectron peaks and is visualised as intensity (electron counts) versus electron energy. The entire process takes place within a chamber that maintains ultra-high vacuum (UHV) which avoids surface contamination and increases the scope of the electrons when ejected.....	38
Figure 2.8: (A) An example of a XPS wide scan spectrum that shows three peaks: a carbon 1s (C1s) peak, an oxygen 1s (O1s) peak and a nitrogen 1s (N1s) peak at their characteristic binding energies. The background originates from electrons that are excited by the X-Ray Bremsstrahlung radiation and from inelastic photoelectron scattering.....	39
Figure 2.9: Simplified schematic of the colorimetric determination of the surface amine content. The samples are incubated in a solution that contains the dye that binds to amine groups at a specific pH. After washing, the pH of the solution is changed, the bound dye is released into the solution whose optical density can then be determined and correlated with the optical density of a standard solution with known dye concentration.	39
Figure 2.10: CBB absorption spectrum and molecule isomeric forms depending on the solution pH.	40
Figure 2.11: Orange 2 absorption spectrum and its isomeric forms.	41
Figure 3.1: Polyacrylate structure. (A) Polyacrylate monomeric and polymeric unit. R ₁ and R ₂ indicate potential functionalities. (B) Representative stick ball schematic of a random polyacrylate with a carbon backbone and a variety of potential representative side chains with different functionalities.	57
Figure 3.2: Integrin receptor. (A) Simplified schematic representation of an integrin hetero dimer with an RGD ligand binding site. (B) Chemical structure and (C) stick and ball model of the RGD motif.	59
Figure 3.3: Schematic representation of polyacrylate substrates that mimic <i>in vivo</i> cell binding motifs (stereo) chemically. ESP 003, ESP 004 and ESP 007 mimic structurally the RGD motif in different conformations whereas BTL 15 mimics a cell binding motif present within collagen.	61
Figure 3.4: Representative XPS spectra obtained from ESP 003. (A) Survey scan highlighting the fitted peaks carbon (C1s), nitrogen (N1s) and oxygen (O1s). (B) O1s (C) N1s and (D) C1s high resolution spectra with fitted peaks. Note: y-scale is different for improved visibility of scans.	63
Figure 3.5: Elemental surface composition. (A) Elemental contribution of each element to the substrate in per cent and (B) Ratio of oxygen/carbon and nitrogen/carbon. All data were obtained via analyses of the survey spectra.	64

- Figure 3.6:** Element peak composition in per cent. (A) Carbon / C1s peak (B) Oxygen / O1s peak and (C) Nitrogen / N1s peak. All data were obtained by curve fitting analyses of C1s, O1s and N1s high resolution spectra. 66
- Figure 3.7:** Polyacrylate CA analyses. All substrates were significantly different from glass (Tukey model, $p < 0.05$). ESP 008, ESP 009 and ESP 010 were significantly more hydrophilic than other polyacrylates. 67
- Figure 3.8:** 2D (top view) and 3D CA maps of polyacrylate substrates. 2D maps show the wettability profile across the surface whereas 3D maps show wettability from one point perspective. Note: These maps do not represent topographical features..... 69
- Figure 3.9:** Polyacrylate CAs obtained using the CB method. All substrates were significantly different from glass (Tukey model, $p < 0.05$). ESP 008, ESP 009 and ESP 010 were significantly more hydrophilic than any other substrate. Delta is the difference between the dry and the in FBS incubated substrate. 70
- Figure 3.10:** DCAs obtained for all polyacrylates coated on 22 mm² coverslips and measured in distilled water. Results represent the mean of 7 measurements \pm SEM. (A) Dry state, (B) 2 h post exposure in water and (C) 2 h post exposure in FBS. Advancing and receding angles of most substrates were significantly (Tukey model, $p < 0.05$) different from glass in both, dry and hydrated state, but not after exposure in FBS. 72
- Figure 3.11:** DCA cycles. Dry 22 mm² polymer coated glass cover slips were repeatedly immersed in distilled water for a duration of 10 cycles. Results represent the mean of three samples. SD is not shown in order to maintain visual clarity. (A) Advancing angle (B) receding angle and (C) hysteresis 73
- Figure 3.12:** Polymer layer thickness of polyacrylates coated on glass cover slips. Asterisks indicate significant difference towards ESP 009, # significant difference towards ESP 010 ($p < 0.05$, Tukey model). 74
- Figure 3.13:** AFM 50 μm^2 3D topographical surface images of all polymer substrates. Brighter colours represent high areas and darker colours represent deeper areas. AFM was operated in tapping mode. Note: Z-scale is different between images to improve visualization. 74
- Figure 3.14:** Height quantification hill like structures on topographical images 50 μm^2 AFM images. Each dot represents one measured hill from a range of a minimum of 3 different substrates and 5 different areas. 75
- Figure 3.15:** Polyacrylate RMS roughness analyses. Asterisks indicate significant difference compared to ESP 003, number signs compared to ESP 004 and plus signs compared to ESP 007 ($p < 0.05$, Tukey model). 76
- Figure 3.16:** Polyacrylate Young's modulus (Elastic modulus) analyses. All substrates showed an elastic modulus of about 2 ± 0.5 GPa. No significant differences were found ($p < 0.05$, Tukey model). 76
- Figure 3.17:** Polyacrylate layer thickness may vary due to polymer dipcoating procedure. (A) The polymer coating procedure may result in thickness variation across the surfaces. (B) As a result polyacrylate thickness may be differing between substrate edges and middle portion. 87
- Figure 3.18:** CA measurement on a smooth (A) and a rough surface (B). General CAs changes depend on hydrophilicity (yellow lines) / hydrophobicity (orange lines) of a sample, but also on the roughness. (C) Apparent (measured) CA. The roughness is not visible when measuring and the CA appears a projection of the real value (dashed line). (D) Actual CA. 90
- Figure 3.19:** Simple schematic of the influence of roughness on substrate wettability. (A) Water droplet (blue) on a smooth surface (grey). The contact between solid and liquid decreases with (B) nanoroughness and (C) microroughness or in a (D) hierarchical manner. The principle is based on and schematic inspired by *Bhushan and Jung et al. [373]*. 90

Figure 4.1: Brightfield microscopic images of mL929 cells exposed to 0%, 10%, 50% and 100% polymer conditioned eluant after 48 h stained with methylene blue. Cells were seeded at a density of 1×10^4 cells / well. Positive (cytotoxic) control was latex, negative control (not cytotoxic) was pure medium. On all substrates cell density decreased with increasing eluant concentration.	96
Figure 4.2: Brightfield microscopic images of mL929 cells exposed to 0%, 10%, 50% and 100% polymer conditioned eluant after 48 h stained with methylene blue. Cells were seeded at a density of 1×10^4 cells / well. Positive (cytotoxic) control was latex, negative control (not cytotoxic) was pure medium. On all substrates cell density decreased with increasing eluant concentration.	97
Figure 4.3: Cytotoxic effects of polymer conditioned (pc) eluant and quantification of cell viability. Cells were seeded at a density of 1×10^4 cells / well. (A) Cytotoxic effects of 50% and 100% polymer conditioned eluant compared to a 0% control for all substrates over time. Data were fitted using nonlinear regression / exponential growth equation. Results represent the mean of 3 biological replicates \pm SEM.	98
Figure 4.3: continued: (B) Quantification of the number of viable cells 96 h post seeding. (C) Population doubling time. Results represent the mean of 3 biological replicates \pm SEM.	99
Figure 4.4: mL929 cells were seeded on polyacrylate substrates at a density of 1×10^4 cells / coverslip. (A) mL929 cells stained with methylene blue 96 h post seeding at 10 x (top) and 40x (bottom) resolution. Corresponding (B) cell number of mL929 cells over the course of 96 h and (C) PDT. Asterisks indicate statistical difference compared to a glass control (Tukey model, $p < 0.05$). Data were fitted using nonlinear regression / exponential growth equation. Results represent the mean of three biological replicates \pm SEM. Scale bar: 100 μ m.	100
Figure 4.5: BAE cells were seeded on polyacrylate substrates at a density of 1×10^4 cells / coverslip. (A) BAE cells stained with methylene blue 96 h post seeding at 10 x (top) and 40x (bottom) resolution. Corresponding (B) cell number of BAE cells over the course of 96 h and (C) PDT. Asterisks indicate statistical difference compared to a glass control (Tukey model, $p < 0.05$). Data were fitted using nonlinear regression / exponential growth equation. Results represent the mean of three biological replicates \pm SEM. Scale bar: 100 μ m.	102
Figure 4.6: mKSCs were seeded at a density of 1×10^3 cells / coverslip and cultured for 96 h. (A) Cell proliferation. (B) Number of viable cells. (C) PDT, as obtained using results from cell number (A). Results represent the mean of three biological replicates \pm SEM. Asterisks indicate statistical difference compared to a glass control (Tukey model, $p < 0.05$). Data were fitted using nonlinear regression / exponential growth equation.	103
Figure 4.7: mKSCs morphological analyses. mKSCs were seeded at a density of 1×10^3 cells / 13 mm polymer coated coverslip. The images show mKSC phase contrast images, as obtained by life cell imaging, and F-actin and DAPI labelled cells at a higher resolution 24 h and 96 h post seeding. Scale bar is 100 μ m.	105
Figure 4.8: mKSC spread analyses. mKSC were seeded at a density of 1×10^3 cells / 13 mm polymer coated coverslip. Cell spread was quantified at four different time points post seeding. Asterisks indicate significant difference compared to a glass control. Results represent the mean of three biological replicates \pm SEM.	106
Figure 4.9: Number of podocyte-like cells. mKSCs were seeded at a density of 1×10^3 cells / polymer coated coverslip. The number of podocyte like cells was quantified. Asterisks indicate significant difference compared to a glass control (Tukey model, $p < 0.05$). Results represent the mean of three biological replicates \pm SEM.	106
Figure 4.10: RT-qPCR analyses of mKSCs for podocyte characteristic genes as relative expression to mKSC gene expression on a glass control. Seeding density: 1×10^3 cells / polymer coated coverslip. <i>Gapdh</i> and <i>beta actin (ACTB)</i> were used as housekeeping genes. Asterisks indicate significant differences compared to a TCP control. Results represent the mean of three biological replicates \pm SEM.	107

- Figure 4.11:** Alkaline phosphatase staining. Blue: DAPI. mKSCs were seeded at a density of 1×10^3 cells / polymer coated coverslip. Scale bar: 100 μm 108
- Figure 4.12:** Megalin staining. Blue: DAPI. Green: Laminin. mKSCs were seeded at a density of 1×10^3 cells / polymer coated coverslip. Cells were co-stained with laminin for better visualisation. Scale bar: 100 μm 109
- Figure 4.13:** Quantification of megalin expressing cells. mKSCs were seeded at a density of 1×10^3 cells / polymer coated coverslip. (A) The number of megalin expressing cells was quantified at three different time points post seeding. (B) Quantification of the fluorescent area 96 h post seeding (ratio of megalin : DAPI). Asterisks indicate significant difference compared to the glass control (Tukey test, $p < 0.0001$). Data were fitted with an exponential growth equation. Results represent the mean of three biological replicates \pm SEM. 110
- Figure 4.14:** Albumin uptake assay. Red: Megalin, green: fluorescently labelled albumin (F-BSA), blue: DAPI. mKSCs were seeded at a density of 1×10^3 cells / polymer coated coverslip. F-BSA and megalin colocalise in higher proportions in cells cultured on ESP 007 and BTL 15. Scale bar: 25 μm 111
- Figure 4.15:** Albumin uptake assay. Flow cytometric analyses of mKSCs that were cultured on substrates. Cells were seeded at a density of 1×10^3 cells/polymer coated coverslip. (A) Flow cytometric representative spectra and (B) quantification. Asterisks indicate significant difference compared to a glass control (Tukey model $p < 0.05$). Results represent the mean of three biological replicates \pm SEM. 112
- Figure 4.16:** RT-qPCR analyses of mKSCs for PTC characteristic genes as relative expression to mKSCs on a glass control. Seeding density: 1×10^3 cells / polymer coated coverslip. *Gapdh* and *beta actin (ACTB)* were used as housekeeping genes. Results represent the mean of three biological replicates \pm SEM. 113
- Figure 4.17:** Morphological analyses of ciPodocytes on representative polyacrylate substrates with cells showing the typical podocyte-like morphology, including a large cell body, arborised cytoskeleton and binuclearity. Cells were seeded at 1×10^3 cells / polymer coated 13mm coverslip and phase contrast images and fluorescence images were taken. Green: F-actin and blue: DAPI. Scale bar is 100 μm 114
- Figure 4.18:** ciPodocytes cell number, PDT and viability assessment on polyacrylate substrates. Cells were seeded at 1×10^3 cells / polymer coated 13 mm coverslip. Asterisks indicate significant difference compared to a glass control (Tukey model, $p < 0.05$) Results represent the mean of three biological replicates \pm SEM. 116
- Figure 4.19:** Cell spread analyses of ciPodocytes on polyacrylate substrates. Cells were seeded at 1×10^3 cells / polymer coated 13 mm coverslip and cell spread was analysed. Asterisks indicate significant difference compared to a glass control (Tukey model, $p < 0.05$). Results represent the mean of three biological replicates \pm SEM. 117
- Figure 4.20:** (A) Nephrin and (B) podocin staining of ciPodocytes on polyacrylate substrates. Cells were seeded at 1×10^3 cells / polymer coated 13 mm coverslip. Blue: DAPI. Scale bar is 100 μm . 118
- Figure 4.21:** Morphological analyses of ciPTCs on representative polyacrylate substrates. Cells were seeded at 1×10^3 cells / polymer coated 13mm coverslip and phase contrast images and fluorescence images were taken. Green: F-actin and blue: DAPI. Scale bar is 100 μm 119
- Figure 4.22:** ciPTC cell number, PDT and viability assessment on polyacrylate substrates. Cells were seeded at 1×10^3 cells / polymer coated 13 mm coverslip. Asterisks indicate significant difference compared to a glass control (Tukey model, $p < 0.05$) Results represent the mean of three biological replicates \pm SEM. 121

- Figure 4.23:** Cell spread analyses of ciPTCs on polyacrylate substrates. Cells were seeded at 1×10^3 cells / polymer coated 13 mm coverslip and cell spread was analysed. Asterisks indicate significant difference compared to a glass control (Tukey model, $p < 0.05$). Results represent the mean of three biological replicates \pm SEM. 122
- Figure 4.24:** (A) Aquaporin 1 and (B) megalin staining of ciPTCs on polyacrylate substrates. Blue: DAPI. Cells were seeded at 1×10^3 cells / polymer coated 13 mm coverslip. Scale bar is 100 μ m. . 123
- Figure 4.25:** Albumin uptake assay. ciPTCs were analysed for their ability to uptake F-BSA. Cells were seeded at a density of 1×10^3 cells / polymer coated 13 mm coverslip. Asterisks indicate statistical difference compared to a TCP control. Results represent the mean of three biological replicates \pm SEM. 124
- Figure 4.26:** Morphological analyses of fKPCs on polyacrylate substrates. Cells were seeded at 5×10^3 cells / polymer coated 13 mm coverslip. Images show phase contrast images and F-Actin labelled cells at a higher resolution at two different time point: 3 and 7 days post seeding. Blue: DAPI. (A) Double negative and (B) double positive population. Scale bar is 100 μ m. 127
- Figure 4.27:** Analyses of iKPC (A) proliferation, (B) PDT (as determined from cell number values in (A) and (C) viability) on polyacrylate substrates. Cells were seeded at a density of 5×10^3 cells / polymer coated 13 mm coverslip. Asterisks indicate significant difference compared to glass control (Tukey model, $p < 0.05$). Data were fitted with an exponential growth equation. Results represent the mean of three biological replicates \pm SEM. 128
- Figure 4.28:** Cell spread analyses of fKPCs on polyacrylate substrates. Cells were seeded at a density of 5×10^3 cells / polymer coated 13 mm coverslip. Cells were cultured for a period of 7 days. Asterisks significant difference compared to glass control (Tukey model, $p < 0.05$). Data were fitted with a non-linear fit / one phase decay equation. Results represent the mean of three biological replicates \pm SEM. 129
- Figure 4.29:** fKPC flow cytometric analyses for assessment of functional PTCs after culture on substrates. Cells were seeded at a density of 1.5×10^4 cells / polymer coated (2x) 19 mm coverslip. An albumin uptake assay was performed and cells were co-labelled with CD13. Asterisks indicate significant difference compared to TCP control. Results represent the mean of three biological replicates \pm SEM. 129
- Figure 4.30:** Assessment of CD133/CD24 of fKPCs on polyacrylates. Cells were seeded at a density of 1.5×10^4 cells / polymer coated (2x) 19 mm coverslip. Asterisks indicate significant significance compared to the TCP control. Results represent the mean of three biological replicates \pm SEM. 130
- Figure 4.31:** Morphological analyses of iKPCs on polyacrylate substrates. Cells were seeded at 5×10^3 cells / polymer coated 13 mm coverslip. Images show phase contrast images and F-Actin labelled cells at a higher resolution at two different time point: 3 and 7 days post seeding. Blue: DAPI. (A) Double negative and (B) double positive population. Scale bar is 100 μ m. 132
- Figure 4.32:** Analyses of iKPC (A) proliferation, (B) PDT (as determined from cell number values in (A) and (C) viability) on polyacrylate substrates. Cells were seeded at a density of 5×10^3 cells / polymer coated 13 mm coverslip. Asterisks indicate significant difference compared to glass control (Tukey model, $p < 0.05$). Data were fitted with an exponential growth equation. Results represent the mean of three biological replicates \pm SEM. 133
- Figure 4.33:** Cell spread analyses of iKPCs on polyacrylate substrates. Cells were seeded at a density of 5×10^3 cells / polymer coated 13 mm coverslip. Cells were cultured for a period of 7 days. Asterisks indicate significant difference compared to glass control (Tukey model, $p < 0.05$). Data were fitted with a non-linear fit / one phase decay equation. Results represent the mean of three biological replicates \pm SEM. 133

Figure 4.34: iKPC flow cytometric analyses for assessment of functional PTCs after culture on substrates. Cells were seeded at a density of 1.5×10^4 cells / polymer coated (2x) 19 mm coverslip. An albumin uptake assay was performed and cells were co-labelled with CD13. Asterisks indicate significant difference compared to TCP control. Results represent the mean of three biological replicates \pm SEM.....	134
Figure 4.35: Assessment of CD133/CD24 of iKPCs on polyacrylates. Cells were seeded at a density of 1.5×10^4 cells / polymer coated (2x) 19 mm coverslip. Asterisks indicate significant significance compared to the TCP control. Results represent the mean of three biological replicates \pm SEM.	135
Figure 4.36: Correlation between polyacrylate surface properties and mKSC differentiation.....	140
Figure 4.37: ciPodocytes analyses on polyacrylate substrates. (A) Cell proliferation (B) cell viability and (C) cell spread followed over 11 days. ciPodocytes were seeded at 1×10^3 cells / polymer coated 13 mm coverslip and cultured for 6 days at 33°C and subsequently 5 days at 37°C. Data were fitted with an exponential growth equation. Results represent the mean of three biological replicates \pm SEM.....	149
Figure 4.38: ciPTC analyses on polyacrylate substrates. (A) Cell proliferation (B) cell viability and (C) cell spread followed over 11 days. ciPTCs were seeded at 1×10^3 cells / polymer coated 13 mm coverslip and cultured for 6 days at 33°C and subsequently 5 days at 37°C. Data were fitted with an exponential growth equation. Results represent the mean of three biological replicates \pm SEM.	150
Figure 5.1: (A) Simplified schematic diagram of the Bell plasma reactor (static type). The monomeric substance (liquid or gas) is led through the system and is cooled down with liquid nitrogen before it enters the reaction chamber, a cylindrical tube. Internal electrodes put the monomer into a plasma state that is composed of a variety of chemical species. The developing polymers then form crosslinked and branched chains and attach to solid surfaces (including substrates). The temperature and pressure inside can be precisely regulated (B) Schematic of the plasma polymerisation process. Plasma polymerisation can occur plasma induced (free-radical induced polymerisation of molecule with C-C double bonds) or through plasma state polymerisation (depends on presence of other reactive species in the plasma). The result is a polymer layer on solid surfaces. (C) Gradientiser.	152
Figure 5.2: List of plasma polymers analysed during the course of this study.	153
Figure 5.3: (A) Quantification of the elemental composition of plasma polymer coated homo- and copolymers (B) Ratio of oxygen/carbon (O/C) and nitrogen/carbon (N/C). Survey (C) and (D) high resolution N1s peak spectra show changes of the elemental composition with increasing AA content.	155
Figure 5.4: (A) Quantification of the elemental composition of plasma polymer gradients (B) Ratio of oxygen/carbon (O/C) and nitrogen/carbon (N/C). Survey (C) and (D) high resolution N1s peak spectra show changes of the elemental composition with increasing AA content.	155
Figure 5.5: (A) C1s peak composition of homo- and copolymers. The proportion of binding states was quantified. All data were obtained by curve fitting analyses of C1s high resolution peaks. (B) Ratio of C-O, C-N / C-C, C-H.....	157
Figure 5.6: C1s peak composition of the gradient. The proportion of binding states was quantified. All data were obtained by curve fitting analyses of C1s high resolution peaks. (B) Ratio of C-O, C-N / C-C, C-H.....	157
Figure 5.7: Surface primary amine quantification. (A) Coomassie Blue (CBB) method (B) Orange 2 method and (C) Correlation between CBB and Orange 2 method.	159
Figure 5.8: Correlation between XPS (N/C ratio) amine group quantification and (A) amine group quantification obtained by CBB method and (B) amine group quantification obtained by Orange 2 method. The XPS error bars correspond to its general 10% error.....	160

Figure 5.9: Change of primary amine density after repeating the CBB method on the same substrate.	161
Figure 5.10: Plasma polymer CAs. (A) Homo- and copolymers and (B) CA values obtained across the gradient in steps of 0.5 mm. * Significant difference compared to a glass control. # Significant difference compared to 100% AA. All substrates were significantly different from glass (Tukey model, $p < 0.05$).	162
Figure 5.11: 2D (top view) and 3D contact angle maps of plasma polymer coated substrates. 2D maps show the wettability profile across the surface whereas 3D maps show wettability from one point perspective. These maps do not represent topographical features.	163
Figure 5.12: CAs obtained by the CB method for plasma homo- and copolymers either directly in water or 2 h post incubation in FBS. Asterisks indicate significant difference compared to a glass control and number signs compared to 100% AA. All substrates were significantly different from glass (Tukey model, $p < 0.05$).	164
Figure 5.13: (A) Plasma polymer layer thickness after application on glass cover slips. No significant difference was detected ($p < 0.05$, Tukey model). (B) Analyses of the RMS roughness of all homo- and copolymer coated substrates. No significant difference was found ($p < 0.05$, Tukey model).	165
Figure 5.14: 2D AFM $5 \mu\text{m}^2$ topographical surface images of homo- and copolymer coated substrates. Brighter colours represent higher areas and darker colours represent lower areas.	166
Figure 5.15: Analyses of the Young's modulus (Elastic modulus) of homo- and copolymer plasma coated substrates. No significant difference was found ($p < 0.05$, Tukey model). All substrates show an elastic modulus of about 1 ± 0.3 GPa.	166
Figure 6.1: Representation of substrates that were investigated for their ability to direct the differentiation of mKSCs during the course of this study. (A) Homo- and copolymer coated substrates (physicochemically analysed in chapter 5). (B) Substrates, coated with a homogeneous layer of 16 nm or 68 nm diameter AuNPs, over-coated with plasma polymers and (C) Substrates, coated with a 16 nm or 68 nm diameter AuNP density gradient layer and coated with plasma polymers.	176
Figure 6.2: mKSC cell proliferation. mKSCs were seeded at a density of 1×10^3 cells / well. Cell number was determined at 5 different time points post seeding on (A) homo- and copolymers and (B) gradient. Results represent the mean of three biological replicates \pm SEM. Black asterisks indicate significant difference compared to a glass control. Blue asterisks indicate significant difference compared to the middle portion at the same time point (Tukey model, $p < 0.05$).	177
Figure 6.3: Population doubling time. mKSCs were seeded at a density of 1×10^3 cells / well. PDT was quantified from cell proliferation over 96 h in culture on (A) homo- and copolymers and (B) gradients. Results represent the mean of three biological replicates \pm SEM. No significant difference was found (Tukey model, $p < 0.05$).	178
Figure 6.4: mKSC cell viability. mKSCs were seeded at a density of 1×10^3 cells / well. Cell viability was determined at 5 different time points post seeding on homo- and copolymers and a glass. Results represent the mean of three biological replicates \pm SEM. Asterisks indicate significant difference compared to a glass control (Tukey model, $p < 0.05$).	178
Figure 6.5: mKSCs cultured on homo- and copolymers. The images show phase contrast images and, correspondingly, F-actin and DAPI labelled cells at a higher resolution at two different time points post seeding. mKSCs were seeded at a density of 1×10^3 cells / well. White arrows indicate podocyte-like cells. Scale bar is $100 \mu\text{m}$	179
Figure 6.6: mKSCs cultured on gradient surfaces. The images show phase contrast images and, correspondingly, F-actin and DAPI labelled cells at a higher resolution at two different time points post seeding. mKSCs were seeded at a density of 1×10^3 cells / well. White arrows indicate podocyte-like cells. Scale bar is $100 \mu\text{m}$	180

- Figure 6.7:** mKSCs spread analyses. mKSCs were seeded at a density of 1×10^3 cells / 13 mm polymer coated coverslip. Cell spread was quantified at five different time points post seeding. Asterisks indicate significant difference compared to a glass control (Tukey test, $p < 0.05$). Results represent the mean of three biological replicates \pm SEM..... 181
- Figure 6.8:** Podocyte like cells. mKSCs were seeded at a density of 1×10^3 cells well. The number of podocyte like cells was quantified. Asterisks indicate significant difference compared to a glass control (Tukey model, $p < 0.05$). Results represent the mean of three biological replicates \pm SEM. 182
- Figure 6.9:** Nephryn staining. mKSCs were seeded at a density of 1×10^3 cells / well and cultured on polyacrylates for 96 h. White arrows indicate podocytes. Blue: DAPI. Scale bar: 100 μ m. 183
- Figure 6.10:** qRT-PCR analyses of mKSCs for podocyte characteristic genes as relative expression to mKSCs on a glass control 96 h post seeding on substrates. Seeding density: 1×10^3 cells / well. *Gapdh* and *beta Actin (ACTB)* were used as housekeeping genes. No significant difference was detected. Results represent the mean of three biological replicates \pm SEM. 183
- Figure 6.11:** Megalin staining 96 h post seeding on polyacrylates. Blue: DAPI and green: Laminin. mKSCs were seeded at a density of 1×10^3 cells / well. Scale bar: 100 μ m. 184
- Figure 6.12:** Quantification of the number of megalin expressing cells. mKSC were seeded at a density of 1×10^3 cells / well. The number of megalin expressing cells was quantified at 3 different time points post seeding on (A) homo- and copolymers and (B) gradients. Asterisks indicate statistical difference compared to a glass control. Results represent the mean of three biological replicates \pm SEM. 185
- Figure 6.13:** Albumin uptake assay. (A) Spectra and (B) Flow cytometric analyses of mKSCs after starvation in serum free medium and subsequent incubation in serum-free medium supplemented with F-BSA. Cells were seeded at a density of 1×10^3 cells/well. Asterisks indicate significant difference compared to a glass control (Tukey model $p < 0.05$). Results represent the mean of three biological replicates \pm SEM..... 186
- Figure 6.14:** qRT-PCR analyses of mKSCs for PTC characteristic genes as relative expression to mKSCs on a glass control. Seeding density: 1×10^3 cells / polymer coated coverslip. *Gapdh* and *beta actin (ACTB)* were used as housekeeping genes. No statistical differences were detected. Results represent the mean of three biological replicates \pm SEM. 187
- Figure 6.15:** mKSC proliferation and PDT on AuNP and plasma coated substrates. Cells were seeded at a density of 1×10^3 cells / well and cultured for 96 h. (A) Cell proliferation and (B) PDT was determined. A glass and a no-topography sample (NTC, 100% AA without AuNPs) were used as controls. No significant differences were found (Tukey model, $p > 0.05$). Results represent the mean of three biological replicates \pm SEM..... 188
- Figure 6.16:** Phase contrast of mKSC seeded onto AuNP and AA and OD plasma coated substrates. Cells were seeded at a density of 1×10^3 cells / well and imaged 24 and 96 h post seeding. White arrows and circles indicate podocyte-like cells. (A) 16 nm and (B) 68 nm AuNPs. 189
- Figure 6.17:** Quantification of podocyte-like cells. mKSC were seeded at a density of 1×10^3 cells / well. A glass and a no-topography sample (NTC, 100% AA without AuNPs) were used as controls. Asterisks indicate significant difference compared to a glass control (Tukey model, $p < 0.05$). Results represent the mean of three biological replicates \pm SEM. 190
- Figure 6.18:** Nephryn staining on mKSCs cultured on AuNP and plasma coated substrates for a period of 96 h. Blue: DAPI. mKSCs were seeded at a density of 1×10^3 cells / well. Scale bar: 100 μ m. 190
- Figure 6.19:** Megalin staining staining on mKSCs cultured on AuNP and plasma coated substrates for a period of 96 h. Blue: DAPI. mKSCs were seeded at a density of 1×10^3 cells / coverslip. Scale bar: 100 μ m..... 191

- Figure 6.20:** mKSC proliferation on AuNP density gradients over coated with plasma. Cells were seeded at a density of 1×10^3 cells / well. Cell number was determined at 24 and 96 h post seeding. Results represent the mean of three biological replicates \pm SEM. A glass and a no-topography sample (NTC, 100% AA without AuNPs) were used as controls. Asterisks indicate significant difference between cells cultured on 68 nm AuNPs compared to the equivalent portion of the gradient coated with 16 nm AuNPs (Tukey model, $p < 0.05$). 193
- Figure 6.21:** Representative phase contrast images of mKSCs cultured for 96 h on AuNP density gradients that were over coated with either 100% AA (representative for 75% AA) and 0% AA (representative for 25% AA) plasma. Cells were seeded at a density of 1×10^3 cells / coverslip. Scale bar is 100 μ m. 194
- Figure 6.22:** Quantification of podocyte-like cells on AuNP density gradient substrates over coated with plasma. mKSCs were seeded at a density of 1×10^3 cells / well. A glass and a no-topography sample (NTC, 100% AA without AuNPs) were used as controls. Asterisks indicate significant difference compared to the portion of the substrates with the lowest AuNP density (Tukey model, $p < 0.05$). Results represent the mean of three biological replicates \pm SEM. 195
- Figure 6.23:** Megalin staining. Blue: DAPI. mKSCs were seeded at a density of 1×10^3 cells / coverslip on a 16 nm AuNP density gradient (representative for 68 nm AuNPs). Images display mKSCs that were seeded on 0% AA coated gradients (representative for 25% AA) and 100% AA coated gradients (representative for 75% AA). Scale bar: 100 μ m..... 196

List of Tables

Table 2.1: Seeding density and cell culture conditions of the particular cell type when meant to be analysed on polyacrylate substrates.....	44
Table 2.2: Seeding density and cell culture conditions of cell lines seeded on substrates and analysed using either FACS or PCR.....	51
Table 2.3: Composition of the primer and cDNA mastermix for cDNA amplification.	54
Table 3.1: Presence of functional groups that polyacrylates are equipped with.	62
Table 3.2: Theoretical trend of functional groups among polyacrylate polymers.....	62
Table 3.3: Theoretical trend of steric hindrance among polyacrylate polymers.	62
Table 3.4: Elemental surface composition. Shown are the elemental percentages of carbon (C), oxygen (O) and nitrogen (N) as analysed for each substrate and the O/C and N/C ratios. All data were obtained via analyses of the survey spectra.	64
Table 3.5: Elemental surface composition in per cent. All data were obtained by curve fitting analyses of C1s / O1s and N1s high resolution spectra.	66
Table 3.6: Average CAs obtained for polyacrylates used in this study.	68
Table 3.7: CB values obtained for polyacrylates in distilled water. Samples were either directly measured or exposed to FBS for 2 h prior measurements.	71
Table 4.1: Qualitative morphological grading of cytotoxicity of extracts, adapted from [274]. These standards allow a relation of cell morphology with cytotoxic effects.	94
Table 5.1: Elemental surface composition of homo- and copolymers. Shown is the elemental percentage of carbon, oxygen and nitrogen as well as the O/C and N/C ratios to allow a compare between substrates. All data were obtained via analyses of the survey spectra.	156
Table 5.2: Elemental surface composition of plasma polymer gradients. Shown is the elemental percentage of carbon, oxygen and nitrogen as well as the O/C and N/C ratios to allow a compare between substrates. All data were obtained via analyses of the survey spectra.	156
Table 5.3: C1s peak composition of homo- and copolymers. All data were obtained by curve fitting analyses of C1s high resolution peaks.	157
Table 5.4: C1s peak composition on gradients. All data were obtained by curve fitting analyses of C1s high resolution peak.	158
Table 5.5: Plasma polymer CAs.....	162
Table 5.6: CB values obtained for homo- and copolymers in distilled water. Samples were either directly in water or 2 h post incubation in FBS.	165

List of Equations

Equation 2.1: Young's equation.....	33
Equation 2.2: Wetting force.....	35
Equation 2.3: Calculation of the root mean square roughness.	36
Equation 2.4: Hooks law.	37
Equation 2.5: Force calculation according to the DMT model.	37
Equation 2.6: Determination of the elemental kinetic energy E_{kin}	38
Equation 2.7: Molar mass.	41
Equation 2.8: Avogadro constant.	41
Equation 2.9: Population doubling time.	47

List of Abbreviations

	AA	Allylamine
	AcAc	Acrylic acid
	AFM	Atomic Force Microscopy
	AKI	Acute kidney injury
	ALDH	Aldehyde-dehydrogenase
	ASC	Adult stem cell
	AuNPs	Gold nanoparticles
	BM	Bone marrow
	BAE cells	Bovine aortic endothelial cells
	BAS	Biologically active peptides
	BTL	Biomer Technology Ltd.
	CA	Contact angle
	CB	Captive bubble
	CBB	Coomassie Brilliant Blue
	CKD	Chronic kidney disease
pp	CCM	Polymer conditioned cell culture medium A
	DCA	Dynamic contact angle
	DG	Diethylene glycol dimethyl ether
	DN	Double negative
	DP	Double positive
	ECM	Extracellular matrix
	EpCAM	Epithelial cell adhesion molecule
	ESCs	Embryonic stem cells
	ESP	Embryonic stem cell polymer
	ESRD	End-stage renal disease
	FACS	Fluorescence-activated cell sorting
	FBS	Foetal bovine serum albumin
	F-BSA	Fluorescently labelled bovine serum albumin
	FWHM	Full width at half maximum
	FZD7	Frizzled-7
	HSCs	Hematopoietic stem cells
	KSCs	Kidney stem cells
m	KSCs	Mouse kidney stem cells
	KPCs	Human kidney progenitor cells
f	KPCs	Human foetal kidney progenitor cells
i	KPCs	Human infant kidney progenitor cells
m	L929	Mouse fibroblasts
	MSCs	Mesenchymal stem cells
	NCAM	Neural cell adhesion molecule
	NTC	No-topography control
	OD	1,7-Octadiene
	Pa	Pascal
	PBS	Phosphate buffered saline

	PDT	Population doubling time
p	HEMA	Poly-2-hydroxyethyl methacrylate
ci	Podocytes	Conditionally immortalised podocytes
	PTCs	Proximal tubule cells
ci	PTCs	Conditionally immortalised proximal tubule cells
	PSCs	Pluripotent stem cell
i	PSCs	Induced pluripotent stem cells
	RGD	Arginylglycylaspartic acid / Arg – Gly - Asp
	RMS	Root mean square
	sccm	Standard cubic centimeters per minute
	SCID	Severe combined immunodeficiency
	TCP	Tissue culture plate
	XPS	X-Ray Photoelectron Spectroscopy

1 Introduction

Kidney disease is common and associated with significant comorbidities, high risk of mortality and high health care costs. The prevalence of chronic kidney disease (CKD) in the UK is estimated at about 6.8 to 8.5% of the adult population and rising, with an associated cost of around £1.45 billion [1, 2]. Ultimately it may lead to end stage renal disease (ESRD), with dialysis or renal transplantation being the only treatment options. The problem with dialysis is that it does not replace all of the functions of the kidney, leading to increased rates of morbidity and mortality. Transplantation is the better option but there is a shortage of suitable organs. Therefore there is a need for novel therapies to improve the outcome of patients suffering from CKD.

There has been a recent interest in potential stem cell therapies for kidney patients, particularly since a number of areas within the nephrons, the kidney's functional units, have been identified that contain putative kidney progenitor or stem cell populations [3-7]. Stem cells are remarkable cells with the potential to self-renew and to differentiate into different cell types of the body. Within the last decades scientists have been working intensely on stem and progenitor cell characterisation, localisation and potential applications for regenerative medicine. If these cells could be isolated, expanded and differentiated *in vitro*, it would allow the study of physiological and pathophysiological processes and the possibility of genetically modifying patient-derived cells. Moreover, by directing the differentiation of the cells into particular specialised cells, it may allow us to explore the underlying mechanisms of disease progression and identify new drug therapies.

However, it can be challenging to devise appropriate cell culture protocols for directing cell differentiation because cell behaviour and differentiation is regulated by various factors in the environment, including soluble factors, such as growth factors and cytokines, and solid

factors, such as extra-cellular matrix molecules. Biomaterials can assist in overcoming these impediments as they can be developed in a way that allows us to mimic physical, chemical and mechanical properties of a cells extracellular environment, which can guide cell behaviour and differentiation.

1.1 Biomaterials as stem cell regulators

Biomaterials have a variety of applications *in vitro*, such as cell culture platforms, but also *in vivo*, i.e. as scaffolds for cell transplantation. Biomaterials can differ widely in their composition depending on their purpose. For example, metals, such as titanium and chromium- based alloys, are often used in orthopaedic prosthesis whereas ceramics, such as hydroxyapatite, are commonly employed for bone reconstruction [8, 9]. Particularly polymers are widely used in implantable devices, such as in cardiovascular and ophthalmic applications [10, 11]. A good material for biological contact should meet a number of criteria, including non-cytotoxicity, promotion of cell-substrate interactions, limited stimulation of immune responses as well as compatibility with aqueous solutions and physiological conditions [12].

Especially in the field of (stem) cell culture polymers are widely used. These are long chain or branched molecules, generally composed of carbon, hydrogen, oxygen and nitrogen that are arranged in repeating monomeric units. Generally one can classify between natural and synthetic polymers [13, 14]. Natural materials, such as hyaluronic acid or agarose, are often employed for repair or replacement of damaged human tissues [15, 16]. On the other hand, many synthetic polymers have been developed and studied in terms of cell culture and biomedical research. They are often more advantageous, as they can be of high purity and are easily reproducible and tuneable in terms of physicochemical properties or in response to external stimuli, including temperature and pH [17-19]. Recently also 3D materials, such

as hydrogels or foams, have become increasingly recognised as they can often more closely represent the physiological environment [17].

1.1.1 Mimicking extracellular matrices and the stem cell niche

An essential part of tissues is the extracellular space that is largely composed of a complex network of macromolecules, and establishes the extracellular matrix (ECM) which is comprised of two major classes of biomolecules: glycosaminoglycans (GAGs) and proteins, such as laminin and collagen ([Figure 1.1](#)). The ECM is a key regulator of cellular function and critical for the maintenance of tissue homeostasis [20-22]. It furthermore provides a supportive scaffold for cells and tissues and presents specific physicochemical cues that influence cell fate. Cells anchor to an underlying substrate through specific cell surface receptors, integrins (transmembrane receptors), that connect the intracellular cytoskeleton to the substrate, which results in the formation of focal adhesions (cell–matrix adhesions) [23]. Moreover, the ECM is an important component of the stem cell niche that is responsible for the regulation of stem cells. An increasing understanding of the interactions between ECM and cells *in vivo* has raised interest in developing biomaterials that mimic the extracellular environment and its physicochemical properties. A number of recent studies have highlighted the importance of surface nano- and microscale structures, chemistry and elasticity of the ECM in regulating cell behaviour, including morphology, differentiation or migration [24-28]. This has led to an increased development of natural biomaterials that are based on ECM proteins [25, 29-32].

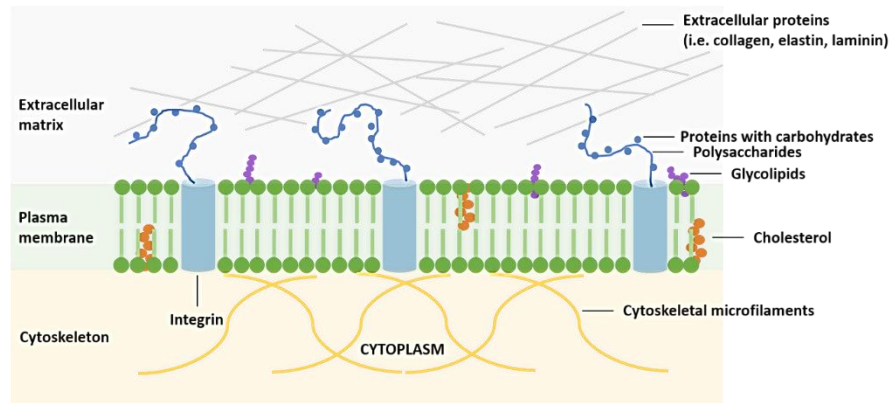


Figure 1.1: The extracellular matrix consists of a complex network of macromolecules: structural proteins, proteoglycans and adhesive glycoproteins that support the attachment of cells to the matrix.

1.1.2 Biomaterial-cell interface and cellular regulation

A large number of proteins that commonly comprise the ECM have been used in order to support and manipulate cell behaviour *in vitro*. Also the modification of synthetic materials with peptide sequences that function as cell-binding motifs within ECM proteins, such as RGD (arginine-glycine-aspartic), PDSGR (proline-aspartic acid-serine-glycine-arginine) and YIGSR (tyrosine-isoleucine-glycine-serine-arginine) have been commonly conjugated to surfaces (chapter 3.1, p 56) [33-37].

However, the cell-substrate interface is a complex microenvironment in which each directs one another's fate. The material directs cell behaviour through its physical and chemical properties, such as topography, elasticity or the presence of chemical cues, whereas cells sense the material properties, can remodel its surface and respond by adapting their behaviour, such as cytoskeletal organisation and differentiation (Figure 1.2) [38-49]. Understanding these interactions between cells and their surroundings in both, *in vivo* and *in vitro*, are highly important for the development of new materials for biological applications. These cues are increasingly adapted in order to create defined biological microenvironments [50]. A major drawback of natural biomaterials is the difficulty to

manipulate their physical and chemical cues, whereas synthetic biomaterials can be designed and tuned in order to mimic these properties.

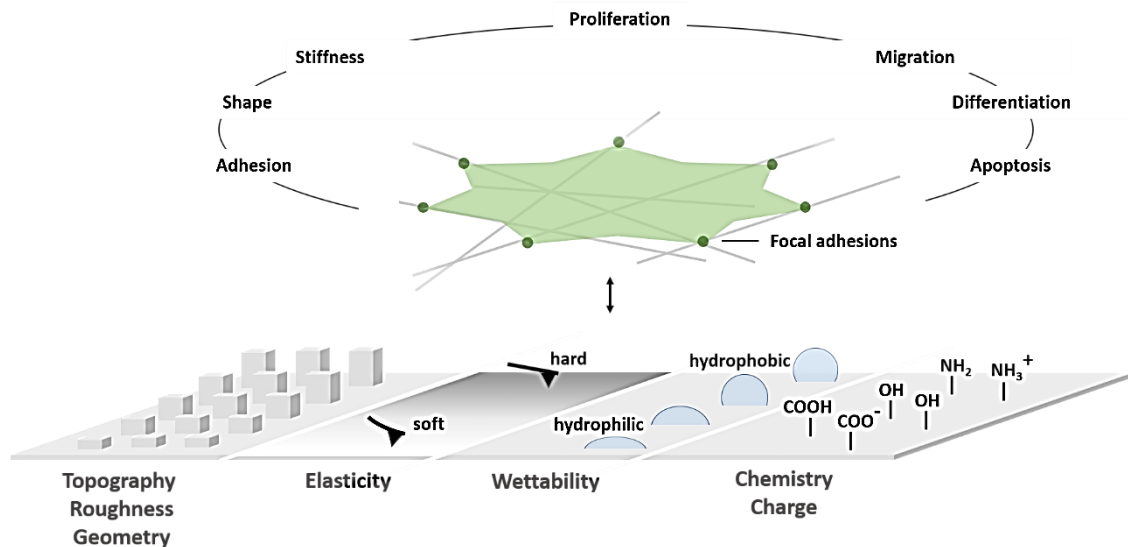


Figure 1.2: Cells adhere to a substrate (i.e. ECM or biomaterial) through focal adhesions and sense its physicochemical cues, including topography, elasticity, wettability and chemistry. Cells then adapt their properties in response.

1.1.2.1 Substrate chemical properties

Surface chemistry is an important parameter that highly influences cell behaviour. Although the exact mechanisms are unclear, it is often correlated with a release of signalling molecules (i.e. growth factors or glycoproteins) through cell adsorption [51]. Therefore, the employment of simple functional groups to direct cell behaviour is rapidly evolving. For example, *Benoit et al.* investigated the effects of small molecules on mesenchymal stem cell (MSC) differentiation on 2D arrays and found that phosphate groups (physiological important for bone mineralisation) directed cell differentiation into osteocytes, whereas carboxyl groups (mimic GAGs in cartilage) directed cell differentiation into chondrocytes and *t*-butyl groups (mimic lipid sustained environment) into adipocytes [45]. Others directed MSC differentiation by modifying silane surfaces with various functional groups (-CH₃, -NH₂, -SH, -OH, -COOH) and have shown that functional groups control protein adsorption and therefore cell behaviour [46]. Furthermore, they discovered that -CH₃ surfaces maintained the MSC

phenotype, while $-NH_2$ and $-SH$ modification directed cells towards osteocytes and $-OH$ and $-COOH$ groups towards chondrocytes [46]. Moreover, material inherent surface groups can be further modified, i.e. by covalent binding of biological molecules, such as peptides, growth factors or GAGs to influence cell behaviour [32, 52-54].

Interestingly, the impact of surface chemistry on cell behaviour and differentiation has opened new possibilities for developing surfaces that allow screening of cellular response on a large number of data points across a single surface to support the identification of the optimal surface composition for the desired cell type [55-57]. In this respect plasma polymer gradients have proven particularly useful, as these can be applied thinly and smoothly onto any surface without changing the underlying topography [32, 56, 58]. For example, the influence of surface chemistry on MSCs has been explored using acrylic acid – diethylene glycol dimethyl ether (AcAc - DG) plasma (surface chemical) gradients, where it was found that cell attachment increased on AcAc rich areas, whereas it was rather inhibited on DG rich areas [56]. Moreover, this resulted in a cell density gradient that in turn triggered cell differentiation into osteocytes whereas differentiation into adipocytes was independent of cell density [56]. Such novel strategies of screening are emerging rapidly.

Alongside surface chemistry, surface charge has been correlated with cell response due to the promotion of attractive or repulsive forces [59]. The cell membrane contains proteins that are negatively charged and therefore adhere to positively charged surfaces [60]. For example, positive surface charge typically enhances cell attachment and spreading of osteoblasts and fibroblasts compared to negative or neutral charges [61]. Similar results were obtained on nerve cells [62].

1.1.2.2 Surface wettability

Surface wettability is a key factor in regulating cell behaviour. Generally, cells show greater adhesion and spreading on hydrophilic surfaces [63-66]. This was shown on a number of cell

types, including osteoblasts and fibroblasts [67, 68]. However, hydrophilic surfaces can also enhance cell differentiation. Osteoblast-like cells, for example, increase cell attachment and metabolic activity, collagen production and osteogenic differentiation on hydrophilic surfaces [69-71]. Similarly, *Ayala et al.* systematically altered substrate hydrophobicity by amending the alkyl side chain length whereas chemical and mechanical properties were kept constant. They found that MSC adhesion, cytoskeletal organisation and differentiation was highly dependent on substrate wettability [72]. In contrast, others claim that there are no direct correlations between wettability and cell response as changes in surface wettability are often accompanied by changes of other surface properties such as chemistry and topography [73, 74]. For example, plasma treated hydrophilic poly (l-lactic acid) was found to support cell adhesion, growth and neurite outgrowth on nerve cells. However, hydrophilicity through plasma treatment was accompanied by chemical changes of these surfaces [75, 76].

It has to be underlined that protein adsorption will occur almost immediately once a surface is in contact with physiological fluids or cell culture medium, which will affect surface wettability [68, 77, 78]. Proteins attach particularly to hydrophobic surfaces, whereas adsorption onto hydrophilic surfaces is energetically unfavourable [79-82]. Moreover, the identity of these proteins might influence cell response. Vitronectin and collagen I for example were shown to promote the differentiation of MSCs into osteocytes [83]. Others claim that these findings cannot be generalised [67, 80].

1.1.2.3 Surface topography

Cells are highly sensitive to nanoscale features of the ECM *in vivo*, which makes the incorporation of topographical cues (roughness) interesting for the development of biomaterials [71, 84-87]. Depending on the extent of surface nanotopographic features it is possible to distinguish between nanoroughness (< 100 nm), microroughness (100nm to 100

μm) or macroroughness ($>100 \mu\text{m}$), all of which will affect cell types differently [88]. For example, neuronal cells displayed enhanced spread on nanorough surfaces, whereas microscale roughness inhibited these effects with cells being rather round-shaped and poorly branched [89]. Osteoblasts responded with higher proliferation and improved formation of osteoblastic features on rough surfaces compared to smooth ones [71, 90-93]. Also, substrate pore size can impact cell response. Osteoblast-like cells show inhibited proliferation and spread with increasing micropore size, but an improved differentiation rate [91]. Similar observations were made on mesenchymal stromal cells that showed increased spreading, adhesion, cytoskeletal organisation and osteoblastic differentiation in response to surface topographical cues [43].

The impact of nanotopography on cell response has caused the rapid emergence of a large number of substrates with various types of surface features. New techniques allow the creation of different shapes of biomaterials, such as nanospheres, nanotubes or nanofibers, but also the introduction of surface features such as gratings, nanoparticles or pits that can be randomly or symmetrically distributed, all of which can effect cell response significantly [94-98]. For example, MSCs were shown to align and elongate along nanogratings and undergo transdifferentiation towards neuronal cell lineages under appropriate cell culture conditions [99, 100]. Endothelial cells form aligned capillary-like tubes when cultured on nanogratings [101]. Also the geometric control of surface topographical cues can influence cell response [42, 102-104].

Another interesting form of biomaterials are nanofibres and nanochannels as they closely display basement-membrane-like fibres (5 to 200 nm) and pore size (3 to 80 nm) [105]. The fibres allow the development of scaffolds and 3D matrices which enable us to explore cell behaviour in another dimension. For example, ESCs cultured on electrospun fibrous scaffolds showed large cell spread, improved cell-cell interactions and differentiation towards

neuronal cell lineages although these findings were simultaneously correlated with substrate stiffness [106]. The design of new biomaterials with nanotopographic cues is rapidly evolving and will contribute to a greater understanding of the mechanisms by which cells respond to and sense nanofeatures.

1.1.2.4 Surface mechanical properties

Another factor that is increasingly recognised to influence cell response are the surface mechanical properties (elasticity / stiffness) [107, 108]. The cellular natural environment contains a large number of external cues, including surrounding cells, biomolecules and the ECM, all of which transmit information to regulate cell fate [109]. The tissue stiffness differs considerably, ranging from 1 kPa (brain) to few kPa (muscles, adipose tissue) to GPa (bones) [26]. *In vitro* it has been shown that MSCs cultured on substrates with varying stiffness commit to differentiate accordingly: soft (brain-like) matrices direct towards neurogenic cells, stiffer (muscle-like) matrices give rise to myogenic cells and rather rigid (bone-like) matrices direct MSC differentiation towards osteocytes [26]. Generally, MSC attachment requires relatively hard substrates that mimic tissue closely [110].

Moreover, tissue mechanical properties are not static but rather change through physiological and pathophysiological processes. For example, injury of the connective tissue causes an alteration of the ECM stiffness. This can be sensed by fibroblasts which, in response, migrate, synthesize ECM (fibrogenesis) and differentiate into myofibroblasts. This is consistent with a study that found fibroblasts being able to remodel collagen gels and increase stiffness of the gels *in vitro* [111]. Moreover fibroblasts were shown to migrate towards stiffer regions when cultured on stiffness gradients *in vitro* [112]. Stiffer substrates also increased fibroblast sensitivity towards transforming growth factor beta (TGF- β 1), which resulted in the increased expression of smooth muscle actin (α -SMA) [113]. Therefore, the

mechanical surface properties are an important cue to direct cell behaviour and may be a great advance in exploring biological process *in vitro*.

1.2 Stem and progenitor cells

1.2.1 Background

Stem cells have the capability to self-renew and differentiate into specialised cells [114-116]. For that they either divide symmetrically to form two identical daughter stem cells or asymmetrically to generate a copy of themselves and another, more committed, stem (progenitor) cell that will eventually undergo lineage specific differentiation [117].

The first steps towards the term “stem cell” arose in the early 20th century when the existence of “(hematopoietic) stem cells” (HSCs) was firstly proposed [118, 119]. Shortly after, scientists first proved the presence of HSCs in mouse bone marrow (BM) [120]. Only a few decades later the first scientific evidence was provided for the existence of self-renewing cells in the BM and stem cell activity in the brain [114, 121]. In the 1980s, *Evans et al.* and *Martin et al.* independently isolated embryonic stem cells (ESCs) from the inner cell mass of mouse embryos [122, 123]. Only one decade later, ESCs were isolated from a human embryo [124].

1.2.2 Embryonic stem cells and their progeny

The fusion of a sperm cell and an egg ultimately results in a fertilised one-cellular egg ([Figure 1.4](#)). This single cell and its early progeny (up to morula stage) are totipotent blastomeres that are capable of differentiating into any cell type in the body as well as extra-embryonic tissues (i.e. placenta and umbilical cord) [125]. After the blastocyst forms, the embryo comprises an outer layer of trophoctoderm, a blastocoel cavity and an inner cell mass containing pluripotent ESCs. These cells generate all three germ layers (ectoderm, endoderm and mesoderm) and the germ line as well as some extraembryonic tissues. ESCs carry a great

potential for studying biological developmental processes as well as in pharmaceutical and medical research areas [126-128].

1.2.3 Adult stem cells and the stem cell niche

Adult (somatic) stem cells (ASCs) are undifferentiated cells that can self-renew, maintain homeostatic conditions and repair and regenerate cell types of the tissue in response to injurious stimuli [129-131]. However, unlike ESCs, they are not pluripotent, but either multi- or unipotent. ASCs are present in many tissues and have therapeutic potential. For example, HSCs are multipotent stem cells that continuously renew blood and give rise to all blood cell types. However, they cannot differentiate into specialised cells of other tissue [132, 133]. Another type of ASCs are MSCs which can differentiate into a variety of specialised cells including osteoblasts [134], chondrocytes [135, 136] and adipocytes [137, 138] and are therefore very beneficial for potential stem cell therapies. If scientists were able to identify and characterise ASCs and be able to control their differentiation precisely, these cells could become the foundation for transplantation-based therapies [139-141].

Within the body stem cells live in tissue specific microenvironments, the so-called 'niches', where they are kept in a quiescent state until they are mobilised to proliferate and/or differentiate [142, 143] ([Figure 1.3](#)). The niche regulates and supports the cells and is the centre of interactions between stem cells and other stem cells, progenitor cells, terminally differentiated cells, adhesion molecules and the extracellular environment, which includes chemokines, cytokines and growth factors [144, 145]. Once injurious signals arise, i.e. due to tissue injury or disease, the stem cells respond to the microenvironment, they proliferate and then self-renew, some then exit the niche and differentiate into the desired cell types in order to repair and regenerate tissue [142, 143]. Within the niches, the ECM is an important component that is characterised by its tissue specific biochemical and physicochemical properties, and has a major impact on tissue homeostasis and regeneration [20, 21].

The stem cell niche starts directing cell behaviour during early fetal development. During adulthood the stem cells and their niche are continuously interacting in order to maintain one another. Within the body various niches have been identified, the first being the HSC niche located in the BM [146]. Many other niches have been identified since, including niches in the skin, brain and within the skeletal muscle [147-149]. However, scientists continue to study the composition of stem cell niches in order to replicate or mimic its properties *in vitro* and much progress has been achieved in recent years [150]. The development of such culture systems is important for the maintenance and expansion of ASCs as these generally undergo ageing *in vitro* which causes the loss of stemness [151-155]. Also synthetic engineered biomaterials offer alternative approaches and hold great promise for regulating stem cells as they can mimic characteristics of stem cell niches and the ECM, particularly biophysical properties, such as topography and elasticity [26, 27, 145, 156, 157]. Both approaches may support the long term cell culture, proliferation and eventually directed cell differentiation.

1.2.4 Progenitor cells

Generally, stem cells generate an intermediate cell type, so-called precursor or progenitor cells that are partly differentiated, cell lineage committed early descendants before they fully differentiate. Progenitor cells can be unipotent [158, 159] and are limited in their self-renewal capacity and differentiation potential [160]. As with less committed stem cells, their main purpose is regeneration of damaged tissue [161, 162]. Therefore, progenitor populations are attractive candidates for studying developmental processes and tissue homeostasis, but also offer alternative treatment options for severe diseases in regenerative medicine, including gene therapy, cell transplantation and tissue engineering [163-166].

1.2.5 Induced pluripotent stem cells

In 2006 *Takahashi et al.* made significant progress in the field of stem cell research by developing a method for the induced dedifferentiation (reprogramming) of somatic cells into

an embryonic stem cell-like state by using retroviral transduction to introduce the 4 transcription factors Oct4, Sox2, Klf4 and cMyc [167, 168]. These cells were called induced pluripotent stem cells (iPSCs). Recent advances in the field show that iPSCs can be used to generate renal progenitor cells and specialised renal cells and therefore have great potential for future use in renal regenerative medicine therapies [169-171].

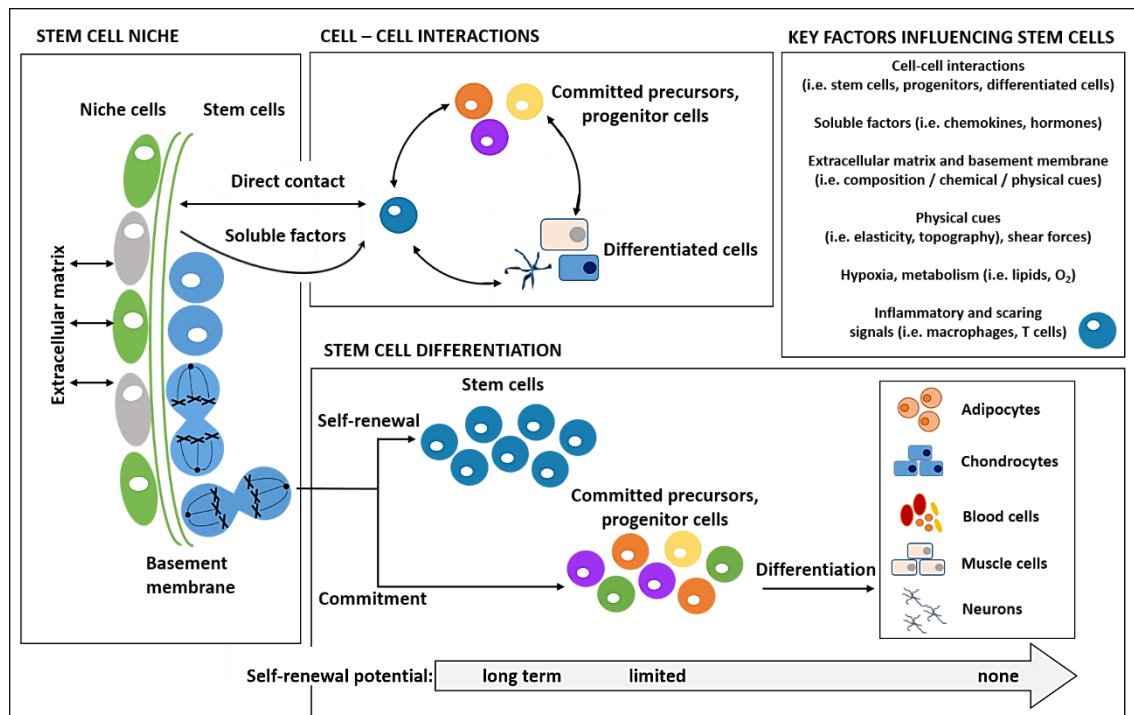


Figure 1.3: Within the stem cell niche, stem cells are kept in a quiescent state and stem cells are continuously interacting with their environment that includes the extracellular matrix, other stem cells, progenitors and differentiated cells. The combination of all signals that derive from the stem cell environment cause self-renewal and the maintenance of a stem cell pool. Once injurious signals arise (i.e. inflammatory cytokines) stem cells self-renew, proliferate and differentiate into functional cells.

1.2.6 Stem cells in regenerative medicine

The ability of stem cells to self-renew and to differentiate into specialised cells makes them very attractive candidates in the field of clinical therapies and regenerative medicine [172, 173]. However, the procurement of human ESCs requires the destruction of the embryo and is thus associated with some ethical issues [174]. On the other hand, ASCs can be harvested easily without ethical concerns from adults, infants, the placenta and umbilical cords but they have limitations [141, 171, 175, 176]. The cells have to be harvested from a source that

provides the specific cell lineage that is required. Moreover, as with ESCs, it remains challenging to culture these cells without loss of stemness [151-153]. However, a number of advances in regenerative medicine have been successfully carried out with these cells.

For example, HSCs, which reside within the BM, peripheral blood and umbilical cord blood, are pluripotent and give rise to all hematopoietic and lymphoid cell lineages [177-180]. The intense growth and expansion of HSCs in the body due to the continuous blood renewal makes them very interesting subjects for clinical therapies. HSCs are already used in clinical therapies, i.e. for the treatment of patients who suffer from leukaemia or lymphoma [181, 182]. Cancer patients who obtain chemotherapy often endure a loss of blood cells which can be counteracted by the transplantation of healthy HSCs in order to refunctionalise and replace damaged and dead cells [183]. Moreover, HSC transplantation can correct several genetic diseases such as blood or immune system disorders, including hemoglobinopathies, defects in leukocyte production, sickle cell anaemia and thalassemia [184-186]. *Abbott et al.* were the first to use HSCs as a vector for delivering genes intended to correct blood diseases [187]. There is, moreover, growing interest in genetically modified HSCs for novel therapies like the creation of resistances against infections, such as the human immunodeficiency virus type 1 (HIV-1) [188].

Also MSCs, multipotent stem cells, are thought to hold great potential in regenerative medicine. The BM stroma and blood vessel walls in most tissues contain MSCs, but MSC-like populations were also identified in other tissues, including adipose, muscle, cartilage and liver [189-193]. Within the body MSCs are involved in processes such as osteogenesis, adipogenesis and cartilage formation. It is widely believed that MSCs are involved in the repair of different tissue types, such as lungs and kidneys [194-196]. Moreover, there is evidence that MSCs can mobilise repair mechanisms via immune system modifications and suppression of inflammatory processes [197, 198]. Therefore MSCs are investigated for their

benefits in a wide range of disease conditions [199, 200]. First promising results were obtained on patients suffering from end-stage osteoarthritis [201].

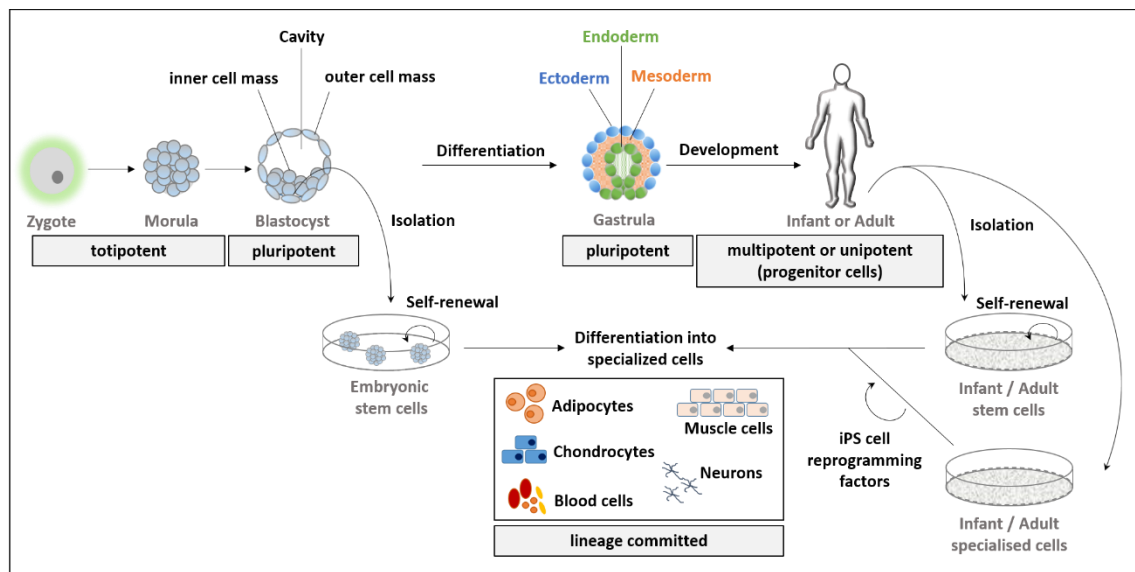


Figure 1.4: The fusion of sperm and egg results in the formation of a zygote, the ultimate, totipotent stem cell. Through cell division these cells will further differentiate to create a blastocyst with an outer and an inner cell mass, the latter one being the source of embryonic stem cells. Embryonic stem cells can continuously self-renew, but also further differentiate into all three germ layers (endoderm, mesoderm and ectoderm). These will then further develop to form an entire organism. Adult stem cells are present in tissue niches. They can also self-renew, but have a rather limited, more committed, differentiation potential. Moreover, specialised cells can be reprogrammed to become pluripotent again. All three cell types, embryonic, adult and induced pluripotent stem cells are known to be able to differentiate *in vitro* under the appropriate cell culture conditions. Adapted from Connor *et al.* [202].

1.3 Kidney disease and kidney stem cells

1.3.1 Background

The kidneys are highly complex organs that are responsible for the removal of metabolic waste products from the blood, tubular reabsorption of nutrients and the tubular secretion of solutes and wastes. Therefore they maintain important homeostatic functions, including the regulation and maintenance of electrolyte, fluid and acid-base balance [203, 204].

The nephrons are the main structural and functional units of the kidney and consist of a renal corpuscle and an associated renal tubule (Figure 1.5, p 17). Blood plasma filtration and urine formation (glomerular filtration) begins in the renal corpuscle through a collection of

capillaries, the glomerulus that is enclosed by an epithelial cup, the Bowman's capsule. The filtrate then enters into the renal tubule where a process of reabsorption and secretion is initiated. Within the proximal convoluted tubule water, nutrients, plasma proteins and ions are actively reabsorbed from the filtrate whereas within the distal convoluted tubule, ions, toxins and drugs are secreted and sodium ions are reabsorbed from the tubular fluid. The filtrate (urine) then enters into a system of collecting and papillary ducts and is taken to the bladder [203, 204].

Kidney diseases generally involve injury of the nephrons and are commonly acute or chronic. In acute kidney injury (AKI) or severe dehydrating illness the kidney function suddenly drops. However, it is mostly short-term, but is associated with a high risk of mortality and morbidity. In addition, AKI can also be caused by intrinsic diseases, such as glomerulonephritis and vasculitis, which can lead to worsening of renal function.

On the other hand, a long-term and progressive loss of the renal function is referred to as chronic kidney disease (CKD) and is generally divided into 5 stages with 1 being the initial and 5 being the most severe. As a result of the consequent limited kidney function, metabolic waste products can build up in the body and cause side effects, such as hypertension and anaemia. It also increases the risks of heart attacks and vascular disease.

The number of patients with CKD worldwide is rising and affects about 5–10% of the world population [205, 206]. Therefore, CKD is already a public health problem and should, if possible, be treated in the early stages [207, 208]. Yearly it is a significant expenditure for the public health system with medical costs for treatment estimated at £1.44 to £1.45 billion in 2009/2010, which is about 1.3% of all NHS costs per year in the UK [164]. Moreover, millions are spent on concomitant health issues such as strokes and myocardial infarctions [209, 210].

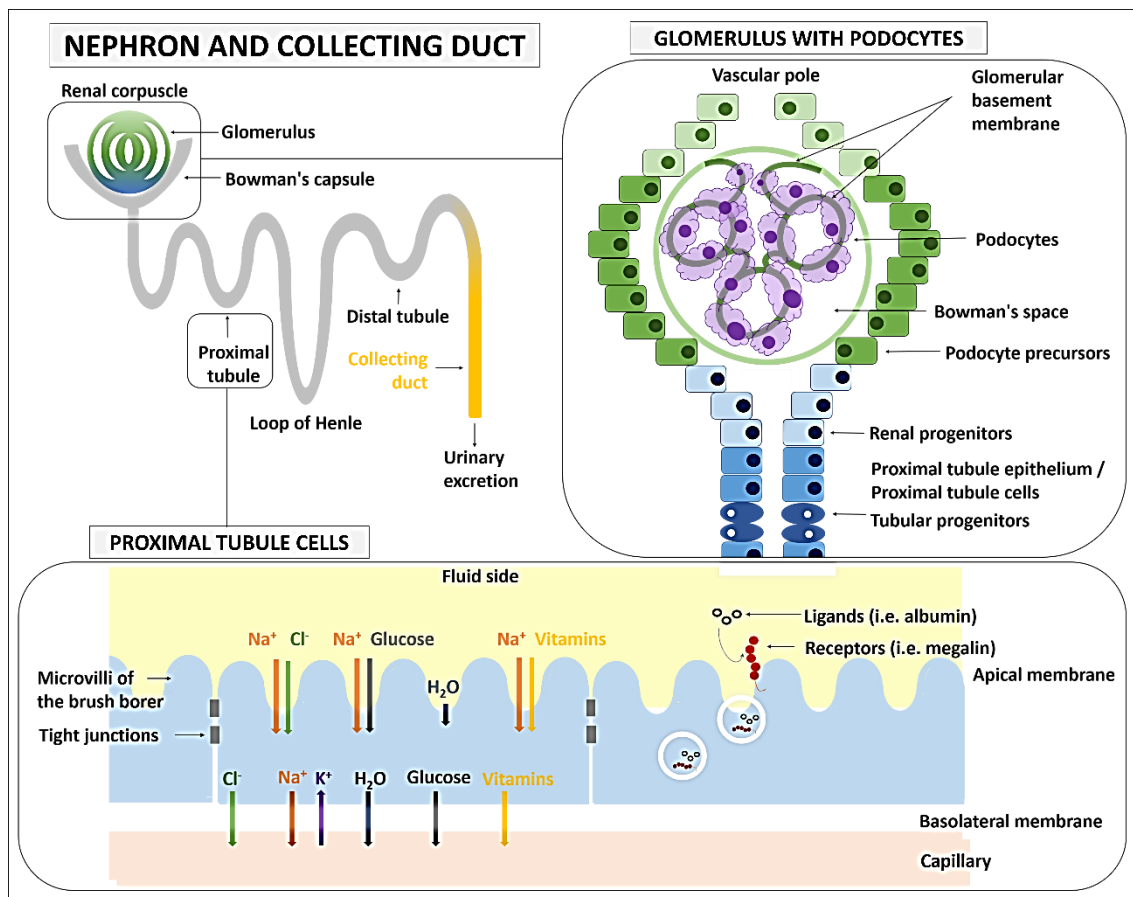


Figure 1.5: Simplified schematic of a nephron, the functional units of the kidney. Each nephron consist of a renal corpuscle which is associated with a renal tubule. The renal corpuscle is the place where blood plasma is filtered and urine formation begins. It consists of an epithelial cup, the Bowman's capsule that encloses a network of capillaries, the glomerulus. Podocytes (visceral epithelial cells) wrap around these capillaries. The current view assumes the presence of renal progenitors at the urinary pole of the Bowman's capsule, tubular progenitors are scattered along the tubules and podocyte precursors localise along the Bowman's capsule. The renal corpuscle is associated with the renal tubule that is comprised of several segments, one of them being the proximal convoluted tubule with the proximal tubule cells. It is responsible for the reabsorption of solutes from the filtrate (tubular fluid). At the fluid side, the proximal tubule cells have microvilli and the entire apical membrane contains a network composed of different receptors, coated pits and endosomes, whereas the basolateral membrane has multiple infoldings to increase surface area. Here most transport processes are driven by Na-K-ATPases.

CKD may eventually lead to kidney failure, also called end-stage renal disease (ESRD, less than 10% kidney function), which will ultimately require life-long dialyses or a kidney transplant [211]. However, dialysis is associated with higher morbidity and mortality rates. Also organ transplantation has drawbacks, such as limited availability of donor organs. Moreover, patients should be in a reasonable healthy state in order to survive the operation and the treatment with special drugs and immunosuppressants [212].

Therefore there is a high demand for novel therapies for kidney disease. An eventual replacement of diseased kidney cells with healthy cells can be difficult as the organs are often small and fibrotic in the later stages of CKD and ESRD, which may hinder the incorporation of such cells physiologically [164]. Research in these areas is ongoing, but will be a long-term goal. On the other hand, another promising approach aimed at preventing and tackling kidney disease is the development of drug-based therapies. However, one limitation is the lack of suitable *in vitro* cell lines and culture systems for relevant renal cell types, including podocytes and PTCs [213]. In this respect, biomaterial engineering holds great opportunities in terms of developing novel cell culture systems due to their advantages in providing relevant physicochemical cues to cells. This has opened new possibilities to direct the differentiation of progenitor and stem cells *in vitro* which can be very beneficial for drug development programs. This includes the identification of new drugs that hold potential for the treatment of patients with CKD or to prevent disease progression, as well as for the screening of new drugs to assess possible nephrotoxicity.

1.3.2 Podocytes

Podocytes (visceral epithelial cells) are complex, terminally differentiated cells and have a characteristic morphology, such as a distinctive voluminous cell body, large foot processes, a well-developed cytoskeleton, high cytoplasmic:nuclear ratio and a tendency to be binuclear (Figure 1.6) [214, 215]. They are located in the Bowman's capsule and wrap around glomerular capillaries. The podocyte foot processes increase cellular surface area and cause the formation of a slit diaphragm to support blood filtration.

Podocytes support glomerular structures and maintain the intra-glomerular hydrostatic pressure [216, 217]. In combination with glomerular endothelial cells and the glomerular basement membrane, they form a glomerular filtration barrier against protein loss. A

limitation of either of these functions can have severe consequences. Most kidney disorders are ascribed some kind of podocyte injury or loss.

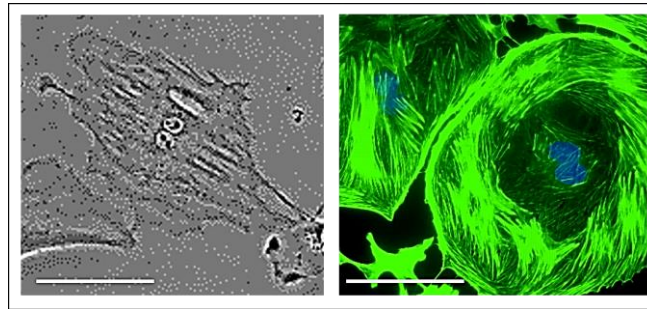


Figure 1.6: Phase contrast image (left) and F-actin and DAPI labelled (right) image of a podocyte. Scale bar is 100 μm .

In case of stress or injury, podocytes respond with vast changes in morphology. These include excessive hypertrophy, shedding of cytoplasm, increased turnover of cell material and foot process effacement (loss of the interdigitating foot process pattern), which is accompanied by cellular flattening and shortening of the foot processes. All of these changes can impair podocyte function [218-221].

A loss of podocytes can also occur as a result of glomerular diseases which often provoke severe symptoms including proteinuria that is often accompanied by nephrotic syndrome and renal failure. Both can lead to glomerulosclerosis, a renal disease with symptoms like glomerular inflammation and renal angiogenesis, and eventually to renal failure [222, 223].

A key stabiliser of the podocyte actin cytoskeleton, regulator of podocytes integrity and key player in the development and maintenance of foot processes is synaptopodin, a proline-rich actin associated protein that is involved in various intracellular signalling pathways and has also been linked to cell migration in kidney podocytes [224, 225]. Synaptopodin gene silencing in podocytes results in the loss of stress fibers, the development of non-polarised filopodia and impaired cell migration [224, 226]. Alongside synaptopodin also nephrin (NPHS1) and podocin (NPHS2) are proteins that are expressed in mature podocytes. Both are

coexpressed strongly in the cell membrane and partially colocalise with actin and are associated with the slit diaphragm, a multiprotein complex that connects podocytes through the pairing of nephrin molecules [227, 228]. Alongside nephrin, podocin is also involved in podocyte foot process formation via actin fibers [228]. Nephrin expression is regulated by the *WT1* gene (Wilms' tumor 1) that controls the differentiation of podocytes and is involved in podocyte homeostasis [229, 230]. Within the kidney, WT1 protein expression is restricted to podocytes [230].

Podocytes lose their proliferation capacity and develop cell junctions in order to connect their unique foot processes in the mature, terminally differentiated state to the glomerular basement membrane [227]. Therefore, the loss of podocytes can cause severe kidney injury and lead to CKD and ESRD. The importance of podocytes for kidney function has given rise to much interest in analysing the underlying mechanisms of podocyte injury and loss. However, the culture of mature podocytes *in vitro* is challenging as these tend to dedifferentiate, a process that is accompanied by the loss of foot processes and synaptopodin [225]. In addition, the culture and dedifferentiation of immature podocytes is accompanied by an irreversible growth arrest. The generation of conditionally immortalised podocytes (ciPodocytes, contain a temperature sensitive T antigen as transgene) that proliferate at a permissive temperature (33°C) and differentiate at a nonpermissive temperature (37°C) has helped to overcome this problem [227, 228].

1.3.3 Proximal tubule cells

The proximal tubule is a section of the renal tubule ([Figure 1.5](#)) with proximal tubule cells (PTCs) being the most populous cell types [231]. PTCs are characterised by a uniform polarised morphology, tight junctions between cells and strong expression of cytokeratin [232]. The PTC surface and function is increased through the presence of microvilli on the apical surface membrane and basal involutions within the basolateral membrane, which

contains Na⁺/K⁺ ATPases for the reabsorption of fluids [204]. Within the nephrons, PTCs are responsible for the reabsorption of many molecules, such as water, amino acids, glucose, urea and ions from the urinary filtrate, its pH regulation and excretion of organic acids (i.e. creatinine) and bases into the filtrate [204, 233]. Being responsible for so many renal physiological processes, these cells are often involved in tubulointerstitial kidney injuries, that may be inherited, congenital or acquired [234].

Megalin, a large glycoprotein, is an endocytic receptor in the PTC cell membrane, localised in cell surface microvilli, coated pits and endocytotic compartments. It is involved in protein reabsorption from the urinary filtrate [235-237]. When the transmembrane receptor cubilin binds to megalin (calcium dependent), albumin can bind to megalin and its endocytic uptake is mediated [238]. This process comprises the binding of albumin in clathrin-coated pits and subsequent endocytosis and degradation in lysosomes [236]. Malfunction of both transmembrane receptors can cause proteinuria [239].

Another characteristic PTC marker is alkaline phosphatase (AlkPhos), an enzyme that within the kidney, is only active in PTCs, where it is located in the brush border. AlkPhos is responsible for the hydrolysis of phosphomonoesters thereby releasing inorganic phosphate (dephosphorylation).

A large variety of drugs have been classified as nephrotoxic and some can cause AKI. For example, cisplatin (cis-diamminedichloroplatinum(II)) is a widely employed chemotherapeutic agent that has many side effects, one of which being nephrotoxicity [240]. High concentrations of cisplatin can induce necrosis in PTC monolayers [241], whereas lower concentrations induce apoptosis. About 20-30% of patients treated with cisplatin develop AKI [242]. Also a direct contact of PTCs with other toxins, such as antibiotics (i.e. gentamicin) or bacteria (i.e. sepsis accompanied by gram-negative bacteria), can result in acute tubular necrosis.

In addition, diseases originating from the glomeruli, such as glomerulonephritis, diabetic nephropathy or vascular injury will progress within the tubules and directly affect PTC function. Lastly, also protein overload can result in PTC injury, a process that is i.e. process characteristic for glomerular diseases.

As with podocytes, culture of PTCs *in vitro* is problematic because the cells tend to de-differentiate and downregulate key proteins, including megalin and organic anion and cation transporters [233, 243-245]. To overcome these problems, a conditionally immortalised PTC (ciPTC) line has been established which has extended proliferation capacity and expresses characteristic PTC markers and functional endogenous ion transporters [246]. As with podocytes, these cells also contain a temperature-sensitive T antigen that allows cell proliferation at a permissive temperature (33°C) and differentiation only at a nonpermissive temperature (37°C). ciPTCs present a powerful tool to study physiological and pharmacological processes.

In summary, podocytes and PTCs are essential components for glomerular filtration and tubular reabsorption processes and therefore key for the treatment of many glomerular and tubular pathologies.

1.3.4 Stem cells in the kidney

Kidney-derived stem cells (KSCs) were first identified in the mouse renal papilla and were found to have differentiation capacity and the ability to form spheres post injury [247, 248]. Our group isolated a clonal KSC line from neonatal mouse kidney (mKSCs) [249, 250]. This mKSC population was shown to have self-renewal capacity, differentiation potential and expressed the renal progenitor markers Pax2 and Wt1 [250, 251]. Moreover, these cells had the potential to differentiate into specialised renal cell types, including podocyte- and proximal tubule-like cells, but also into non-renal cell types, such as adipocytes and osteocytes under appropriate cell culture conditions. Therefore, this cell line presents a great

model system and enables the study of renal physiological processes but is also valuable for toxicological studies *in vitro*.

In recent years it has been suggested that progenitor cells exist in the adult human kidney [5, 7, 164, 252-257]. These cells often express two stem cell characteristic markers, CD133 (prominin-1) and CD24 (small cell lung carcinoma cluster 4 antigen) [258]. CD24 is a glycosyl-phosphatidylinositol-anchored protein that is expressed on immature cells, whereas CD133 is a transmembrane glycoprotein that is often found within cellular protrusions and is expressed in immature cells, but also differentiated epithelial cells [259, 260].

These putative CD133⁺/CD24⁺ progenitor cells were located within the parietal layer at the urinary pole of the Bowman's capsule and following isolation, displayed self-renewal potential and the capacity to differentiate into podocytes and PTCs [5-7, 261].

Lineage tracing studies have also shown that the kidney tubular epithelium contains mature cells (intrinsic tubular epithelial cells) that can initiate renal regeneration after injury [262, 263]. Upon injurious stimuli these cells lose the brush border, dedifferentiate into mesenchymal-like cells and migrate into regions with cell detachment and death. Subsequently they proliferate and redifferentiate into epithelial-like cells and contribute to the repair of the post-ischemic nephron [264, 265]. These results suggest that, within the mouse kidney, renal cellular replacement post injury is mediated by epithelial cells rather than stem cells. However, these experiments were only performed in mouse models and cannot be implemented in humans.

Based on these findings it is clear that particularly CD24 and CD133 have gained much recognition in terms of identifying KPCs. Double positive cells do indeed have self-renewal potential, maintain a stable phenotype in cell culture and can differentiate into podocytes and tubular cells *in vitro* and *in vivo* [5-7, 266]. However, there is still a dispute whether CD133⁺/CD24⁺ positivity is indeed sufficient to designate progenitors in the kidney.

In consideration of the above, it is still not clear whether there are stem or progenitor cells in the kidney. However, there are cell populations within embryonic, fetal and adult kidneys that have stem cell properties [6, 261, 267]. Many studies are focused on the identification of other potential KPC markers and new conjectures are published regularly. Among them are NCAM (neural cell adhesion molecule), EpCAM (epithelial cell adhesion molecule), FZD7 (frizzled-7) and ALDH (aldehyd-dehydrogenasen) [266-269].

1.3.5 Potential of kidney-derived stem/progenitor cells for renal therapies and drug discovery

Although dialysis supports kidney function, it is only a temporary solution and far from a healthy kidney. Therefore it is necessary to find new methods in order to repair or replace injured tissue. Generally the potential of stem and progenitor cells for regenerative therapies and tissue engineering is widely considered. There are numerous forms of kidney injury, within all of which different cell types are affected, which makes cell replacement therapies difficult and moreover require customised therapies for individual patients.

However, in terms of renal therapies a number of potential cell types have been identified. The molecular mechanisms of nephron generating fetal cells have been thoroughly analysed in the past, but their activation and the involvement in renal homeostasis and repair remains indistinct [270]. Putative KPCs have been isolated from different parts of the nephrons and were shown to have regenerative potential in animal models of renal disease [5-7, 271]. Therefore, adult KPCs may have the potential for regenerative therapies in patients with renal injury. However, KPC therapies are restricted to the limited availability of source, a short period of proliferation and senescence. Another potential candidate are iPSCs, as they allow the ethical issues of embryonic stem cells to be circumvented and the production of autologous tissue from a patient's own cells. However, their differentiation towards renal

cell types is time consuming, long-term culture is difficult and iPSCs have tumorigenic potential [270].

On the other hand, biomaterial engineering provides an alternative solution to study renal disease. Developing platforms that support the proliferation and differentiation of KPCs would allow the study of (patho) physiological processes *in vitro* and therefore support the development of novel therapies for patients suffering from kidney disease or help delaying disease progression. At present, drug therapies cannot prevent further damage but only delay disease progress. A drawback is that patients often respond to these drugs by developing side effects. Biomaterials could offer a solution to allow not only long-term culture of renal cells, but also generation of kidney-derived progenitor cells *in vitro* and therefore offer a solution for understanding disease progression. Therefore, biomaterials would allow the identification new drug therapies, provide scale-up opportunities for drug screening to predict eventual toxicity and, in the future, may support the *ex vivo* production of cells for subsequent transplantation.

1.4 Motivation and aim of this work

A major drawback in the field of stem cell research and therapies are the difficulties associated with culturing, expanding and directing differentiation on a large scale into specialised cells. The availability of numerous stem and progenitor cells is raising hope both for cell replacement therapies and also for understanding (patho) physiological processes and developing new drugs for potential therapies. In this respect, biomaterials are valuable tools as they have the potential to regulate cell function and direct cell fate. Biomaterials have been engineered and successfully used on a large scale to differentiate stem and progenitor cells, with MSCs being generally the cell type of choice. However, there is still a requirement for such platforms for directing stem cells and more committed progenitors in higher quantities. Although a number of renal progenitors and other stem cells, such as iPSCs

or MSCs, have been identified and successfully used to repair kidney injury, there are only a limited number of publications on culturing kidney progenitors and directing their differentiation into specialised renal cells.

Within this study, two physicochemically different types of polymers, polyacrylates and plasma polymers, were investigated for their potential to facilitate cell growth, expansion and differentiation of kidney stem/progenitor cells without the need for adding supplements, such as growth factors, to the cell culture medium. Mouse kidney-derived stem cells (mKSCs) were used as a renal stem cell model system which were explored for their ability to proliferate and generate functional renal cell types *in vitro*. These cells have typical stem cell properties, including unlimited self-renewal and multilineage potential, clonogenicity and have been previously shown to generate terminally differentiated renal cell types *in vitro*, such as podocytes and PTCs [249-251, 272]. In addition, preliminary studies were performed using fetal and infant human kidney-derived putative progenitor cells (KPCs). These cells do not have the capacity for extensive self-renewal and are therefore not stem cells. Moreover, their potential to be progenitor cells is also not convincing, as robust data showing their ability to differentiate to renal cell types is lacking. However, these cells have been extensively studied in recent years for their ability to ameliorate injury in models of kidney disease [5, 7, 261, 263].

Therefore, the aims of this study are as follows:

- (1) To develop novel polyacrylate substrates and thoroughly characterise their physicochemical properties, including surface chemistry, wettability, nano- and microscale topography and elasticity ([chapter 3](#), p 56)
- (2) To interrogate whether polyacrylates have the ability to direct the differentiation of mKSCs into specialised renal cell lines, namely podocytes and proximal tubule cells (PTCs) ([chapter 4](#), p 92).

- (3) To investigate whether polyacrylates can stimulate the differentiation of human putative fetal and infant KPCs into specialised renal cell lines, namely podocytes and PTCs (chapter 4, p 92).
- (4) To thoroughly characterise the physicochemical properties of plasma polymers composed of allylamine and octadiene, including surface chemistry, wettability, nano- and microscale topography, elasticity and surface nitrogen functional group densities (chapter 5, p 151)
- (5) To examine whether plasma polymer coated substrates have the capability to direct the differentiation of mKSCs into specialised renal cell lines, namely podocytes and PTCs (chapter 6, p 174).
- (6) To modify the surface topography of plasma polymer coatings using gold nanoparticles, in a homogeneous manner or in form of density gradients, to investigate the combined effects of surface chemistry and topography on the differentiation of mKSCs (chapter 6, p 174)

In summary, the main motivation of this work is the discovery of novel biomaterials that support the differentiation of mKSCs and KPCs into podocytes and PTCs as these are commonly effected in kidney injury. In the future, this would allow the study of (i) renal (patho) physiological processes (ii) the mechanisms that cause renal cells to be damaged in response to injurious signals and (iii) support the discovery of novel drugs for applications in drug discovery programmes to prevent or delay kidney disease and progression.

2 Materials and Methods

All solutions, chemicals, molecular compounds and equipment underlined are listed in the appendices (pp 239 - 245).

2.1 Biomaterial coatings

All polymer substrates were designed and synthesised by Biomer Technology Ltd. (BTL). The polymers were coated on glass coverslips using a dip coating procedure. The size of the underlying substrate was chosen corresponding to the analyses method employed.

2.1.1 Polyacrylates

2.1.1.1 Substrate preparation

All samples were prepared in-house at BTL. Substrates (glass coverslips) were coated with the polymer through a dip coating and subsequent drying process under clean conditions (Figure 2.1). Each polymer batch was tested for consistency of chain length by gel permeation chromatography prior all experiments. Glass cover slips were handled with tweezers, mounted to a tensile testing unit (*Lloyd Instruments LRX plus*) and subsequently dipped once into the polymer solution (3% in dimethylformamide (DMF) at a rate of 75 mm/min to coat ~50% of the coverslip and subsequently raised at the same rate. Samples were then transferred to a clip holder and placed into a fan assisted oven (*Shell lab*) at 85°C for approximately 15 mins to evaporate the solvent. The coverslips were then inverted and the dip coating – drying procedure was repeated once under the same conditions. Once all solvent evaporated and the samples were in undamaged condition, they were transferred into sterile tissue culture plastic (TCP) dishes and sealed until further use. Samples were only used within 4 weeks of production.

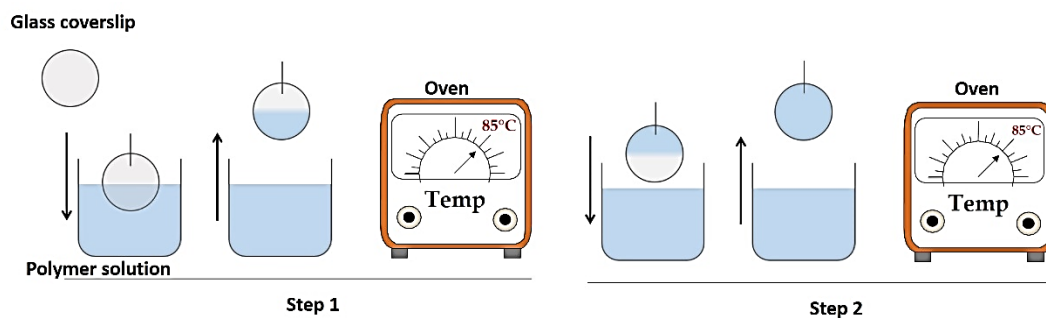


Figure 2.1: Polymer dipcoating procedure. Step 1: A glass coverslip was immersed halfway through into the polymeric solution (polymer diluted in organic solvent) and subsequently dried in an oven at 85°C for 15 min to evaporate the solvent. Step 2: The half coated coverslip was then inverted and the other, uncoated half was immersed into the polymeric solution. The polymer coated coverslip was then taken back to the oven and heated another 15 min at 85°C to evaporate the solvent. Samples were stored in sealed tissue culture plates.

2.1.1.2 Substrate sterilisation

If samples were used for *in vitro* cell culture, they were sterilised using a UV ozone sterilisation unit within the laminar flow hood for 10 mins each side. Subsequently samples were transferred into the cell culture dishes using sterilised tweezers.

2.1.1.3 Substrate cytotoxicity analyses

Cytotoxicity studies were performed on all polyacrylates to assess whether there were any toxic effects on cells. Non-direct contact (solution) analyses were performed using mouse fibroblasts (mL929), whereas direct-contact studies were implemented on mL929 cells and primary bovine aortic endothelial (BAE) cells ([chapter 2.4](#), p 45). 13 mm glass cover slips (VWR) were coated due to the ease of handling when using 24 well plates.

Polyacrylate coated substrates (22 x 64 mm²) were investigated for cytotoxicity in consistency with the British Standards ISO 10993 part 5 [273, 274]. All experiments were performed in three biological and technical replicates.

Experimental setup was as follows (Figure 2.2):

Start point / 0 h:

- (1) mL929 cells were seeded in 24 well plates at a density of 1×10^4 cells / well and left for 48 h (confluence reached) under standard cell culture conditions.
- (2) Contemporaneously, eluant (polymer conditioned cell culture medium A, pcCCM) was prepared as follows: for each experiment, 60 cm² of sterile polymer coated coverslips were incubated in 20 mL cell culture medium A in sterile 50 mL centrifuge tubes, shaken vigorously and incubated under cell culture conditions (5% CO₂, 37°C).

Half-time , 48 h:

- (1) After 48 h the eluant (pcCCM) was filter sterilised through a sterile 0.2 um filter. Subsequently this eluant was diluted in standard cell culture medium (cell culture medium A) to obtain concentrations of eluant (pcCCM) : cell culture medium A of 10%, 50% and 100% (v/v).
- (2) mL929 cells were then incubated in these (diluted) eluant solutions for a further 48 h. The negative control (not cytotoxic) was cell culture medium A (0% eluant) and positive control (cytotoxic) was in latex incubated medium.
- (3) Cells were examined for cell death 24 and 48 h post incubation in the eluant and the experiment was only continued when the positive control showed healthy cells and the negative control cell death.

End point, 96 h:

- (1) After 48 h exposure to the eluant (pcCCM), cells were washed twice with PBS, fixed with 4% (w/v) paraformaldehyde (PFA) and stained with methylene blue (0.04% (v/v) in ddH₂O) for 15 mins at room temperature. Subsequently cells were washed until PBS was clear and visualised under the light microscope.

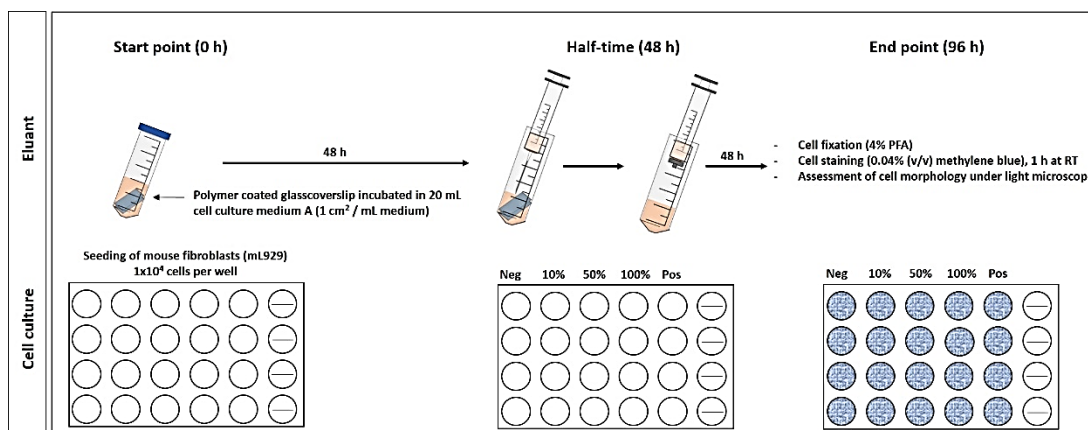


Figure 2.2: Experimental setup of cytotoxicity experiments on polyacrylate substrates using mL929 cells.

2.1.2 Plasma polymer coatings

All plasma polymer coated substrates were provided by the University of South Australia. Cytotoxicity studies were not performed on plasma polymer coatings as these were already established and analysed as cell culture platforms before [275].

2.1.2.1 Substrate preparation

2.1.2.1.1 Plasma deposition

Plasma polymerisation was performed in a custom-built 13.56 MHz radiofrequency plasma reactor described previously [276]. 13 mm thermanox coverslips were cleaned by treatment with air plasma for 3 min. Allylamine (AA) and 1,7-octadiene (OD) were used as precursors for plasma deposition to generate thin films. For generation of heteropolymers, AA and OD were mounted onto two separate needle valves and the plasma flow was carefully controlled with automated needle valves. Homopolymers were either 100% AA or 100% OD. Copolymers fabricated were (i) 75% AA / 25% OD (ii) 50 AA / 50% OD and (iii) 25% AA / 75% OD. In the following these coating will be referred to as 100 % AA, 75% AA, 50% AA, 25% AA and 0% AA. Plasma layers were deposited at a flow rate of 10 standard cubic centimetres per minute (sccm) for 3 min.

For fabrication of AA-OD gradients the gradient shape was controlled by the rate at which AA:OD ratio was changed and has been described previously [277].

2.1.2.1.2 Gold nanoparticle synthesis

Gold nanoparticles (AuNPs) were synthesised by reduction of hydrogen tetrachloroaurate with trisodium citrate as described previously [278]. AuNPs of a diameter of either 16 or 68 nm in diameter were fabricated. The AuNP suspensions were stored at 4°C in the dark.

2.1.2.1.3 Nanorough plasma polymer films

AA plasma films were immobilised with 16 or 68 nm gold nanoparticles (AuNPs). For homogeneous coatings substrates were immersed into the AuNP solution for 2 h (16 nm) and 6 h (68 nm), which initiated the covalent binding of AuNPs to AA. For fabrication of AuNP gradients substrates were gradually immersed into the AuNP solution by conducting a linear motion drive dip coater (*Zaber T-LSR series*) for 5 mm/h and 1.66 mm/h for the 16 and 68 nm AuNPs, respectively. Subsequently substrates were washed with ddH₂O. The AuNP coated substrates were then overcoated with a 5 nm plasma layer composed of (i) 100% AA (ii) 75% AA/25% 1,7-octadiene (OD), (iii) 25% AA / 75% OD or (iv) 100% OD. The total precursor flow rate was 10 sccm and the plasma polymer films were deposited for 30 s at 30 W.

The AuNP density on substrates with homogeneous AuNP coating equalled the AuNP density of the gradient section with highest AuNP density on gradients for both, 16 and 68 nm AuNPs.

2.1.2.2 Substrate sterilisation

Prior to cell culture experiments plasma coated glass coverslips were incubated in Penicillin/Streptomycin for 10 mins, then carefully washed with sterile 1x Dulbecco's Phosphate Buffered Saline (PBS) and left to dry.

2.2 Physicochemical substrate characterisation

2.2.1 Surface wettability analyses

2.2.1.1 Sessile drop technique

The sessile drop method is the most commonly used method to measure surface energy / wettability. A droplet of liquid (here ddH₂O) with a known surface energy was placed onto the surface of a solid and an image was recorded. Once the water comes in contact with the surface the contact angle (CA) occurs at the three interfaces liquid/solid surface (γ_{SL}), liquid/gas (γ_{LG}) and gas/solid (γ_{GS}) (Figure 2.3) and was calculated using the Young equation (Young's contact angle θ_Y , Equation 2.1) [279].

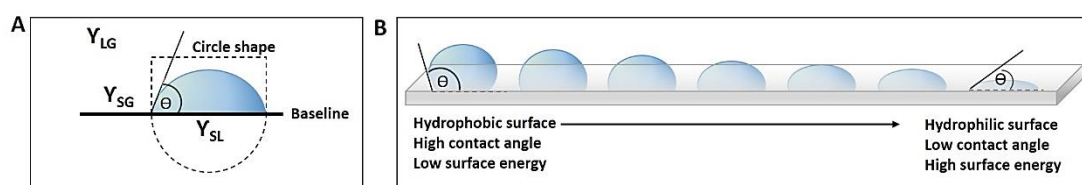


Figure 2.3: Simple schematic of the sessile drop technique. (A) Schematic diagram of a drop contour where the CA is measured at the interface (γ) between solid-gas (SG), solid-liquid (SL) and liquid-gas (LG) and (B) change of drop shape with increasing surface wettability.

Equation 2.1: Young's equation.

$$\gamma_{SG} = \gamma_{SL} + \gamma_{LG} \cos \theta_Y$$

All sessile drop CA measurements were conducted using a drop shape analysis system (*DSA100m, Krüss*) that consisted of a piezo dosing head which dispensed drops in picolitre volume, a camera combined with a microscope and a software controlled micro-step x-y stage. Droplets of 80 μ L degassed and deionised water were dropped on the substrate and images were recorded. The CAs in degree were collected using the circular segment method. A minimum of 5 samples and 7 different areas across the surface was measured.

For collection of CA maps, the stage with the sample was laterally moved in x and y direction and CAs were collected every 5 mm (~400 drops / 13 mm coverslips). For mapping only one representative single sample per polymer was chosen. Two and three dimensional CA maps were designed using Origin software (OriginLab, Northampton, MA).

2.2.1.2 Captive bubble

The captive bubble (CB) contact angle measurements were conducted using a drop shape analysis system (*DSA100m, Krüss*). A bubble was placed on the underside of the sample in liquid with a syringe connected to a needle ([Figure 2.4](#)). Each bubble was approximately 10 μL in volume and an image was taken. 6 samples were measured 5 times and the average was taken. The CA was determined using the circular segment method and the Young's CA was calculated using [Equation 2.1](#).

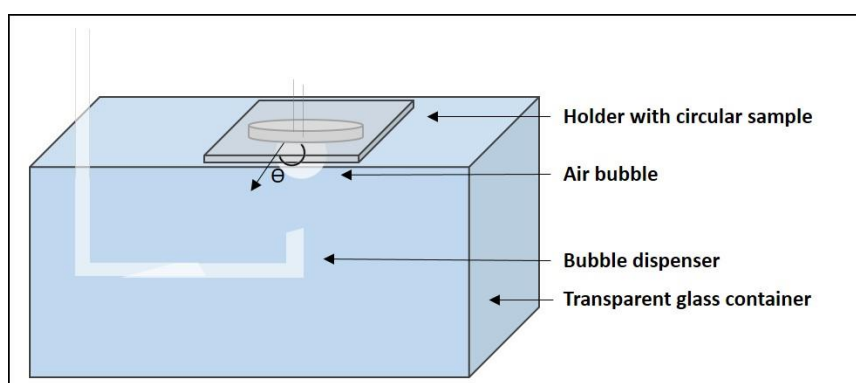


Figure 2.4: Schematic set up of the contact angle measurements using the CB method.

2.2.1.3 Dynamic contact angle

Dynamic contact angle (DCA) measurements were conducted using the Wilhelmy plate method utilising a *Cahn DCA322 microbalance*. The samples were slowly immersed into ddH₂O and subsequently withdrawn. Advancing and receding angles of 6 samples (22 mm² coverslips) were recorded in ddH₂O and results were analysed using *WinDCA322* (Thermo Cahn, USA) software.

The mass (m in g) of the sample that is attached to the balance is measured once the solid comes into contact with the liquid (ddH₂O, [Figure 2.5](#)). Three forces (F in N) occur: gravity force (g), upthrust buoyancy (F_b) and the capillary forces [280]. The contact angle was then determined using immersion depth, surface tension of the liquid (72.6 dyne cm^{-1} for ddH₂O) / surface free energy γ_{LG} (mN/m) and sample perimeter (P) ([Equation 2.2](#)).

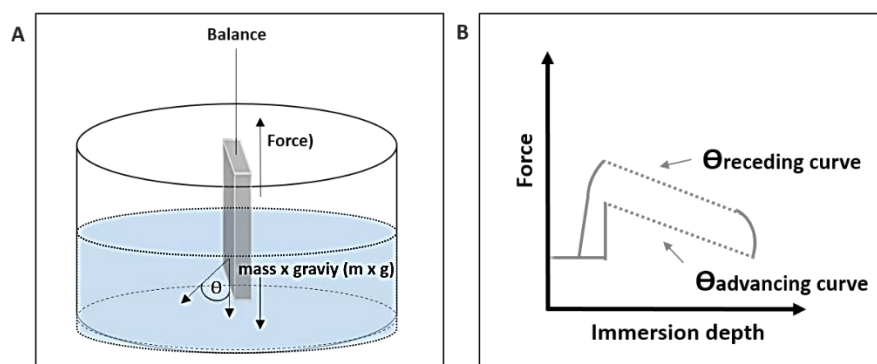


Figure 2.5: Simple schematic of the Wilhelmy plate method to assess substrate DCA. (A) Experimental setup. The substrate is immersed into the liquid downwards and subsequently taken out upwards. (B) Simultaneously advancing and receding curves are acquired using the associated software.

Equation 2.2: Wetting force.

$$F = m \times g + P \times \gamma_{LG} \times \cos\theta - F_b$$

2.2.2 Atomic Force Microscopy

The Atomic Force Microscopy (AFM) experimental set up is shown in [Figure 2.6](#). All AFM analyses (thickness, topographical imaging, surface roughness and nanomechanical properties) were performed using a *NanoScope 8 MultiMode AFM* (Bruker Nano Inc., Nano Surfaces Division, Santa Barbara, CA) equipped with a 150 x 150 x 5 μm scanner (J-scanner) operated with PFQNM modality [281]. Polymer coated glass cover slips were measured using silicon nitride tips with a nominal tip radius of 8 nm and a 5 $N m^{-1}$ spring constant (Bruker AFM Probe TAP150A).

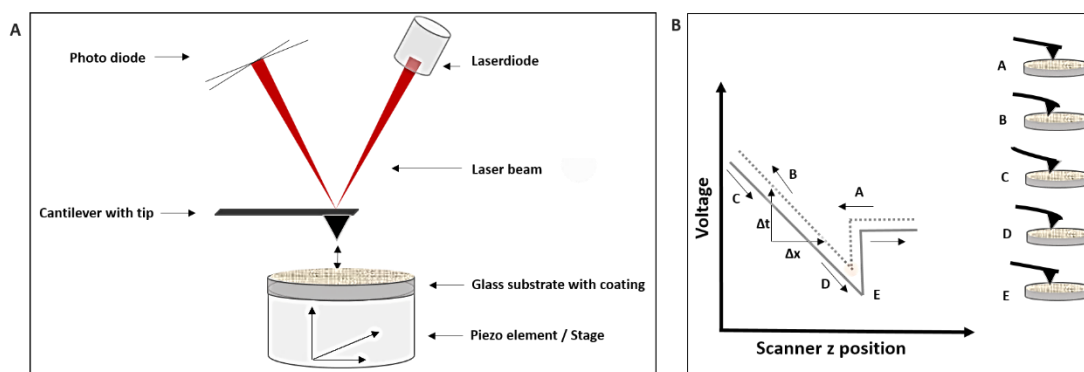


Figure 2.6: Atomic force Microscopy. (A) Simple illustration of the AFM setup. A tip attached to a cantilever raster scans a sample that is attached to a piezo element. An optical laser beam is focussed on the cantilever and the deflection is transferred onto a Photodiode. From here the detector analyses the deflection signal and gives a 3D image. (B) Schematic of a typical force curve measurement. The tip is in distance from the surface, no force (1). Once the tip approaches the surface, attractive forces (deflection downwards) occur and the tip contacts the surface (deflection upwards) (2). When the tip is retracted from the surface, adhesion forces maintain a certain distance between tip and sample (3 → 4) until the spring force allows to overcome adhesion forces (5) and the tip returns to position (1).

For thickness analyses a part of the film was removed by scratching the samples with a scalpel. The resulting scan image showed a decline between the polymer coating and the underlying glass substrate and the height between coated and uncoated part was measured.

For roughness analyses $5 \mu\text{m}^2$ images were taken, corrected using a plane fit and the root-mean-square roughness (RMS) was calculated under utilisation of [Equation 2.3](#) where z_i is the z value for specific pixel, z_{av} is the average of the z values in the scan area and N is the number of pixels within the same scan area. The AFM was operated in tapping mode.

Equation 2.3: Calculation of the root mean square roughness.

$$RMS = \sqrt{\frac{1}{N} \sum_{i=1}^N (z_i - z_{av})^2}$$

The same tip was used for a large number of measurements to ensure a fair comparison between the samples.

For determination of the elastic properties, the deflection (displacement) was converted into force using Hooks law, where F is the force, K_c the cantilever stiffness / spring constant and z_c the distance the cantilever is deflected ([Equation 2.4](#)) [282].

Equation 2.4: Hooks law.

$$F = -k_c z_c$$

PeakForce quantitative nanomechanical property mapping (PFQNM) was employed to analyse substrate mechanical properties (elasticity). Prior to all measurements the tip (deflection) sensitivity was updated using a sapphire 12- μ m sample and the spring constant k was determined by thermal tuning. A polystyrene sample with known elastic modulus was employed to calibrate the instrument in order to measure mechanical properties that were then determined by employing the DMT model (Derjagin, Muller, Toropov) using [Equation 2.5](#), where F is the force, δ is indentation, R the tip radius, E^* the reduced elastic modulus (comprises elastic modulus and Poisson's ratio of the material to be indented) and γ the work of adhesion.

Equation 2.5: Force calculation according to the DMT model.

$$F = \frac{4}{3} E^* \sqrt{R\delta^3} - 2\pi R\gamma$$

A minimum of 3 samples and 5 areas for each coating were used for all analyses, all of which were performed by employing NanoScope Analysis v1.50 software.

2.2.3 Characterisation of surface chemistry

2.2.3.1 X-Ray Photoelectron Spectroscopy

The experimental X-Ray Photoelectron Spectroscopy (XPS) set up is shown in [Figure 2.7](#). All XPS analyses were conducted using a VSW ESCA XPS spectrometer, which was fitted with a multicrystal Al K α X-ray monochromator. The sample holder was able to accommodate larger sample sizes (12x12 mm²) and was mounted on an x–y–z stage with ability to be rotated through 360°. A sample area of 15.7 mm² was analysed.

Survey spectra were recorded at a 45° take-off angle at 150 eV, 0.8 mm slit at 1.8 kW. High resolution C1s, O1s and N1s spectra were obtained at pass energies of 20 eV for improved resolution. The sample electrons were excited with a low energy electron flood gun (*Scienta FG300*) in the analyses chamber under optimal spectral resolution.

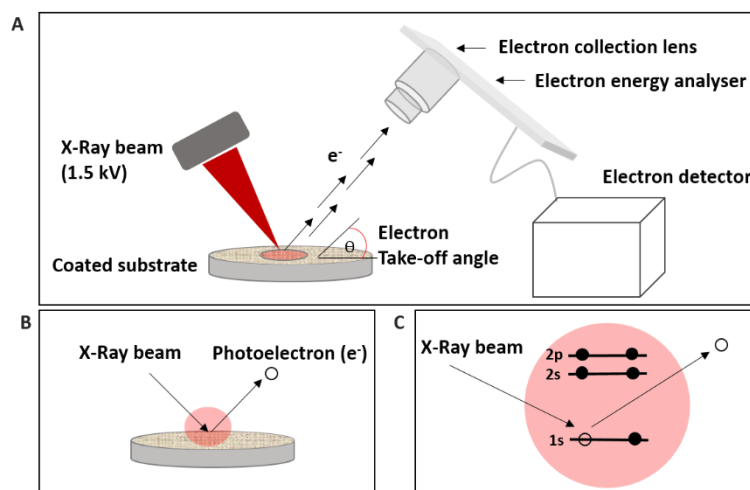


Figure 2.7: X-Ray Photoelectron Spectroscopy. (A) Simplified schematic of the instrumental XPS set up. An X-Ray source is focused on the substrate and excites core electrons in the upper layers of a substrate surface (B and C). These photoelectrons are ejected from an atomic level or valence band of the sample surface. Photoelectron energy is determined using a concentric hemispherical analyser. The signal then becomes transferred to a detector, resulting in a spectrum with a series of photoelectron peaks and is visualised as intensity (electron counts) versus electron energy. The entire process takes place within a chamber that maintains ultra-high vacuum (UHV) which avoids surface contamination and increases the scope of the electrons when ejected

The recorded spectra were analysed by curve fitting using CasaXPS (Casa software Ltd) software. The photoelectron specific kinetic energy (E_{kin}) was determined using [Equation 2.6](#), where $h\nu$ is the excitation energy, E_B the binding energy and ϕ the work function [283, 284].

Equation 2.6: Determination of the elemental kinetic energy E_{kin} .

$$E_{kin} = h\nu - E_B - \phi$$

Carbon, oxygen and nitrogen content was quantified by peak fitting (determination of peak edges) of the survey (wide scan) spectra by calculation of the area underneath the curve ([Figure 2.8 A](#)). The hydrocarbon C-C/C-H peak was referenced to a binding energy of 285.0 eV for all spectra recorded in order to account for sample charging. Other peaks that

corresponded to carbon binding states were added and fitted to the core level. The background was removed linearly and symmetrical peaks with a 80:20 Gaussian : Lorentzian shape were employed for line-shape fitting with suitable relative sensitivity factors. (Figure 2.8 B). Equal full width at half maximum (FWHM) values were used for each component for all core levels. Binding energy peak shifts were taken from available literature [285, 286].

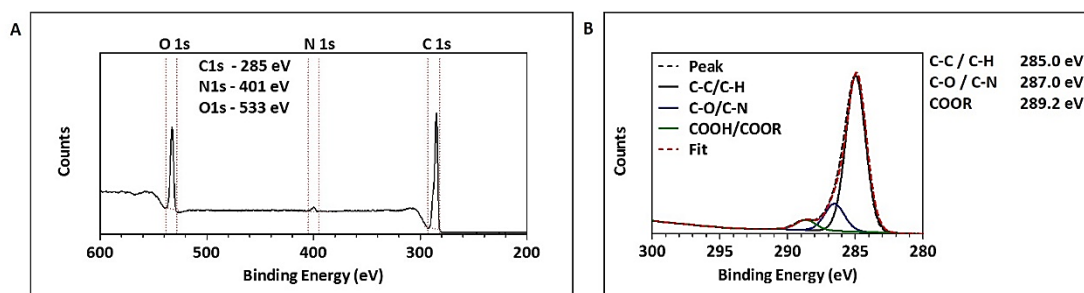


Figure 2.8: (A) An example of a XPS wide scan spectrum that shows three peaks: a carbon 1s (C1s) peak, an oxygen 1s (O1s) peak and a nitrogen 1s (N1s) peak at their characteristic binding energies. The background originates from electrons that are excited by the X-Ray Bremsstrahlung radiation and from inelastic photoelectron scattering.

2.2.3.2 Amine content quantification

The surface primary amine density was quantified as previously described using either Coomassie Brilliant Blue (CBB) [287] or Orange 2, [288-290] (Figure 2.9).

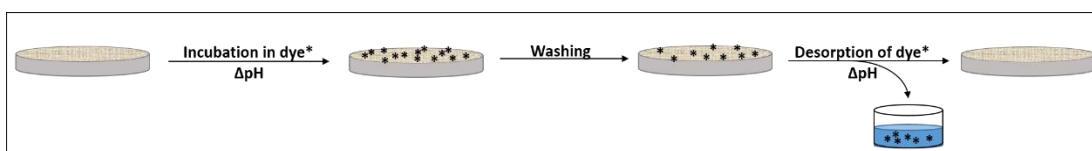


Figure 2.9: Simplified schematic of the colorimetric determination of the surface amine content. The samples are incubated in a solution that contains the dye that binds to amine groups at a specific pH. After washing, the pH of the solution is changed, the bound dye is released into the solution whose optical density can then be determined and correlated with the optical density of a standard solution with known dye concentration.

2.2.3.2.1 Coomassie Brilliant Blue method

Coomassie Brilliant Blue (CBB) is a large bivalent dye and was used to quantify surface amine groups quantitatively. For primary amine density determination, polymer coated substrates were immersed in 0.3 mL of a solution of 0.5 mg/mL CBB in acidic solution (85:10:5 v/v

dH₂O/methanol/acetic acid, pH 2.2) for 5 min at room temperature. To eliminate any excess dye, the samples were then thoroughly washed with the acidic solution without dye until the rinsing solution was clear. The samples were then dried at room temperature in air. To remove the amine-bound dye, 0.3 mL of an alkaline solution (0.125 M K₂CO₃ in 50:50 v/v dH₂O/methanol, pH 11.25) was added. The alkaline solution was then transferred into a 96 well plate and adjusted to pH 3 (by adding 7.5% v/v of 3 M HCl). The optical density (OD) of the solution was measured at 615 nm using an *Anthos labtec instruments spectrophotometer LP400* (Figure 2.10).

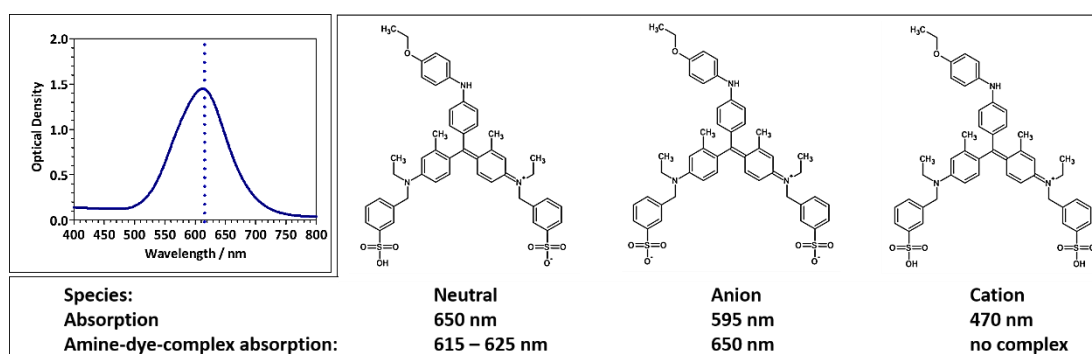


Figure 2.10: CBB absorption spectrum and molecule isomeric forms depending on the solution pH.

2.2.3.2.2 Orange 2 method

Orange 2 is a small, monovalent dye and therefore assumed to be able to reach steric hindered or covered primary amines easier than CBB (Figure 2.11). Polymer coated samples were immersed in 0.3 mL of a solution of 14 mg/mL Orange 2 dye in acidic solution (dH₂O at pH 3 adjusted with 1 M HCl) for 30 min at 40°C. To eliminate any excess dye, the samples were subsequently thoroughly washed in the acidic solution without dye until the rinsing solution was clear. The samples were then dried at room temperature in air. To remove the amine-bound dye, 0.3 mL of an alkaline solution (dH₂O at pH 12 adjusted with 1 M NaOH) was added. The alkaline solution was then transferred into a 96 well plate and adjusted to pH 3 (by adding 1% v/v of 12.3 M HCl). The optical density (OD) of the solution was measured at 484 nm using an *Anthos labtec instruments spectrophotometer LP400*.

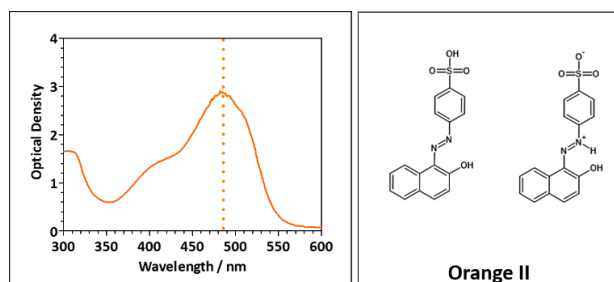


Figure 2.11: Orange 2 absorption spectrum and its isomeric forms.

2.2.3.2.3 Quantification of primary amines

Prior all measurements, a stock solution of 0.05 g/mL CBB in acidic solution (85:10:5 v/v dH₂O/methanol/acetic acid, pH 2.2) or 0.05 g/mL Orange 2 in acidic solution (dH₂O at pH 3 adjusted with 1 M HCl) was prepared. From these, standard solutions were prepared by taking a certain volume of stock solution and topping up with acidic solution to reach a final volume of 0.3 mL in 96 well plates. CBB and Orange 2 interact with N⁺ in a ratio of 1:1 (N_{dye} = N_{NH₂}). Therefore, one molecule dye reacts with one single primary amine group [291]. As solution volume and concentration were known, the mass *m* of dye was calculated and, using its molar mass *M* (M_{CBB} = 854.02 g/mol, M_{Orange II} = 350.32 g/mol) the amount of substance was determined (Equation 2.7). The particle number *N* was then calculated using the Avogadro constant *N_A* (Equation 2.8).

Equation 2.7: Molar mass.

$$M = \frac{m}{n}$$

Equation 2.8: Avogadro constant.

$$N_A = \frac{N}{n} = 6.02214129 * 10^{23} mol^{-1}$$

From the absorption of the standard solutions the particle number N per coverslip was then calculated and the amine density was determined in pmol/mm². Background measurements were taken alongside and subtracted from the absorbance values.

2.2.3.2.4 Correlation of amine content

Linear correlation between primary amine density determined by CBB and Orange 2 was determined to compare both methods with each other as well as with the amine content determined by XPS (N/C).

2.3 Cell culture

2.3.1 Cell lines

Throughout the course of this study seven cell lines were used and assessed for their cell response to biomaterial substrates used in this study.

- i) mouse fibroblasts (mL929) cells, provided by Biomer Technology Ltd.
- ii) bovine aortic endothelial (BAE) cells, provided by Biomer Technology Ltd.
- iii) mouse kidney-derived stem cells (mKSC), established by the Stem Cell Research group (University of Liverpool) [249]
- iv) conditionally immortalised podocytes (ciPodocytes), provided by *Saleem et al.* [227]
- v) conditionally immortalised proximal tubule cells (ciPTCs), provided by *Masereeuw et al.* [246]
- vi) putative fetal kidney progenitor cells (fKPCs), pre-sorted to be double negative or double positive for CD133 and CD24, provided by *Winyard et al.* [292]
- vii) putative infant kidney progenitor cells (iKPCs), pre-sorted to be double negative or double positive for CD133 and CD24, established by the Stem Cell Research group (University of Liverpool)

2.3.2 Routine cell culture

All cell culture procedures were performed under sterile conditions in a *Biomat class II safety cabinet*. Surfaces and equipment used during cell culture were cleaned with 70% ethanol. Solutions and buffers were pre-warmed to 37°C before use. Cells were cultured in their particular cell culture medium in standard tissue culture plates (TCPs). The medium was exchanged every 2-3 days and cells were kept in a humidified chamber with 5% CO₂ at 37°C. Conditionally immortalised (ci) cell lines were kept at 5% CO₂ at 33°C for proliferation, whereas the conditions were changed to 5% CO₂ at 37°C in order to initiate cell differentiation.

mL929, BAE cells and mKSCs were kept in cell culture medium A ciPodocytes in cell culture medium B, ciPTCs in cell culture medium C and fKPCs and iKPCs in cell culture medium D (Appendix I, p 239).

Cells were passaged when confluent as follows; two washing steps in PBS that was then aspirated and cells were incubated in 1% trypsin at 37°C for 3-5 mins until cells were detached from the culture dish. Subsequently cell culture medium was added to neutralise the trypsin and cells were carefully transferred into a 15 mL centrifuge tube and spun down at 233 x *g* for 3 mins. Supernatant was then aspirated and the cell pellet was resuspended in the required volume of cell culture medium. Cell number determination for cell seeding was performed as follows: 10 µL of cell suspension were transferred into a 96 well plate and mixed with 10 µL trypan blue. 10 µL of this solution were transferred into a cell counting plate and cell number was determined using a *TC20™ Automated Cell Counter*. The required number of cells was seeded into TCPs for cell culture expansion.

2.3.3 Cell culture on biomaterial substrates

Cells were handled under standard cell culture conditions as described above. If cells were to be seeded on substrates, a solution of the required cell number in the required volume of medium was made up. The cell number required was seeded directly on substrates in a volume of 150 μ L / 13 mm polymer coated coverslip and left for attachment under the cell culture hood (Table 2.1). After 2 h the wells were topped up with 1 mL medium. For mKSC culture on substrates, 1×10^3 cells were diluted in 1 mL medium and directly placed into the well for maintenance of a homogeneous cell distribution.

Table 2.1: Seeding density and cell culture conditions of the particular cell type when meant to be analysed on polyacrylate substrates.

Cell type	Seeding density	Cell culture conditions
mL929 cells	1×10^4 cells / 13 mm coverslip	96 h / 37°C
BAE cells	1×10^4 cells / 13 mm coverslip	96 h / 37°C
mKSCs	1×10^3 cells / 13 mm coverslip	96 h / 37°C
ciPodocytes	1×10^3 cells / 13 mm coverslip	6 days / 37°C, 5 days / 37°C
ciPTCs	1×10^3 cells / 13 mm coverslip	6 days / 37°C, 5 days / 37°C
fKPCs	5×10^3 cells / 13 mm coverslip	7 days / 37°C
iKPCs	5×10^3 cells / 13 mm coverslip	7 days / 37°C

2.3.4 Cryopreservation

Cells were washed with PBS, trypsinised and centrifuged for 2.5 min / 233 xg . The medium was then aspirated and cells were resuspended in Recovery™ cell culture freezing medium at 1×10^6 cells / 0.5 mL and subsequently transferred into cryovials. Aliquots were then frozen overnight in freezing containers that were filled with 2-propanol and kept in a freezer at -80°C thereby cooling down 1°C / min. The next day vials were transferred in liquid nitrogen containers for long term storage.

2.3.5 Cell recovery

Frozen cell aliquots stored in cryovials were removed from the liquid nitrogen tank, quickly thawed in a 37°C water bath and immediately suspended in 10 mL cell culture medium. The cell solution was then centrifuged for 2.5 min / 233 *xg*, medium was aspirated, cells were resuspended in fresh medium and seeded into 10 cm TCPs. All cells were left for recovery for at least 3 days and passaged at least once before usage for *in vitro* experiments.

2.4 Evaluation of the cell response

For quantitative studies cells were seeded onto sterile 13 mm polymer coated glass cover slips. Plain glass cover slips and TCP were used as controls. Cell seeding densities can be found in [Table 2.2](#).

2.4.1 Morphological assessment using methylene blue

The methylene blue (MB) staining was performed in either 24 well TCPs (cytotoxicity studies) or on polymer coated samples. The medium was aspirated, cells were washed twice with PBS, subsequently fixed with 4% (w/v) PFA for 10 mins at room temperature and washed three times with PBS. Following that the cells were stained with a solution of 0.04% (v/v) MB in ddH₂O for 10 min at room temperature and again washed with PBS until rinsing solution was clear. Samples were morphologically investigated using a light microscope.

2.4.2 Cell viability

The viable cell number was determined at different time points, generally every day (mL929, BAE cells and mKSCs) or every other day (ciPodocytes, ciPTCs, fKPCs, iKPCs).

For analyses, cell culture medium was aspirated and cells were washed with PBS. Then 150 µL of a solution of 10% Cell Counting Kit-8 (CCK-8) in cell culture medium (1:10, respectively) was added to each well and cells were incubated for 1.5 h. Subsequently, the dye- medium

solution was transferred into a 96 well plate. The absorbance of the solution was measured in an *Anthos labtec instruments spectrophotometer LP400* at wavelengths of 450 nm for detection (620 nm reference filter). A standard curve was set up prior all experiments using the same cell batch in order to interpolate the obtained data. Alongside all measurements a background measurement (blank medium) was collected and subtracted from all values.

CCK-8 is a readily available solution (WST-8 [2-(2-methoxy-4-nitrophenyl)-3-(4-nitrophenyl)-5-(2,4-disulfophenyl)-2H-tetrazolium]). It becomes reduced through the biological activity of dehydrogenase of living cells into a colorimetrically detectable dye.

2.4.3 Cell proliferation, population doubling time and cell spread

Cells were fixed at the required time point using 4% PFA and subsequently incubated in Alexa Fluor® 488 Phalloidin (diluted in PBS 5:200) for 30 min at room temperature in the dark. Subsequently cells were washed with PBS three times and incubated in a solution of 4',6-diamidino-2-phenylindole (DAPI) (300 nM in PBS) for 30 min at room temperature in the dark. The cells were then washed another three times with PBS and coverslips were carefully lifted with tweezers and cell side-down mounted onto microscopy slides using Dako fluorescence mounting medium. The coverslips were then analysed under epifluorescence illumination using a *Leica DM2500 microscope* coupled to a Leica DFC420C camera. Cell number was quantified by counting stained nuclei from the images obtained. Cell number was determined at different time points, generally every day (mL929, BAE cells and mKSCs) or every other day (ciPodocytes, ciPTCs, fKPCs, iKPCs).

Population doubling time (PDT) was determined with Graphpad software from these cell numbers by employing nonlinear regression (exponential growth equation) analysis (Equation 2.9), where K is the rate constant.

Equation 2.9: Population doubling time.

$$PDT = \frac{\ln(2)}{K}$$

Cell spread was calculated from actin stained cells using ImageJ [293, 294]. An average of 10 images per coverslip was taken. All images depicted are representative for the entire surface from one sample from three biological and technical replicates.

2.4.4 Immunostaining

All staining procedures were accomplished on cells seeded on 13 mm polymer coated coverslips, a 13 mm glass control or on TCPs. The general procedure was as follows; cell culture medium was aspirated, cells were washed twice with PBS and fixed with 4% (w/v) PFA for 10 mins at room temperature. Subsequently cells were washed 3 times with PBS and blocked for 1 h at room temperature with 10% serum (goat or chicken, depending on the host animal the secondary antibody was raised in). The serum was then removed and a primary antibody solution, that contained 1% of specific serum and 0.1% Triton-X 100 in PBS and the primary antibody (AB¹) at the required concentration, was added and left at on the cells at 4°C over night in the dark. The following day cells were washed 3 times with PBS and the secondary antibody solution, containing 1% of specific serum and 0.1% Triton-X 100 in PBS and the secondary antibody (AB²) at the required concentration, was added and cells were incubated for 2 h at room temperature in the dark. Antibody solutions were centrifuged using a *Microcentaur centrifuge* (Sanyo Electroc Co. Ltd. Osaka, Japan) for 1 min at 233 *xg* prior usage. After another three washes with PBS, cell nuclei were stained with DAPI (300 nM in PBS) for 30 min at room temperature in the dark. Alongside all immunofluorescence experiments a negative control was included that was treated the exact same way as all other substrates except that no primary antibody was added. The coverslips were then washed three times with PBS, carefully removed from the 24 well plates and mounted with Dako

Fluorescence Mounting Medium. Images were acquired under epifluorescence illumination using a *Leica DM2500 microscope* coupled to a Leica DFC420C camera.

All primary and secondary antibodies, including dilutions used within this study, are listed in the Appendix II (p 241).

If images were to be quantified, an average of 10 images were taken of each sample and number of positive cells was quantified using ImageJ software [293, 294]. All experiments were accomplished in three biological and technical replicates and images shown represent the entire sample surface as well as an average of all experiments.

2.4.5 Alkaline phosphatase staining

Following 10 min cell fixation with 4% (w/v) PFA at room temperature cells were washed 3 times with PBS and incubated in Tris-HCl at pH 9.2 for 5 min at room temperature. Subsequently Tris-HCl was removed and cells were incubated in a solution of 2 mg (0.02% (w/v)) naphthol AS-MX phosphate and 10 mg (0.1% (w/v)) Fast Red TR in 10 mL Tris-HCl (pH 9.2) for 15 min at room temperature in the dark. In the presence of the alkaline phosphatase, the naphthol AS-MX is liberated from the phosphate and interacts with the Fast Red diazonium salt to give the red precipitate that is fluorescently detectable. The staining solution was then removed and cells were washed once with Tris-HCl pH 9.2 and twice with PBS. Cells were co-stained with DAPI for 30 min in the dark at room temperature. The coverslips were then carefully removed from the 24 well plates and mounted with Dako Fluorescence Mounting Medium and images acquired under epifluorescence illumination using a *Leica DM2500 microscope* coupled to a Leica DFC420C camera.

2.4.6 Live cell imaging

For live cell imaging, cells were seeded at the required density and left to attach and proliferate in an incubator for 24 h as described previously. The following day the well plate

was transferred to a life cell imaging instrument (*Cell-IQ*[®], CM Technologies) and phase contrast images were taken every hour for a determined period of time. The Cell-IQ allows long term cell culture under the required culture conditions.

2.4.7 Podocyte quantification

For podocyte quantification, life cell images taken every 24 h were chosen and the number of podocyte like cells was quantified from their typical morphological characteristics, such as a voluminous cell body with an arborised well-developed cytoskeleton and binuclearity [214, 215, 250]. Life cell imaging allowed quantification at the same area throughout the cell culture period. A minimum of four spots per substrate was chosen and all experiments were performed in three biological triplicates.

2.4.8 Fluorescence activated cell sorting

2.4.8.1 Separation of cell populations

Fluorescence activated cell sorting (FACS) was used to separate fetal and infant KPCs to be either double positive (DP) or double negative (DN) for the putative kidney progenitor cell markers CD133 and CD24. Cells to be sorted were kept under cell culture conditions. The medium was aspirated, cells were washed with PBS, trypsinised and centrifuged at 233 *xg*. The pellet was then resuspended in the antibody solution, containing the antibody diluted in PBS, for 10 mins at 4°C. Subsequently PBS was added and the cells were centrifuged at 233 *xg*. The washing step was repeated another two times. Cells were transferred into round-bottom glass tubes and kept on ice until sorted. FACS sorting was accomplished using a using a *BD FACSAria* (BD Biosciences) instrument by employees of the FACS Facility of the University of Liverpool. Sorted cells were collected in FACS buffer and kept on ice until they were seeded into TCPs in their medium.

2.4.8.2 Routine cell sorting

Cells were routinely analysed using cytofluorometry to determine the percentage of fluorescently labelled cells within a population. Cell culture conditions and seeding densities are listed in [Table 2.2](#).

For analyses, medium was aspirated, cells were washed with PBS, trypsinised and centrifuged at 233 *xg*. The pellet was then resuspended in the antibody solution that contained the antibody diluted in PBS, for 10 min at 4°C. Afterwards PBS was added and the cells were centrifuged at 233 *xg*. The washing step was repeated twice. The labelling procedure was repeated if cells were co-stained with a second antibody. The cells were kept on ice in Eppendorf tubes in [FACS buffer](#) until analysis.

In order to sort cells these were transferred into glass tubes and analysed using a *BD FACScalibur* (BD Biosciences) instrument, using the required lasers to detect the fluorescently labelled cells. The results were analysed using Flowing Software 2. The baseline was set by using non-labelled cells prior analysis of labelled cells. This control served as a threshold. All antibodies used are listed in the [Appendix III](#) (p 242).

2.4.8.3 Uptake of fluorescently labelled albumin

Cells were seeded on polymer coated coverslips and kept in routine cell culture under the required conditions ([Table 2.2](#)). One day before the end of the cell culture cells were washed three times thoroughly with PBS and cultured for another 24 h in serum-free medium (without [FBS](#)). Cells were then incubated for 1 h in serum-free medium that contained 40 µg/mL of [FITC-conjugated bovine serum albumin](#) (F-BSA) for 1 h at 37°C.

If a competitive inhibition was performed, cells were parallel cultured for 15 min in serum-free medium that contained 40 µg/mL of F-BSA and 4 mg/mL of unlabelled [bovine serum albumin](#) (albumin, BSA). Afterwards cells were washed 3 times with PBS.

If cells were to be analysed immunofluorescently under the microscope, cells were fixed with 4% PFA at this point, co-stained with the desired antibody and DAPI for 30 min in the dark at room temperature. The coverslips were then carefully removed from the 24 well plates and mounted with Dako fluorescence mounting medium and images were acquired under epifluorescence illumination using a *Leica DM2500 microscope* coupled to a Leica DFC420C camera.

If cells were to be analysed using cytofluorometry, these were trypsinised, serum-free medium was added and cells were centrifuged at 233 *xg*. The medium was then aspirated, the pellet was resuspended in FACS buffer and cells were kept on ice until analysed. The cell solution was then sorted using a *BD FACScalibur* (BD Biosciences) instrument under employment of the FL1 detector. The results were analysed as described above.

Table 2.2: Seeding density and cell culture conditions of cell lines seeded on substrates and analysed using either FACS or PCR.

Cell type	Seeding density (number of coverslips combined per replicate)	Cell culture conditions
mKSCs	2.5×10^3 cells / 19 mm coverslip (x3)	96 h / 37°C
ciPTCs	2.5×10^3 cells / 19 mm coverslip (x3)	6 days / 37°C, 5 days / 37°C
fKPCs	1.5×10^4 cells / 19 mm coverslip (x3)	7 days / 37°C
iKPCs	1.5×10^4 cells / 19 mm coverslip (x3)	7 days / 37°C

2.4.9 Reverse transcription quantitative real-time polymerase chain reaction

Reverse transcription quantitative real-time polymerase chain reaction (qRT-PCR) was used to evaluate relative mRNA expression between cells seeded on different substrates. For analyses, cells were seeded on 19 mm polymer coated coverslips in order to get enough RNA material and thus cDNA to analyse (Table 2.2). A minimum of 3 biological replicates was performed for each cell line.

2.4.9.1 Primer design

If not present in-house, primer pairs for qRT-PCR were designed using NCBI Primer Blast [295]. The primers were optimised for the following parameters: T_m of 60°C, product size of 50-200 base pairs, length of 18-23 base pairs and GC content between 40 to 60% as suggested by *Udvardi et al.* [296].

2.4.9.2 Total RNA extraction

Medium was aspirated, TRIzol[®] reagent was added (volume as chosen corresponding to the well size) and left for 5 min at room temperature on cells in order to recover ribonucleic acids (RNAs). Cells were then triturated and the solution was transferred into microfuge tubes. The chloroform (1/5 of the existing volume) was added, the vial was shaken for 15 seconds and the solution was centrifuged at 4°C for 15 min at 12000 *xg*. From this solution, now separated into 3 phases, the upper phase was transferred into a fresh 1.5 mL Eppendorf tube that already contained 1 µL glycogen. Subsequently isopropanol (1/2 of the existing volume) was added, the solution inverted a few time and then incubated for 10 min at room temperature. Following that, the solution was centrifuged at 4°C for 10 min at 12000 *xg*. The supernatant was then removed and the pellet was washed with 75% ethanol (diluted in nuclease free water). The pellet was either stored at -80°C or, if immediate to be used, supernatant was removed and pellet air dried for a few minutes and diluted in about 20 µL nuclease free water.

RNA concentration was determined using a 1 µL *NanoDrop™ 1000 Spectrometer* (NanoDrop Technologies, Wilmington, USA).

2.4.9.3 DNase treatment

The required amount of RNA was transferred into a 0.2 mL microfuge tube, 1 µL DNase buffer and 1 µL DNase were added. The solution was topped up with nuclease free water to obtain

a volume of 10 µl and incubated 37°C for 30 min. Subsequently 1 µl of Stop buffer was added and the solution incubated for 15 min at 60°C. Both steps were employed using a *2720 Thermal Cycler*. The solution was either kept at -80°C or, if to be used immediately, kept on ice.

2.4.9.4 cDNA synthesis

A mastermix was prepared containing 4 µl 5x buffer, 1µl 0.1M dithiothreitol (DTT) and 1µl Superscript III (200U/µl) per reaction. 8 µL DNase treated RNA were transferred into a fresh 0.2ml microfuge tube. 1 µl of a 100ng/µl stock solution of random hexamers, 1 µl of desoxy-nucleotides (dNTP mix, 10mM stock). Additionally nuclease free water was added to give a final volume of 14 µl. The solution was incubated at 65°C for 5 min and then rested on ice for a minimum of 1 min. Then 6 µl of the master mix were added. The final solution was incubated for 5 mins at 25°C, 60 mins at 50°C. For enzyme inactivation, the solution was then incubated for 15 mins at 70°C. All steps were performed using a *2720 Thermal Cycler*. The solution (cDNA) was subsequently diluted in 30 µl nuclease free water and either kept at -80°C or, if to be used immediately, kept on ice.

2.4.9.5 Quantitative PCR

For quantitative analyses two solutions were prepared: a primer master mix and a cDNA master mix (Table 2.3). 4.5 µL primer mix and 5.5 µL were transferred into the well of a 96 well PCR plate. Each sample and primer was run in triplicates. Alongside these analyses two controls were run: a no-template-control (NTC) were as well as a no-reverse-transcriptase (NRT) control in order to verify the purity of genomic DNA. All primers are listed in the Appendix IV (p 243).

Table 2.3: Composition of the primer and cDNA mastermix for cDNA amplification.

Primer mix	cDNA mix
0.5 µl forward primer (6.25 pmol/µl)	0.5 µl diluted cDNA
0.5 µl reverse primer (6.25 pmol/µl)	5 µl 2X Sybr Taq mix
3.5 µl nuclease-free water	
4.5 µl	5.5 µl

The cDNA amplification was performed using a *Biorad CFX Connect Real-Time PCR detection system*. The cycling conditions were as follows: initial enzyme activation for 3 mins at 95°C, followed by a 2-step amplification cycle of 95°C for 10 s and annealing (T_A) at 60°C for 30 s (mKSCs). The PCR reaction was ended after 40 cycles. Following that a dissociation curve was recorded, in which temperature was increased 0.5°C every 5 s thereby detecting the product melting temperature. The final amplification curves were analysed using the Bio-Rad CFX System Test Software. The cycle threshold (Ct) value was then transferred to Microsoft Excel software and fold change was assessed by employing the Pfaffl method in order to analyse the fold changes [297]. *Gapdh* and *beta Actin (ACTB)* were used as reference genes.

2.4.9.6 Agarose gel electrophoresis

The amplified product was run on an agarose gel in order to visualise and verify fragment identity and estimate the product size.

A 2% (w/v) agarose gel was prepared by adding agarose into 1 x TAE buffer to a conical flask. The mixture was melted for a few minutes in a microwave, cooled down at room temperature and ethidium bromide was added (1 µL / 50 mL) in order to allow posterior detection of nucleic acids under ultraviolet (UV) light. Subsequently the gel was poured into an electrophoresis gel tray and a comb was inserted into the gel to introduce pockets. The gel was left to set for a minimum of 1 h to set at room temperature. Afterwards the gel tray was transferred into an electrophoresis chamber filled with 1 x TAE buffer.

5x HyperLadder™ loading buffer was added to the cDNA product (1 x final concentration) to increase the product density. Of this solution, 10 µL were pipetted into the gel pockets and the products were run at 80 V for 40 min. Alongside 2 references were run: HyperLadder™ I (200 bp-10 kb) and / or HyperLadder™ IV (100 bp-1000 bp), depending on the expected product lengths.

2.5 Statistical analyses

Standard deviation (SD) error was used for descriptive analysis and standard error of the mean (SEM) for inferential statistics with a minimum of 3 independently conducted experiments (n=3). One-way analyses of variance (ANOVA) and post-hoc Tukey test were performed to evaluate statistical significances between two groups of samples. All statistical analyses were performed using Graphpad (GraphPad Prism v5.0 software for Windows, GraphPad Software Inc., San Diego, CA). P < 0.05 was considered as statistically significant.

3 Physicochemical characterisation of polyacrylates

3.1 Introduction

Confidentiality Agreement

All polyacrylates used in this study are proprietary to Biomer Technology Ltd. including the polymerisation process and the chemical composition and quantities of the individual monomers. Detailed chemical properties of the substrates remain confidential.

In the field of tissue engineering and (stem) cell research, cell behaviour is often investigated and manipulated in combination with biomaterials [110, 156, 298, 299]. It is advantageous for such biomaterials to mimic the cells extracellular environment in order to present the cells with natural cues, which can be physical, chemical or biochemical in nature [299-301]. All of these features have been shown to influence cell behaviour on different levels, including adhesion, proliferation and differentiation [59, 302-304].

This study focuses on novel, synthetic, polyacrylate materials, all of which were developed, manufactured and provided by Biomer Technology LTD (BTL). These polymeric substrates were synthesised from discrete acrylic monomers using a propriety free radical polymerisation technique. The free radical process reacts at the carbon-carbon double bonds opening it to form the polyacrylate carbon backbone structure (Figure 3.1).

One advantage of this approach is the range of acrylic monomers available for synthesis. It opens up the possibility to design the polymers with functional group chemistry and stereochemistry in such a way that allows them to mimic (in a simple synthetic analogue) protein sequences, such as cell binding motifs that are present within a cells *in vivo*

extracellular environment. Accordingly, all polymer substrates were composed of multiple acrylic monomers with different key functional groups that include amine (-NH₂), hydroxyl (-OH) and carboxyl (-COOH) groups. Two discrete monomers, comprising ethyl and butyl chains, were used to create hydrophobic spacer groups. By modulating the ratio of these monomers it was possible to introduce varying degrees of steric hindrance into the polymers. The number of monomers used was determined by the proportion and distribution of the individual functional group chemistries and stereochemistry. There were also practical considerations dependent upon the target polymer molecular weight and the multi-monomer compatibility. Each polyacrylate batch was internally tested, by the company, for chemical consistency, purity and chain length using gel permeation chromatography.

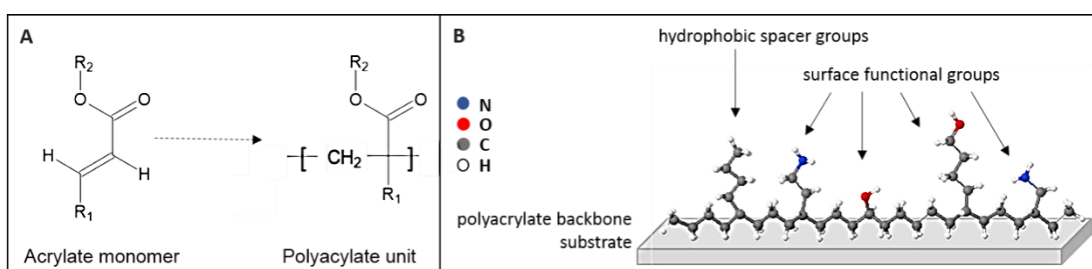


Figure 3.1: Polyacrylate structure. (A) Polyacrylate monomeric and polymeric unit. R₁ and R₂ indicate potential functionalities. (B) Representative stick ball schematic of a random polyacrylate with a carbon backbone and a variety of potential representative side chains with different functionalities.

To date, the polyacrylates can be divided into two primary groups, the BTL series and the ESP series. The BTL series was structurally based on a particular collagen cell binding motif and its modifications. The series was initially designed for the Company's propriety coronary stent coating application and was, in this respect, shown to influence cell adhesion and proliferation of human aortic endothelial cells and coronary artery smooth muscle cells [305-307]. The BTL series substrates differed primarily in the proportion of the hydrophobic spacer chain monomers which influence steric hindrance within the polymer chain. Such spacer groups are generally important as functional units as they influence physicochemical properties and additionally induce flexibility and stability into the polymer chain [308].

Moreover, from a biological point of view, such side chains may influence biological accessibility of e.g. certain proteins, biological ligands, growth factors or cells [308-311].

In contrast, the development of the embryonic stem cell polymer (ESP) series was inspired by the composition of other functional protein sequences / cell binding motifs within a variety of extracellular matrix (ECM) proteins such as fibronectin and laminin.

One motif of great interest was RGD, a three amino acid sequence (Arginine-Glycine-Aspartic Acid), which was first identified in fibronectin [312]. However, it has since been detected within a number of ECM proteins including fibrinogen, entactin, vitronectin and laminin and is within each protein present in a different conformation depending on the immediate surrounding components and structures [313-315]. The RGD motif is well known as a cell attachment motif that cells can bind to through integrin-mediated adhesion [316, 317] and is additionally involved in cell behavioural features such as the formation of focal adhesions and cell polarisation [318]. Therefore it is commonly utilised to modify biomaterial surfaces to enhance cell attachment and eventually migration [317, 319, 320]. Since then a large variety of synthetic polymers has been developed that incorporate the RGD motif, such as GRGDS (Glycine–Arginine–Glycine–Aspartic acid–Serine) [321], RGDS (Arginine–Glycine–Aspartic acid–Serine) [322] or GRGDVY (Glycine-Arginine-Glycine-Aspartic acid-Valine-Tyrosine) [323] and show that these also mediate cell attachment, notwithstanding that these sequences are much shorter than actual ECM proteins. Figure 3.2 shows a simplified schematic representation of an integrin with an RGD binding site as well as a representation of the RGD motif (created using Chems sketch©, ACDlabs).

Additionally the RGD motif has been shown to influence stem cell differentiation [37]. The RGD density on a solid support, for example, affects cell differentiation of myoblasts with a high density directing cells towards myofibrils whereas a lower density directs the differentiation towards hepatocytes [324]. Similarly, *Ding et al.* showed that mesenchymal

stem cells (MSCs) showed differences in their differentiation behaviour depending on RGD nanopatterns and nanospacing. Their results strongly suggested that the RGD nanospacing directly regulates stem cell differentiation [35, 36, 325].

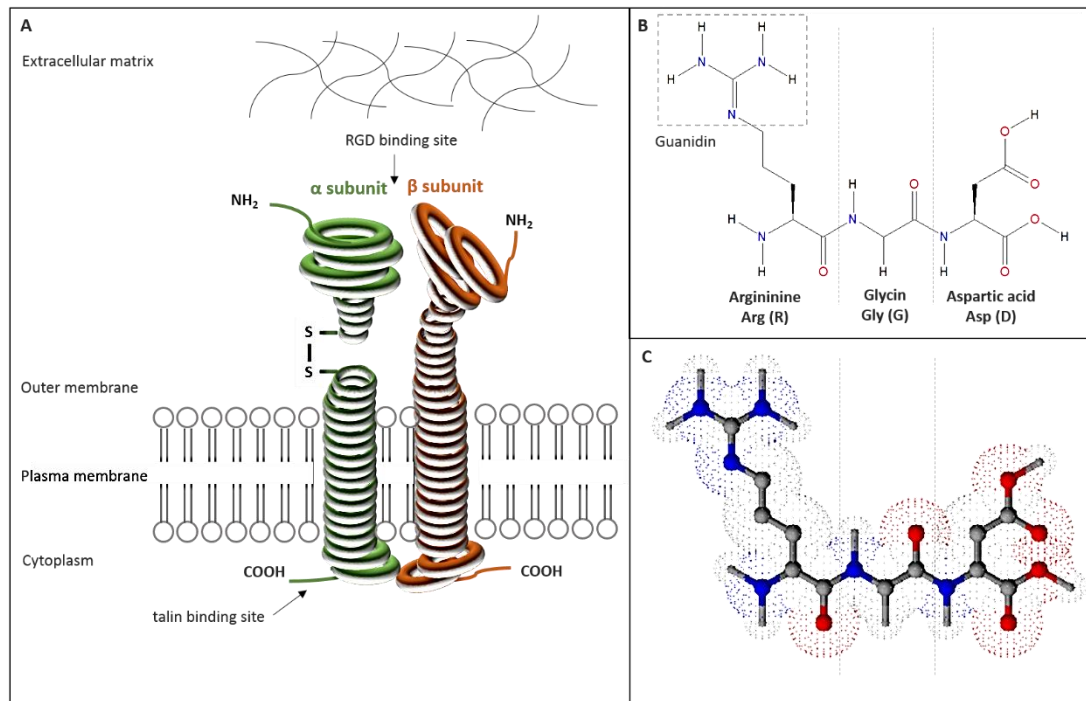


Figure 3.2: Integrin receptor. (A) Simplified schematic representation of an integrin hetero dimer with an RGD ligand binding site. (B) Chemical structure and (C) stick and ball model of the RGD motif.

Many integrin receptors such as α v β 3 and α 5 β 1 bind directly to RGD, but the presence of an PHSRN (Proline–Histidine–Serine–Arginine–Asparagine) sequence within fibronectin synergises with the RGD sequence in order to increase the activation of the α 5 β 1 integrin, and thus cell adhesion, about 100-fold [326–329]. Likewise the PDSGR (Proline–Aspartic acid–Serine–Glycine–Arginine) sequence and the RYVVLPR (Arginine–Tyrosine–Valine–Valine–Proline–Arginine) sequence promote cell binding to the YIGSR (Tyrosine–Isoleucine–Glycine–Serine–Arginine) domain of laminin [33, 34]. Thus, when developing biomaterials, it is a useful approach to consider the combination of certain cell binding motifs with beneficial functional peptide domains. This knowledge has been increasingly utilised in the field of biomaterial engineering in terms of altering cell behaviour [12, 317, 330, 331].

Many of these cell binding motif sequences are rich in nitrogen (such as arginine) or contain carboxyl groups (such as aspartic acid). Therefore, such groups are increasingly recognised and considered when developing biomaterials for improvement of cell attachment and regulation [332]. For example, the RGD motif as part of a protein shows very high affinity to integrins, whereas the motif as part of a very short peptide or even alone is much less effective. *Hautanen et al.* found that the GRGDSP (Glycine-Arginine-Glycine-Aspartic acid-Serine-Proline) motif within fibronectin is 1000 times more effective in cell attachment as part of the fibronectin compared to the sequence motif alone [333]. Notwithstanding, integrin specificity is still maintained. However, if the aspartic acid is exchanged against glutamic acid (both carry a carbonyl functional group) or glycine replaced by alanine, the activity of the motif is reduced about 100 fold [333]. Moreover, the conformation (L or D) of the given amino acids is of great importance. For example, *Pierschbacher et al.* demonstrated that, within proteins, aspartic acid is only active in the L-form [334].

Alongside RGD, various ECM peptides were identified that encourage cell adhesion [335-338]. Many of these show high similarities to the RGD motif. Some examples include the KGD motif (Lysine-Glycine-Aspartic acid, i.e. in barbourin, a desintegrin)[339], the RHD motif (Arginine-Histidine-Aspartic acid, i.e. in amyloid β) [340, 341] or the NGR motif (Asparagine-Glycine-Arginine, i.e. in fibronectin)[342, 343], all of which are affine towards particular integrins [344].

A large range of the BTL and ESP materials had been investigated previously with respect to their ability to influence cell behaviour and stem cell differentiation [305, 345]. Considering the outcome of these studies, the most promising substrates were chosen for this study: ESP 003, ESP 004, and ESP 007, and BTL 15 ([Figure 3.3](#)). The first three substrates are stereochemical analogues of the RGD motif in different conformations. ESP 003 and ESP 004 were designed using amine and carboxyl functional group chemistries. ESP 007 is an analogue

to ESP 004, but with the carbonyl functionality replaced with hydroxyl functionality which allows the comparison of these functional groups. BTL 15 on the other hand was equipped with all three functional groups ([Table 3.1](#)).

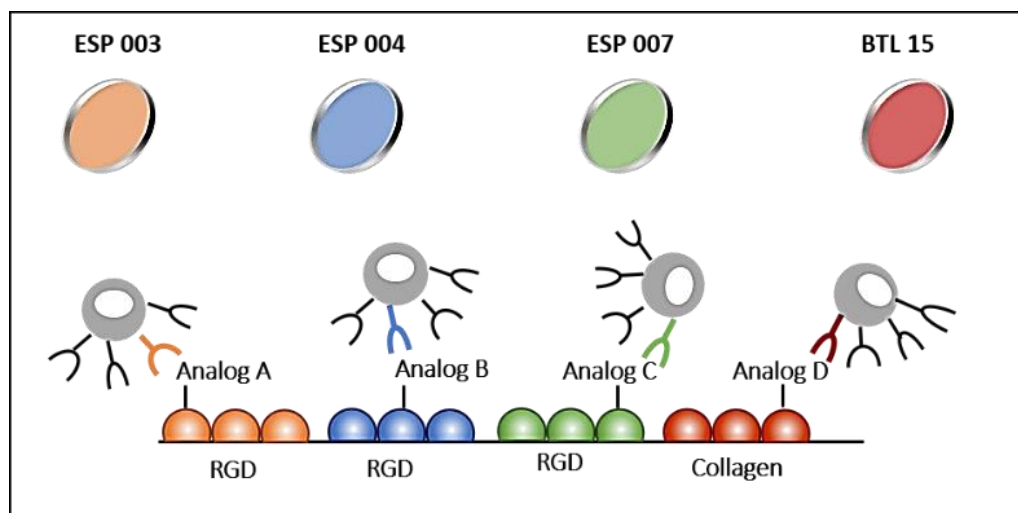


Figure 3.3: Schematic representation of polyacrylate substrates that mimic *in vivo* cell binding motifs (stereo) chemically. ESP 003, ESP 004 and ESP 007 mimic structurally the RGD motif in different conformations whereas BTL 15 mimics a cell binding motif present within collagen.

During the course of this study a range of additional substrates have been developed that include stereochemically modified versions of these polymers or new designs that target other promising ECM cell binding motifs that were identified from the literature: ESP 008 (Perlecan), ESP 009 (Laminin), ESP 010 (Collagen), ESP 011 (RGD, modified ESP 007) and ESP 012 (laminin, modified ESP 009).

Aims of this chapter

This chapter aims to introduce the Biomer Technology Ltd. polyacrylate substrates used in this study as well as a thorough analysis of their physicochemical properties. The following information were provided by Biomer Technology Ltd in order to enable data analyses and interpretation ([Table 3.1](#), [Table 3.2](#), [Table 3.3](#)).

Table 3.1: Presence of functional groups that polyacrylates are equipped with.

Polymer/functional groups	-NH ₂	-COOH	-OH
ESP 003	X	x	
ESP 004	x	x	
ESP 007	x		x
ESP 008	x	x	x
ESP 009	x	x	X
ESP 010	x	x	
ESP 011	x		X
ESP 012	x	x	X
BTL 15	x	x	X

Table 3.2: Theoretical trend of functional groups among polyacrylate polymers.

functional group	Trend
-NH ₂	ESP 009 > ESP 007 = ESP 010 > ESP 004 = ESP 008 > ESP 003 > BTL 15 > ESP 011 > ESP 0012
-COOH	ESP 010 > BTL 15 = ESP 003 > ESP 004 > ESP 009 > ESP 008 > ESP 012
-OH	ESP 008 > ESP 009 > ESP 011 > ESP 012 > ESP 007 > BTL 15

Table 3.3: Theoretical trend of steric hindrance among polyacrylate polymers.

Trend of steric hindrance
ESP 009 < ESP 010 < ESP 008 < ESP 003 = ESP 004 = ESP 007 = ESP 011 = ESP 012 = BTL 15

3.2 Results

3.2.1 Surface characterisation using X-Ray Photoelectron Spectroscopy

Polyacrylate surfaces were analysed using X-Ray photoelectron spectroscopy (XPS) in order to determine the surface elemental composition and the binding states of these elements within the surface. Representative fitted survey and high resolution spectra from ESP 003 are shown in [Figure 3.4](#).

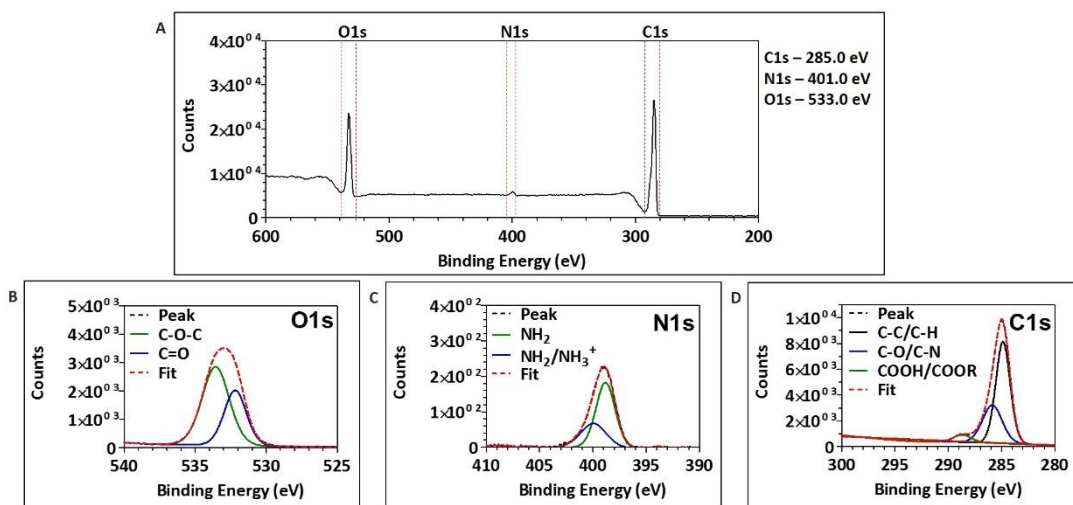


Figure 3.4: Representative XPS spectra obtained from ESP 003. (A) Survey scan highlighting the fitted peaks carbon (C1s), nitrogen (N1s) and oxygen (O1s). (B) O1s (C) N1s and (D) C1s high resolution spectra with fitted peaks. Note: y-scale is different for improved visibility of scans.

All substrates were composed of a carbon based polymer backbone and various functional group chemistries ([chapter 3.1](#), 56). [Figure 3.5](#) shows the quantification of the surface elemental composition obtained for each polyacrylate and [Table 3.4](#) the corresponding values. Notably, the component present in the highest percentage was carbon, as the polymer backbone and the aliphatic spacer monomers were primarily composed of it. Nitrogen was only present in pendant functional groups and therefore only occurred in reasonably low percentages ([Figure 3.5 B](#)).

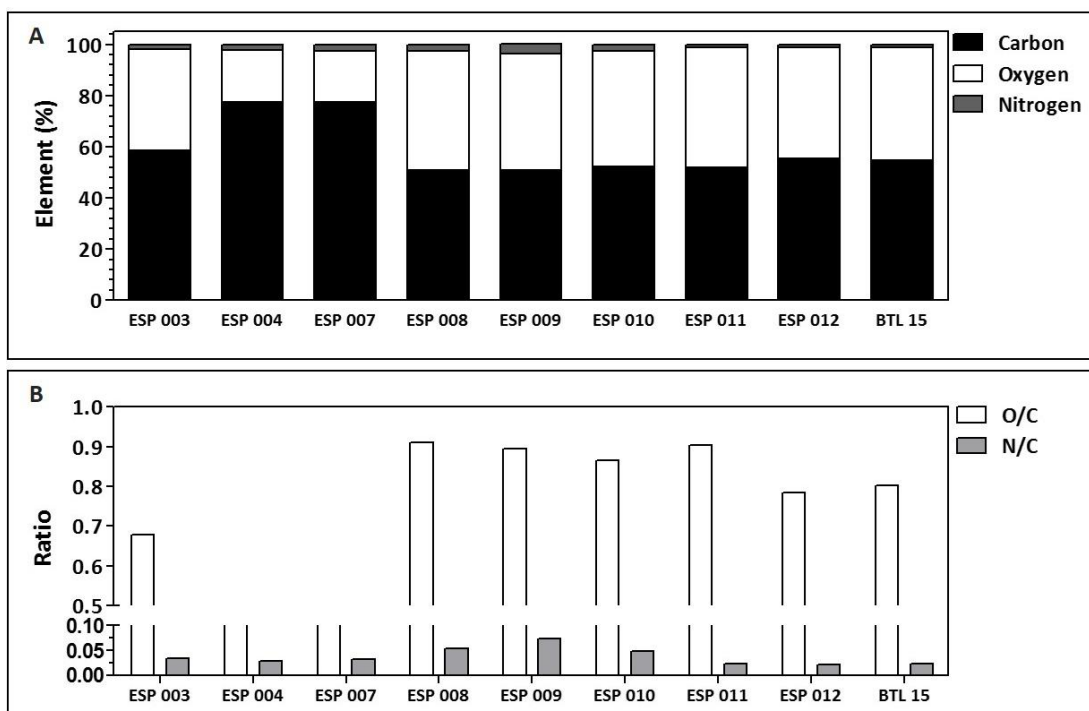


Figure 3.5: Elemental surface composition. (A) Elemental contribution of each element to the substrate in per cent and (B) Ratio of oxygen/carbon and nitrogen/carbon. All data were obtained via analyses of the survey spectra.

Table 3.4: Elemental surface composition. Shown are the elemental percentages of carbon (C), oxygen (O) and nitrogen (N) as analysed for each substrate and the O/C and N/C ratios. All data were obtained via analyses of the survey spectra.

	Element			Ratio	
	Carbon (%)	Nitrogen (%)	Oxygen (%)	N (%) / C (%)	O (%) / C (%)
ESP 003	58.45	1.95	39.6	0.03	0.68
ESP 004	77.56	2.3	20.15	0.03	0.26
ESP 007	77.52	2.57	19.91	0.03	0.26
ESP 008	50.9	2.75	46.35	0.05	0.91
ESP 009	50.89	3.75	45.54	0.07	0.89
ESP 010	52.25	2.55	45.2	0.05	0.87
ESP 011	51.9	1.22	46.88	0.024	0.90
ESP 012	55.39	1.17	43.44	0.02	0.78
BTL 15	54.8	1.24	43.96	0.02	0.80

Further analyses of the elemental peaks allowed quantification of the elemental binding states present. [Figure 3.6](#) shows the analyses of the carbon (C1s), oxygen (O1s) and nitrogen (N1s) peaks and [Table 3.5](#) the corresponding values. The C1s peak composition ([Figure 3.6 A](#)) showed that three types of carbon bonds were present in all substrates: C-C/C-H (aliphatic,

non-polar bonds from the backbone and hydrophobic monomer spacer groups) and C-O/C-N and COOH/COOR groups (polar functional groups and ester groups). ESP 011 and ESP 012 appeared to contain more carboxyl (COOH/COOR), a larger content of C-O / C-N groups and less non-polar C-C/C-H-bonds compared to the other substrates. ESP 003, ESP 004 and BTL 15 on the other hand contained very little carboxyl groups but more non-polar bonds.

O1s peak analyses ([Figure 3.6 B](#)) revealed that three main bonds were present within the substrates: C-O-C (ester), C=O (carbonyl) and C-OH (hydroxyl), with the latter one being incorporated as functional groups in order to mimic cell binding motifs accordingly. However, ESP 003, ESP 004 and ESP 010 were not equipped with hydroxyl groups whereas all other substrates contained these to a certain extent. ESP 008 and ESP 011 had the highest hydroxyl group content amongst the polyacrylate substrates.

The nitrogen component was only present as part of the amine functional groups and was either charged or uncharged. Quantification of the nitrogen sub peaks to determine the composition was difficult as the peaks generally contain significant background noise. However, only a small difference between uncharged and charged nitrogen groups among the polyacrylates was detected ([Figure 3.6 C](#)) with ESP 003, ESP 004, ESP 12 and BTL 15 containing a higher amount of charged groups compared to other substrates.

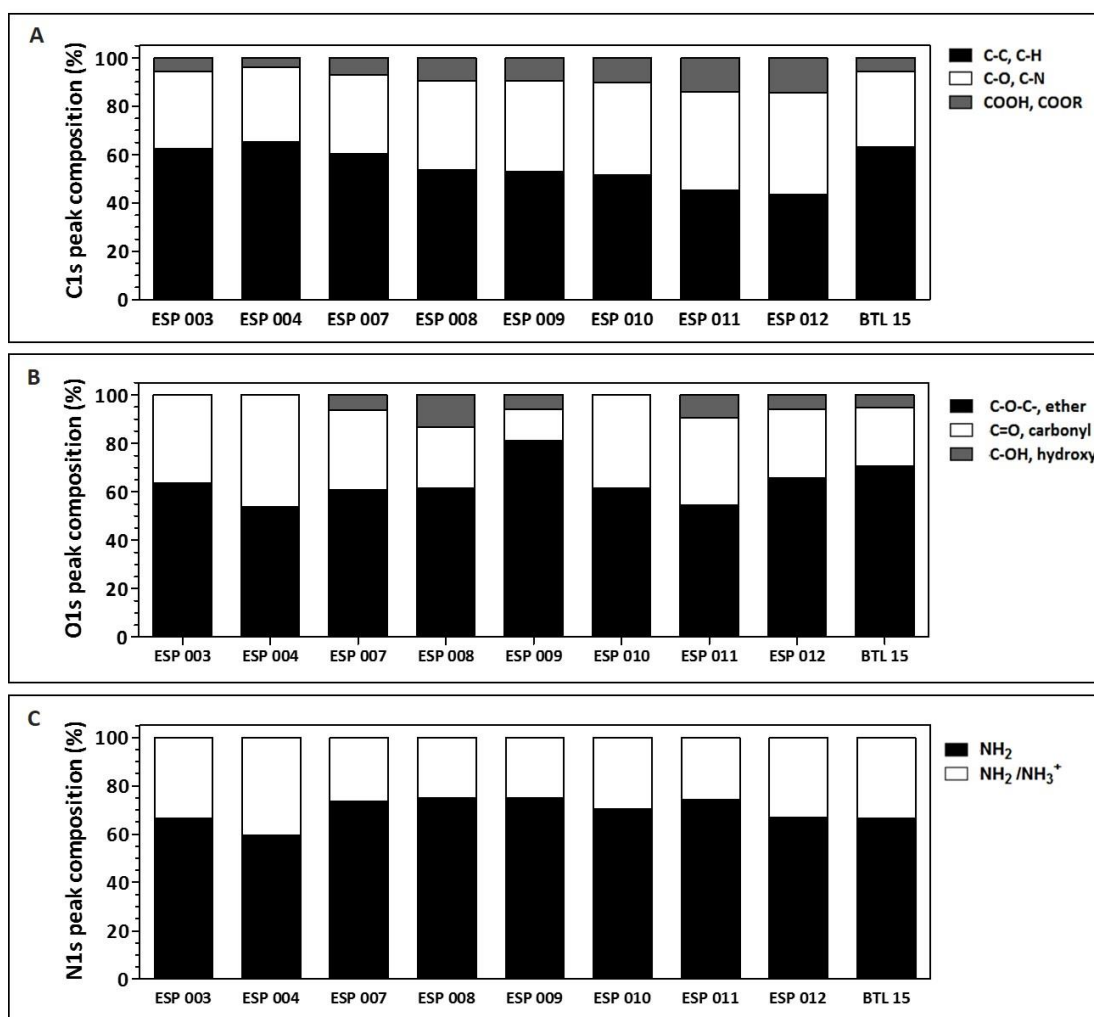


Figure 3.6: Element peak composition in per cent. (A) Carbon / C1s peak (B) Oxygen / O1s peak and (C) Nitrogen / N1s peak. All data were obtained by curve fitting analyses of C1s, O1s and N1s high resolution spectra.

Table 3.5: Elemental surface composition in per cent. All data were obtained by curve fitting analyses of C1s / O1s and N1s high resolution spectra.

	Carbon C1s			Oxygen O1s			Nitrogen N1s	
	C-C/C-H	C-O/C-N	COOH/COOR	C-O-C	C=O	C-OH	NH ₂	NH ₂ /NH ₃ ⁺
ESP 003	62.46	31.97	5.57	63.52	36.48		66.69	33.31
ESP 004	65.34	30.59	4.07	53.84	46.16		59.58	40.42
ESP 007	60.40	32.44	7.16	60.66	32.90	6.44	73.5	26.50
ESP 008	53.59	36.99	9.42	61.66	24.91	13.43	74.85	25.15
ESP 009	53.08	37.46	9.46	81.16	12.94	5.90	74.89	25.11
ESP 010	51.52	38.26	10.22	61.61	38.39		70.37	29.63
ESP 011	45.38	40.39	14.04	54.34	36.13	9.53	74.36	29.63
ESP 012	43.64	41.92	14.43	65.62	28.31	6.06	66.93	33.07
BTL 15	62.99	31.44	5.57	70.63	23.97	5.40	66.61	33.39

3.2.2 Surface wettability analyses

3.2.2.1 Sessile drop

Theoretically all substrates were considered to be relatively hydrophobic and thus expected to have high contact angles (CAs) as the main element within the substrates was carbon. [Figure 3.7](#) shows the CAs obtained for the polyacrylates. All materials showed highly significant differences from the glass control suggesting that the coverslips were completely coated. CAs revealed high and hydrophobic values for most substrates that were in the range of $71 \pm 1^\circ$. Three substrates, ESP 008, ESP 009 and ESP 010 were significantly more hydrophilic with CAs of about $64 \pm 2^\circ$.

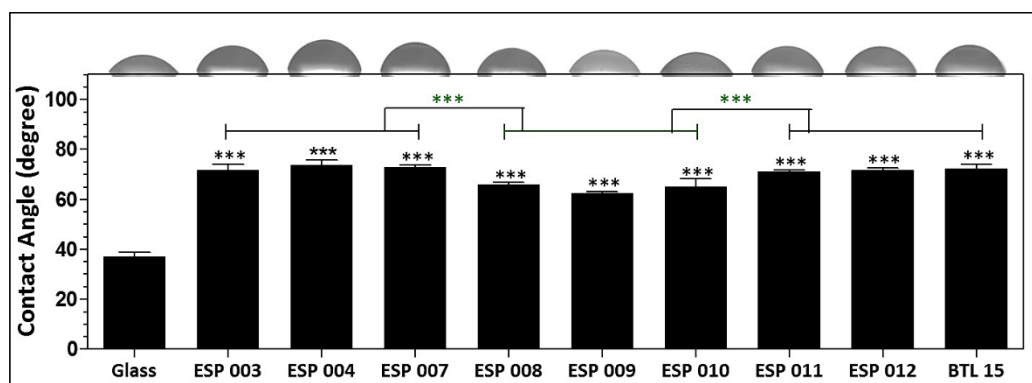


Figure 3.7: Polyacrylate CA analyses. All substrates were significantly different from glass (Tukey model, $p < 0.05$). ESP 008, ESP 009 and ESP 010 were significantly more hydrophilic than other polyacrylates.

Irrespective of the number of substrates measured to get an average CA value, there are various factors that might influence results such as contaminations (e.g. dust particles), surface oxidation through contact with air or surface roughness that might occur through nonhomogeneous surface coating. Therefore, surface CA maps were recorded that displayed the distribution of CA values across the entire surfaces. [Figure 3.8](#) shows CA maps in a top view 2D perspective and in 3D. These highlighted indeed an uneven spreading of CAs across the entire substrate. However, when comparing the average CA values obtained by measuring replicates ([Table 3.6](#)), both methods were found to give results in a very similar

range. Therefore, the outcome of sessile drop CA can be seen as an accurate measure of the surface wettability.

Table 3.6: Average CAs obtained for polyacrylates used in this study.

Sample	Static Contact Angle – 7 Replicates	Static Contact Angle - Map
ESP 003	71.03 ± 3.06	69.82 ± 4.27
ESP 004	73.06 ± 3.02	73.98 ± 4.49
ESP 007	72.76 ± 3.79	63.45 ± 6.62
ESP 008	66.00 ± 2.43	57.98 ± 7.97
ESP 009	62.45 ± 2.06	63.97 ± 9.69
ESP 010	66.07 ± 5.11	64.04 ± 5.17
ESP 011	71.22 ± 1.93	67.19 ± 1.78
ESP 012	71.76 ± 1.32	71.57 ± 2.64
BTL 15	71.87 ± 3.65	73.34 ± 2.85
Glass	37.06 ± 5.60	45.70 ± 4.79

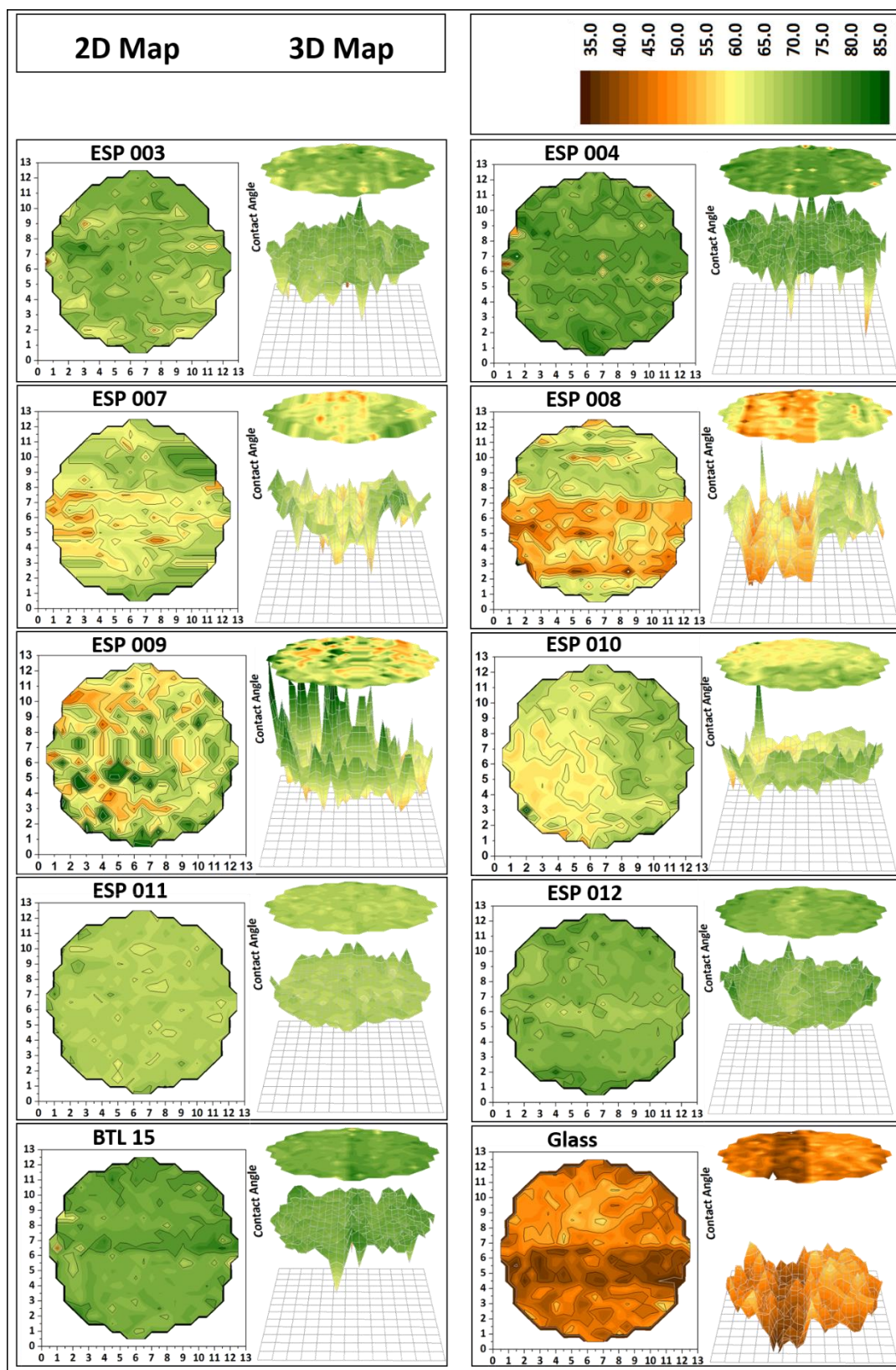


Figure 3.8: 2D (top view) and 3D CA maps of polyacrylate substrates. 2D maps show the wettability profile across the surface whereas 3D maps show wettability from one point perspective. Note: These maps do not represent topographical features.

3.2.2.2 Captive bubble

Another option to investigate surface wettability is measuring the CA of an air bubble applied to a liquid-exposed substrate. [Figure 3.9](#) shows the values obtained for the CAs either when the substrate was directly immersed in water or 2 h post exposure in FBS. Noticeably, all substrates were significantly different from glass. Consistent with the static CAs, ESP 008, ESP 009 and ESP 010 were found to be more hydrophilic than the other substrates with ESP 004 being the only exception. When substrates were exposed to FBS prior to CA measurements, a significant decrease of about 10° was noticed ([Figure 3.9](#), [Table 3.7](#)). The only exceptions were ESP 008 and ESP 010 where the CA remained constant. Overall, static CA data for all substrates, excluding glass, were found to be between 60° and 80°, whereas values for the CB contact angles were between 40° and 60° and were thus about 20° lower.

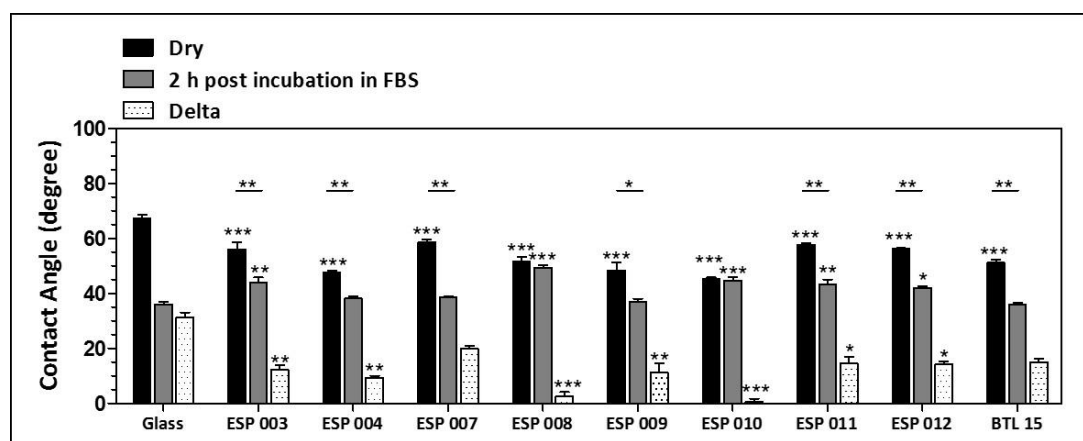


Figure 3.9: Polyacrylate CAs obtained using the CB method. All substrates were significantly different from glass (Tukey model, $p < 0.05$). ESP 008, ESP 009 and ESP 010 were significantly more hydrophilic than any other substrate. Delta is the difference between the dry and the in FBS incubated substrate.

Table 3.7: CB values obtained for polyacrylates in distilled water. Samples were either directly measured or exposed to FBS for 2 h prior measurements.

Sample	Captive bubble	Captive bubble post incubation in FBS
ESP 003	57.28 ± 7.28	43.96 ± 5.55
ESP 004	47.48 ± 4.78	38.14 ± 4.54
ESP 007	58.54 ± 3.91	38.67 ± 2.85
ESP 008	51.46 ± 5.00	49.31 ± 5.52
ESP 009	48.34 ± 7.95	37.07 ± 3.44
ESP 010	45.08 ± 4.50	44.61 ± 5.49
ESP 011	57.74 ± 3.72	43.19 ± 6.95
ESP 012	56.11 ± 2.72	41.91 ± 4.52
BTL 15	51.14 ± 4.12	36.07 ± 2.42
Glass	67.34 ± 6.19	35.99 ± 4.53

3.2.2.3 Dynamic contact angle

Dynamic contact angles (DCAs) were recorded to further assess substrate wettability. As the dry state was not representative for physiological conditions, DCAs were also collected after substrates were exposed to either water for 2 h (swollen state) or FBS (protein adsorption).

All polyacrylates showed overall DCA values in a similar range in the dry state (Figure 3.10). The substrates showed significantly different advancing angles from glass ($p < 0.05$, Tukey model). All substrates showed high advancing angles (maximum possible CA / hydrophobic maximum) up to 100° with ESP 010 being the highest with 120°. The receding angles (minimum possible CA / hydrophilic minimum) were considerably lower with $30 \pm 5^\circ$. Receding angles differed slightly between polyacrylates with ESP 007, ESP 011 and ESP 012 being not significantly different from glass (Tukey, $p < 0.05$). The hysteresis, particularly in dry state, strongly varied between substrates with ESP 004, ESP 011 and ESP 012 being the lowest.

When substrates were pre-exposed to water for 2 h prior the actual DCA measurement (Figure 3.10 B) the substrates showed similar values for the hysteresis as in dry state. Overall, advancing and receding angles changed minimally. ESP 003 and ESP 004 were very similar

with respect to functional group composition: ESP 003 has less amine groups but more carboxyl groups. Little significant difference was found in the receding angle and no difference was detected in the hysteresis ($p < 0.05$, Tukey model). Structurally, ESP 007 was an analogue of ESP 004 with the only difference being that carboxyl groups were replaced by hydroxyl groups. However, no significant difference in CA was found between both ($p < 0.05$, Tukey model).

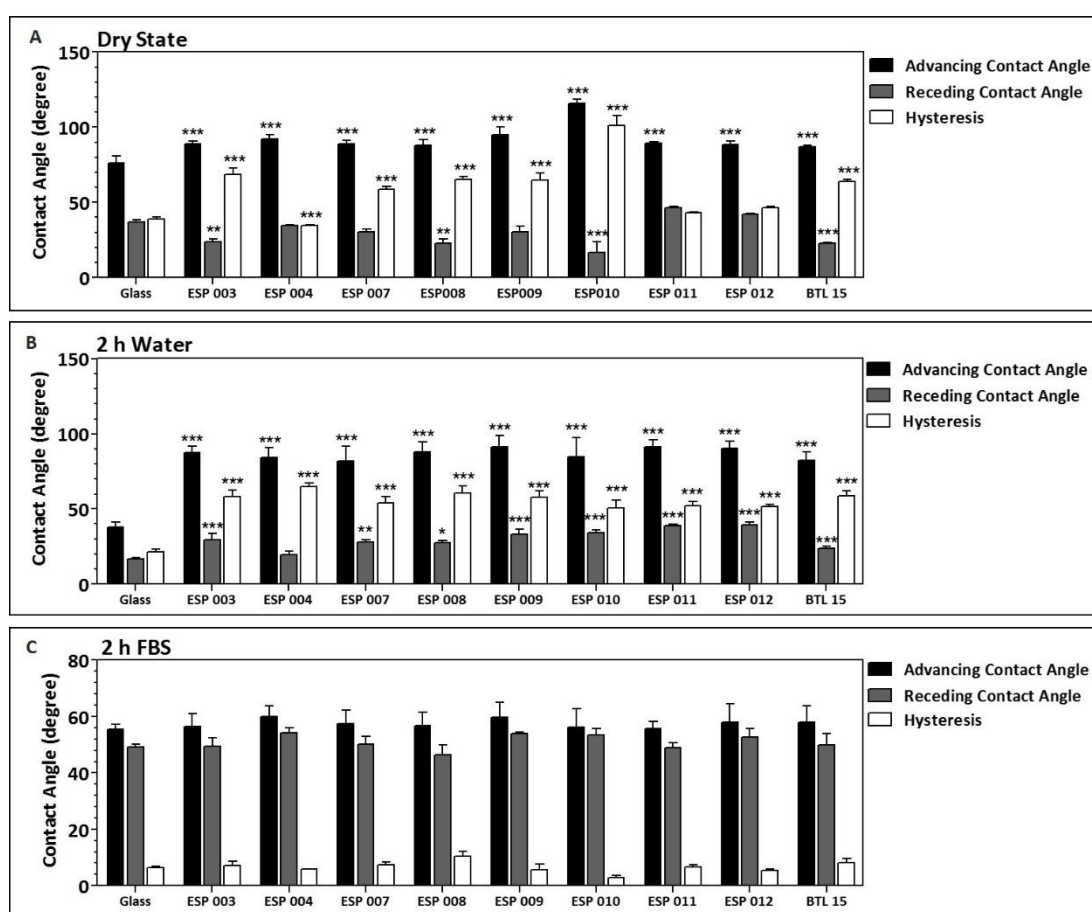


Figure 3.10: DCAs obtained for all polyacrylates coated on 22 mm² coverslips and measured in distilled water. Results represent the mean of 7 measurements \pm SEM. (A) Dry state, (B) 2 h post exposure in water and (C) 2 h post exposure in FBS. Advancing and receding angles of most substrates were significantly (Tukey model, $p < 0.05$) different from glass in both, dry and hydrated state, but not after exposure in FBS.

When the dry substrates were directly immersed in water for 10 repeated cycles, only little changes, depending on the substrate a decrease or an increase, occurred between the first and second wetting cycle. Afterwards the DCAs were essentially constant (Figure 3.11).

To further mimic a situation that resembles cell culture conditions, polyacrylates were immersed for 2 h in FBS prior DCA measurement (Figure 3.10 C). Interestingly this caused very prominent changes. The advancing CAs decreased in general about 40° whereas the receding angles increased about 30°. This resulted in a very small hysteresis. This trend was consistent throughout the range of substrates.

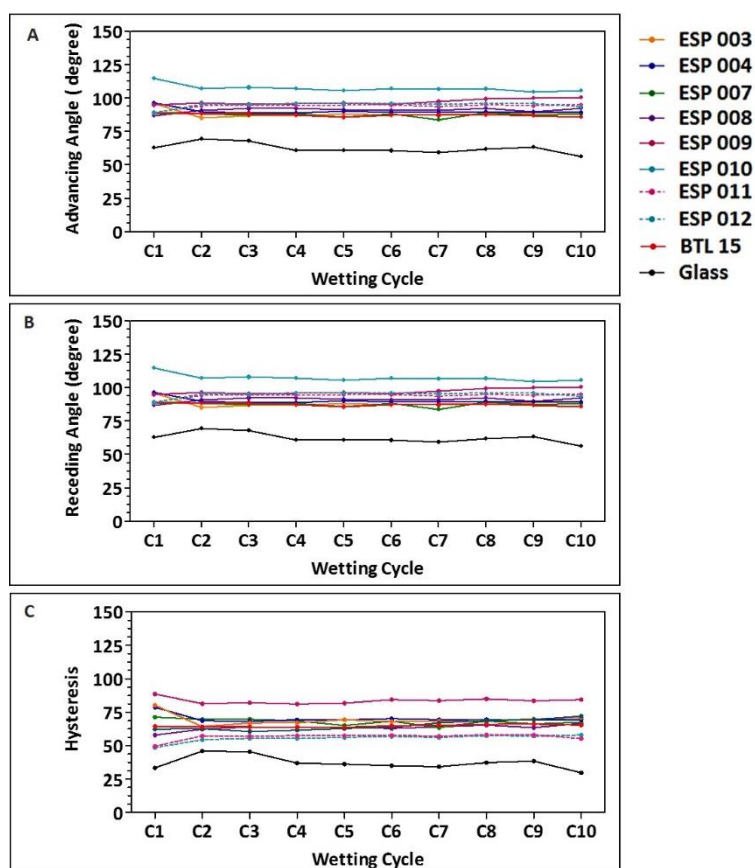


Figure 3.11: DCA cycles. Dry 22 mm² polymer coated glass cover slips were repeatedly immersed in distilled water for a duration of 10 cycles. Results represent the mean of three samples. SD is not shown in order to maintain visual clarity. (A) Advancing angle (B) receding angle and (C) hysteresis

3.2.3 Substrate characterisation using Atomic Force Microscopy

3.2.3.1 Surface topography and roughness

Substrate thickness, nano- and microscale topography and elasticity were analysed using Atomic Force Microscopy (AFM). Figure 3.12 shows the thickness of the layer for each substrate. The polyacrylate layers were between 0.5 and 1 µm thick. ESP 009 and ESP 010

were thinner with values lying between 0.3 and 0.5 μm and therefore significantly lower than most other polyacrylates ($p < 0.05$, Tukey model).

Generally, surface roughness and topography are important parameters that may influence accurate measurements of film thickness. [Figure 3.13](#) shows $50 \mu\text{m}^2$ 3D images of the polyacrylate surfaces. These images showed that some surfaces had larger hills (i.e. BTL 15) whereas others showed rather small / low hills (i.e. ESP 007). Also the shape and spreading of these features differed strongly between surfaces.

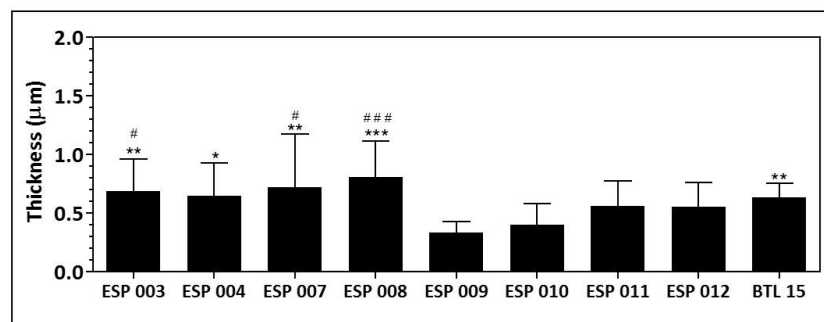


Figure 3.12: Polymer layer thickness of polyacrylates coated on glass cover slips. Asterisks indicate significant difference towards ESP 009, # significant difference towards ESP 010 ($p < 0.05$, Tukey model).

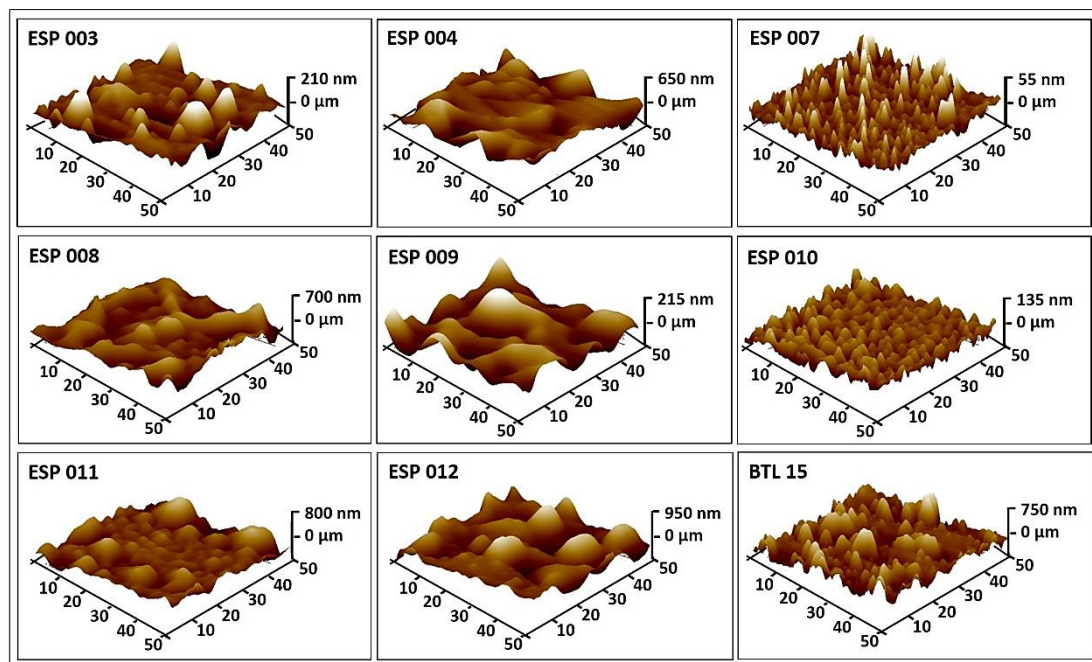


Figure 3.13: AFM $50 \mu\text{m}^2$ 3D topographical surface images of all polymer substrates. Brighter colours represent high areas and darker colours represent deeper areas. AFM was operated in tapping mode. Note: Z-scale is different between images to improve visualization.

Figure 3.14 shows the quantification of the heights of these structures. It is notable that all polyacrylates showed a heterogeneous surface topography with many hill-like structures that are unevenly distributed across the surface. The quantification showed that there were very distinctive differences between substrates. ESP 011, ESP 012 and BTL 15 showed hills that were quite evenly distributed in height with hill-like structures reaching up into μm range, whereas ESP 007 and ESP 010 on the other hand appear lower with hill-like structures ranging between 50 and 200 nm height. Others, including ESP 003, ESP 004 and ESP 008, showed rather intermediate hill height. Notwithstanding that many substrates showed hills that differ strongly in height, the quantification still allowed a superficial observation and interpretation of topographical differences between substrates.

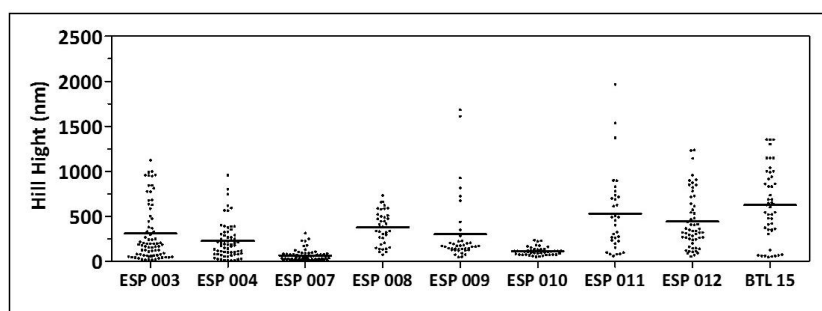


Figure 3.14: Height quantification hill like structures on topographical images $50 \mu\text{m}^2$ AFM images. Each dot represents one measured hill from a range of a minimum of 3 different substrates and 5 different areas.

Additionally, roughness was quantified on a smaller scale (nanoscale) by determination of the root mean square (RMS), a statistical measure based on an algorithm (Equation 2.3, p 36). Figure 3.15 shows the analyses of the RMS roughness of all substrates. Notably most substrates showed RMS values of about 7-12 nm. ESP 007, ESP 008 and ESP 010 were much smoother compared to the other substrates. Interestingly this trend was similar to the hill height determined in Figure 3.14, where these three substrates appeared to have the smallest overall hill heights and therefore appeared smoother.

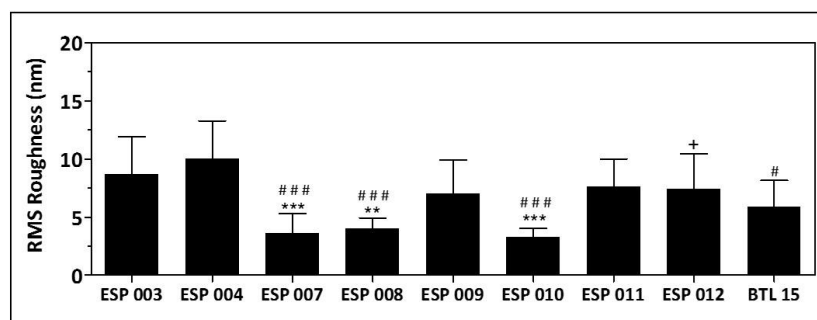


Figure 3.15: Polyacrylate RMS roughness analyses. Asterisks indicate significant difference compared to ESP 003, number signs compared to ESP 004 and plus signs compared to ESP 007 ($p < 0.05$, Tukey model).

3.2.3.2 Surface mechanical properties

Also surface mechanical properties were analysed using the AFM. [Figure 3.16](#) showed the Young's modulus (elastic modulus) that was obtained for each of the polyacrylates. All substrates had an elastic modulus of about 2 ± 0.5 GPa without any significant differences between them ($p < 0.05$, Tukey model).

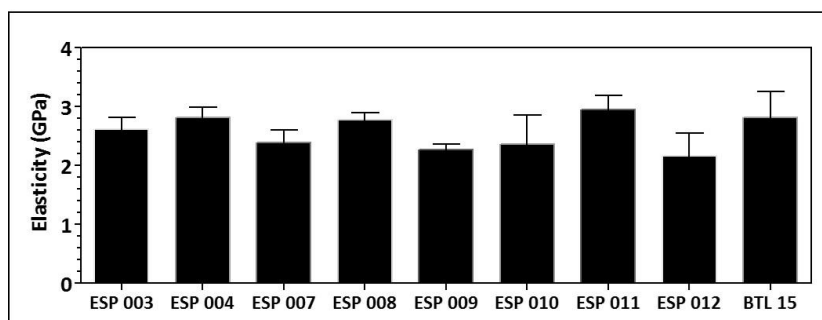


Figure 3.16: Polyacrylate Young's modulus (Elastic modulus) analyses. All substrates showed an elastic modulus of about 2 ± 0.5 GPa. No significant differences were found ($p < 0.05$, Tukey model).

3.3 Discussion

3.3.1 Surface characterisation using X-Ray Photoelectron Spectroscopy

The effects of small functional groups on cell behaviour and differentiation have been intensely studied in recent years [272, 346, 347]. The functional groups that were used in this

study were chosen as they are present in the amino acids that peptides / proteins are composed of, which allowed us to mimic, to a certain extent, *in vivo* cell binding motifs.

The polyacrylates investigated in this study were similar in that they all were composed of an acrylate based carbon backbone structure. The XPS results showed only small differences in their general surface composition with ESP 004 and ESP 007 being the only exceptions. All substrates were shown to have a very high carbon content (polymer backbone), which explains why the C1s peak revealed a high content of non-polar bonds throughout the range of substrates and was only slightly decreased with increasing presence of polar functional groups. Moreover, it can be assumed that substrates with a large degree of steric hindrance (higher amount of hydrophobic spacer groups) will have a higher carbon content. ESP 008, ESP 009 and ESP 010 had, among all substrates, less steric hindrance. However, their carbon content was not higher nor was the contribution of non-polar C-C/C-H bond notably higher within these substrates compared to other polyacrylates. This suggests that the surface functional groups did not necessarily have a large impact on substrate composition.

All substrates were equipped with particular functional group chemistries, namely -OH, -COOH or -NH₂, wherein polyacrylates differed in identity and proportion of these groups as well as in stereochemistry and spatial distribution through the inclusion of alkyl hydrophobic spacer groups which were introduced by choosing monomers that presented these alkyl side chains. These appeared to influence carbon and nitrogen proportionally (decreasing oxygen and nitrogen percentages with higher carbon content). For example, BTL 15, that was equipped with a high number of hydrophobic spacer groups to introduce steric hindrance (see [chapter 3.1](#), p 56), did not show apparent differences in elemental composition when compared to other substrates. It contained all three types of polar functional groups which influenced the overall elemental composition. However, it belonged to the substrates with

the highest percentage of non-polar bonds and consequently contained comparably less C-O / C-N bonds (-NH₂, -OH).

Notably, the trend of functional group chemistry obtained by XPS did not necessarily confirm the theoretical trend. For example, looking at the carbon C1s peak of ESP 011 and ESP 012 ([Figure 3.6](#)), both contained a high amount of C-O / C-N and COOH / COOR bonds compared to other substrates. Theoretically both substrates contained -NH₂ and -OH groups. Contrary to the theoretical trend both substrates, ESP 011 and ESP 012, contained relatively fewer -NH₂ and -OH groups. Moreover, a high concentration of -COOH/-COOR groups was found within both substrates, nevertheless ESP 011 did not contain -COOH functional groups and, looking at the theoretical trend, ESP 012 contained the lowest amount of carboxyl groups compared to other substrates. It has to be noted that -COOH and -COOR (ester) bonds, which were present within all polyacrylates, were fitted within the component peak fit which impeded exact quantification of the carboxyl functional group composition. However, the quantification of the three carbon binding states was very similar between the two substrates. Only small variations between the other polyacrylates, with respect to these three carbon binding states, were found though all lay within each other's typical XPS error ($\pm 10\%$) range [348].

Analyses of the oxygen O1s peak revealed that most substrates contained -OH groups with exception of ESP 003, ESP 004 and ESP 010. Again, there were apparent differences in the amount of -OH groups, which showed a trend very similar to the theoretical one ([Table 3.2](#), p 62). Similarly to the carbon binding states, most variations of ester and carbonyl binding states were small and did not appear to be highly different between the substrates except ESP 009 which, compared to the other substrates, had very little carbonyl content. Otherwise all substrates showed a similar content of carbonyl and ester groups, again, lying within the range of XPS accuracy [348].

In summary, very little differences have been detected between substrates in the elemental composition and elemental binding states and it was therefore difficult to draw final conclusions from these. Although XPS is a widely known technique to analyse surface chemistry it has limitations. The general accuracy of XPS is only about $\pm 10\%$ [348]. Moreover, the X-Ray beam photons penetrate the surface to a depth of about 5 to 10 nm [349]. This means the elements and binding states detected comprise the chemistry within this range and therefore did not allow us to draw any conclusions about the immediate surface chemistry at the substrate - air interface. These drawbacks will affect the outcome of the analyses and might be the reason for the differences between actual findings and theoretical expectations.

Another perspective on the disparity between theoretical and actual values arises from the stereochemistry of the substrates. In theory, the polymers were designed using required monomers equipped with functional groups as well as hydrophobic alkyl spacer groups in order to mimic peptide sequences. Nevertheless, practically the spacer groups might have masked the functional groups or the functional groups might in turn have orientated towards the polymer bulk instead of reaching out of the surface [350, 351]. These conditions in turn could have been caused by unconsidered chemical interactions that influenced the stereochemistry of the bulk, such as attraction or repulsion of these groups [352]. For example, some of the functional groups within the substrates were charged. This was shown by N1s peak analyses that showed about $30 \pm 5\%$ of amines were charged with ESP 004 being the only exception (40%). Similarly, oxygen species might be charged, which is not detectible by XPS. The charge content could thus contribute to eventual unforeseen changes in stereochemistry. Additionally, nitrogen peaks are difficult to fit as the percentage is very low within all substrates and nitrogen peak background is generally very noisy. Moreover, surface contamination or oxidation could have potentially caused the presence of different types of

oxygen species on the polymer surface that could have influenced the quantification of functional groups.

The quantification of surface primary amine groups using colorimetric analyses did not work well on the polyacrylates substrates, as these had the tendency to non-specifically adsorb the dye in high amount and it could not be entirely removed although the substrates were intensely washed with PBS (data not shown).

3.3.2 Surface wettability analyses

There is a dispute whether wettability alone is in fact altering cell behaviour, as it is often accompanied by other altered surface properties, such as topography and chemical composition. However, many studies suggest that wettability of a substrate influences cell behaviour through protein adsorption [68, 77, 78]. In example, *Redey et al.* investigated osteoblast cell behaviour on stoichiometric hydroxyapatite and type A carbonate apatite and found that low wettability decreased cell attachment and collagen production and thus suggested that surface modification with polar components might lead to improved cell attachment and osteoconduction [70]. Another study suggested that the wettability of titanium surfaces can modulate osteoblastic differentiation of osteoblast lineage cells [71]. Controversially, others claims there are no direct correlations [74] as other chemical or physical properties could be responsible that often entail a change in wettability. This highlights that it is challenging, in some cases, to relate cell behaviour to only one single surface property.

Contact angles (CAs) measured by sessile drop technique revealed that the polyacrylates were hydrophobic with values in the range of $71 \pm 1^\circ$. This was expected as all substrates contained large amounts of non-polar carbon bonds. The two substrates with the largest carbon content were ESP 004 and ESP 007. However, the CAs were not more hydrophobic than those of other substrates. Interestingly, ESP 008, ESP 009 and ESP 010 were found to be

significantly more hydrophilic ($64 \pm 2^\circ$). This was in line with the provided theoretical degree of steric hindrance that revealed the lowest degree for these three substrates. Therefore, polar, hydrophilic groups would be less covered and more accessible by water. From XPS analyses it was revealed that the nitrogen/carbon ratio was larger than in other substrates and would therefore cause a CA decrease. This could also be related to the elevated presence of nitrogen functional groups within these three polyacrylates as were detected by XPS analyses. The sessile drop CA maps show variability in the values across the entire substrate surface and demonstrate inhomogeneity. During the sessile drop method on the other hand a water droplet is applied on a presumably topographically heterogeneous surface and reaches the state of equilibrium. The final CAs reached are generally dependent on several parameters, including initial drop energy, interactions with the surface and energy barriers, all of which might influence the final results rather randomly [353].

Instead of placing a water droplet on a dry surface, a substrate can be immersed in water and the CA of an air bubble can be measured. In this way, the substrate affinity to water can be analysed in a swollen / hydrated state. CAs obtained using a captive gas (air) bubble revealed values of about $58 \pm 5^\circ$. Similar to the sessile drop technique ESP 008, ESP 009 and ESP 010 appeared more hydrophilic with values of about $48 \pm 3^\circ$. As explained above, the reason for that could be their degree of steric hindrance that was lower within these three substrates and would therefore allow better accessibility of polar and hydrophilic groups by water. Additionally, ESP 004 and BTL 15 were found within the hydrophilic range which was surprising since ESP 004 had a very large carbon content (similar to ESP 007) and BTL 15 contained many hydrophobic alkyl groups, which would theoretically cause rather high hydrophobicity. Compared to the sessile drop technique, the CB method has a range of advantages including limitation of contamination due to the exposure in water and the liquid (water) maintains a saturated environment.

The CAs obtained by the CB method were about 20° lower than those obtained using the sessile drop method. The exposure of substrates to water might have caused swelling due to its penetration into the bulk. This in turn could have caused rotational changes of the backbone and functional groups leading to polar groups reaching vertically out of the substrates and therefore making substrates more hydrophilic. Generally, in macromolecules (i.e. biomolecules or synthetic polymers), hydrophobic areas will accumulate in a non-polar environment to reduce contact with water (hydrophobic effect, favourable in terms of the free energy in the system) and *vice versa* [354-356]. Therefore, the substrates would ideally reorganise in order to minimise the systems free energy. However, the degree of reorganisation and rotation will be determined by the proportion of functional groups and the degree of steric hindrance through aliphatic groups, which will in turn determine the extent of interactions. Similarly hydrogen bonding will occur between hydrophilic groups within the polymers as well as with water molecules (i.e. O–H...N, O–H...O) which will cause changes of the polymer conformation. The interaction with water molecules could potentially cause the water to be trapped within the polymer bulk which would result in a restriction of freely rotating water molecules that are trapped within the bulk as well as at the substrate-liquid interface which will in turn influence cell behaviour [357, 358].

The non-polar carbon backbone and bulky groups will not only increase substrate hydrophobicity, they might also mask hydrophilic functional groups, such as amine or hydroxyl groups and thus increase hydrophobicity even further [350]. The DCA analyses showed that all substrates had a very high hydrophobic maximum (advancing angle) and a very low hydrophilic minimum (receding angle). Most interesting however is the hysteresis which is the difference (Δ) of those two. Substrates with the largest hysteresis were ESP 003 and ESP 010. These outstanding values might be related to swelling behaviour of the substrates in water and eventually subsequently developing changes in surface topography. On the other hand, the lowest hysteresis was found to be present in ESP 004, ESP 011 and

ESP 012. The reason for that might be an inhibition of liquid penetrating the surface which might be caused by non-polar groups that eventually stick out from the surface. Overall, the hysteresis of CAs in dry and liquid (2 h water exposure) state ranged from 30 to 50°. This supported findings from the CA maps that showed distinct regions of hydrophobicity and hydrophilicity across the surfaces. This will cause altering behaviour of water towards particular regions (hydrophilic – water attracting / hydrophobic – water retracting). Such patterns might appear randomly, but they might also indicate a clustering of functional groups due to intramolecular interactions [359]. Moreover, as previously mentioned, surface functional groups may relocate once they are in contact with water which will change wettability, either of the entire surface or within such clusters [360]. The Wilhelmy plate (DCA) method generally holds some limitations. The practical advancing angle is usually lower than expected whereas the receding angle turns out higher due to the normal laboratory environment [353].

Three different methods for CA analyses have been applied all of which gave a different answer to one question. As theoretically expected, all methods confirmed that substrates were relatively hydrophobic and significantly different from a hydrophilic glass control which is explainable with the elemental surface composition being mainly determined by carbon non-polar bonds.

All CA measurements will be influenced by a variety of external parameters, including temperature and humidity. Moreover, substrate storage, ageing and contamination will influence wettability. This includes for example surface oxidation that can cause areas to be more hydrophilic than they were initially. Additionally, surface preparation might influence the data. When dip coating samples, thickness inhomogeneities might occur through an uneven distribution of polymer solution which in turn might change physical properties of the substrates, such as thickness and topography, which are known to influence substrate

wettability. Wettability differences were also found on a glass substrate that was cleaned before analysis.

Additionally other surface properties will influence the CA measurements. These include surface chemistry and steric hindering groups that may mask hydrophilic functional groups and might therefore distort measurements. Also surface nano-roughness can be an important factor when measuring wettability [361, 362]. In any case, the standard error of all CA throughout the three different methods was about $\pm 5^\circ$, indicating that each technique in itself is satisfactory. However, there were prominent differences of the CAs between the three methods of about 20° . This suggests, that one method alone might not be sufficient to get accurate data on these substrates whereas analysis by a combination of methods may allow a better understanding of the polymer behaviour to be determined.

The influence of protein presence (adsorption) on the CA was investigated using the CB as well as the DCA method. DCA measurements showed that with incubation in FBS the advancing angle decreased $\sim 40^\circ$ and the receding angle increase $\sim 30^\circ$ which consequently resulted in a very small hysteresis. Similarly the CA measured by the CB method showed a decrease of about 10° . Therefore, the exposure to FBS in both cases caused a decrease in wettability and indicated that proteins were adsorbed onto the surfaces. Proteins are composed of amino acids of which most contain hydrophilic functional groups (i.e. -OH in serine or -NH₂ in lysine). Their adsorption might be promoted due to surface topography or the formation of chemical interactions, such as electrostatic bonds or van der Waals forces from the non-polar groups. Moreover, surface energy has always been linked to protein adsorption. Proteins in solution are much hydrated and will generally attach to hydrophobic surfaces (low energetic surface) once they are in contact with it. This process occurs due to the strong hydrophobic interactions [79]. Conversely, hydrophilic surfaces are designated for repulsive solvation forces due to water molecules that bind to the surfaces [80, 81].

Generally, the mechanism of protein adsorption onto hydrophilic surfaces is energetically unfavourable [82].

When the DCA was measured on samples that are continuously immersed into water for a number of 10 cycles, there was only a small change of the advancing angle noticeable between the first and second immersions. Receding angles did not show any difference which caused an equivalent trend of advancing angle and hysteresis. An increase of these two implies a decrease in hydrophobicity suggesting that water penetrated the polymer coating and therefore caused them to be more hydrophilic and *vice versa*. However, when the substrates were removed from the water and immersed the second time, excess water from the first cycle will still be attached to the substrate and come in contact with the liquid contemporaneously as the substrate resulting in the CA change. Contrary to this however, was that some substrates showed a decrease and others an increase of the CA which allowed us to conclude this change was related to the actual polymer properties.

The DCA measurements were additionally performed after substrates were immersed in water for 2 h. Surprisingly this did not have any effects on advancing and receding angles compared to dry substrates. Moreover, the values were equal to those obtained when a dry substrate was immersed into distilled water for 10 cycles. This suggests that water itself does penetrate the surface quickly as soon as it is in contact with the substrate. No further changes will be caused by this penetration. This suggests that water induced a small change in the presentation of functional, hydrophilic or hydrophobic, groups which would in turn cause a change of the CA. Moreover, the constancy suggests that no more water is penetrating the surfaces as the substrate coating might have swollen and, following that, these would become more hydrophilic.

Once substrates were in the cell culture environment (rather aqueous condition enriched with biological molecules) the CA will be of great importance as it is influencing cellular

response. *Berg et al.* suggested that, if a substrate CA is below 65° (hydrophilic), the surface will exert repulsive forces (Berg-limit) and *vice versa* [82, 363]. Moreover, it has been shown previously that surface CAs in the range of the Berg limit promote cell attachment. However, the ideal CA is dependent on the cell type [77, 364]. 2 h post exposure to either water or FBS led to receding angles of about 30-40°, which can be considered as hydrophilic.

Finally it has to be emphasised that the glass cover slip might not have been the most suitable control for wettability measurements. All substrates were consistently and significantly different from glass, regardless of the method used, suggesting that the polymers covered the entire glass coverslip. When analysed by the sessile drop method, the CA was hydrophilic (~35°) as expected whereas determination using the CB approach revealed a more hydrophobic value (~68°). Cover slip glass is a hydrophilic substrate due to the presence of -OH groups. The CA increase most likely occurred due to surface damage, such as small scratches or due to contamination, such as dust particles or air born lipids. The glass had not been specially treated with detergent / surfactant solution, neither had it undergone velocity jet cleaning or any kind of plasma or acid treatment prior measurements [365, 366]. An additional reason for differences between sessile drop / CB and DCA method is most likely the difference in the manufacturing process. The 13 mm as well as 22 mm² coverslips were obtained from different companies ([Appendix V](#), p 245). The wettability properties of glass will vary depending on the exact composition, including silicon concentration on the glass surface as well as and -OH groups density [367].

3.3.3 Surface characterisation using Atomic Force Microscopy

3.3.3.1 Surface thickness and topography

All polyacrylates showed a similar thickness with relatively high standard deviations and therefore variations within particular substrate layers. A possible explanation for this could lie in the coating procedure, which could lead to differences in thickness between substrate

edges and the middle regions (Figure 3.17). Interestingly, ESP 009 and ESP 010 had the lowest thickness and variations within the layers, which could also explain their increased hydrophilicity compared to most other substrates. Moreover, thickness alterations between polyacrylate coatings may in turn effect surface roughness.

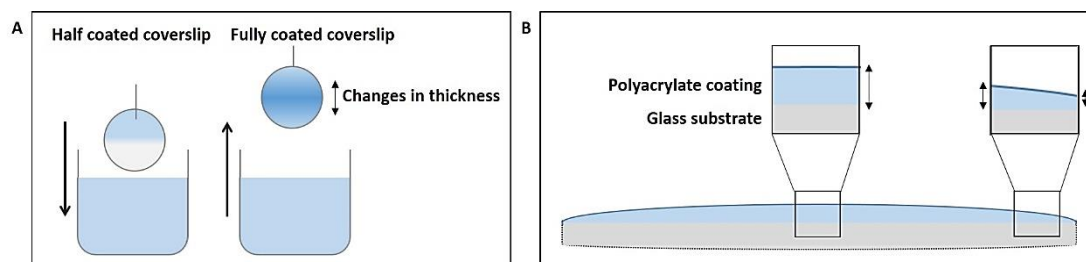


Figure 3.17: Polyacrylate layer thickness may vary due to polymer dipcoating procedure. (A) The polymer coating procedure may result in thickness variation across the surfaces. (B) As a result polyacrylate thickness may be differing between substrate edges and middle portion.

Surface roughness cannot be accurately described using one single parameter. In this study AFM was applied to get information about the polyacrylate surface topography and roughness. For general roughness analyses, small AFM images ($1-5 \mu\text{m}^2$) were taken and the RMS value was determined (Equation 2.3, p 36). This information limits the interpretation latitude as it only gives data on a very small area of the surface in a nanoscale. Therefore, besides the characterisation of such topographical 2D parameters in the nanoscale, also 3D parameters were applied which gave more insight into the actual surface topography in microscale and allowed a more thorough analyses of the substrate surfaces [368].

From the surface 3D images of the polyacrylates it was clear that all substrates were rather rough and showed both, deep hole-like and high hill-like structures. These differed immensely in their distribution across the surfaces of both single substrates as well as between different substrates. The quantification of the height of hill-like structures revealed that ESP 007 and ESP 010 had, when compared to other substrates, much lower hills. Interestingly those two showed also differences in the chemical composition. Both contained amine groups, but ESP 007 contained hydroxyl groups whereas ESP 010 contained carboxyl

groups. However, BTL 15 was eventually the roughest polyacrylate with a rather homogeneous distribution of hill heights throughout the surface, closely followed by ESP 011 and ESP 003. When analysing the distribution of these structures there was no direct correlation with chemical composition. Again, neither of these substrates showed similarities with respect to surface chemistry. A preliminary conclusion would be that surface chemistry did not influence surface roughness notably. However, as discussed before ([chapter 3.3.1](#), p 76), the presence and interaction of surface functional groups with the polymer backbone and with other surface functional groups (charged / uncharged / aliphatic) could lead to orientation of the polymer structures which could in turn result in such hill-like formations. This process is, however, unpredictable and might be dependent on the actual stereochemical state, the presentation of functional groups and even on the coating procedure itself.

Differences were found when comparing the topographical data (quantification of hill-like structures) from 3D images with the data obtained for nano RMS roughness. ESP 007, ESP 008, ESP 010 and BTL 15 have the lowest RMS roughness. This was in compliance with the data found in 3D image analyses with BTL 15 being the only exception. BTL 15 had the largest hill-like structures but a small RMS nanoroughness compared to other substrates. However, again, no suggestive correlations can be made between surface chemistry and nanoroughness.

The microscale topography of polyacrylates leaves large room for speculations. Although there are variations in hill height between substrates, but also within substrates, this may present a case of “organised disorder”. Therefore, it is possible that particular patterns of these hill-like structures may repeat themselves within the individual polyacrylates and that these patterns are indeed a typical characteristic of the individual polymers. There are a number of publications that highlight the effects of ordered and disordered, or random,

surface topographical features and these studies often emphasize the impact of such topographical effects on cell fate [44, 369, 370]. However, to our knowledge there are no publications that focus on the effects of such “organised disorder” phenomena and our results emphasize the importance of studying these further.

As mentioned before, surface roughness has a strong impact on the CA of surfaces. The polyacrylates do not represent ‘ideal’ substrates in terms of confidence in CA measurements as they are rather chemically and topographically heterogeneous surfaces. This in turn will influence the CA hysteresis (difference between advancing and receding angle). For example, the DCA method showed that particularly ESP 010 had an advancing angle that was notably high, whereas its receding angle was notably low. This resulted in a high hysteresis (significantly different to all other substrates) which indicated a high roughness. This is contrary to the data obtained for ESP 010 which had, compared to other substrates, lower nano- as well as microscale roughness. On the other hand, ESP 010 belonged with ESP 008 and ESP 009 to the group of substrates with the lowest (more hydrophilic) CA when measured using the sessile drop and CB method, which correlates with their smoother appearing surfaces. Thus, the heterogeneity of ESP 010 that occurs during DCA measurements might be related to the general difference in the methods. The DCA method takes the entire substrate surface into account while the substrate is cycled in and out of the liquid (substrate dynamic). This technique might detect overall surface features that might be related to surface chemistry or topography, but could not be detected with another method. There are two models that are attempting to explain the wetting behaviour of non-ideal, rough surfaces: the Wenzel model and the Cassie model. The Cassie model claims that air becomes trapped once the drop comes in contact with a surface which would increase surface hydrophobicity (water droplet sits on air). The Wenzel model on the other hand claims that water penetrates the surface and thereby increases the surface area which in turn influences surface geometry and roughness. It also states that the introduction of roughness to a substrate will enhance

the wettability that is caused by surface chemistry. Thus a hydrophilic surface will become more hydrophilic and *vice versa* (Figure 3.18) [371, 372]. Naturally, the actual CA will vary depending on the local chemical composition and the area of the surface that is measured.

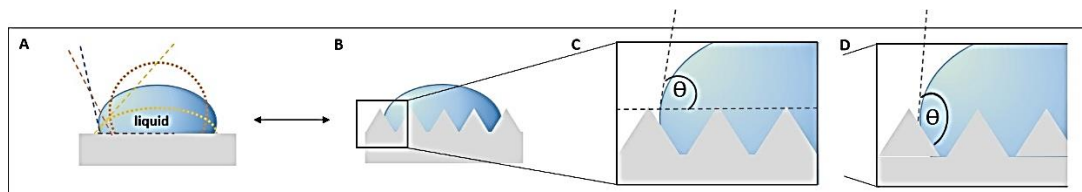


Figure 3.18: CA measurement on a smooth (A) and a rough surface (B). General CAs changes depend on hydrophilicity (yellow lines) / hydrophobicity (orange lines) of a sample, but also on the roughness. (C) Apparent (measured) CA. The roughness is not visible when measuring and the CA appears a projection of the real value (dashed line). (D) Actual CA.

Moreover, the CA maps obtained by sessile drop method revealed patterns of wettability that could, apart from chemical features, be related to the surface roughness.

However, there are no strict guidelines that describe how rough a surface has to be in order to influence the CA. Therefore it is challenging to determine whether nano- or microroughness are influencing CA measurements in a particular case. Most likely both factors will influence surface wettability. *Bhushan et al.* developed a model to explore the effect of nano- and micropatterns on wettability (Figure 3.19) [373]. Although this model was developed to understand the interactions of liquids with superhydrophobic substrates, it still allows to hypothesise about how the combination of nano- and microroughness generally influence surface wettability.

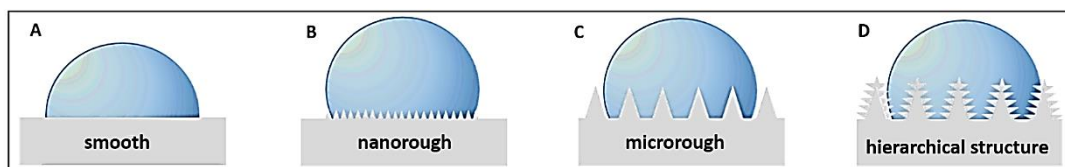


Figure 3.19: Simple schematic of the influence of roughness on substrate wettability. (A) Water droplet (blue) on a smooth surface (grey). The contact between solid and liquid decreases with (B) nanoroughness and (C) microroughness or in a (D) hierarchical manner. The principle is based on and schematic inspired by *Bhushan and Jung et al.* [373].

Both, surface nano- and microscale roughness can influence cell response [374]. For example, *Xu et al.* showed that endothelial cell function was enhanced on smooth compared to rough surfaces [375, 376], whereas osteoblast-like cells were found to attach preferably to rougher surfaces [377]. Lastly, topographical surface features can influence interactions with proteins which may alter cell response additionally, including adsorption, density, orientation and spatial distribution [378]. This is supported by recent research that has shown that the nanotopography does not influence cell behaviour in serum free medium [93]. However, this process was not further analysed in the course of this study.

3.3.3.2 Surface mechanical properties

Several recent studies have shown the importance of material stiffness on cell attachment, and differentiation [26, 47, 379]. Polyacrylates are plastics and generally rather rigid and inflexible substrates. Surface elasticity was found to be consistently about 2.5 GPa. Therefore, other surface properties did not appear to influence substrate mechanical properties that will therefore not be further discussed.

3.4 Conclusions

Surface analyses revealed that all polymers showed only small differences in the surface elemental composition (carbon, nitrogen, oxygen). However, there were relative differences in the COOH, OH and NH₂ content between the polyacrylates. The general high carbon content resulted in hydrophobic surfaces with ESP 008, ESP 009 and ESP 010 being exceptions. These three substrates had a significantly lower CA, which is most likely related to the higher amount of nitrogen, surface primary amine groups, respectively. Topographic surface analyses showed that substrates differed in the RMS roughness with values being in the range of 3 – 13 nm. Prominent differences were found in the presence of surface elevations (hills) that were low (ESP 007 and ESP 010) or intermediate (ESP 003, ESP 004, ESP 008 and ESP 12), for some substrates, but reached up into micrometre range for other substrates (ESP 009, ESP 011 and BTL 15). Polyacrylates did not differ with respect to their mechanical properties.

4 Effect of polyacrylates on kidney progenitor / stem cells

4.1 Introduction

In recent years there has been much research with promising outcomes in the field of biomaterials for stem cell differentiation [17, 110, 380-383]. A large variety of biomaterials of both, natural and synthetic origin, have been developed and successfully applied to direct the differentiation stem cells [301, 384-386].

Acrylic substrates are commonly used and investigated as potential substrates for cell culture [387, 388]. They have various advantages, such as the ease of 'tuning' of their physical properties. Moreover, they can be conjugated with biologically active peptides (BAS). For example, acrylic substrates have been shown to be very suitable for the cell culture of undifferentiated human embryonic stem cells (hESCs) as well as for sustaining their self-renewal. Moreover these substrates were shown to be suitable platforms for the differentiation of hESCs into differentiated progeny of cardiomyocytes [389].

Another well studied acrylic - based biomaterial is poly-2-hydroxyethyl methacrylate (pHEMA). It has been shown to be biocompatible and biodegradable in the presence of macrophages [390, 391]. However, the presence of hydroxyl groups often hinder its recognition by cells, but when combined with other acrylates, such as poly (methyl methacrylate), or in combination with natural ECM proteins it is recognised. For example, in combination with collagen it was shown to promote myogenesis of muscle stem cells [392]. Moreover pHEMA was found to be a suitable candidate for bone implantation [393, 394].

The polyacrylate substrates used in this study have various advantages. They are cheap, simple to manufacture and can be easily applied to a large variety of surfaces. Moreover,

they differ from other acrylic substrates insofar as they are composed of a range of monomeric units that all differ in their functional groups. The incorporation of amine, hydroxyl and carboxyl groups as well as non-polar groups that introduce steric hindrance to the system allowing the polymers to be designed in such a way that they can mimic cell binding motifs found within the extracellular matrix (ECM) ([chapter 3.1](#), p 5656). Therefore, a large range of substrates can be produced that are designed to precisely mimic different ECM features. The main aim of using these substrates is however, to circumvent the need for expensive growth factors in order to regulate cell behaviour and maintain stem cell expansion and differentiation.

So far the BTL polyacrylate range has been shown to influence cell adhesion and proliferation of human aortic endothelial cells and coronary artery smooth muscle cells. These substrates are based upon a single cell binding motif, but each with having a differing degree of steric hindrance within the polymer backbone which in turn influences the surface functional groups that will be presented to the cells. The BTL range of polymers were designed and studied with the aim of developing coronary stent coating [305-307].

The ESP polymer range was designed to mimic particular cell binding motifs present in the extracellular environment of individual cells of interest. The substrates have been shown to direct the differentiation of mouse and human mesenchymal stem cells (MSCs) into chondrocytes without the addition of growth factors into the medium [13, 345].

Aims of this chapter:

- (1) Analyse substrates for possible cytotoxic effects using mouse fibroblasts and bovine endothelial cells
- (2) Investigate the ability of polyacrylate substrates to influence behaviour and differentiation of mouse kidney stem cells

- (3) Investigate the ability of polyacrylate substrates to influence behaviour of conditionally immortalised podocytes and proximal tubule cells
- (4) Investigate the ability of polyacrylate substrates to influence behaviour of human derived kidney progenitor cells.

4.2 Results

4.2.1 Polyacrylate biocompatibility

4.2.1.1 Cytotoxicity assessment

According to the British Standards ISO 10993, all materials with application in the medical devices industry have to undergo biological evaluation (ISO 10993-1) [395]. All substrates that were developed within this study were, prior any further cell experiments, evaluated for cytotoxic effects following the ISO 10993-5 guidelines ([chapter 2.1.1.3](#), p 29) [274]. For evaluation of substrate cytotoxicity a commercially available mouse fibroblast cell line (mL929) was used. These cells are recommended for cytotoxicity studies on materials [396]. Morphological abnormalities typical for cytotoxic effects are listed in [Table 4.1](#) corresponding to ISO 10993-5 [274].

Table 4.1: Qualitative morphological grading of cytotoxicity of extracts, adapted from [274]. These standards allow a relation of cell morphology with cytotoxic effects.

Grade	Reactivity	Conditions of all cell cultures
0	None	Discrete intra-cytoplasmatic granules, no cell lysis, no reduction of cell growth
1	Slight	Less than 20% of the cells are round, loosely attached, without intra-cytoplasmatic granules, changes in morphology; occasional lysed cells present; only slight growth inhibition
2	Mild	Less than 50% of the cells are round, devoid of intra-cytoplasmatic granules, no extensive cell lyses not more than 50 % growth inhibition observable.
3	Moderate	Less than 70% of the cell layers contain rounded cells or are lysed; cell layers not completely destroyed but more than 50 % growth inhibition observable.
4	Severe	(Nearly) complete destruction of the cell layers.

Figure 4.1 shows images of mL929, stained with methylene blue, 48 h post incubation in polymer conditioned eluant (chapter 2.1.1.3, p 29) at different concentrations of 0%, 10%, 50% and 100% (neat eluant) and a cytotoxic, positive control. Notably, regardless of the polyacrylate, cell numbers decreased with increasing polymer eluant concentration. Cells at a higher resolution (Figure 4.2) maintained the typical fibroblastic elongated and spindle shaped morphology on most substrates, but a number of cells appeared rounded and to undergo cell death. Particularly cells that were incubated for 48 h with the eluant of ESP 008, ESP 009 and ESP 010 showed this phenotype. However, from phenotype analyses these cells were graded level 1 and therefore still passed ISO standards (Table 4.1). Moreover, the viability of cells was assessed after exposure in polymer conditioned eluant at 0%, 50% and 100%. These confirmed that the number of viable cells was slightly decreasing with increasing polymer eluant concentration, but cells were still proliferating and increasing in number with time. No significant difference of cell viability was found between substrates nor when changing the eluant concentration that originated from one single polymer. This suggested that substrates were not cytotoxic. As expected, no cytotoxic effects were noticed on the negative control either (TCP, no polymer conditioned eluant), whereas cells within the positive control (medium exposed to latex) were rounded and lysed with 100% of the cells being not viable / dead. Determination of the PDT (Figure 4.3 C) confirmed that cells needed about 20 h to double their population. This number was consistently maintained throughout the number of substrates at 50% eluant concentration. A small, non-significant, increase was only notable at 100%.

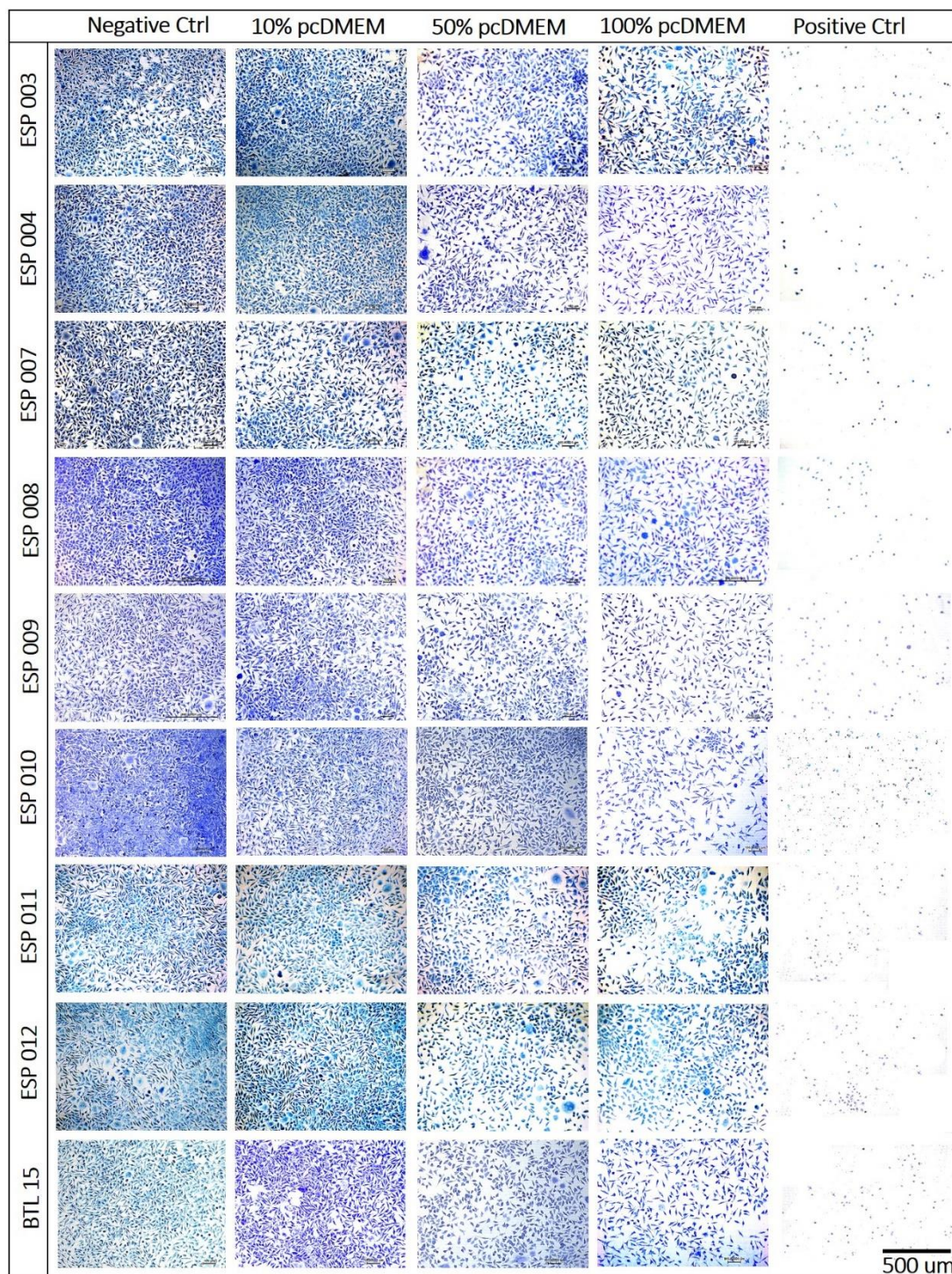


Figure 4.1: Brightfield microscopic images of mL929 cells exposed to 0%, 10%, 50% and 100% polymer conditioned eluant after 48 h stained with methylene blue. Cells were seeded at a density of 1×10^4 cells / well. Positive (cytotoxic) control was latex, negative control (not cytotoxic) was pure medium. On all substrates cell density decreased with increasing eluant concentration.

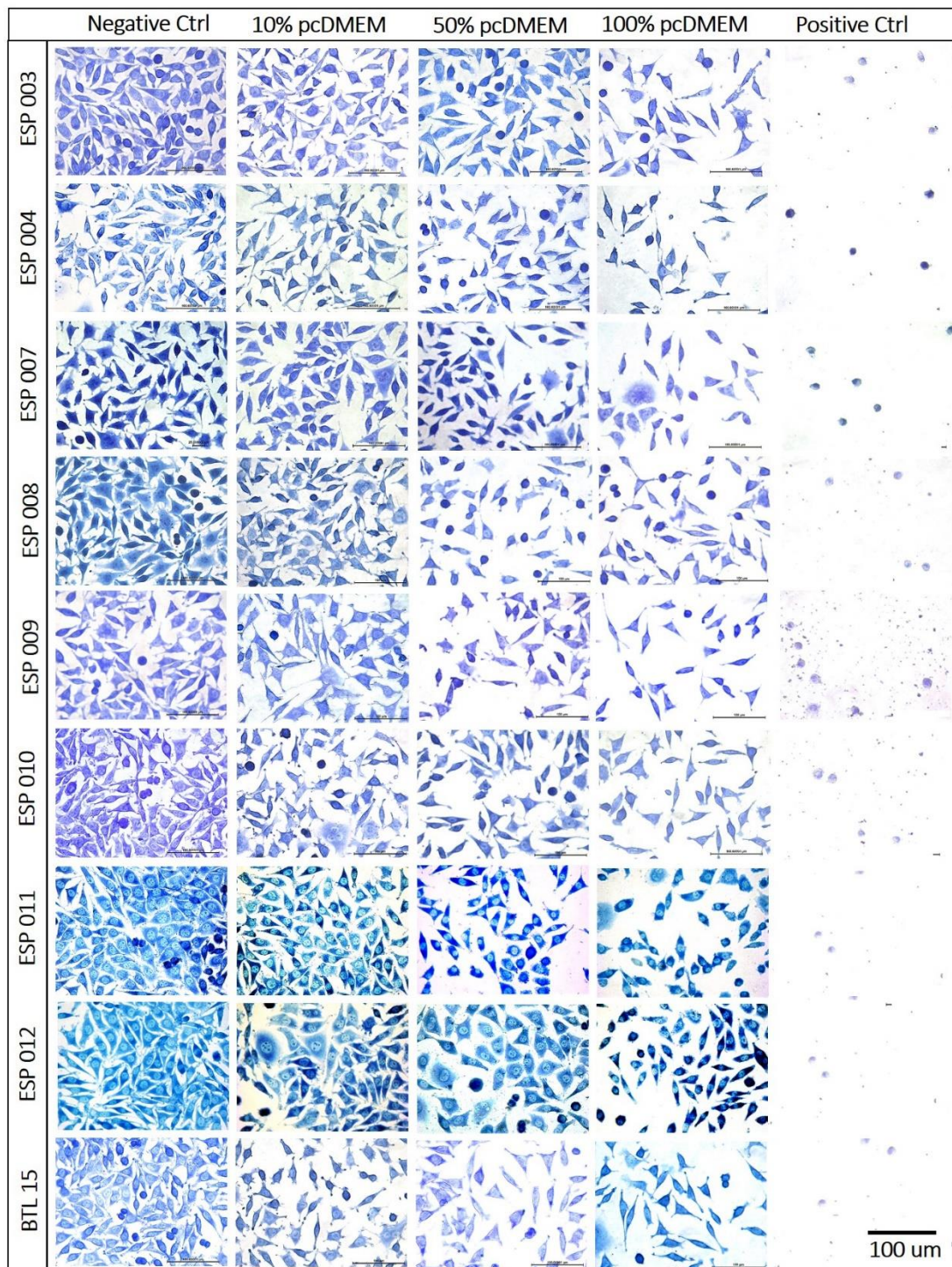


Figure 4.2: Brightfield microscopic images of mL929 cells exposed to 0%, 10%, 50% and 100% polymer conditioned eluant after 48 h stained with methylene blue. Cells were seeded at a density of 1×10^4 cells / well. Positive (cytotoxic) control was latex, negative control (not cytotoxic) was pure medium. On all substrates cell density decreased with increasing eluant concentration.

A

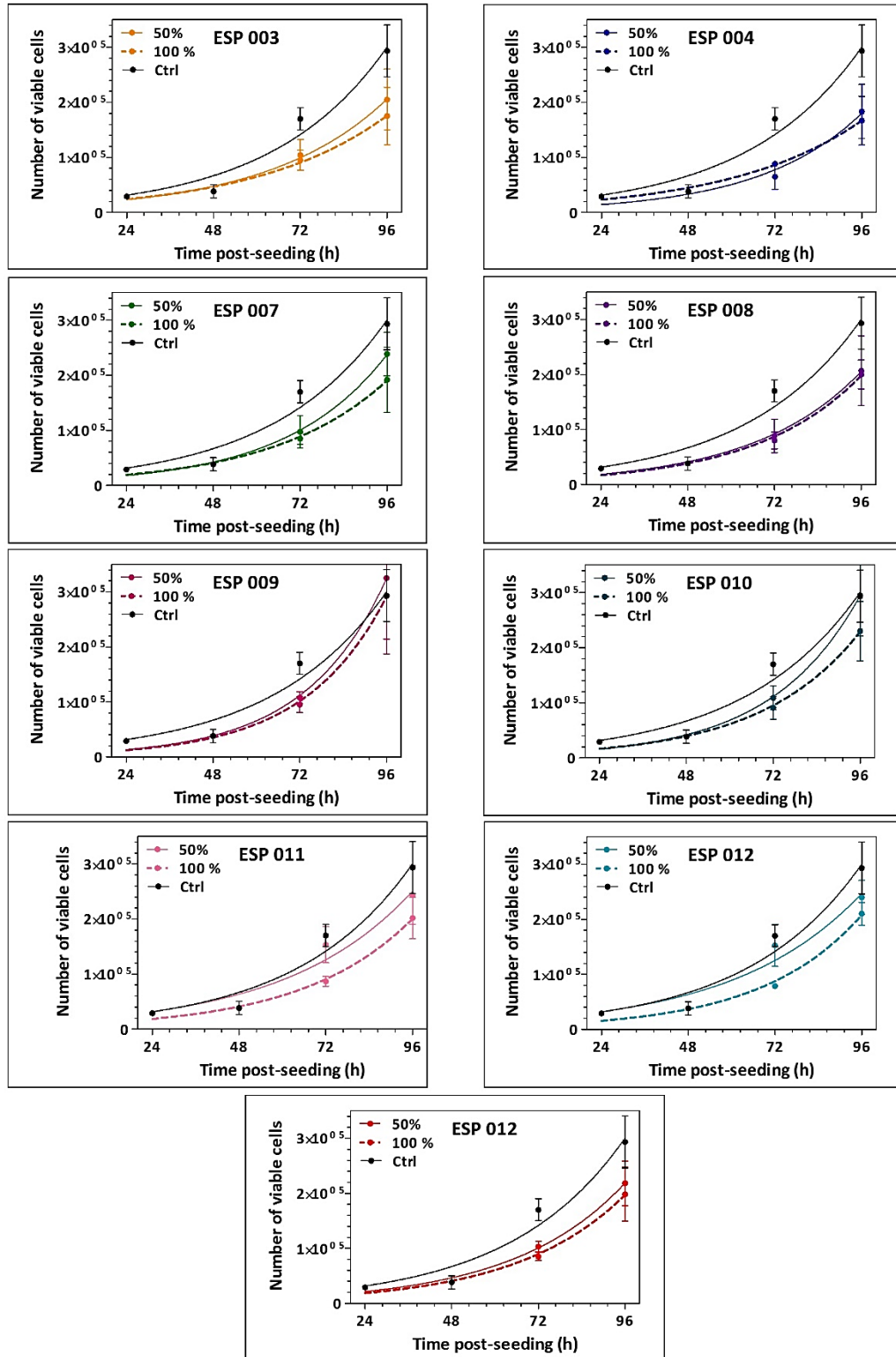


Figure 4.3: Cytotoxic effects of polymer conditioned (pc) eluant and quantification of cell viability. Cells were seeded at a density of 1×10^4 cells / well. (A) Cytotoxic effects of 50% and 100% polymer conditioned eluant compared to a 0% control for all substrates over time. Data were fitted using nonlinear regression / exponential growth equation. Results represent the mean of 3 biological replicates \pm SEM.

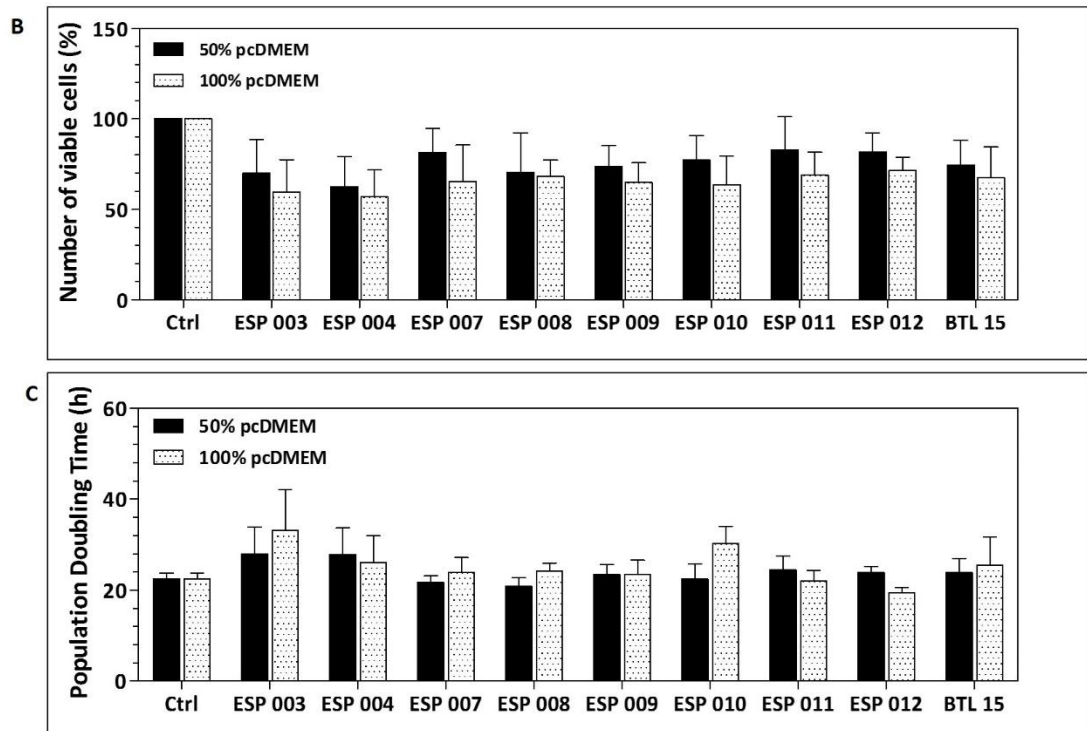


Figure 4.3: continued: (B) Quantification of the number of viable cells 96 h post seeding. (C) Population doubling time. Results represent the mean of 3 biological replicates \pm SEM.

3.2.1.2. Analyses of mL929 and BAE cells on polymer substrates

Once determined that the polyacrylates did not have a cytotoxic effect on the cells, two cell types, the mouse fibroblast cell line mL929 and bovine endothelial cells (BAE), were seeded onto substrates and analysed. mL929 cells are easy to handle and very proliferative cells that easily attach well to most substrates / materials [396, 397]. However, BAE cells are much more sensitive and their cell behaviour can provide a general indication on how more specialised cells may respond to a particular substrate / material. For analyses, both cell types were individually seeded on the polyacrylate substrates and left to grow for 96 h. [Figure 4.4 A](#) shows mL929 cells stained with methylene blue at 10x and 40x resolution. The images show that the cells were proliferating and maintained a healthy phenotype on all substrates. There were no obvious differences in cell morphology on most polymers. However, there were visibly more rounded cells on ESP 009 and ESP 010 that had a rounded phenotype

characteristic for cell lysis and cell death. The cell number was quantified at four time points post seeding and cell proliferation and PDT was quantified (Figure 4.4 B and C).

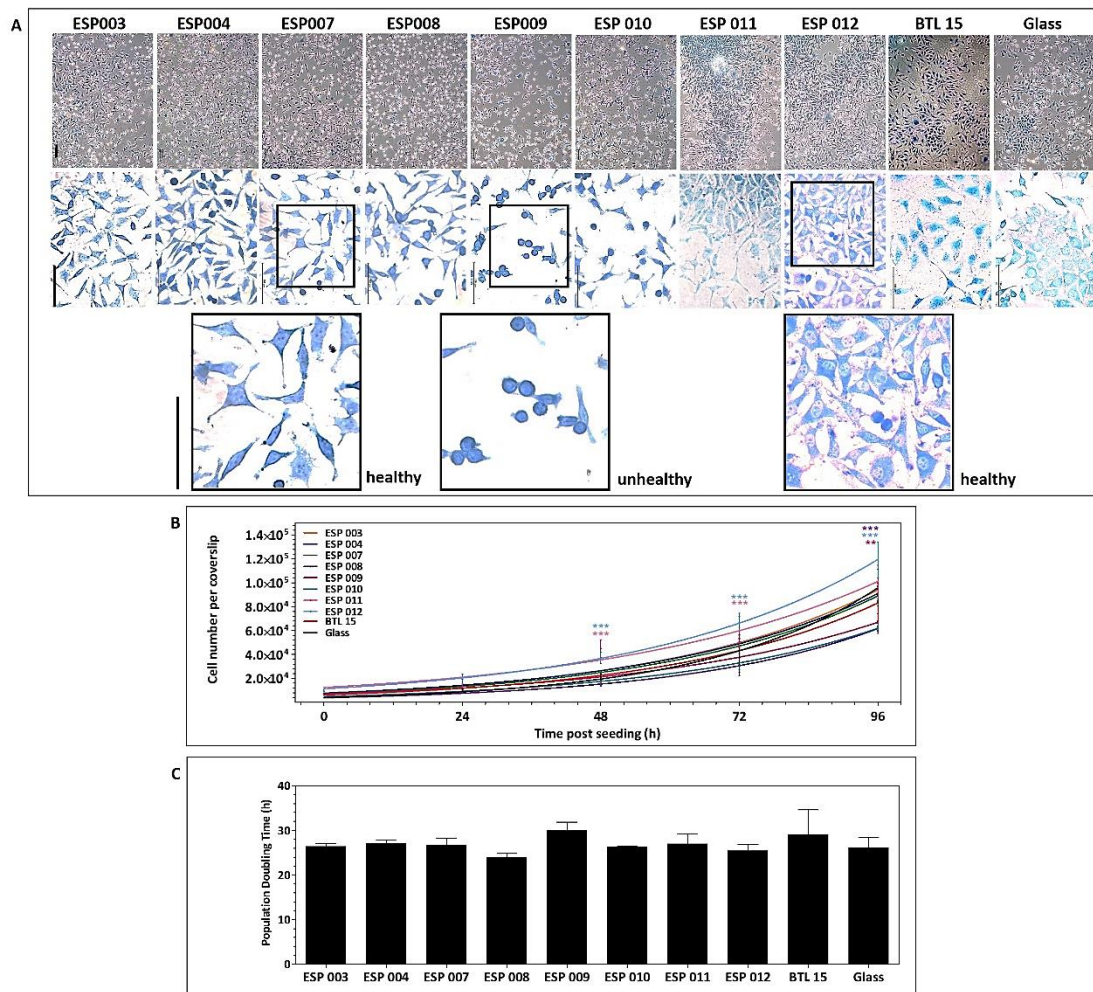


Figure 4.4: mL929 cells were seeded on polyacrylate substrates at a density of 1×10^4 cells / coverslip. (A) mL929 cells stained with methylene blue 96 h post seeding at 10 x (top) and 40x (bottom) resolution. Corresponding (B) cell number of mL929 cells over the course of 96 h and (C) PDT. Asterisks indicate statistical difference compared to a glass control (Tukey model, $p < 0.05$). Data were fitted using nonlinear regression / exponential growth equation. Results represent the mean of three biological replicates \pm SEM. Scale bar: 100 μ m.

The cell proliferation was similar on all substrates with little significant difference only 48 h post seeding. Otherwise cells were proliferating similarly on all substrates with no significant difference when compared to a glass control ($p < 0.05$). Also PDT did not show a significant difference between cells seeded on different polyacrylates, nor compared to a glass control.

Figure 4.5 A shows BAE cells stained with methylene blue at 10x and 40x resolution 96 h post seeding on polyacrylates. BAE cells were proliferating and maintained the characteristic BAE

cell phenotype on nearly all substrates with exception of ESP 008, ESP 009 and ESP 010. Only very little increase in cell number over time was found particularly on ESP 009 and ESP 010. Images of BAE cells on these substrates showed rounded and elongated cells. The cell number was quantified on all substrates at four time points and cell proliferation and PDT was quantified ([Figure 4.5 B and C](#)). The data confirmed that cell proliferation was very low on ESP 009 and ESP 010 and the corresponding PDT showed that cells on these substrates took 6 times longer to double the population compared to cell cultured on other substrates. Moreover, cells on ESP 011 and ESP 012 proliferated very fast initially. However, by 96 h in culture the cell numbers were in line with the other substrates. The PDT was moreover slightly increased on both substrates but did not show any significant difference compared to a glass control (Tukey model, $p < 0.05$).

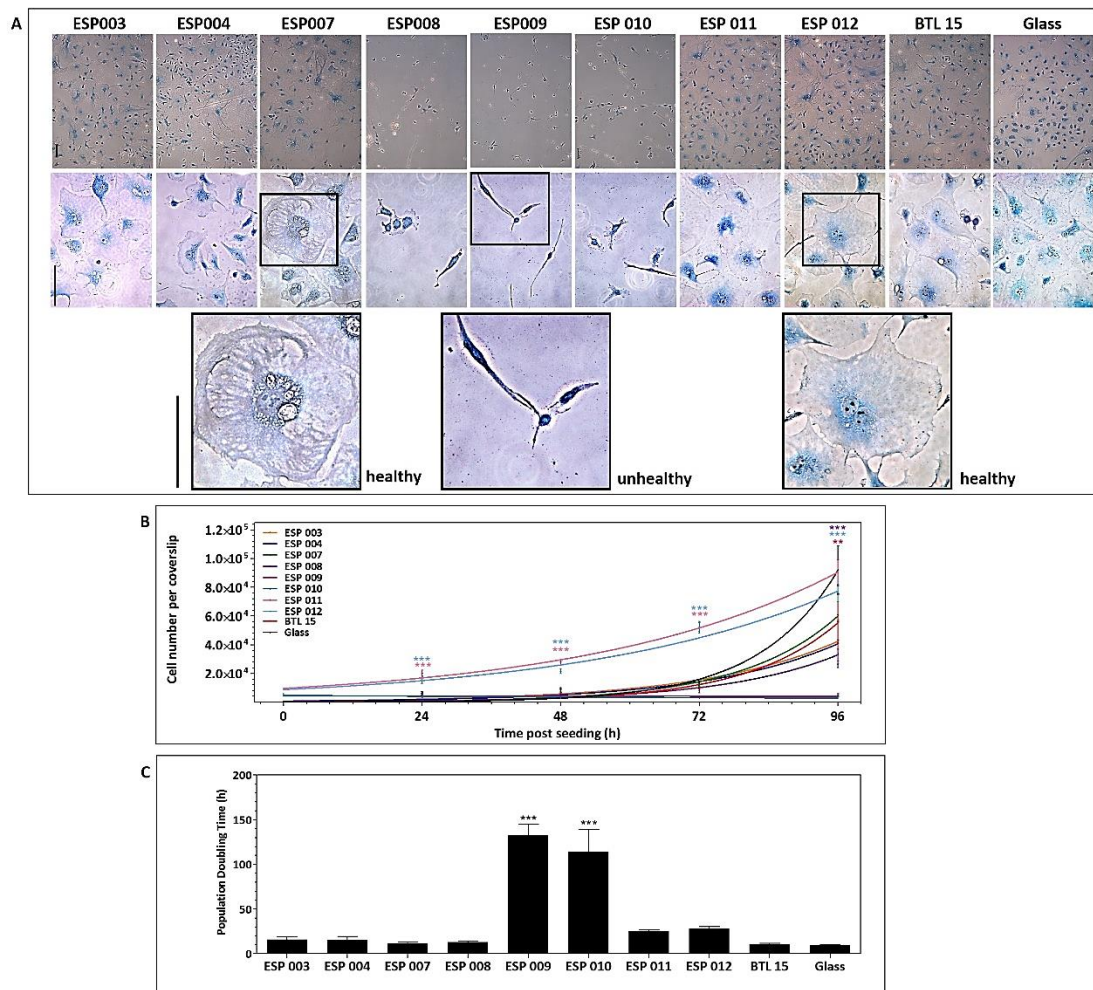


Figure 4.5: BAE cells were seeded on polyacrylate substrates at a density of 1×10^4 cells / coverslip. (A) BAE cells stained with methylene blue 96 h post seeding at 10 x (top) and 40x (bottom) resolution. Corresponding (B) cell number of BAE cells over the course of 96 h and (C) PDT. Asterisks indicate statistical difference compared to a glass control (Tukey model, $p < 0.05$). Data were fitted using nonlinear regression / exponential growth equation. Results represent the mean of three biological replicates \pm SEM. Scale bar: 100 μ m.

4.2.2 Effect of polyacrylates on mouse kidney-derived stem cells

4.2.2.1 Effect of polyacrylates on mouse kidney-derived stem cell behaviour

Mouse kidney-derived stem cells (mKSCs) were seeded on four polyacrylate substrates that appeared to have potential to direct stem cell differentiation based on previous studies: ESP 003, ESP 004, ESP 007, BTL 15 [13, 345]. Glass and tissue culture plate (TCP) were used as controls. The cells were seeded at a density of 1000 cells / well (24 well plate containing a polymer coated 13 mm coverslip). Cell number and cell viability were analysed at four different time points and population doubling time (PDT) was determined (Figure 4.6).

The cells were proliferating similarly on all substrates with little significant differences compared to a glass control. However, on ESP 003 cells were proliferating significantly less (Tukey model, $p < 0.05$). Cell viability analyses confirmed that cells were proliferating on all substrates with exponential growth, but showed less growth compared to a glass control. Determination of PDT showed that the cells needed on average about 20 h to double their population on all substrates, including controls. No significant difference was found (Tukey model, $p < 0.05$).

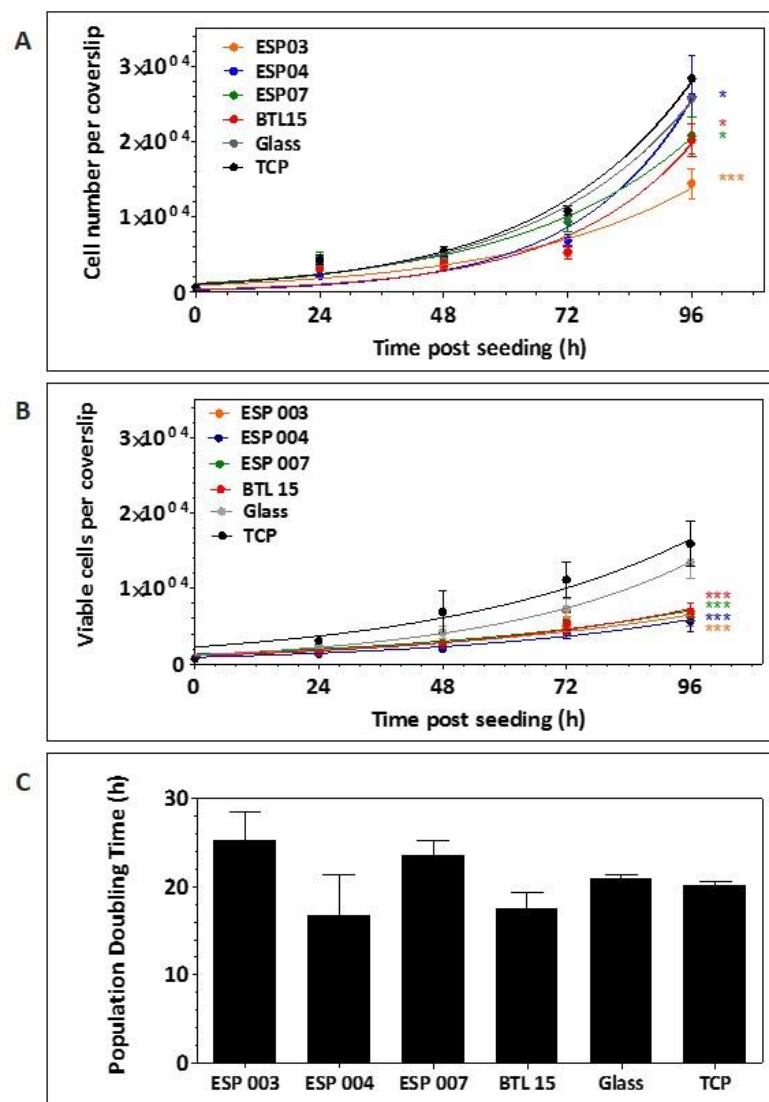


Figure 4.6: mKSCs were seeded at a density of 1×10^3 cells / coverslip and cultured for 96 h. (A) Cell proliferation. (B) Number of viable cells. (C) PDT, as obtained using results from cell number (A). Results represent the mean of three biological replicates \pm SEM. Asterisks indicate statistical difference compared to a glass control (Tukey model, $p < 0.05$). Data were fitted using nonlinear regression / exponential growth equation.

4.2.2.2 Effect of polyacrylates on mouse kidney-derived stem cell differentiation into podocytes

For morphological analyses, mKSCs were seeded onto substrates and either analysed using live cell imaging or fixed and labelled with phalloidin and DAPI ([Figure 4.7](#)). The images show that 24 h post seeding cells looked similar in morphology. At 96 h post seeding changes in morphology were observed. Particularly on ESP 003 and ESP 004 cells were spread and rounded with a podocyte-like cell morphology ([chapter 1.3.2](#), p18). Moreover, these large cells often contained two nuclei which is another indicator of podocytes.

Subsequently, mKSC spread was analysed using phalloidin stained cells and the image analysis software ImageJ [293, 294]. [Figure 4.8](#) shows the quantification of mKSC spreading. Notably, on ESP 003 and ESP 004 the mKSC spread area was significantly higher than the cell spread on glass. However, cells on other substrates showed only a small increase in cell spreading post seeding (about 1500 μm^2) over time, whereas cells on ESP 003 and ESP 004 showed a spreading of about 3000 – 4000 μm^2 .

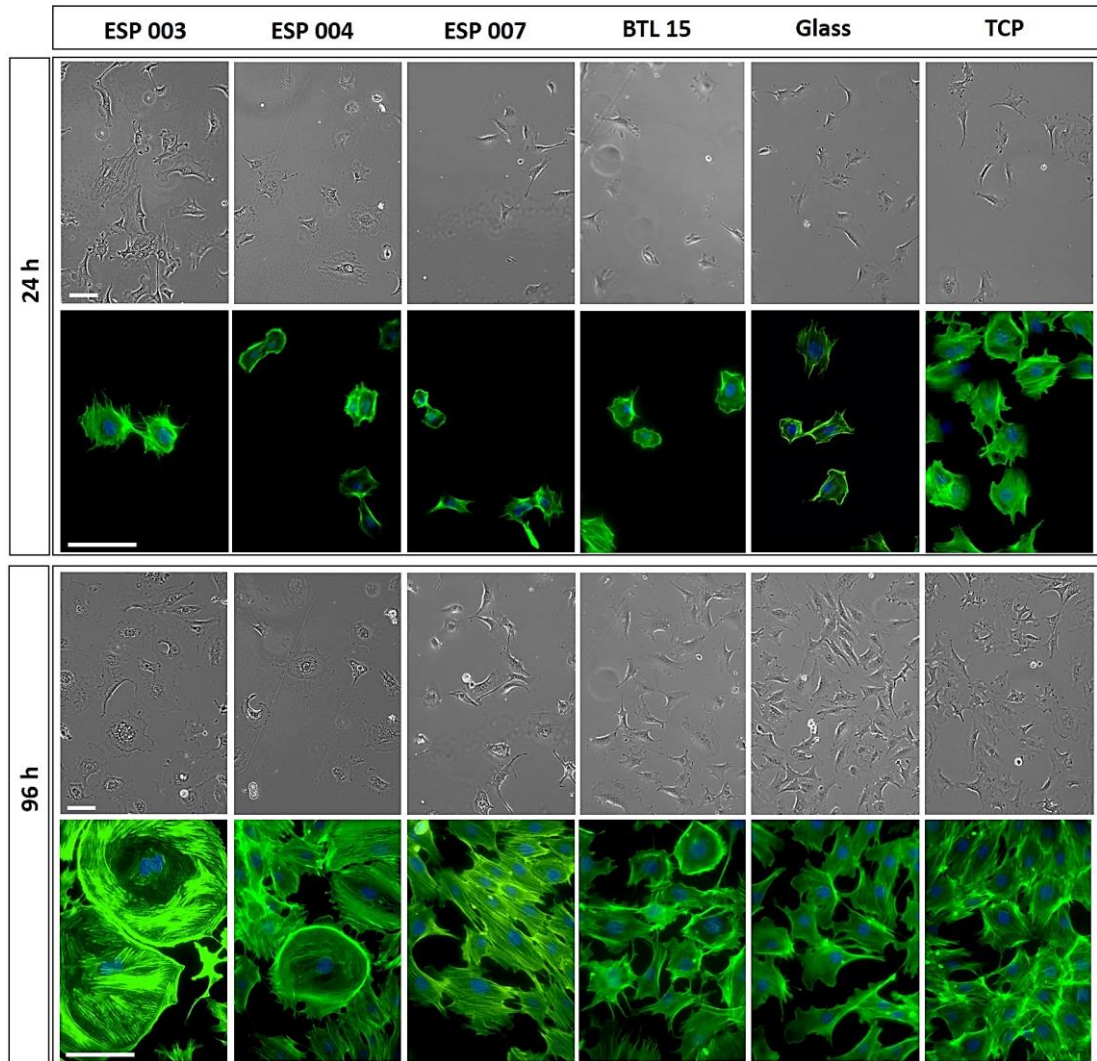


Figure 4.7: mKSCs morphological analyses. mKSCs were seeded at a density of 1×10^3 cells / 13 mm polymer coated coverslip. The images show mKSC phase contrast images, as obtained by life cell imaging, and F-actin and DAPI labelled cells at a higher resolution 24 h and 96 h post seeding. Scale bar is 100 μ m.

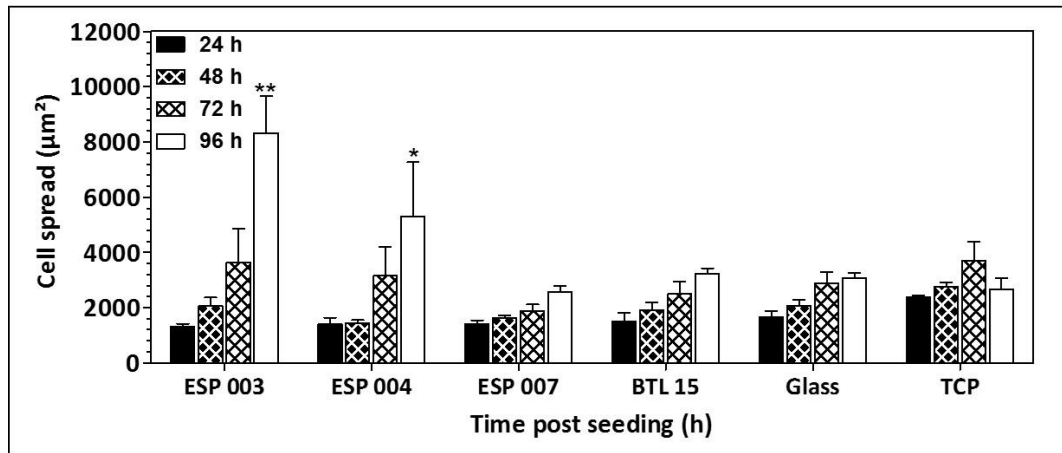


Figure 4.8: mKSC spread analyses. mKSC were seeded at a density of 1×10^3 cells / 13 mm polymer coated coverslip. Cell spread was quantified at four different time points post seeding. Asterisks indicate significant difference compared to a glass control. Results represent the mean of three biological replicates \pm SEM.

Cell morphology was then analysed and the number of podocyte-like cells quantified at two time points: 24 and 96 h post seeding (Figure 4.9). About 10-15% of the cells showed initially a podocyte-like morphology on all substrates (spontaneous differentiation) whereas, after 96 h, this number was only little increasing on ESP 007, BTL 15 and on the controls. However, the number of podocyte-like cells was increased on ESP 004 and significantly increased on ESP 003 (Tukey test, $p < 0.05$).

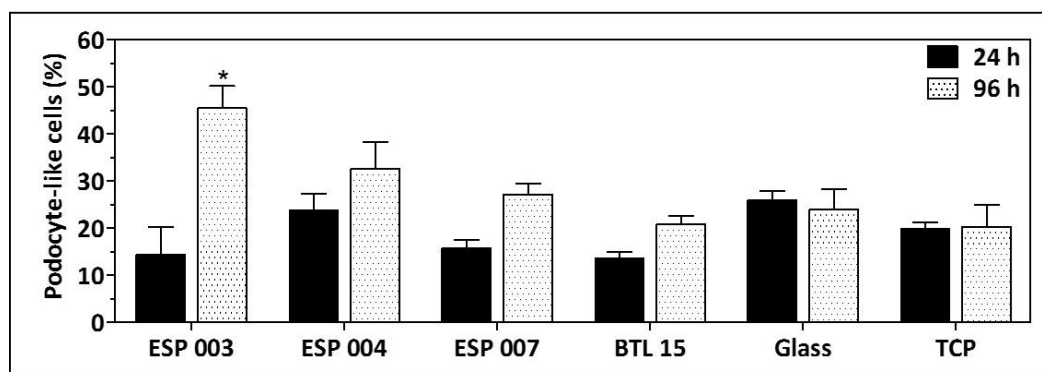


Figure 4.9: Number of podocyte-like cells. mKSCs were seeded at a density of 1×10^3 cells / polymer coated coverslip. The number of podocyte like cells was quantified. Asterisks indicate significant difference compared to a glass control (Tukey model, $p < 0.05$). Results represent the mean of three biological replicates \pm SEM.

Finally mKSCs were analysed for the expression of three podocyte-specific genes: *Synaptopodin (Syn)*, *Podocalyxin (Pdx)* and *Wilms Tumor Gene 1 (WT1)*. Figure 4.10 shows

the results of the RT-qPCR. The results showed a trend of increased podocyte gene expression on ESP 003 and ESP 004. *Pdx* expression was significantly increased on ESP 004 and ESP 007 whereas it showed a trend for downregulation on BTL 15. However, *Synpo* and *WT1* only showed a trend of higher expression on ESP 003 and ESP 004, but no significant difference was detected.

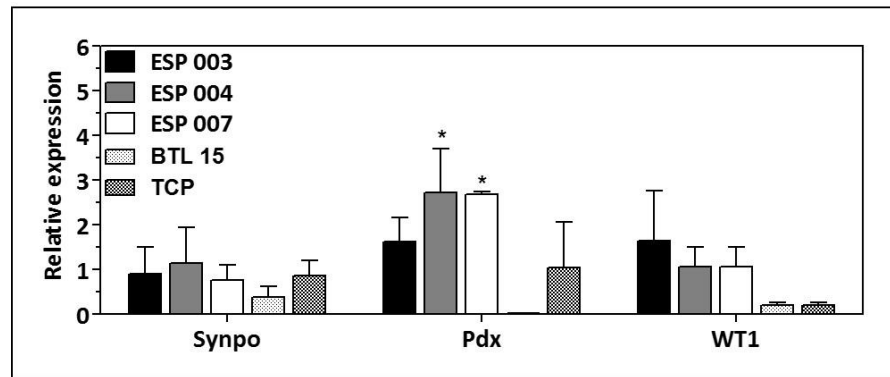


Figure 4.10: RT-qPCR analyses of mKSCs for podocyte characteristic genes as relative expression to mKSC gene expression on a glass control. Seeding density: 1×10^3 cells / polymer coated coverslip. *Gapdh* and *beta actin* (*ACTB*) were used as housekeeping genes. Asterisks indicate significant differences compared to a TCP control. Results represent the mean of three biological replicates \pm SEM.

4.2.2.3 Effect of polyacrylates on mouse kidney-derived stem cell differentiation into proximal tubule cells

In order to analyse whether the mKSCs were differentiating into PTCs two markers were used: Alkaline Phosphatase and the immunofluorescence marker megalin. [Figure 4.11](#) shows mKSCs that were stained for alkaline phosphatase after 96 h in culture on the polyacrylate substrates. On ESP 007 notably more cells showed high alkaline phosphatase activity. Also cells cultured on BTL 15 showed a higher number of cells with the active enzyme. Cells on ESP 003 and ESP 004 showed, similarly to the glass and TCP control, only a small number of cells with alkaline phosphatase activity. Megalin staining confirmed an increased number of PTCs on ESP 007 and BTL 15 ([Figure 4.12](#)). Similar to the previous finding, cells on ESP 003, ESP 004 and those on the controls showed only a small number of megalin expressing cells.

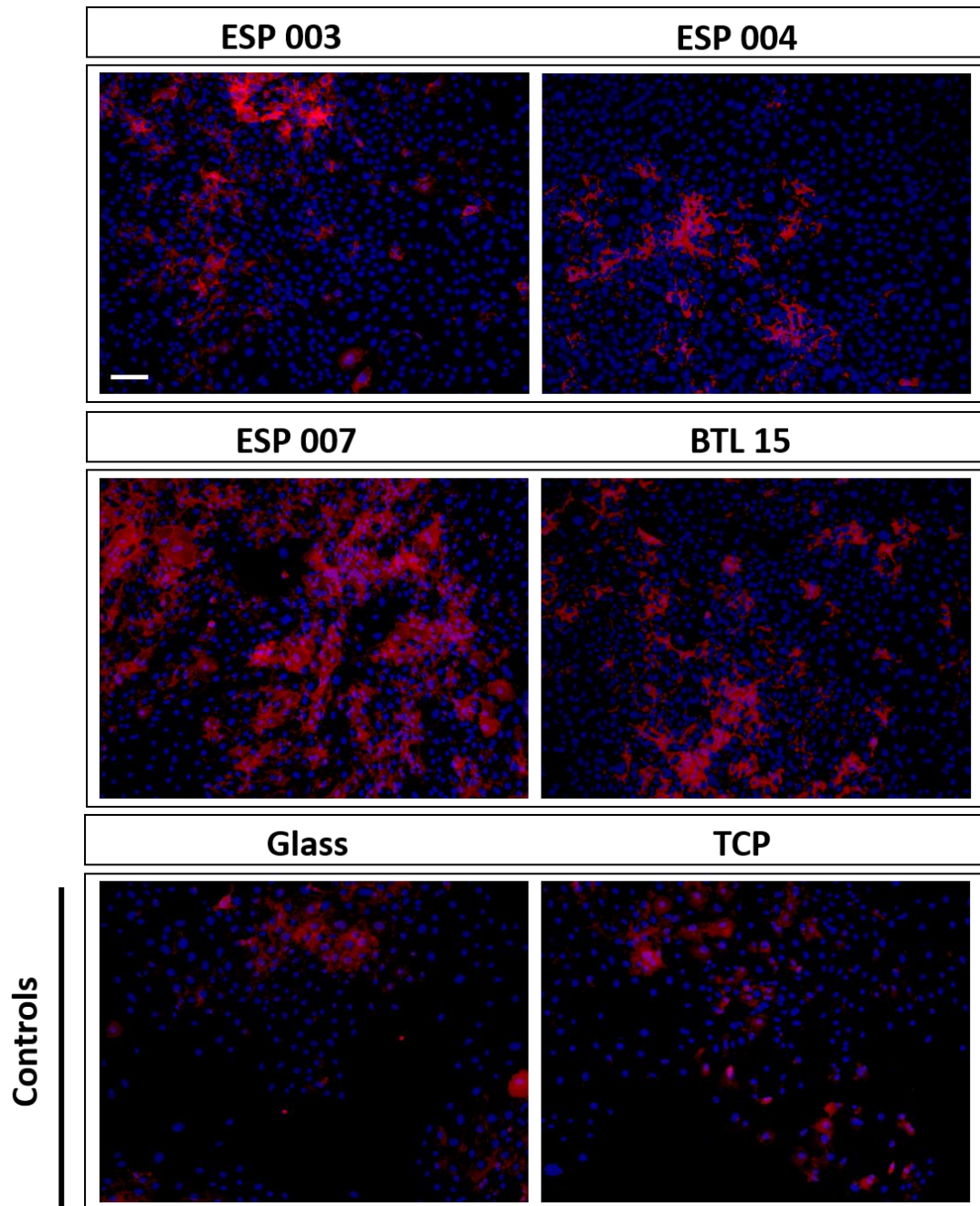


Figure 4.11: Alkaline phosphatase staining. Blue: DAPI. mKSCs were seeded at a density of 1×10^3 cells / polymer coated coverslip. Scale bar: 100 μm .

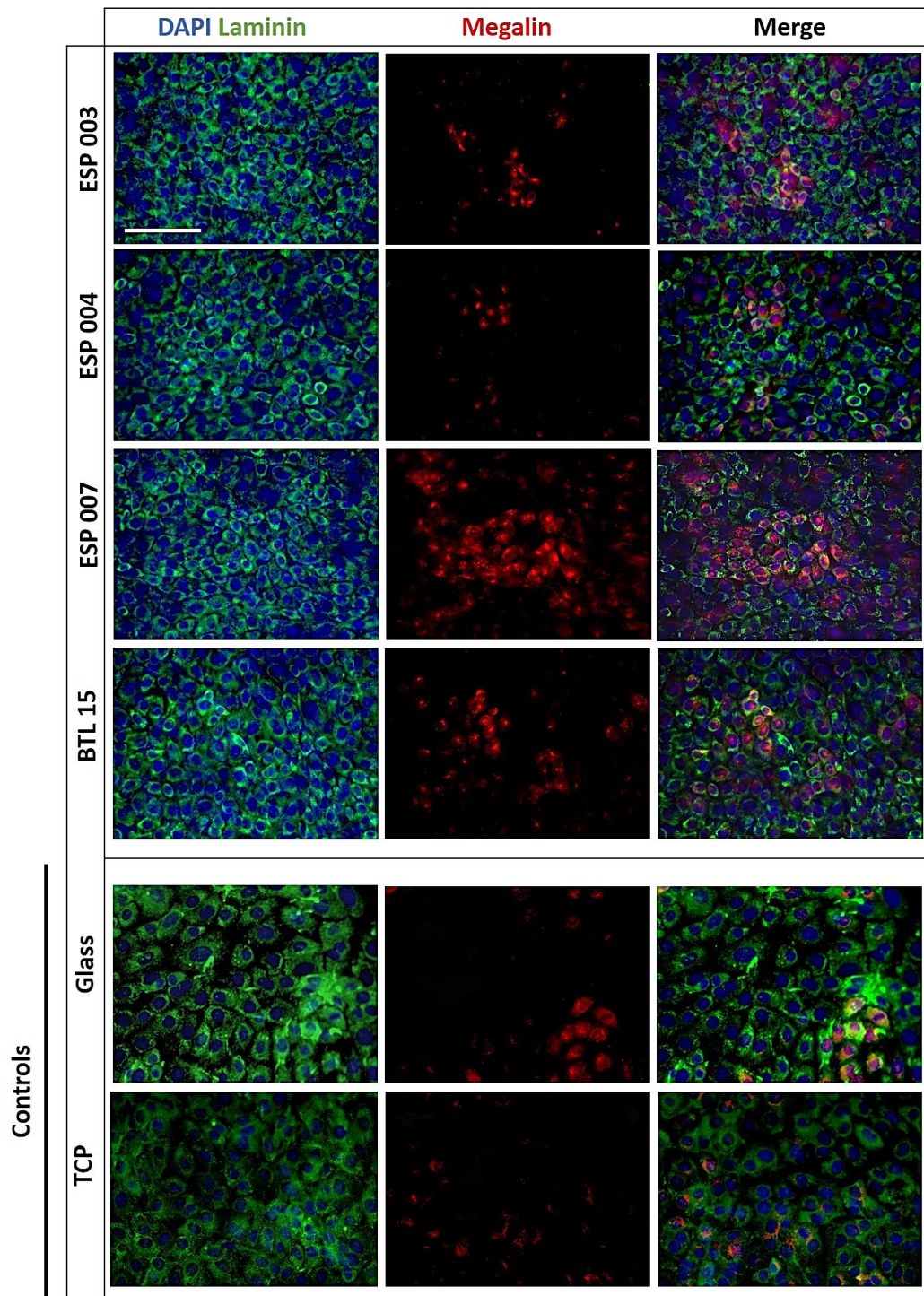


Figure 4.12: Megalin staining. Blue: DAPI. Green: Laminin. mKSCs were seeded at a density of 1×10^3 cells / polymer coated coverslip. Cells were co-stained with laminin for better visualisation. Scale bar: 100 μ m.

To confirm that the increased number of megalin positive cells in fact resulted from the influence of the polyacrylate substrates, the cell number of megalin expressing cells was quantified at three different time points: 6, 48 and 96 h post seeding. Glass was used as a

control (Figure 4.13). The results showed that 6 h post seeding the same amount of cells (about 10%) were megalin positive (spontaneous differentiation). After 48 and 96 h a larger number of cells was expressing megalin on ESP 007 (40%) and BTL 15 (30%).

In addition also the fluorescent area per image was quantified on images at 96 h post seeding and confirmed that there was indeed significantly higher megalin fluorescence (area) on ESP 007 and BTL 15 (Figure 4.13 B), whereas this area remained low on ESP 003, ESP 004 and the glass control.

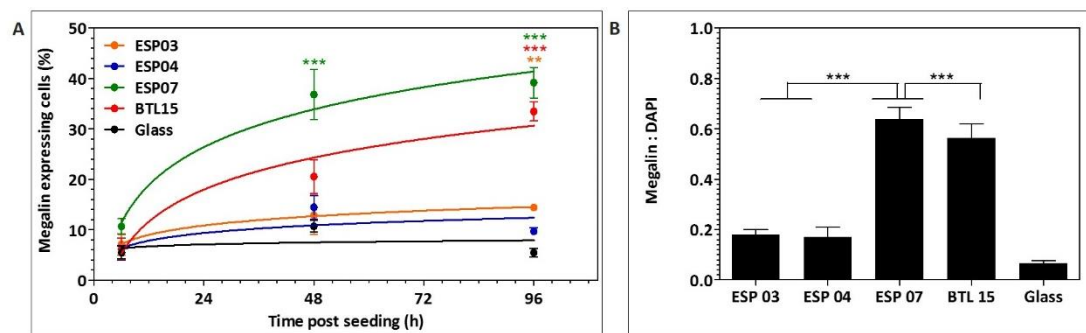


Figure 4.13: Quantification of megalin expressing cells. mKSCs were seeded at a density of 1×10^3 cells / polymer coated coverslip. (A) The number of megalin expressing cells was quantified at three different time points post seeding. (B) Quantification of the fluorescent area 96 h post seeding (ratio of megalin : DAPI). Asterisks indicate significant difference compared to the glass control (Tukey test, $p < 0.0001$). Data were fitted with an exponential growth equation. Results represent the mean of three biological replicates \pm SEM.

Subsequently, the ability of the mKSCs to uptake albumin via megalin-dependent endocytosis was assessed. Figure 4.14 shows mKSCs cultured on polyacrylate substrates that were stained for megalin and analysed for their ability to uptake fluorescently labelled bovine serum albumin (F-BSA). Cells that expressed megalin showed the typical punctuate staining pattern of endocytosed F-BSA. The results indicated that a large number of cells on ESP 007 and BTL 15 did uptake the F-BSA that also colocalised with megalin. Only a small proportion of cells within the populations on ESP 003, ESP 004 and controls did appear to uptake F-BSA.

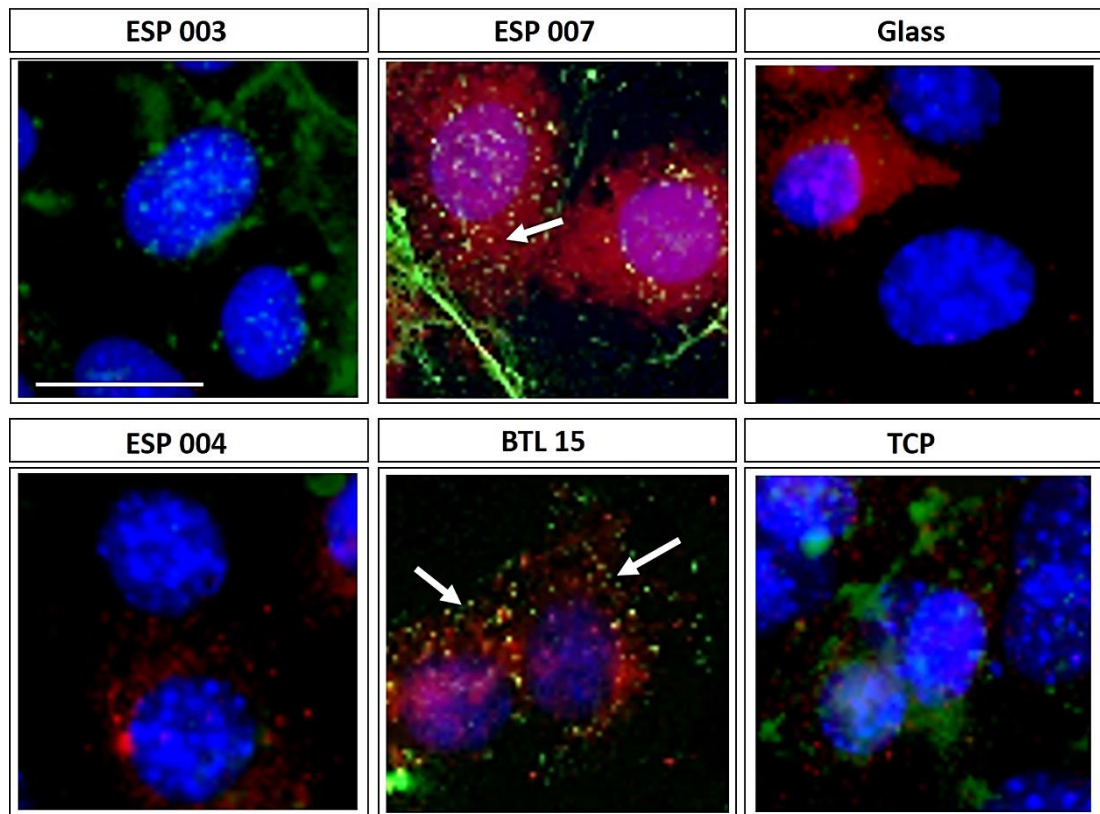


Figure 4.14: Albumin uptake assay. Red: Megalin, green: fluorescently labelled albumin (F-BSA), blue: DAPI. mKSCs were seeded at a density of 1×10^3 cells / polymer coated coverslip. F-BSA and megalin colocalise in higher proportions in cells cultured on ESP 007 and BTL 15. Scale bar: 25 μ m.

The F-BSA uptake of mKSCs was then quantified using flow cytometry after incubation of the cells either alone in F-BSA or in the presence of excess unlabelled bovine serum albumin (BSA) as a competitive inhibitor of the uptake process [236] (Figure 4.15). Notably, the results showed that the number of cells that did uptake F-BSA was highest on ESP 007 and BTL 15 (about 35-40%). Moreover, after simultaneous incubation of mKSCs in F-BSA and unlabelled albumin, the number of F-BSA⁺ cells decreased on all substrates. Only about 20% of cells within the population of mKSCs cultured on ESP 003 and ESP 004 displayed F-BSA uptake and only about 10% of cells cultured on the control substrate.

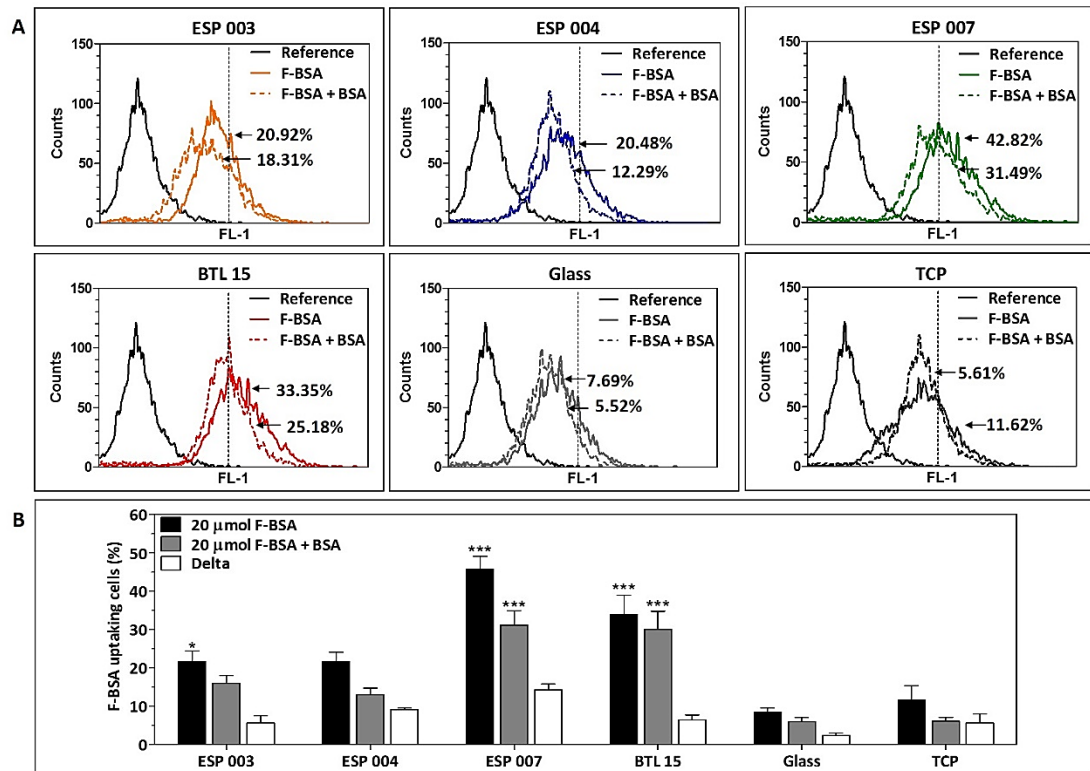


Figure 4.15: Albumin uptake assay. Flow cytometric analyses of mKSCs that were cultured on substrates. Cells were seeded at a density of 1×10^3 cells/polymer coated coverslip. (A) Flow cytometric representative spectra and (B) quantification. Asterisks indicate significant difference compared to a glass control (Tukey model $p < 0.05$). Results represent the mean of three biological replicates \pm SEM.

The gene expression of mKSCs was analysed for the expression of three PTC marker genes: *megalyn (Meg)*, *alkaline phosphatase (AlkPhos)* and *aquaporin 1 (Aqp1)*. [Figure 4.16](#) shows the results of the RT-qPCR analyses. The results showed a trend of increased PTC gene expression on ESP 004, ESP 007 and BTL 15. The trend showed that particularly *Megalyn* and *AlkPhos* expression was higher in cells cultured on ESP 007 and BTL 15, whereas PTC gene expression on ESP 003 and TCP was lower compared to other substrates. However, no significant difference was found.

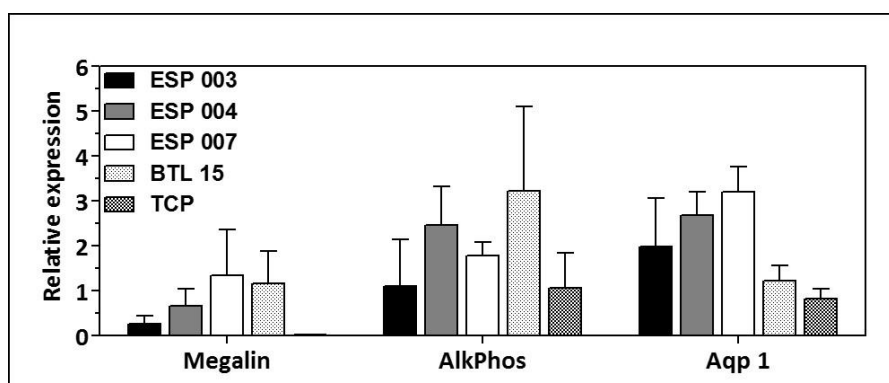


Figure 4.16: RT-qPCR analyses of mKSCs for PTC characteristic genes as relative expression to mKSCs on a glass control. Seeding density: 1×10^3 cells / polymer coated coverslip. *Gapdh* and *beta actin* (*ACTB*) were used as housekeeping genes. Results represent the mean of three biological replicates \pm SEM.

4.2.3 Effect of polyacrylates on conditionally immortalised kidney cell lines

It has previously been shown that the mKSCs used in this study are multipotent, able to generate functional PTCs and podocytes and display long-term self-renewal in culture [251]. However, human kidney progenitor cells (KPCs) have not been so well-characterised and there is little information regarding their capacity to differentiate and self-renew *in vitro*. For this reason, our strategy was to use conditionally immortalised (ci) human podocytes and PTCs in the first instance, in order to identify substrates that were able to support the growth of these cell types and maintain their differentiated phenotype. Selected substrates would then be tested for their ability to promote the differentiation of human derived putative KPCs. In addition to the substrates previously tested (ESP 003, ESP 004, ESP 007 and BTL 15), five additional substrates were included that mimic cell binding motifs in the extracellular environment of podocytes and PTCs *in vivo* (ESP 008, ESP 009, ESP 010, ESP 011, ESP 012).

4.2.3.1 Effect of polyacrylates on conditionally immortalised podocytes

The ability of polyacrylates to support growth and viability and to maintain the differentiation of conditionally immortalised podocytes (ciPodocytes) was investigated. [Figure 4.17](#) shows phase contrast and high resolution F-actin labelled images of cells cultured on ESP 007

(representative for ESP 003, ESP 004 and glass), ESP 012 (representative for ESP 011 and BTL 15) and ESP 008. Cells on ESP 009 and ESP 010 showed cell death 24 h post seeding and no proliferation was observed. Until day 5 cells were kept at the permissive temperature, 33°C, to allow them to proliferate and then transferred to a non-permissive temperature, 37°C, to allow differentiation.

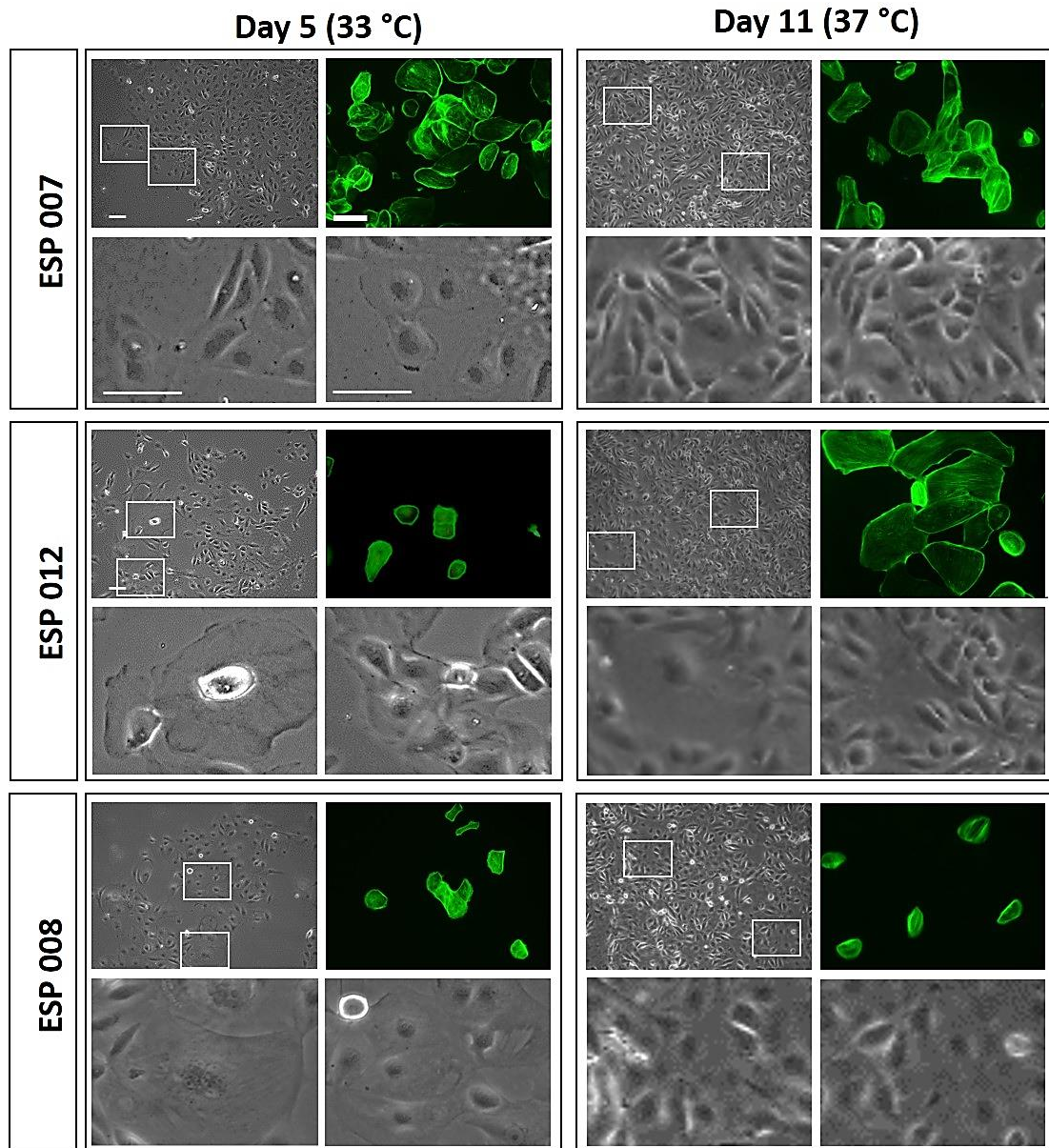


Figure 4.17: Morphological analyses of ciPodocytes on representative polyacrylate substrates with cells showing the typical podocyte-like morphology, including a large cell body, arborised cytoskeleton and binuclearity. Cells were seeded at 1×10^3 cells / polymer coated 13mm coverslip and phase contrast images and fluorescence images were taken. Green: F-actin and blue: DAPI. Scale bar is 100 μ m.

The images show ciPodocytes that looked similar on most substrates with cells being rounded. Actin was mainly present at the periphery of the cells. Once cells were transferred to the non-permissive temperature (37°C) to promote their differentiation, they started spreading and the actin cytoskeleton appeared more pronounced and distinctive, especially on ESP 011, ESP 012 and BTL 15 where the cells were very large and showed the typical podocyte-like morphology. On ESP 008, cells appeared to proliferate slower compared to cells cultured on all other substrates.

Subsequently, quantitative analyses were performed to determine the effect of the substrates on PDT and viability ([Figure 4.18](#)). The results showed that cells proliferated on all substrates with the exception of ESP 009 and ESP 010. Highest levels of proliferation were found to be on BTL 15 and glass ([Figure 4.18 A](#)). Cells on ESP 003, ESP 004 and ESP 007 also showed a notable increase in cell number. However, cells on ESP 008, ESP 11 and ESP 012 showed only a very small increase in cell number and viability over time. From the manual cell counts the PDT was quantified for cells culture at 33°C (day 1 to day 6) and 37°C (day 6 to day 11). It was found that on all substrates PDT increased once cells were transferred to the non-permissive temperature (37°C) with ESP 009 and ESP 010 being the only exceptions. This was expected, as the cell culture temperature increase leads to cells undergoing a growth arrest. Although ciPodocytes continued to proliferate, the PDT was notably increased and was highest on ESP 007. PDT of ciPodocytes was similar on all other substrates and showed no significant differences compared to glass.

A more detailed analyses of these results of cell proliferation and viability analyses can be found in the supplementary information ([chapter 4.5, p 149](#)).

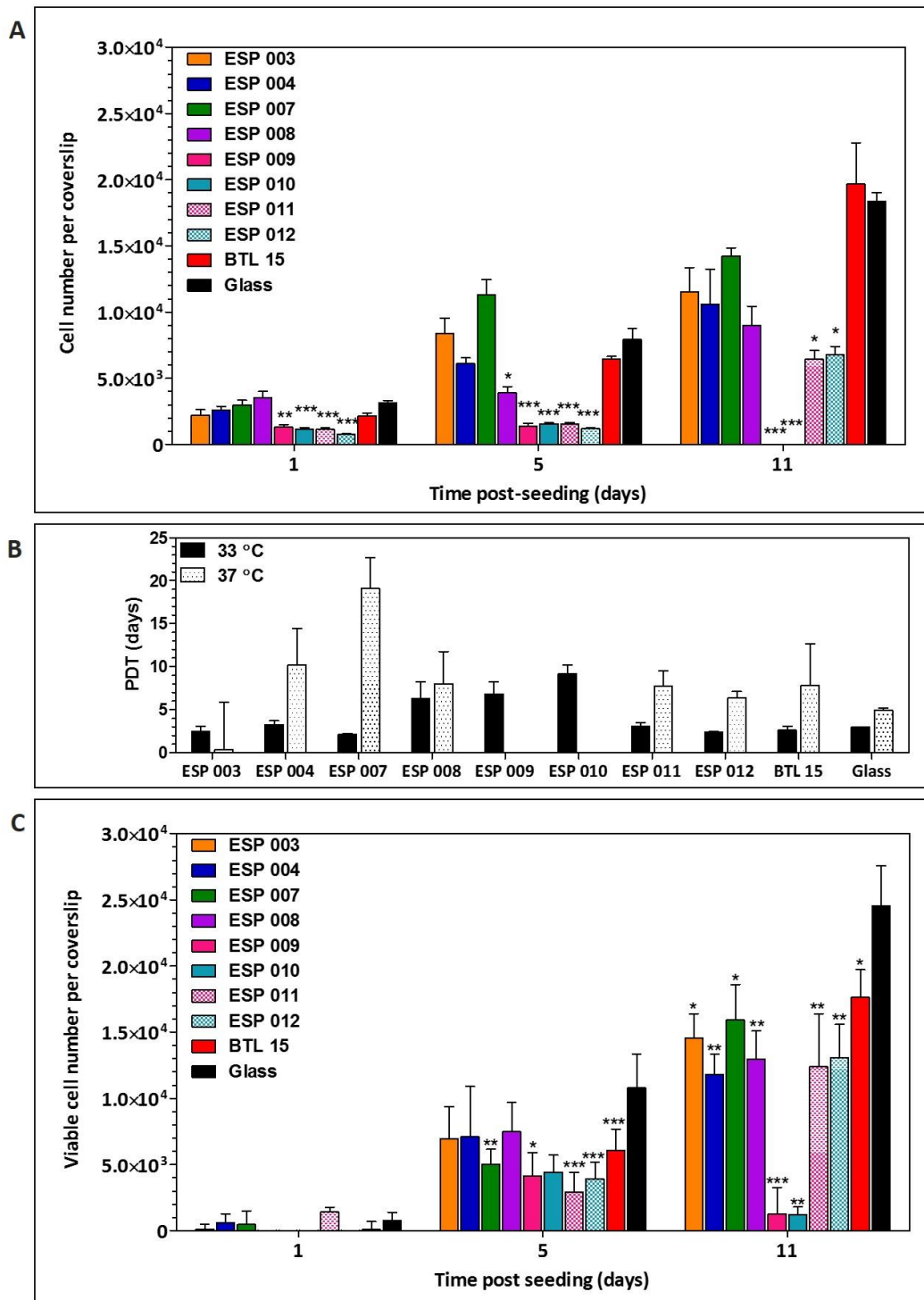


Figure 4.18: ciPodocytes cell number, PDT and viability assessment on polyacrylate substrates. Cells were seeded at 1×10^3 cells / polymer coated 13 mm coverslip. Asterisks indicate significant difference compared to a glass control (Tukey model, $p < 0.05$) Results represent the mean of three biological replicates \pm SEM.

With cell spread being an important characteristic of differentiated podocytes, the extent of cell spread was followed over time (Figure 4.19). The results confirmed the trend that was

observed from phase contrast images (Figure 4.17). Cell spread was the largest on BTL 15, ESP 012, ESP 011 and ESP 007. On ESP 009 and ESP 010 cell spread was not quantified at day 11 as cells appeared to undergo cell death, were very small and rounded. ciPodocytes on ESP 004 and ESP 010 showed an intermediate degree of spreading compared to cells seeded on other substrates.

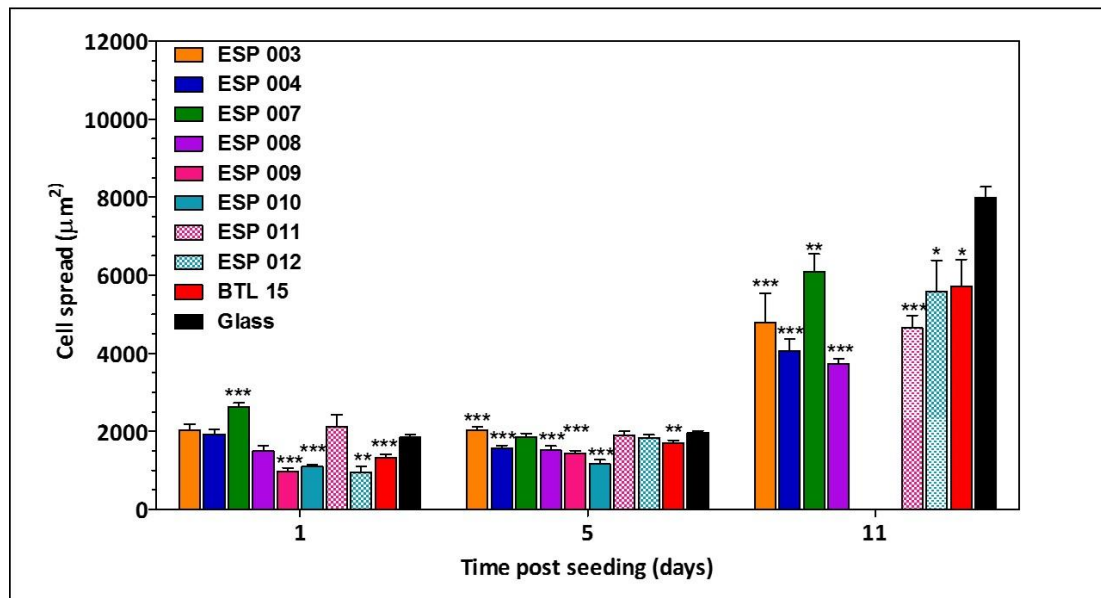


Figure 4.19: Cell spread analyses of ciPodocytes on polyacrylate substrates. Cells were seeded at 1×10^3 cells / polymer coated 13 mm coverslip and cell spread was analysed. Asterisks indicate significant difference compared to a glass control (Tukey model, $p < 0.05$). Results represent the mean of three biological replicates \pm SEM.

Subsequently, the expression of podocyte markers was analysed. Figure 4.20 shows ciPodocytes that were cultured for 11 days on polyacrylates substrates and labelled for two characteristic markers: nephrin and podocin. ciPodocytes showed the typical large and rounded structure and expressed the characteristic markers on all substrates. Nevertheless cells on ESP 008 were less spread compared to cells cultured on other substrates, but they still did expressed these markers. Images of cells cultured on ESP 009 and ESP 010 could not be obtained as no more cells were present at this time point.

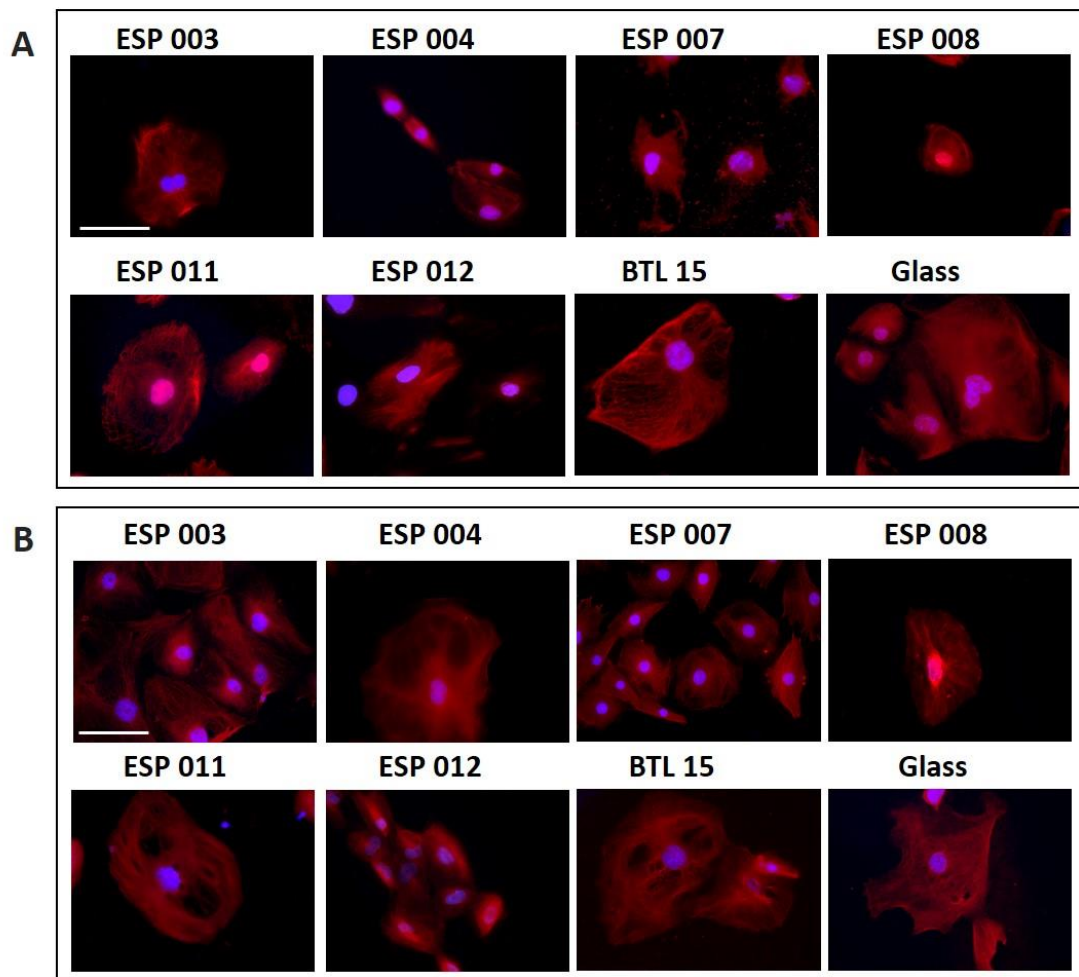


Figure 4.20: (A) *Nephtrin* and (B) *podocin* staining of ciPodocytes on polyacrylate substrates. Cells were seeded at 1×10^3 cells / polymer coated 13 mm coverslip. Blue: DAPI. Scale bar is 100 μ m.

4.2.3.2 Effect of polyacrylates on conditionally immortalised proximal tubule cells

The ability of polyacrylates to support growth and viability and to maintain the differentiation of conditionally immortalised PTCs (ciPTCs) was investigated. As with ciPodocytes, ciPTCs were cultured at a permissive temperature (33°C) for proliferation and then transferred to a non-permissive temperature (37°C) in order to initiate cell differentiation. [Figure 4.21](#) shows phase contrast images and high magnification images of phalloidin labelled cells cultured on ESP 007 (representative for ESP 003, ESP 004 and glass), ESP 012 (representative for ESP 011 and BTL 15) and ESP 008. Cells on ESP 009 and ESP 010 showed cell death 24 h post seeding and no proliferation was observed. The images showed that ciPTCs varied in morphology between the substrates. 5 days post seeding the ciPTCs were rather elongated and partially

rounded on most substrates. Once cells were incubated at 37°C for differentiation, they started spreading on all substrates except ESP 009 and ESP 010 where no more cells were observed from day 5 post seeding.

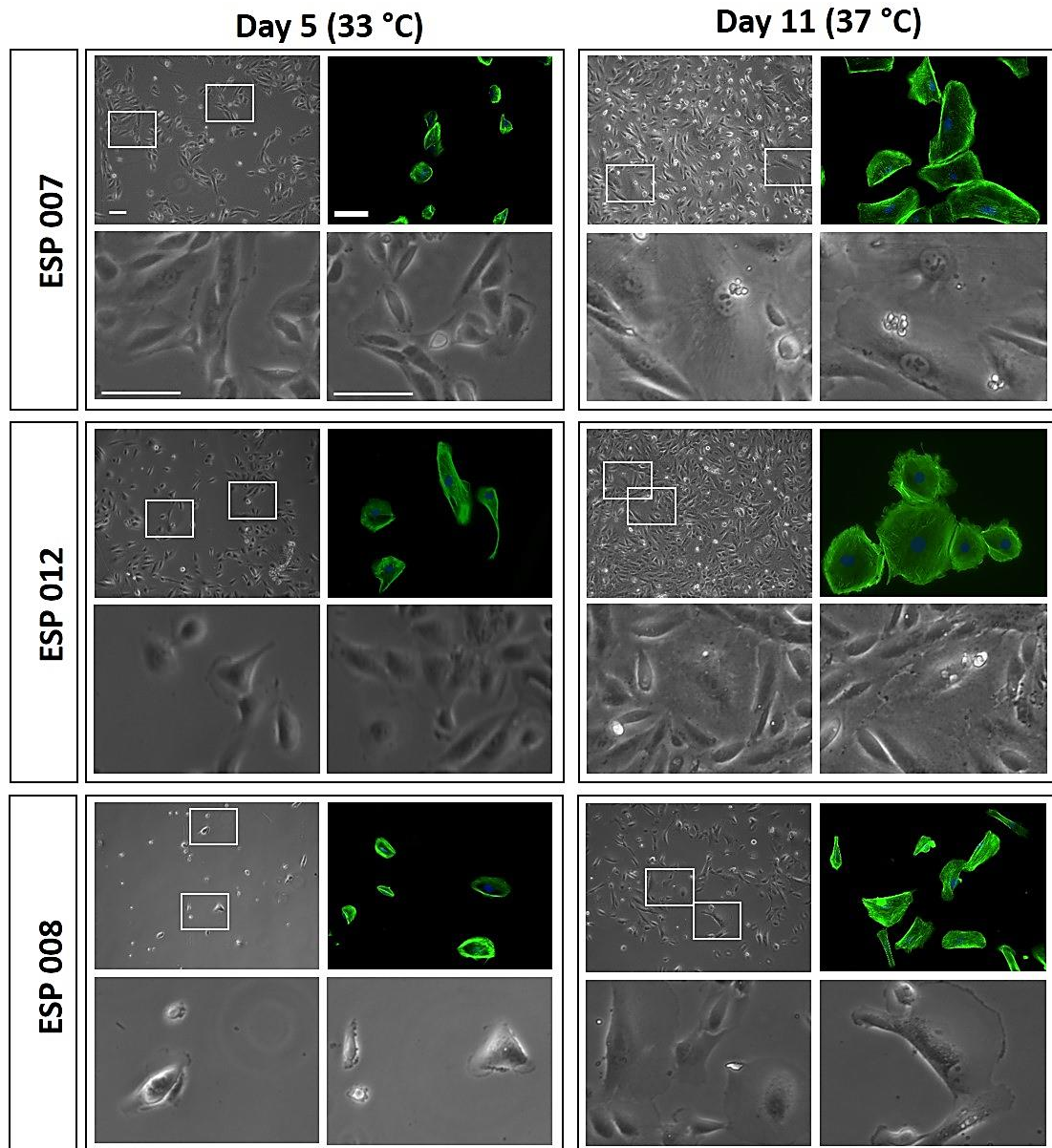


Figure 4.21: Morphological analyses of ciPTCs on representative polyacrylate substrates. Cells were seeded at 1×10^3 cells / polymer coated 13mm coverslip and phase contrast images and fluorescence images were taken. Green: F-actin and blue: DAPI. Scale bar is 100 μ m.

To support these observations, cell number, PDT and cell viability were determined ([Figure 4.22](#)). The analyses of cell number and viability showed that cells were proliferating on all substrates with those cultured on ESP 009 and ESP 010 being the only exceptions. Highest levels of proliferation were observed on ESP 007, ESP 004, ESP 003 and glass. Compared to these, proliferation on other substrates was lower. The assessment of cell viability confirmed these findings. In addition, PDT was analysed at both temperatures, as, ideally, ciPTCs would undergo growth arrest once transferred to the non-permissive temperature (37°C). It was found that on most substrates PDT was similar or lower at 33°C compared to 37°C (cells at 37°C take more time to double the population). As cells cultured on ESP 009 and ESP 010 did not proliferate, but rather decreased in cell number over time, PDT was zero on these substrates. However, cell proliferation was on all substrates significantly less compared to a glass control.

A more detailed analyses of these results on cell proliferation and viability can be found in the supplementary information ([chapter 4.5, p 149](#)).

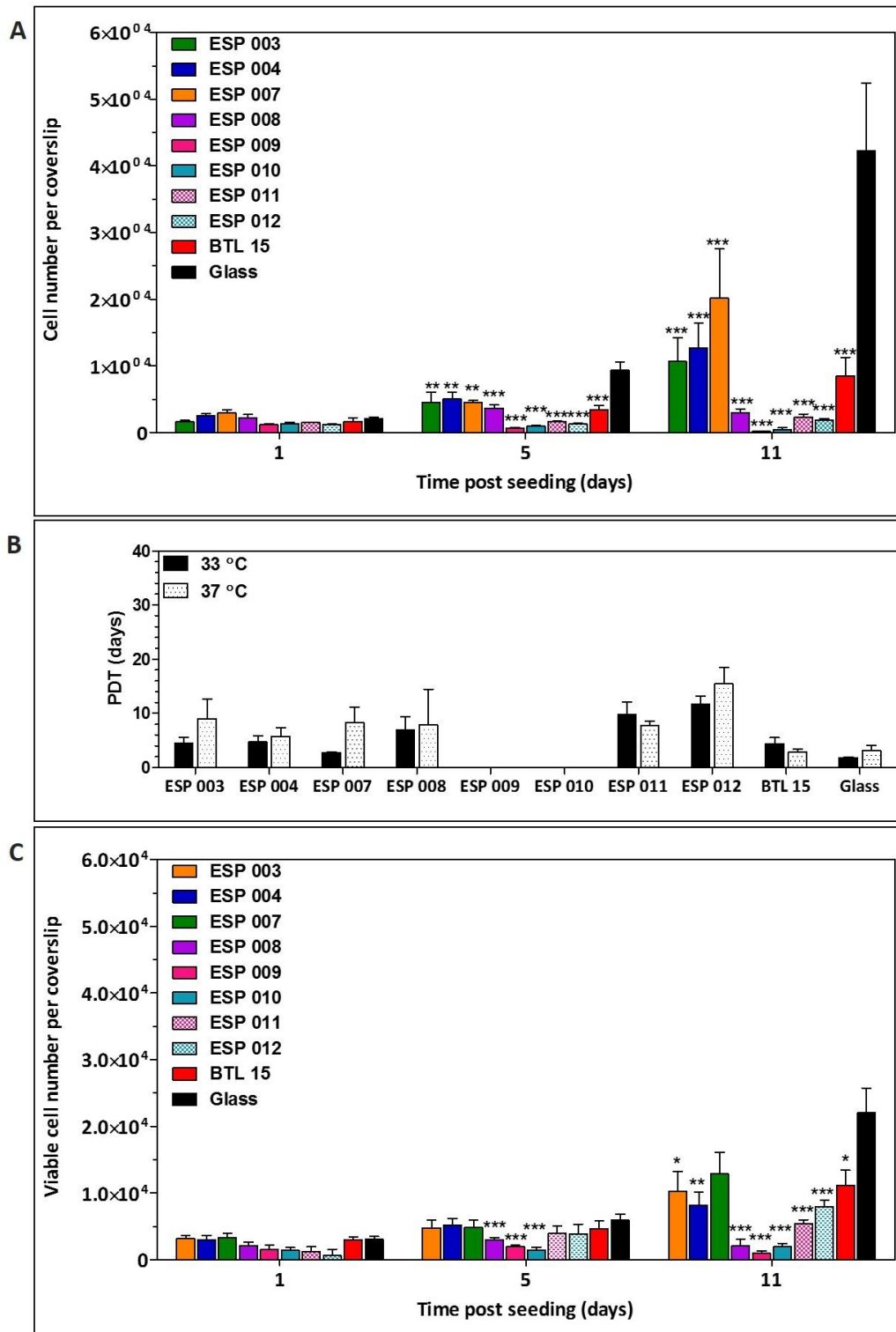


Figure 4.22: ciPTC cell number, PDT and viability assessment on polyacrylate substrates. Cells were seeded at 1×10^3 cells / polymer coated 13 mm coverslip. Asterisks indicate significant difference compared to a glass control (Tukey model, $p < 0.05$) Results represent the mean of three biological replicates \pm SEM.

Cell spread is generally an indicator for adhesion and interactions of cells with substrates. Therefore the ciPTCs extend of cell spreading was assessed on all polyacrylates over time (Figure 4.23). The cell spread was similar on all substrates with ESP 007, ESP 011, ESP 012 and BTL 15 supporting cell spread to the highest extent. On ESP 009 and ESP 010 no more cells were detected post day 5.

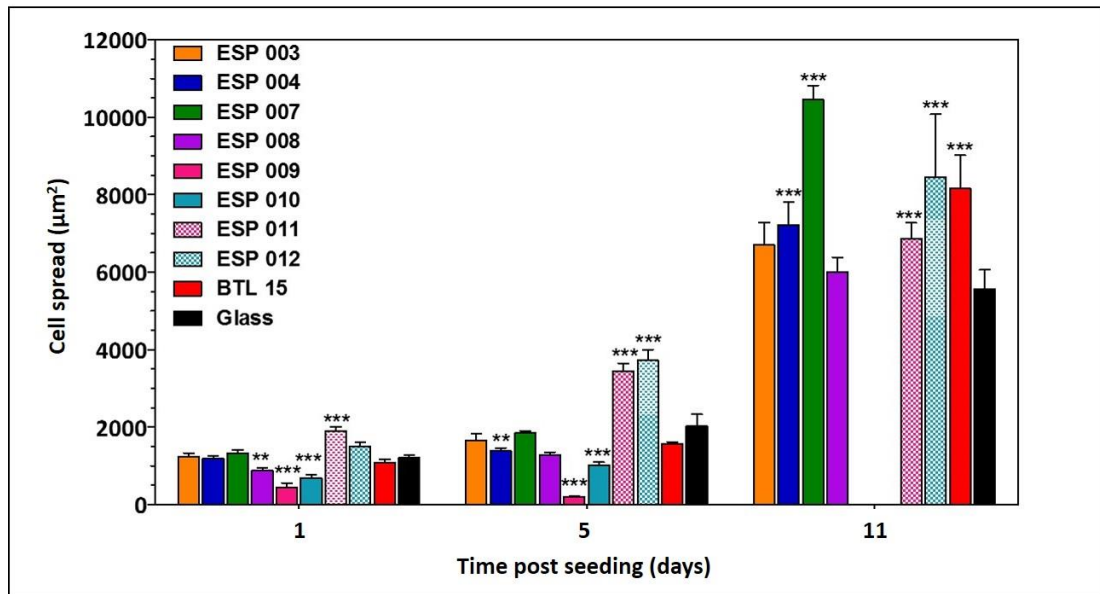


Figure 4.23: Cell spread analyses of ciPTCs on polyacrylate substrates. Cells were seeded at 1×10^3 cells / polymer coated 13 mm coverslip and cell spread was analysed. Asterisks indicate significant difference compared to a glass control (Tukey model, $p < 0.05$). Results represent the mean of three biological replicates \pm SEM.

Subsequently, ciPTC were assessed for the expression of characteristic markers. Figure 4.24 shows ciPTCs that were cultured for 11 days on polyacrylate substrates and labelled for two characteristic markers: aquaporin 1 and megalin. The images show that ciPTCs expressed both markers on all substrates. Images of cells on ESP 009 and ESP 010 could not be obtained as no more cells were present at this time point.

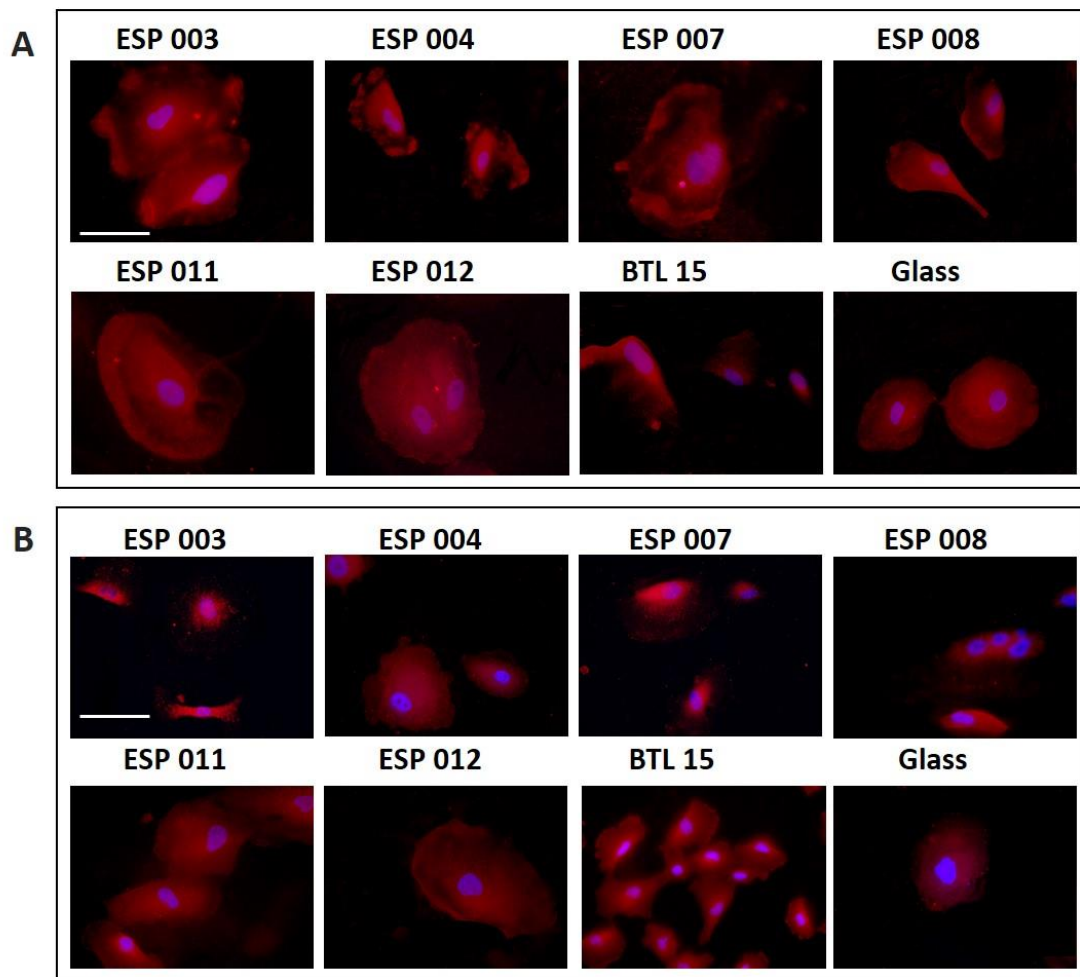


Figure 4.24: (A) *Aquaporin 1* and (B) *megalyn* staining of ciPTCs on polyacrylate substrates. Blue: DAPI. Cells were seeded at 1×10^3 cells / polymer coated 13 mm coverslip. Scale bar is 100 μm .

Lastly, the functionality of ciPTCs on substrates was analysed by investigating their ability to uptake fluorescently labelled albumin (F-BSA) through the transmembrane receptor megalin (Figure 4.25). The analyses showed that on nearly all substrates about 65% of the cells did uptake F-BSA. This percentage was significantly decreased on ESP 008 and glass. Once cells were incubated in F-BSA enriched medium and an excess of unlabelled albumin (competitive inhibition), the number of F-BSA up-taking cells decreased to about 20%.

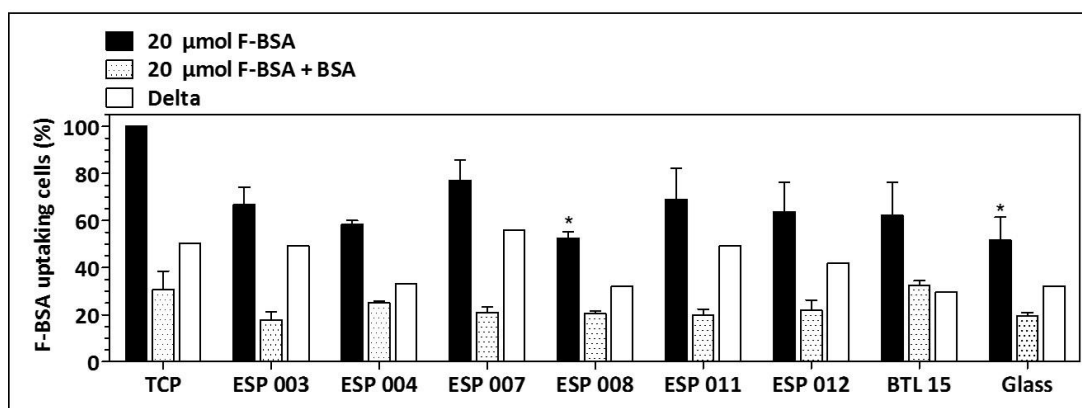


Figure 4.25: Albumin uptake assay. ciPTCs were analysed for their ability to uptake F-BSA. Cells were seeded at a density of 1×10^3 cells / polymer coated 13 mm coverslip. Asterisks indicate statistical difference compared to a TCP control. Results represent the mean of three biological replicates \pm SEM.

4.2.4 Effect of polyacrylates on putative human kidney progenitor cells

The identification and characterisation of human kidney derived progenitor cells (KPCs) would be a great advantage for studying kidney function, regeneration and disease. However, there is still a scientific debate whether KPCs exist in the adult body and if so, whether these derive from one ultimate progenitor cell [252, 398, 399]. Some niches containing putative KPC populations were identified within the nephrons, mainly characterised by the expression of specific (progenitor/stem cell) markers, namely CD133 and CD24, and many were found to support regeneration of kidney structure and function after renal injury [5, 7, 164, 252-258]. Putative human KPCs have been identified in the renal papilla and expressed, besides CD 133 also nestin [400]. Others identified KPC niches within the renal tubules and these cells were shown to, besides CD133 and CD24 also express Pax 2 (embryonic renal marker) and vimentin [271]. Lastly, also within the parietal layer at the urinary pole of the Bowman’s capsule, putative KPCs were identified and these cells also expressed, in addition to CD133 and CD24, the stem cell–specific transcription factors Oct-4 and Bmi-1 [5-7, 10, 16, 312] and others found that some of these cells also expressed CD106 (vascular cell adhesion molecule 1) [5]. All of these cell lines had in common that they were

generally able to self-renew (highly proliferative), differentiate into specialised renal cell lines, often also displayed multilineage potential, and to initiate recovery post renal injury [5-7, 261, 266, 271, 401-403].

Based on these findings it is clear that particularly CD24 and CD133 have gained much recognition in terms of identifying kidney progenitors. CD133⁺/CD24⁺ cells do indeed have self-renewal potential, maintain a stable phenotype in cell culture and can differentiate into podocytes and tubular cells *in vitro* and *in vivo* [5-7, 266]. Although it is still not clear whether there are stem or progenitor cells in the kidney, it is assumed that there are cell populations within embryonic, fetal and adult kidneys as well as within the amniotic fluid that have stem cell properties [6, 261, 267, 404]. Further investigation of these population might lead to the establishment of the ultimate kidney progenitors. Many studies are focused on the identification of other potential KPC markers and new conjectures are published regularly. Among them are NCAM (neural cell adhesion molecule), EpCAM (epithelial cell adhesion molecule) and FZD7 (frizzled-7) and ALDH (aldehyd-dehydrogenasen) [266-269].

Within this study two putative KPC lines derived from either fetal or infant kidneys were obtained and FACS sorted to be either CD133⁺/CD24⁺ double positive (DP) or CD133⁻/CD24⁻ double negative (DN) to further interrogate their potential to differentiate into specialised renal cell lines on the here studied biomaterials. In conclusion from the results of our studies, the following three substrates were selected: ESP 003, ESP 007 and ESP 011. ESP 003 and ESP 007 were selected because they were able to promote the differentiation of mKSCs into podocytes and PTCs, respectively, whereas ESP 011 supported growth and spreading of conditionally immortalised podocytes and PTCs. Moreover, ESP 011 was developed in close structural resemblance to ESP 007.

4.2.4.1 Effect of polyacrylates on fetal human kidney progenitor cells

4.2.4.1.1 Effect of polyacrylates on morphology and behaviour of fetal kidney progenitor cells

Fetal kidney progenitor cells (fKPCs) were FACS sorted to be either DP or DN for two putative kidney progenitor markers: CD24 and CD133. Therefore, it was expected that DP cells were kidney progenitor cells, whereas DN cells may represent a variety of kidney cells, such as differentiated cells. [Figure 4.26](#) shows images obtained from both populations, DP and DN fKPCs 3 and 7 days post seeding. It was found that, on all substrates, the DN population had a higher rate of proliferation compared to DP cells. Both DN and DP cells adhered to all substrates, started to form monolayers and became more elongated over time. On ESP 003, however, cell proliferation appeared to be slower than on the other substrates and compared to controls.

No morphological changes of either cell type seeded on different substrates could be found. However, when comparing the DN and the DP population the cells showed striking differences in their general phenotype and behaviour ([Figure 4.26](#), [Figure 4.27](#)). Cell proliferation and viability analyses showed a consistent exponential growth of DN fKPCs with the obtained cell numbers being very similar on all substrates. The DP population on the other hand showed no or only little proliferation and presumably attachment: out of 5000 seeded cells only about 1/5 was detected on all substrates 24 h post seeding. The assessment of cell viability confirmed these findings.

In addition, the assessment of PDT confirmed these results. PDT of DN cells was found to be about 2 days, whereas it was about 4 ± 1 days for DP cells. PDT was consistent between substrates for both, the DP and DN population.

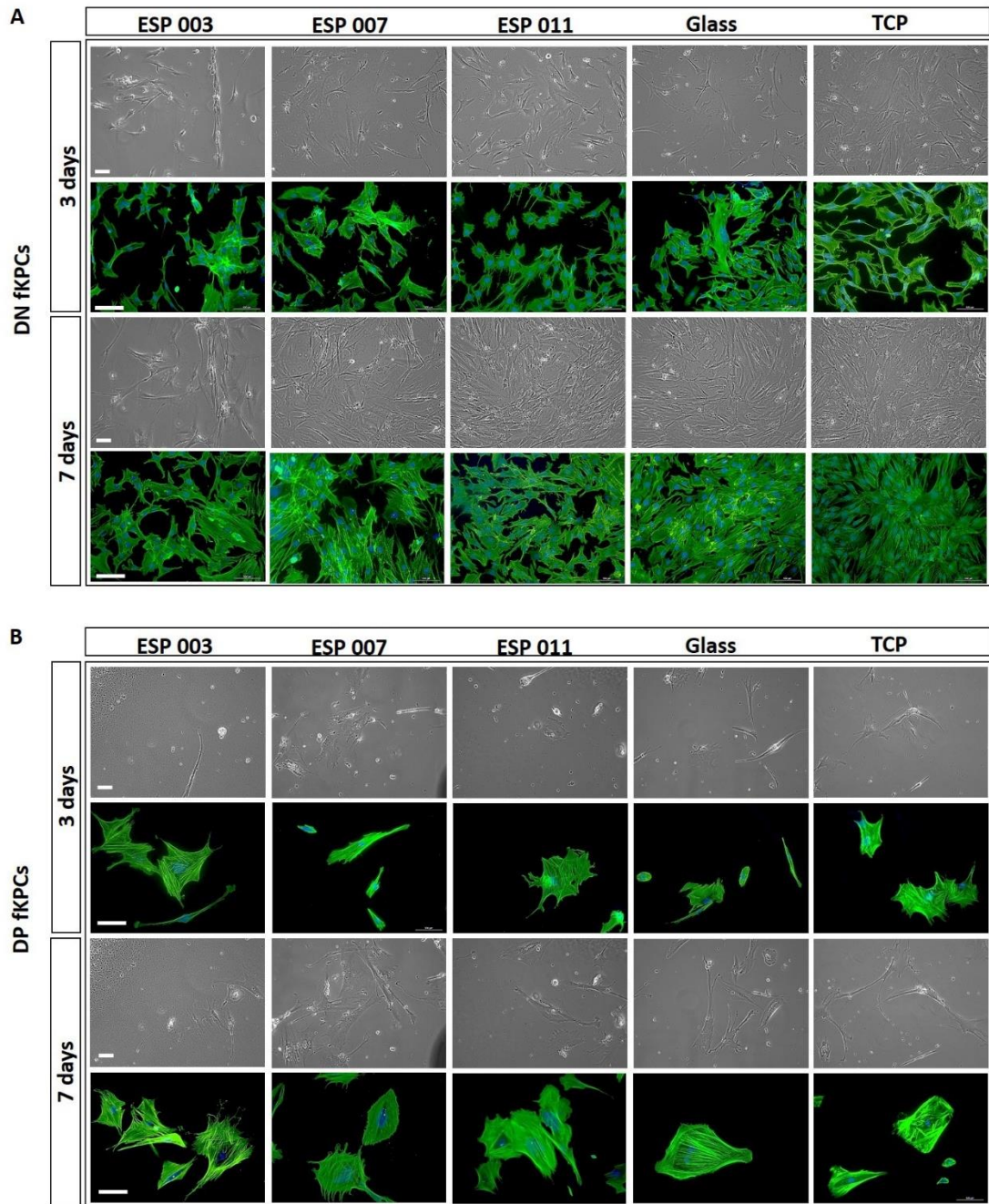


Figure 4.26: Morphological analyses of fKPCs on polyacrylate substrates. Cells were seeded at 5×10^3 cells / polymer coated 13 mm coverslip. Images show phase contrast images and F-Actin labelled cells at a higher resolution at two different time point: 3 and 7 days post seeding. Blue: DAPI. (A) Double negative and (B) double positive population. Scale bar is 100 μ m.

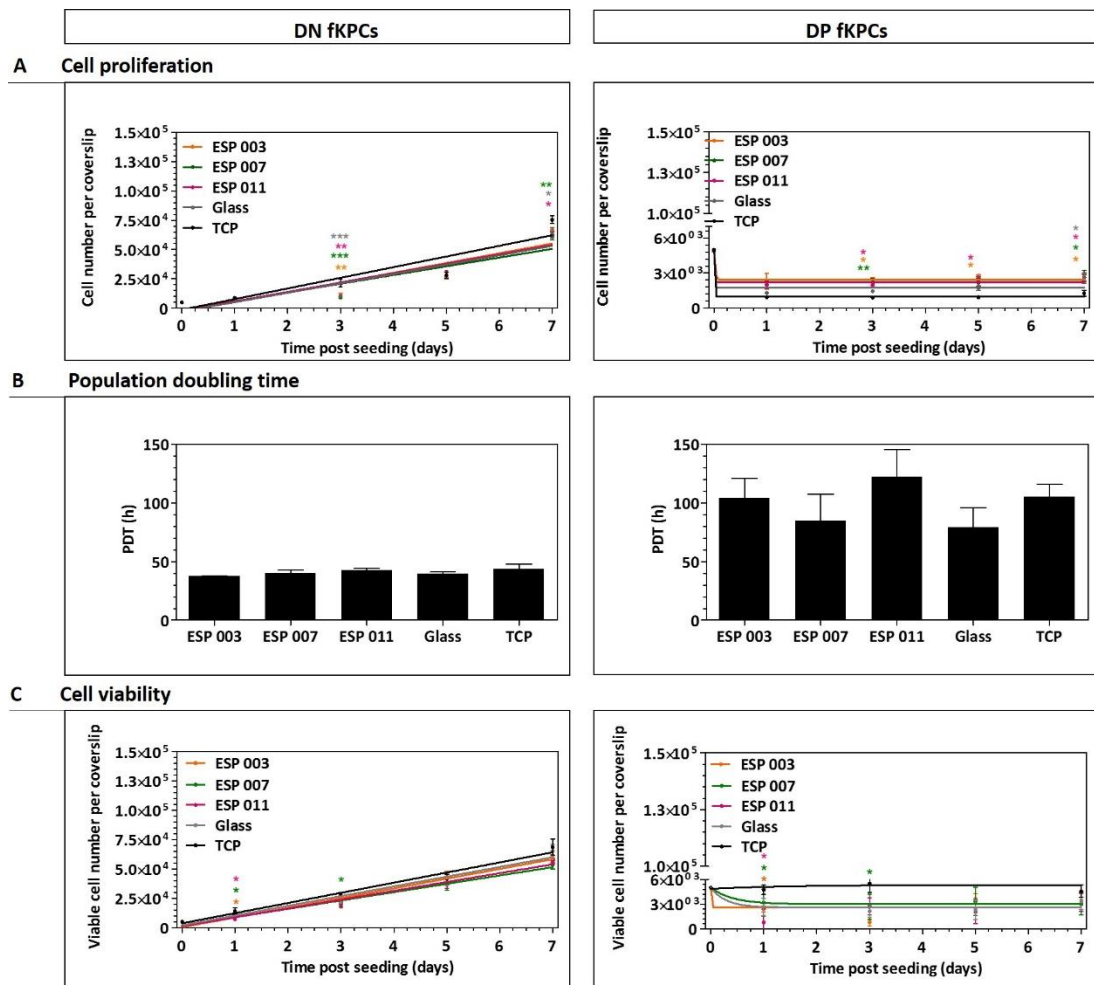


Figure 4.27: Analyses of iKPC (A) proliferation, (B) PDT (as determined from cell number values in (A) and (C) viability on polyacrylate substrates. Cells were seeded at a density of 5×10^3 cells / polymer coated 13 mm coverslip. Asterisks indicate significant difference compared to glass control (Tukey model, $p < 0.05$). Data were fitted with an exponential growth equation. Results represent the mean of three biological replicates \pm SEM.

Cell spread analyses was consistent with the microscopic images (Figure 4.28). The DN cell population showed a spread area of about 2000-3000 μm^2 with this number being constant over the entire cell culture period. The DP cell population on the other hand showed an increased spread area over time (about 10000 μm^2) after 7 days. Cells cultured on the glass control were the only exception with cells spreading up to 15000 μm^2 .

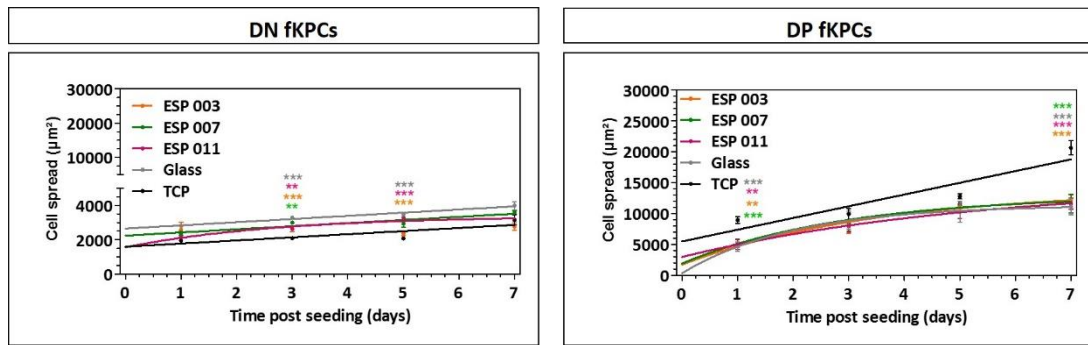


Figure 4.28: Cell spread analyses of fKPCs on polyacrylate substrates. Cells were seeded at a density of 5×10^3 cells / polymer coated 13 mm coverslip. Cells were cultured for a period of 7 days. Asterisks significant difference compared to glass control (Tukey model, $p < 0.05$). Data were fitted with a non-linear fit / one phase decay equation. Results represent the mean of three biological replicates \pm SEM.

4.2.4.1.2 Effect of polyacrylates on the differentiation of fetal kidney progenitor cells

After 7 days in cell culture on polyacrylate substrates, fKPCs were analysed for the presence of PTCs within the population. For that, a BSA uptake assay was performed and cells were co-labelled with the PTC marker alanine aminopeptidase (CD13) (Figure 4.29). fKPCs were then sorted using flow cytometry. It was found that the DN population contained about 25% CD13⁺ cells, of which about 2% were functional. No statistical difference was detected regardless of the substrate. The DP population on the other hand contained about 80% CD13⁺ cells of which about 20% were functional. The number of these functional PTCs within the DP population was significantly decreased on all these substrates, including the glass control, compared to the TCP control.

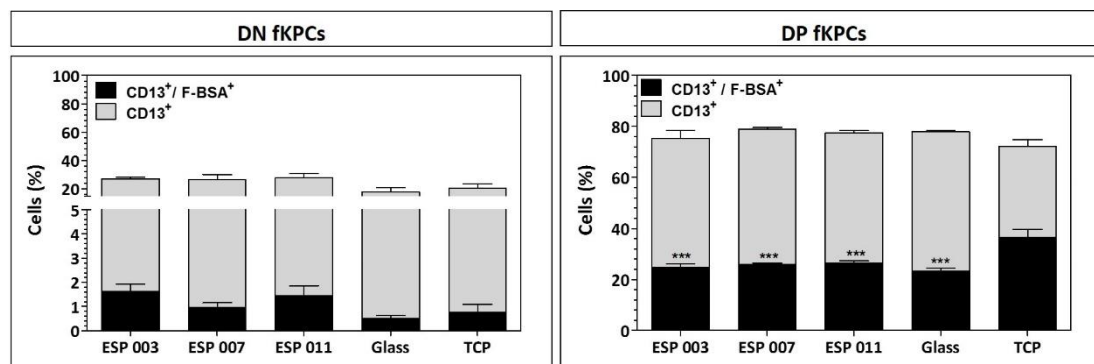


Figure 4.29: fKPC flow cytometric analyses for assessment of functional PTCs after culture on substrates. Cells were seeded at a density of 1.5×10^4 cells / polymer coated (2x) 19 mm coverslip. An albumin uptake assay was performed and cells were co-labelled with CD13. Asterisks indicate significant difference compared to TCP control. Results represent the mean of three biological replicates \pm SEM.

4.2.4.1.3 Effect of polyacrylates on the expression of the CD133⁺ and CD24⁺

fKPCs are known to lose CD133⁺ and CD24⁺ in *in vitro* cell culture after only few passages. Therefore, it was assessed whether polyacrylates can support the expression of these markers. Cells between the passages 6 to 9 were cultured on substrates and subsequently analysed for expression of CD24 and CD133 using flow cytometry (Figure 4.30). As expected, nearly 100% of the DN cells remained DN over the course of the cell culture period. Only a negligible number of cells were found to be CD24⁺/CD133⁺ (1%) and a small percentage of cells were single positive for either CD24⁺ or CD133⁺ (1-8 %). Interestingly, the DP fKPC population did not remain DP over the cell culture period. After 7 days about 75% of these cells were CD24⁻/CD133⁻ and only 2-4% of the cells remained CD24⁺/CD133⁺.

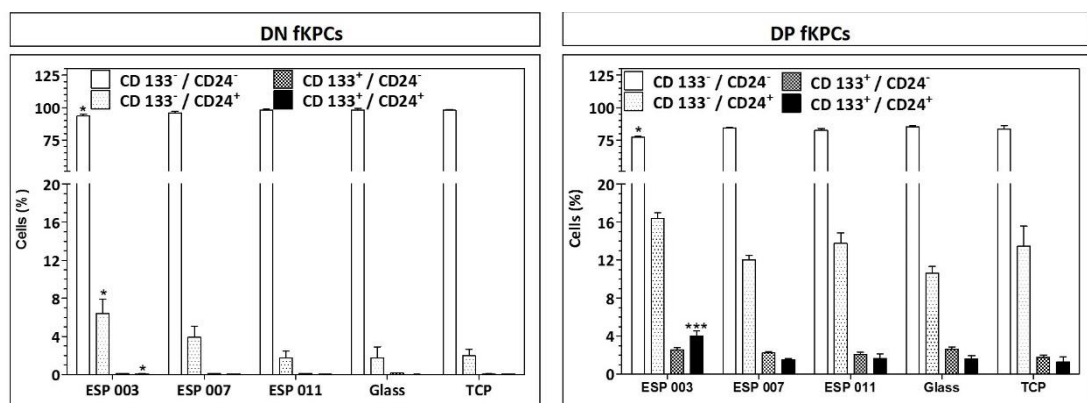


Figure 4.30: Assessment of CD133/CD24 of fKPCs on polyacrylates. Cells were seeded at a density of 1.5×10^4 cells / polymer coated (2x) 19 mm coverslip. Asterisks indicate significant significance compared to the TCP control. Results represent the mean of three biological replicates \pm SEM.

4.2.4.2 Effect of polyacrylates on infant human kidney progenitor cells

4.2.4.2.1 Effect of polyacrylates on morphology and behaviour of infant kidney progenitor cells

Infant kidney progenitor stem cells (iKPCs) were FACS sorted to be either DP or DN for two putative kidney progenitor markers: CD24 and CD133. Figure 4.31 shows images obtained from both, DP and DN iKPCs 3 and 7 days post seeding. As found for fKPCs, the DN population proliferated on all substrates. The cells adhered to and spread on all substrates, however, no

morphological changes were detected over time. DP iKPCs showed a similar morphology but appeared less proliferative compared to the DN population. However, neither DP nor DN iKPCs showed morphological differences in dependence of the underlying substrate.

Quantitative assessment of iKPCs proliferation showed that both populations grew on all substrates. However, the DN iKPCs cultured on ESP 003 showed significantly less proliferation compared to those DN cells cultured on the other substrates ([Figure 4.32](#)). Cell proliferation and viability of the DP population was less compared to the DN population ([Figure 4.32](#)).

Analyses of the PDT confirmed these findings and showed that DN iKPCs took about 60 h to double the population, whereas DP cells took about 70 h. This was consistent, regardless of the underlying substrate.

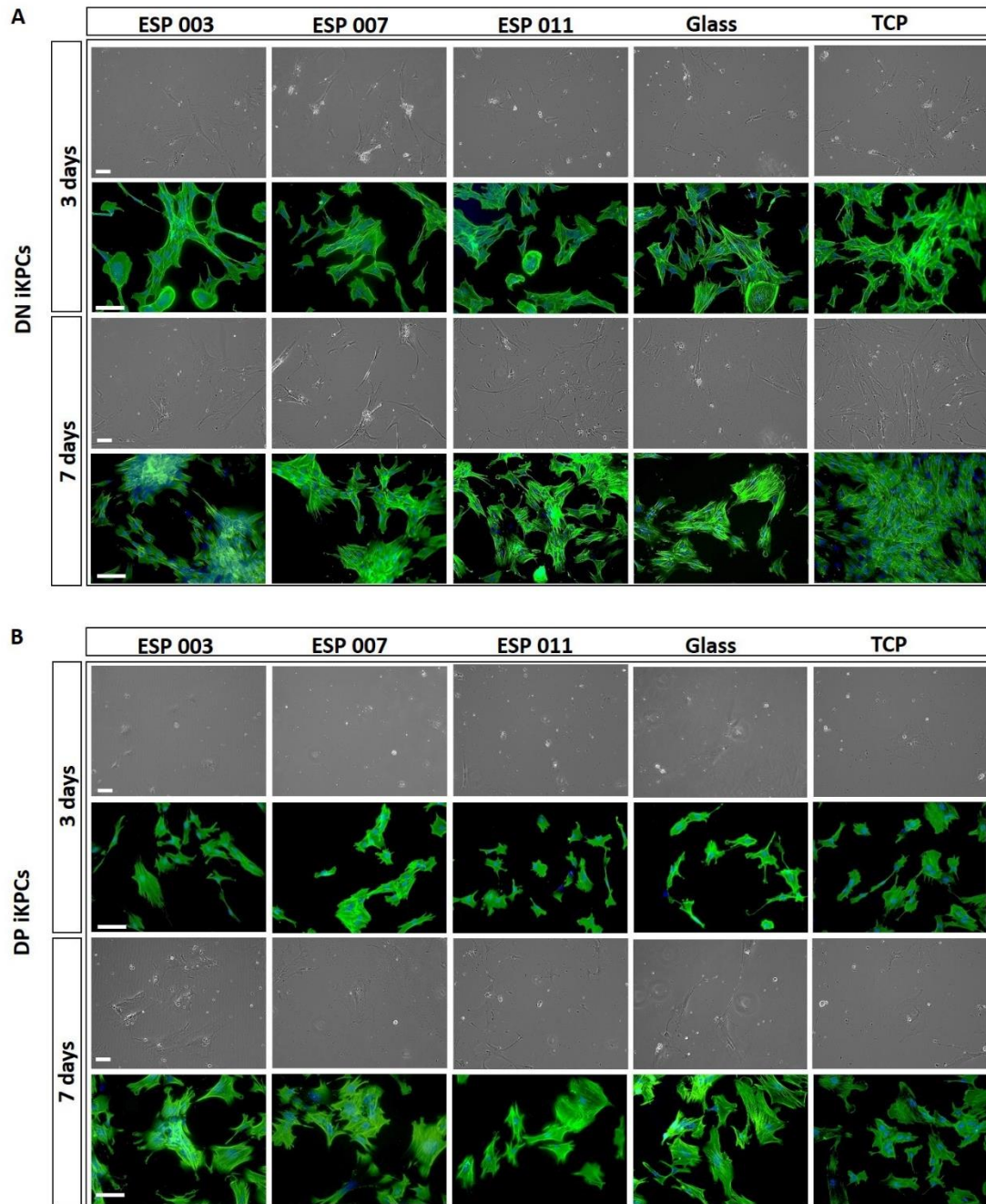


Figure 4.31: Morphological analyses of iKPCs on polyacrylate substrates. Cells were seeded at 5×10^3 cells / polymer coated 13 mm coverslip. Images show phase contrast images and F-Actin labelled cells at a higher resolution at two different time point: 3 and 7 days post seeding. Blue: DAPI. (A) Double negative and (B) double positive population. Scale bar is 100 μm .

In addition the extent of cell spreading was analysed on all substrates (Figure 4.33). Both, the DN and DP iKPC population showed a spread area of about 3000-4000 μm^2 with this number remaining constant over the entire cell culture period regardless of the substrate. However, DP iKPCs showed significantly more spread on all substrates compared to a TCP control.

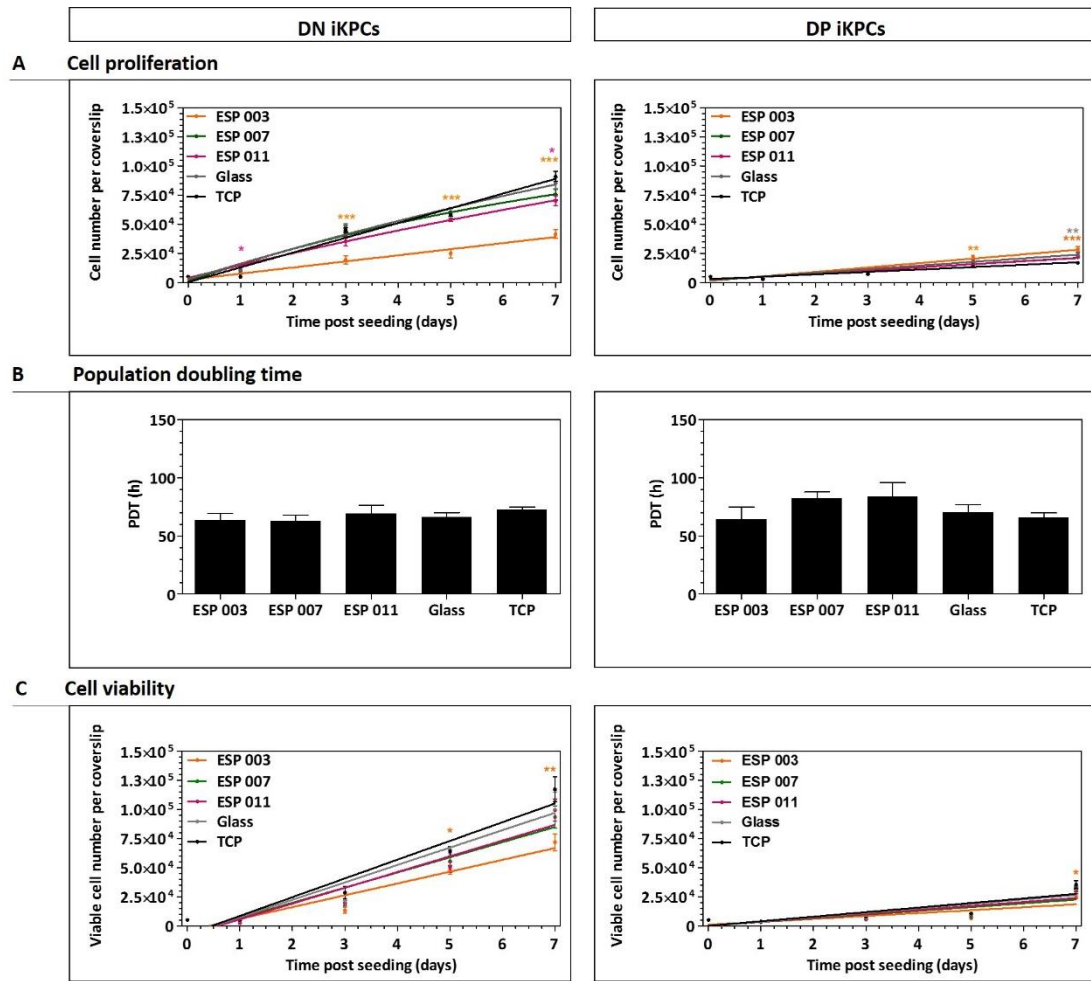


Figure 4.32: Analyses of iKPC (A) proliferation, (B) PDT (as determined from cell number values in (A) and (C) viability) on polyacrylate substrates. Cells were seeded at a density of 5×10^3 cells / polymer coated 13 mm coverslip. Asterisks indicate significant difference compared to glass control (Tukey model, $p < 0.05$). Data were fitted with an exponential growth equation. Results represent the mean of three biological replicates \pm SEM.

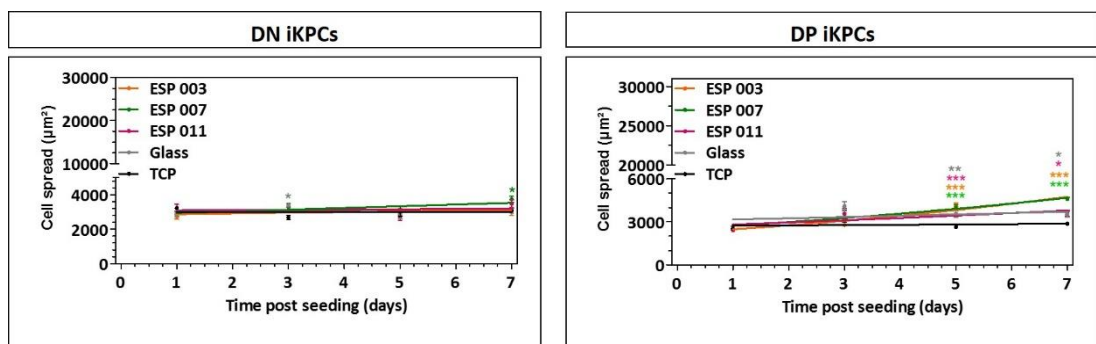


Figure 4.33: Cell spread analyses of iKPCs on polyacrylate substrates. Cells were seeded at a density of 5×10^3 cells / polymer coated 13 mm coverslip. Cells were cultured for a period of 7 days. Asterisks indicate significant difference compared to glass control (Tukey model, $p < 0.05$). Data were fitted with a non-linear fit / one phase decay equation. Results represent the mean of three biological replicates \pm SEM.

4.2.4.2.2 Effect of polyacrylates on the differentiation of infant kidney progenitor cells

After 7 days in culture on polyacrylate substrates, iKPCs were analysed for the presence of PTCs within the population. For that, a BSA uptake assay was performed ([chapter 2.4.8.3](#), p 50) and cells were co-labelled with the PTC marker CD13 ([Figure 4.34](#)). fKPCs were then sorted using flow cytometry. DN iKPCs cultured on polyacrylates contained about 95% CD13⁺ cells on all substrates, including controls. About 40% of these cells were functional on polyacrylates and 80% on controls. DP iKPCs on the other hand contained about 75% CD13⁺ cells. Moreover, about 35% of these were functional on glass and TCP control. This number was significantly decreased when cells were cultured on polyacrylate substrates (20%).

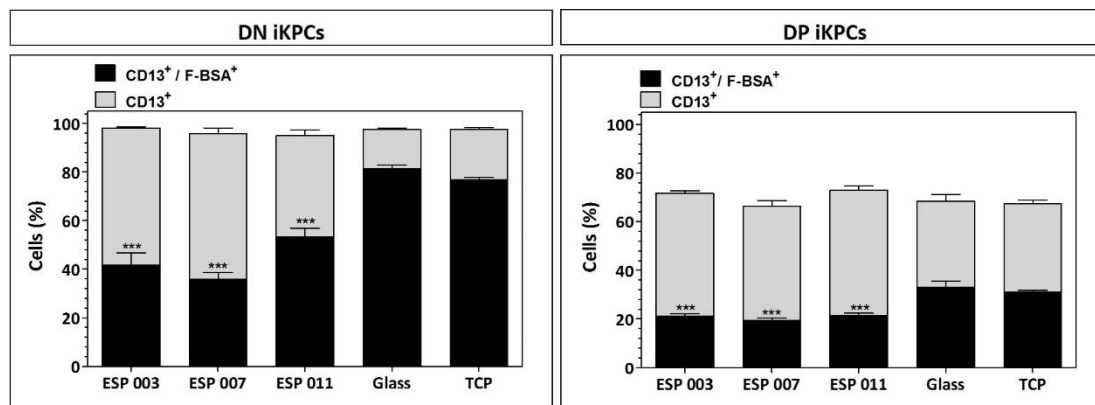


Figure 4.34: iKPC flow cytometric analyses for assessment of functional PTCs after culture on substrates. Cells were seeded at a density of 1.5×10^4 cells / polymer coated (2x) 19 mm coverslip. An albumin uptake assay was performed and cells were co-labelled with CD13. Asterisks indicate significant difference compared to TCP control. Results represent the mean of three biological replicates \pm SEM.

4.2.4.2.3 Effect of polyacrylates on the expression of the CD133⁺ and CD24⁺

As fKPCs, also iKPCs lose CD133⁺ and CD24⁺ in *in vitro* cell culture within a few passages. Therefore, iKPCs between the passages 7 to 10 were cultured on substrates and analysed for expression of CD24 and CD133 using flow cytometry ([Figure 4.35](#)). As expected, nearly 100% of the DN cells remained DN over the course of the cell culture period. In line with the findings on the fKPCs, the DP iKPC population did not remain CD24⁺/CD133⁺ over the cell culture

period. After 7 days in culture about 75% of the cells were CD24⁻/CD133⁻ and only 1-2% of the cells remained CD24⁺/CD133⁺.

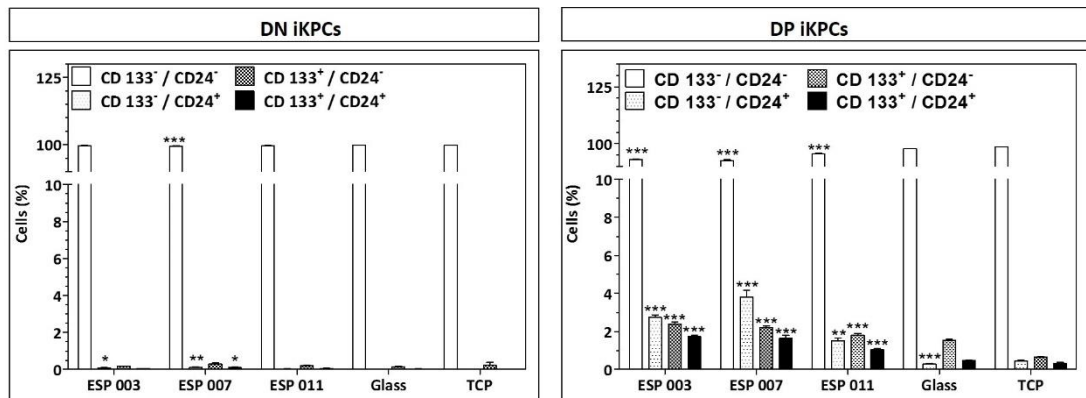


Figure 4.35: Assessment of CD133/CD24 of iKPCs on polyacrylates. Cells were seeded at a density of 1.5×10^4 cells / polymer coated (2x) 19 mm coverslip. Asterisks indicate significant significance compared to the TCP control. Results represent the mean of three biological replicates \pm SEM.

4.3 Discussion

4.3.1 Polyacrylate biocompatibility

Cellular response to biomaterials is a key factor in their design and application [405]. One of many methods to evaluate cell response towards a material is to analyse *in vitro* cytotoxicity and to determine material influence on cell behaviour and regulation [406, 407]. The typical consequence of a cytotoxic environment is cell lysis / cell death or an inhibition of proliferation.

In order to investigate eventual cytotoxic effects of polyacrylates on cells, a mouse fibroblast cell line (mL929) was employed and analysed after incubation in polymer conditioned medium ([chapter 2.1.1.3](#), p 29) according to ISO British standards 10093- 5 [395]. The cell response was then analysed for changes in morphology, proliferation and viability.

Of the range of polyacrylates tested, none achieved a reactivity grade worse than grade 1 (slight reactivity). The majority of polymers tested were graded level 0 (non-cytotoxic). After incubation in the eluent of most substrates the mL929 appeared healthy and had the typical

morphology as with the negative (unconditioned, non-cytotoxic) control. The only exceptions were found to be ESP 009 and ESP 010, where a larger number of cells appeared to undergo cell death as indicated by the rounded morphology.

It was also found that cell proliferation was generally slowed down with increasing polymer eluant concentration compared to a negative control. However, cell proliferation and PDT were not significantly affected, thus suggesting that the presence of eluant had only a minor influence on cell proliferation and that the polyacrylate substrates did not have a cytotoxic effect on mL929 cells.

In addition to the standard cytotoxicity evaluation, direct substrate contact tests were performed. This did not only allow us to analyse the substrates influence on both the mL929 cell line and more sensitive bovine aorta endothelial (BAE) cell line, they also provided a level of understanding of their biocompatibility and wider potential function as a substrate platform for cell culture [396, 397].

It was found that mL929 cells were proliferative and showed the typical morphology on all substrates with exception of ESP 009 and ESP 010, where a notable number of cells looked rounded and appeared to have difficulties to attach to or maintain attachment on the substrates. In this respect, direct and indirect cytotoxicity analyses coincided with each other. The direct contact method had a greater localised concentration of the biomaterial and therefore a greater and more sensitive impact on cellular behaviour. When comparing indirect and direct cytotoxicity test, the cellular response did not show any notable changes in cell morphology or disruption of the monolayer structure.

On the other hand BAE cells showed differences in cell behaviour. Cell death and detachment was greatest during the direct contact tests on ESP 009 and ESP 010. This confirmed that both substrates were unsuitable culture substrates. However, there was a large initial increase of BAE cell number on ESP 011 and ESP 012, indicating that these substrates are very suitable

for cell culture. Moreover it was found that the BAE cell morphology was notably different between substrates. On ESP 003, ESP 007, ESP 011 and ESP 012 cells were well spread and displayed the characteristic BAE cell morphology, confirming that these substrates would be suitable for cell culture with other sensitive cell lines, such as stem and progenitor cells.

4.3.2 Effect of polyacrylates on mouse kidney-derived stem cells

The mKSC line studied here was isolated from neonatal mouse kidneys by *Fuente-Mora et al.* and has the ability to spontaneously generate podocyte-, mesangial- and proximal tubule-like cells *in vitro*. However, they do not generate distal tubule or collecting duct cells [249, 251]. Moreover, recent research has shown that most kidney stem cells (KSCs) can differentiate *in vitro* not only into a number of renal cells but also into non-renal cells [7, 271, 408]. It would be of great benefit if cell differentiation could be directed in a way that allows large and pure populations of a desired cell type to be obtained, as this would be useful for drug development programmes and various other applications, such as furthering our understanding of (kidney) stem cell differentiation. Moreover, the human equivalent of such cell lines could have potential use in the field of regenerative medicine.

Within this study, mKSC behaviour and differentiation was assessed using four novel polyacrylate substrates: ESP 003, ESP 004, ESP 007 and BTL 15. Therefore, the current study was aimed at identifying polyacrylate substrates that could direct the differentiation of mKSCs into specialised renal cell lines, namely podocytes or PTCs.

The assessment of mKSC behaviour on polyacrylates ESP 003, ESP 004, ESP 007 and BTL 15 showed that cells were viable and proliferating on all substrates. The cell morphology on ESP 007, BTL 15 and glass looked very similar with cells maintaining a mKSC-like morphology. However, we found that about 40 - 45% of the cells cultured on ESP 003 and ESP 004 differentiated into podocytes as evidenced by their large spread, the arborised cytoskeleton and often binuclearity which are typical characteristics of podocytes [250]. Compared to

mature podocytes, a large number of cells on ESP 003 and ESP 004 showed such a distinctive podocyte-like morphology. Considering these morphological changes that were followed and found to be increasingly present with increasing cell culture time on these two substrates our study has shown that these polyacrylates have the ability to direct mKSC differentiation into podocytes to high percentages.

Further interrogation of cells cultured on the remaining two substrates, ESP 007 and BTL 15, has shown that these substrates promoted PTC differentiation as evidenced by megalin immunostaining and alkaline phosphatase activity. Following a 96 h cell culture period, about 35 - 40% of cells on ESP 007 and BTL 15 expressed megalin, which was about 3-fold higher compared to other substrates, including controls. The number of megalin expressing cells was similar to the number of cells that stained positively for F-BSA (50% of cells on ESP 007; 40% of cells on BTL 15). Therefore, our results also prove that ESP 007 and BTL 15 promoted cell differentiation into functional PTCs.

However, although we have shown cell differentiation into PTC and podocytes, we did not detect significant difference in gene expression of mKSCs. It should be noted that gene expression is controlled by a number of factors, including transcriptional and post-transcriptional regulation (such as RNA processing, splicing and translation) [409-411]. The half-life of various proteins can range from minutes to days and is therefore often larger than the degradation rate of mRNAs. Moreover, the rate of mRNA transcription is lower than the rate of protein translation [412]. Furthermore, protein concentration itself is influenced by various parameters, such as synthesis and cleavage. Therefore it is possible to have low mRNA expression but high concentration of protein, i.e. if a protein directly influences its own expression [413].

However, we have shown by assessment of morphological features, protein expression and functionality studies as well as enzyme activity studies (alkaline phosphatase) that mKSCs indeed differentiated to significant percentages into the desired renal cell types compared to controls. A possible explanation of these findings lies in the polyacrylates structure and physicochemical features as all of these differed nano- and microscale topography, associated wettability and surface chemistry as caused by the identity and proportion of functional group chemistries. In addition, three substrates, ESP 003, ESP 004 and ESP 007 mimicked the RGD binding motif, but appeared to have a different effect on cell differentiation. BTL 15 on the other hand mimicked a cell attachment motif from collagen (particular motif is company proprietary). However, ESP 007 and BTL 15 directed mKSC differentiation into PTCs. Both these substrates had two characteristics in common: (1) they contained hydroxyl groups alongside carboxylic acid and primary amine groups and (2) they had a lower degree of nanoroughness of about 4 ± 1.5 nm compared to the other substrates. Both these properties might have promoted cell differentiation into PTCs. Interestingly, the analyses of surface artefacts, hill heights, respectively, showed that ESP 007 had small hills in the range of about 100 nm whereas BTL 15 contained hills that reached up to 1.5 μ m.

Compared to ESP 007 and BTL 15, ESP 003 and ESP 004 contained (1) carboxylic acid and primary amine functional groups, but no hydroxyl groups and (2) higher nanoroughness (10 ± 2.5 nm). The hill heights of both levelled around 300 nm. These results suggested that cell differentiation might be influenced by the nanoscale roughness of a substrate in addition to the presence of specific surface functional group chemistries and it is assumed that also the spatial distribution and stereochemistry had an impact on cell differentiation, whereas hill height did not appear to have significant impact on it ([Figure 4.36](#)).

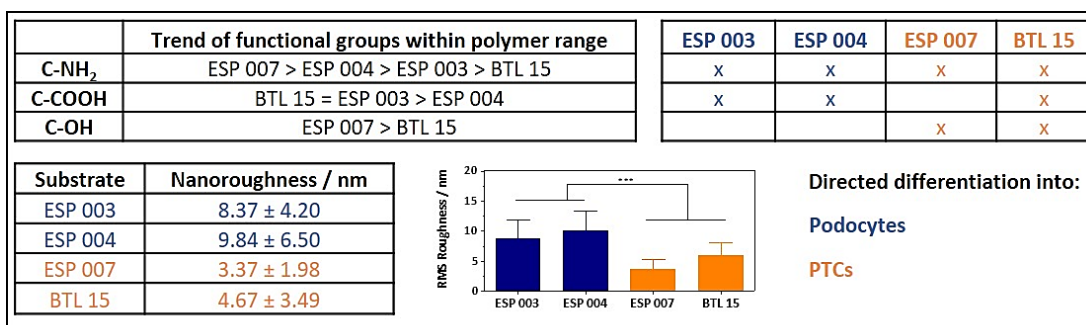


Figure 4.36: Correlation between polyacrylate surface properties and mKSC differentiation.

However, we assume that surface topography presented a relevant cue for initiating cell differentiation. As discussed before ([chapter 3.2.3.1](#), p 73) we here suggest that our surfaces may present a particular distribution of these hill like-structures that we refer to as “organised disorder” assuming that, within individual polymers, there may be a repetition of the pattern of such surface artefacts and this may in turn be another reason for promoted differentiation. Therefore it would be interesting to study this phenomenon further.

The impact of surface topography on cell behaviour and differentiation has been shown in numerous studies and many of these studies investigated the effects of ordered versus disordered topographical features [42-44, 414]. For example, ordered topographical patterns inhibited cell adhesion of fibroblasts to underlying substrates [415], whereas disordered nanoscale topography increased promoted cell adhesion and differentiation of i.e. MSCs [42, 416]. Particularly in the case of MSCs it was found that cell differentiation is favoured on disordered surface topography [42]. However, the nanotopographies present within stem cell niches are not highly ordered, but rather disordered and this makes it difficult to perfectly design biomaterial topography [414, 417]. Consequently more research is now focussing on developing surfaces with such controllable disorder and some progress has been made: For example, *Dalby et al.* have developed topographies displaying controlled disorder using electron beam lithography and found that these substrates promoted differentiation of MSCs

into osteocytes in much higher percentage compared to highly ordered and random nanoscale features [42].

Moreover the combinatory effects of nano- and microscale topography have to be considered as a possible effect on cell differentiation. For example, *Gittens et al.* have developed surfaces with micron- and submicron-scale surface roughness and found synergistic effects of micro and nanoscale hybrid structures on osteoblast activity and differentiation [24, 71]. Also other groups have suggested that cells do not only alter their cell behaviour in response to micro, but also nano topography by i.e. aligning along presented topographies of a cell culture surface [418, 419].

It has to be noted that substrate XPS and AFM analyses were performed in dry, and in the case of XPS under ultra-high vacuum conditions whereas biological experiments were performed in liquid (cell culture medium). This may have very likely altered the substrate properties, such as the direction of surface functional group chemistries. Therefore, in the case of this study, it is challenging to draw final conclusions about the influence of chemical functionalities on cell behaviour [420, 421].

To summarise our findings, all four substrates had significant effects on mKSC differentiation into podocytes or PTCs compared to glass and TCP controls. However, it is challenging to correlate only one surface feature to the particular cellular response. The available results suggested that surface chemistry and nanotopography were the key factors for regulating mKSC differentiation. However, the best way to verify that would be to develop substrates that only differ in a single parameter and compare results with cells. In addition, the polymer surface steric properties of the mimicked cell binding motifs were of great importance in this study, but a method to precisely determine the “true” conformation and steric properties of functional groups could not be identified as no methods with higher sensitivity in atomic scale were available.

Lastly it has to be noted that some recent research has explored the ability of some of the polyacrylate substrates studied here to induced differentiation of mKSCs into chondrocytes under appropriate cell culture conditions [13, 345] and ESP 004 in particular was found to induce chondrogenesis. These findings were not observed within this study, which could be due to the fact that in the chondrogenesis study, mKSCs were seeded at a higher density (1×10^4 cells / coverslip) and kept in culture for a longer time period (14 days).

4.3.3 Effect of polyacrylates on conditionally immortalised renal cell lines

Prior to investigating the differentiation potential of human putative kidney-derived progenitor cells (KPCs), conditionally immortalised renal cell lines were used to identify substrates that could support their growth and differentiation. The reason for doing this was because it was reasoned that substrates that were unable to support the growth of conditionally immortalised human renal cells would be unlikely to support the growth and differentiation of human KPCs. This approach would therefore enable us to exclude some substrates from subsequent experiments.

Within this study two conditionally immortalised cell lines were used: PTCs (ciPTCs) and podocytes (ciPodocytes). Both cell lines proliferated in cell culture at the permissive temperature of 33°C and differentiated at the nonpermissive temperature of 37°C.

ciPodocytes were obtained from *Saleem et al.* [227, 422]. At the permissive temperature (33°C) the cells proliferated and showed a small surface area and a low cytoplasmic : nuclear ratio [227, 422]. Therefore, cells behaved as expected on most polyacrylates. ESP 009 and ESP 010 were the only exceptions as cell number decreased over time and cells appeared to undergo cell death.

ciPTCs were obtained from *Masereeuw et al.* [246, 423]. Also ciPTCs proliferated on all substrates with ESP 009 and ESP 010 being the only exceptions. As with ciPodocytes, ciPTCs

cell number decreased over time and cells appeared to undergo cell death on these substrates.

The substrates used for mKSC culture, ESP 003, ESP 004, ESP 007 and BTL 15, allowed good cell attachment and proliferation of both conditionally immortalised cell types. However, three further substrates that were developed within this study, ESP 008, ESP 011 and ESP 012, were also able to support the growth of the cell lines. ESP 011 and ESP 012 contained hydroxyl groups, which were also present in ESP 007 and BTL 15 and were assumed to be a potential feature to direct mKSC differentiation into PTCs. Considering that ESP 011 and ESP 012 also allowed cell attachment and growth of mL929 and BAE cells it is assumed that the chemical and physical properties would also support further studies on human kidney derived progenitor cells. Both substrates were shown to allow the development of characteristic features, including morphology and protein expression of conditionally immortalised cell lines and were therefore classified as substrates with potential use in the field of biomaterial science to influence (progenitor / stem) cell fate.

All substrates had different physicochemical properties with the main difference being the particular mimicked cell binding motif and the proportion and identity of surface functional groups. However, generally it was noted that all cell lines investigated on ESP 008, ESP 009 and ESP 010 showed notably different behaviour compared to all other substrates. This included a small and rounded cell morphology, cell detachment from surfaces and presumable cell death. From a topographical point of view, surface hill features showed an intermediate height when compared to other substrates and surface root mean square (RMS) roughness of these three polyacrylates was also comparable to other substrates. Therefore, topography can be excluded as a cell growth inhibiting factor. However, all three substrates had in common that they (1) had the lowest degree of steric hindrance and (2) contained more primary amine groups compared to the remaining polyacrylates and had

therefore a significantly lower CA (sessile drop). It is well known that surface amines have a substantial influence on cell behaviour including improvement and prevention of cell attachment and this might be in turn related to the surface's ability to adsorb proteins. Therefore, the identity or conformation of amine groups might have influenced the polymer's ability to adsorb proteins and therefore cell adhesion. CB and DCA measurements have shown that all substrates had an equal CA after exposure to FBS, which indicated protein adsorption. However, this did not give information about protein identity, their molecular state nor accessibility of single functional groups.

A number of studies has been focussed on studying such phenomena. For example, *Broderick et al.* has shown that the small hydrophobic n-decylamine promoted cell adhesion of fibroblasts, whereas the hydrophilic amine-containing carbohydrate D-glucamine inhibited it [424]. They suggested that this effect is partially caused by the ability of the substrates / molecules to promote or prevent protein adsorption [425]. Such an effect might have influenced the results presented within this study as well.

Another potential cause for the cell response to biomaterial substrates in this study could be that neighbouring sterically hindering groups covered primary amines and therefore made them inaccessible for cells. The design of the polyacrylate structure was done manually and, so far, there is a possibility that the polymers were not behaving as expected due to unforeseen inter- and intramolecular interactions. Therefore, possible conformational changes could have arisen from and influenced cell behaviour. For instance, ESP 004 and ESP 007 both mimicked the RGD motif with the difference being the composition and identity of the functional groups (both contained primary amines, but ESP 004 contained –COOH groups whereas ESP 007 –OH groups). However, ESP 004 directed mKSC differentiation into podocytes and ESP 007 into PTCs.

4.3.4 Effect of polyacrylates on putative human kidney progenitor cells

The kidney has a high potential to regenerate and repair itself to a certain extent after injury [426]. However, the origin of cells that contribute to renal repair has not been identified yet and the debate about whether there are in fact progenitor cells in the kidney has been going on for many years (chapter 1.3, p 15).

In recent years a number of putative human kidney progenitor cells has been isolated that displayed stem cell properties, including self-renewal, clonogenicity, multidifferentiation potential and expression of specific markers with particular focus on CD133 and CD24 (chapter 1.3.4, p 22) [5-7]. CD133 is a stem cell marker in normal and also cancerous tissues [427] and is already used to identify and isolate putative stem cells, sometimes in combination with other markers and from other tissues, such as bone marrow or brain [427-429]. CD24 is a protein that is expressed within immature cells and generally absent from mature, fully differentiated cells and was shown to be present in putative renal progenitors [430, 431].

Here we investigated the potential of polyacrylates to influence proliferation, spreading and differentiation of these CD24⁺/CD133⁺ putative human kidney-derived progenitor cells (KPCs). Two cell lines, fetal and infant KPCs (fKPCs / iKPCs) were sorted to be either CD24⁺/CD133⁺ (double positive, DP) or CD24⁻/CD133⁻ (double negative, DN). Based on the obtained results on polyacrylates so far, three substrates were chosen: ESP 003, as is directed differentiation of mKSCs into podocytes, ESP 007, as it directed differentiation of mKSCs into PTCs and ESP 011, as it supported the growth and differentiation of conditionally immortalised cell lines and was moreover designed to mimic the promising features from ESP 007 with little structural and chemical differences.

Both, fKPCs and iKPCs DN populations, showed similarities in that, they were stable in culture on polyacrylates and controls. Their proliferation rate was very similar with a PDT of about 50-55 h on all substrates, including controls.

Within the DN fKPC population about 25% were CD13⁺ (PTCs) with only 2% being functional, whereas iKPCs contained 90% CD13⁺ cells (PTCs) with about 40% being functional on polyacrylate substrates and 80% on controls. These results indicated that polyacrylates did not support the growth of PTCs that displayed characteristic marker expression and functionality. Particularly the DN iKPCs showed a significant decrease in functionality when cells were cultured on substrates (40%) compared to a glass control (80%). However, in general, iKPCs contained more functional PTCs (CD 13⁺) than the fKPCs population, which might be due to the fact that infant kidneys are more mature than fetal ones.

If one considers the DP cells as kidney progenitor cells, than it could be that the DN population is a mixture of various kidney cells that might therefore contain differentiated and mature cells, including podocytes and PTCs [403]. However, a problem with such primary cells is that they often do not display characteristic biochemical and transport properties *in vitro* [232]. This could be contributing to the high number of non-functional PTCs (CD13⁺/F-BSA⁻). In addition, recent research has indicated that also podocytes are able to uptake albumin, which might have contributed to the number of F-BSA⁺ / CD13⁻ cells [432, 433].

Compared to DN cells, DP KPCs did show different behaviour on substrates and controls. DP fKPC proliferation and viability was slow with a population doubling time (PDT) of about 100 h. However, these cells showed increased cell spreading with time. On the other hand, the infant DP cells showed an increase in proliferation and a PDT of 60 h, which was significantly higher compared to fKPCs. iKPCs on the other hand did not increase cell spreading over time. Both DP populations contained about 70-80% PTCs with 20% of these showing functionality on polyacrylates, and 40% functionality on controls. This indicated that polyacrylates did not

support the differentiation of putative KPCs into PTCs as no significant increase of CD13⁺ was detected. Particularly the DN iKPCs showed a decrease in functionality (the ability to uptake F-BSA) when cells were cultured on substrates (40%) compared to a glass control (80%).

Lastly, KPCs were analysed for expression of CD133 and CD24 after the cell culture period. As expected, both DN populations remained DN over the cell culture period. However, DP cells were found to lose these markers during cell culture on substrates and controls. It has to be noted that the cells used in this study were only sorted to be DP or DN after isolation from tissues (passage 1) and then expanded. Therefore, cells analysed on substrates were considerably late passages (P7-P10) and were not repeatedly assessed for expression of these markers during expansion. However, as discussed before, there is still a debate whether CD24⁺ / CD133⁺ cells are in fact progenitor cells and the above data also do not support the progenitor cell potential. A number of recent studies have suggested isolating KPCs based on other markers including CD34, c-Kit, CD90, CD105 EpCAM (CD326) [267]. It would be worth investigating these cells on polyacrylates in the future, as the substrates had great potential in terms of directing the differentiation of mKSCs and MSCs [13, 345]. As the results on KPCs were not promising, no further experiments were performed.

In summary, there were differences in the general behaviour of DP and DN KPCs with respect to proliferation and spreading. However, polyacrylates did not promote KPC differentiation. All KPCs populations contained a consistent number of PTCs with some of them being functional. However, polyacrylates appeared to inhibit the functionality of the differentiated cells significantly compared to glass and TCP control.

4.4 Conclusions

This chapter comprised the analyses of polyacrylates in order to identify suitable substrates for cell culture and cell differentiation. A large number of polyacrylate substrates was found to support cell culture (ESP 003, ESP 004, ESP 007, ESP 011, ESP 012 and BTL 15). These showed biocompatibility and supported growth and differentiation of conditionally immortalised cell lines. Three substrates (ESP 008, ESP 009, ESP 010) were excluded from (progenitor / stem) cell analyses as they did not support cell growth and attachment.

Moreover, two substrates were identified, that promoted the differentiation of mKSCs: ESP 007 promoted differentiation into functional PTCs (40% 96 h post seeding) and ESP 003 promoted differentiation into podocytes (40%, 96 h post seeding). Following these results, ESP 003, ESP 007 and its structural equivalent ESP 011 were analysed for their capability to promote the differentiation of putative human kidney progenitor cells (KPC). The results did not suggest KPC differentiation. It is not clear if the cells did not differentiate into committed cell lineages because of the inability of polyacrylates to influence their differentiation, or if the cells were actually not progenitors after all. However, polyacrylates did have an effect on mKSCs differentiation and were shown in the past to promote the differentiation of MSCs. Therefore, polyacrylates are certainly substrates that deserve attention in terms of stem cell culture and differentiation in the future. As ESP 003 and ESP 007 had a significant impact on mKSC differentiation these would be worth to be investigated in order to promote the differentiation of true human renal progenitor cells. Potential candidates are cells that have recently been isolated from pre-term neonates [434], but also pluripotent (embryonic and induced) stem cells [435-437].

4.5 Supplementary information

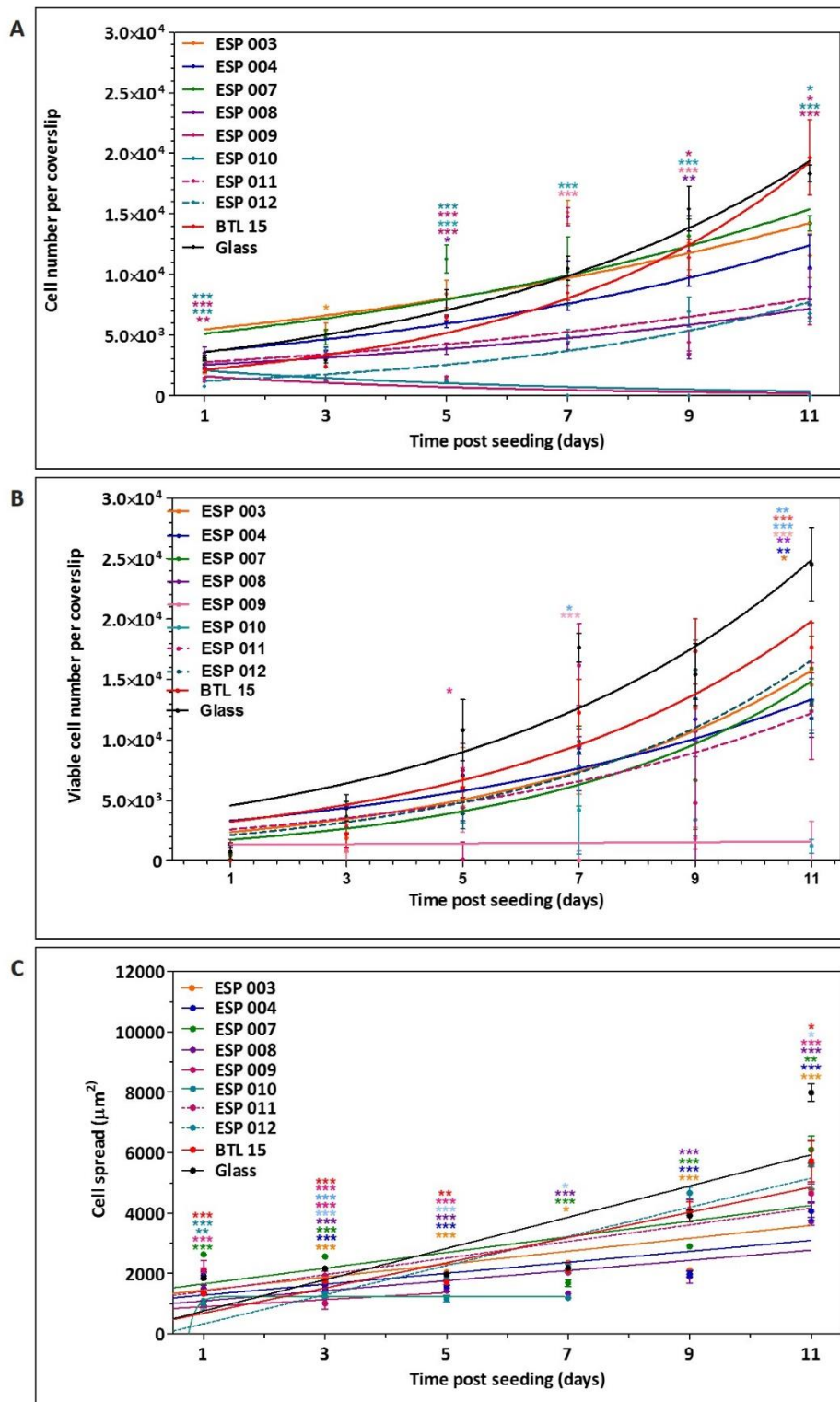


Figure 4.37: ciPodocytes analyses on polyacrylate substrates. (A) Cell proliferation (B) cell viability and (C) cell spread followed over 11 days. ciPodocytes were seeded at 1×10^3 cells / polymer coated 13 mm coverslip and cultured for 6 days at 33°C and subsequently 5 days at 37°C . Data were fitted with an exponential growth equation. Results represent the mean of three biological replicates \pm SEM.

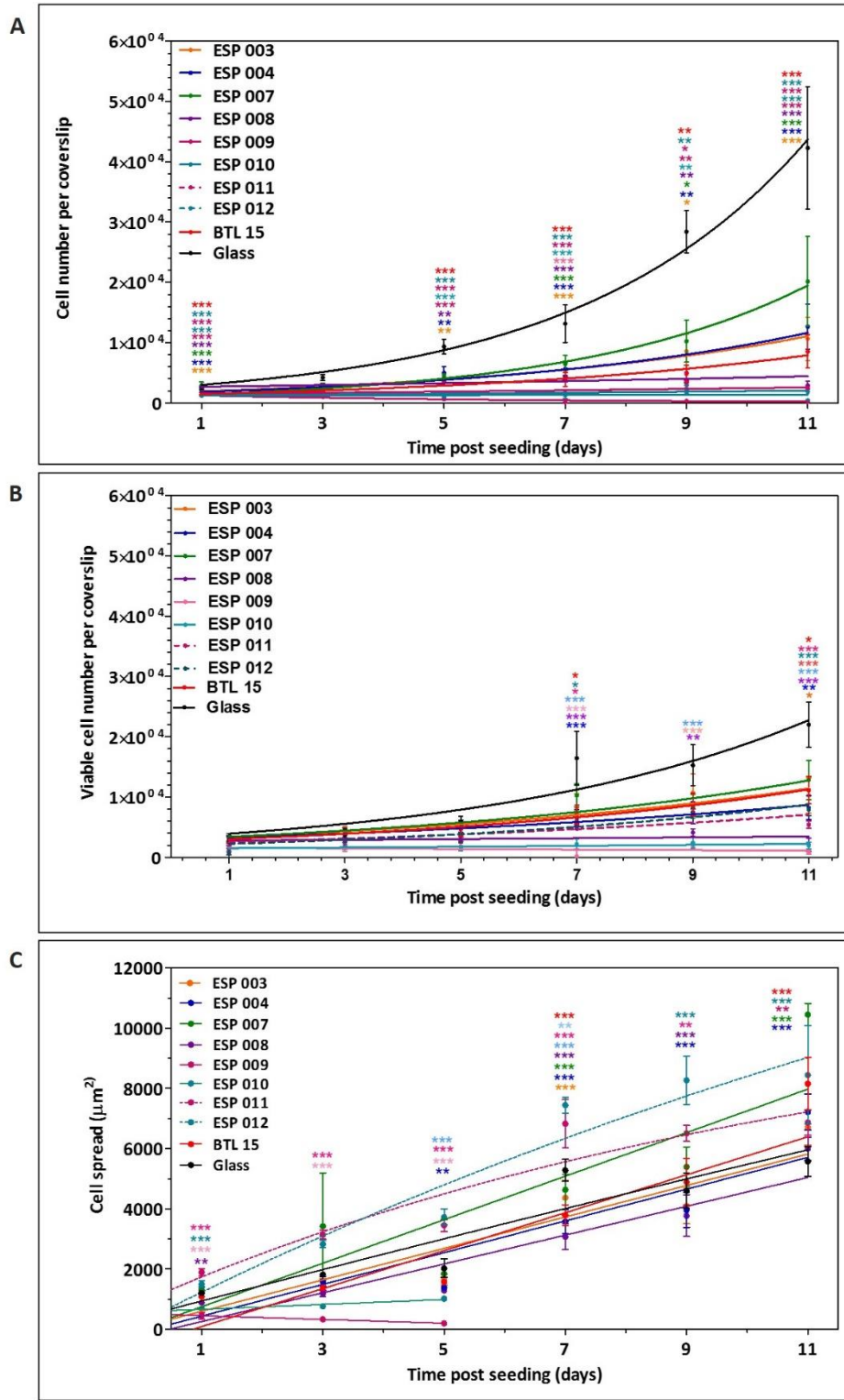


Figure 4.38: ciPTC analyses on polyacrylate substrates. (A) Cell proliferation (B) cell viability and (C) cell spread followed over 11 days. ciPTCs were seeded at 1×10^3 cells / polymer coated 13 mm coverslip and cultured for 6 days at 33°C and subsequently 5 days at 37°C . Data were fitted with an exponential growth equation. Results represent the mean of three biological replicates \pm SEM.

5 Physicochemical characterisation of plasma polymer coatings

5.1 Introduction

Plasma polymerisation is based on the ionisation of a monomeric compound under high pressure, resulting in the development of chemically reactive species that combine to form solid polymers [438, 439]. During ionisation, atoms or molecules acquire a positive or negative charge due to the gain or loss of electrons, which causes the formation of ions. Free electrons gain energy from the surrounding electric field and lose it through collisions with other molecules. The dynamic within the gas is determined by Coulomb (electrostatic) interactions between charged particles [440]. The developing gases can be weakly (small fractions of charged particles) or strongly ionised. Ideally, the sum of all positive and negative charges would be neutral (quasineutral state) [441]. Therefore a plasma can be described as an ionised, quasi-neutral gas and is composed of different particles / molecules, such as electrons, ions or photons [442]. The resulting polymer layers can be very complex with some fragments being short whereas others might form large, crosslinked and highly branched chains [443]. Although it was proposed that modification of plasma deposition parameters, such as temperature, monomer flow rate and input power can influence its composition [444-446], the films remain heterogeneous, not well defined layers and the underlying inter- and intramolecular processes are complex. However, the exact processes of plasma polymer formation are complex process and are not fully understood yet [438, 447-449].

A schematic set up of a plasma polymerisation unit is shown in [Figure 5.1 A](#). Substrates in this study were coated using a custom build gradientiser ([Figure 5.1 C](#)). The entire polymerisation process occurs within a reaction chamber, in which any solid support can be entirely coated with a plasma polymer [450]. An advantage of plasma polymerisation is that very thin films

can be deposited on a large number of materials using a fast, solvent free and simple one-step coating procedure [451]. Moreover, a high variety of surface treatments is now available that allow modification of plasma physicochemical properties, such as wettability, topography or even functionalisation of the plasma with chemical groups or biological molecules [452-454]. This has led to novel developments in different scientific areas, including composite materials, membranes, protective coatings, dielectric films as well as biomaterials and biomedical applications [455-464].

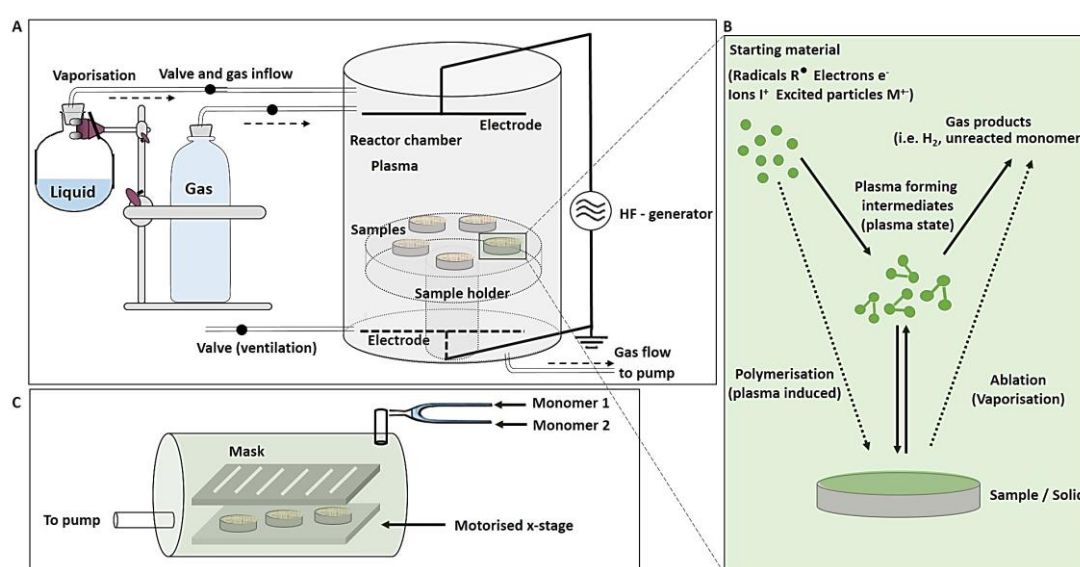


Figure 5.1: (A) Simplified schematic diagram of the Bell plasma reactor (static type). The monomeric substance (liquid or gas) is led through the system and is cooled down with liquid nitrogen before it enters the reaction chamber, a cylindrical tube. Internal electrodes put the monomer into a plasma state that is composed of a variety of chemical species. The developing polymers then form crosslinked and branched chains and attach to solid surfaces (including substrates). The temperature and pressure inside can be precisely regulated (B) Schematic of the plasma polymerisation process. Plasma polymerisation can occur plasma induced (free-radical induced polymerisation of molecule with C-C double bonds) or through plasma state polymerisation (depends on presence of other reactive species in the plasma). The result is a polymer layer on solid surfaces. (C) Gradientiser.

Nitrogen rich precursors are of great interest in the field of plasma polymerisation as they lead to the formation of a number of nitrogen based functional groups, including primary amines [465-467]. These films can be deposited using (1) a nitrogen based gas, i.e. allylamine or propyl amine [459, 468-470] or (2) a gaseous mixture of an amine containing gas and hydrocarbons i.e. ammonia [466, 468, 471]. For example, allylamine (AA) that is used in this study, is a frequently used plasma precursor as it contains besides an amine also a vinyl group

which is advantageous for the initiation of the polymerisation [302, 456, 468, 472, 473]. The plasma films are stable under different conditions, including high salt concentration and temperature [470].

Here we investigated the physicochemical properties of glass cover slips coated either with 100% AA or 100% OD (homopolymers) or with copolymers (1) 75% AA / 25% OD (2) 50% AA / 50% OD and (3) 25% AA / 75% OD. These will be referred to as 0% AA, 25% AA, 50% AA, 75% AA and 100% AA through the course of this study (Figure 5.2)¹ [474]. The stability of AA films in aqueous solution can be increased through crosslinking with octadiene (OD) in which functional groups will be retained [473, 475, 476]. Additionally, substrates that showed a gradual increase of AA concentration across the substrate¹, were investigated (Figure 5.2) [58, 277, 477]. Such gradients allow high-throughput screening of cells on a large variety of physicochemical data points which may allow the optimal surface properties for a particular cell type to be identified. This would also circumvent the need for testing large numbers of different, homogeneous substrates in order to find the optimal properties in the future [478]. All substrates used in this study were coated under employment of a custom-built gradientiser (Figure 5.1 C).

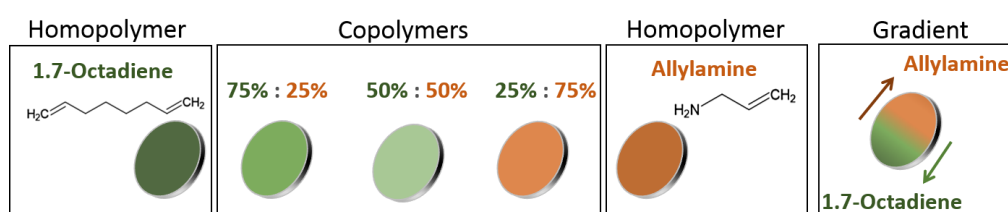


Figure 5.2: List of plasma polymers analysed during the course of this study.

Aims of this chapter

To perform a thorough physicochemical analyses of plasma polymer layers.

¹ All plasma polymer coated substrates were provided by collaborators of the University of South Australia, Adelaide.

5.2 Results

5.2.1 Characterisation of surface chemistry

5.2.1.1 Surface characterisation using X-Ray Photoelectron Spectroscopy

Plasma polymer coated glass cover slips were analysed using X-Ray photoelectron spectroscopy (XPS) in order to determine the surface elemental composition and the binding states of these elements within the surface. As the substrates were composed of allylamine (AA) and 1,7-octadiene (OD), carbon and nitrogen were expected. However, as the substrates have undergone surface oxidation once in contact with air, oxygen was present on the surfaces and therefore included in the analyses [479]. [Figure 5.3](#) shows the elemental composition of homo- (100% AA, 100% OD) and copolymers (75% AA, 50% AA, 25% AA) and [Figure 5.4](#) the gradient substrates. The 100% AA plasma coated substrates contained about 30% oxygen components on the substrate surface. This percentage was slightly decreasing with increasing OD concentration. The O/C ratio showed a linear correlation of an increased amount of oxygen species with increasing AA concentration for homo and copolymers ($R^2 = 0.8898$, $p < 0.001$) as well as for gradients ($R^2 = 0.7591$, $p < 0.001$). A further analyses (binding states) of oxygen species was not performed.

As expected, all substrates showed an increase of surface nitrogen species with increasing AA concentration. This was confirmed by survey spectra and high resolution nitrogen spectra ([Figure 5.3](#) and [Figure 5.4](#)) that showed an increase of nitrogen with increasing AA concentration. Also here a linear correlation was found for homo- and copolymers ($R^2 = 0.8898$, $p < 0.001$) and for gradients ($R^2 = 0.9672$, $p < 0.001$). The corresponding values are listed in [Table 5.1](#) (homo- and copolymers) and [Table 5.2](#) (gradient).

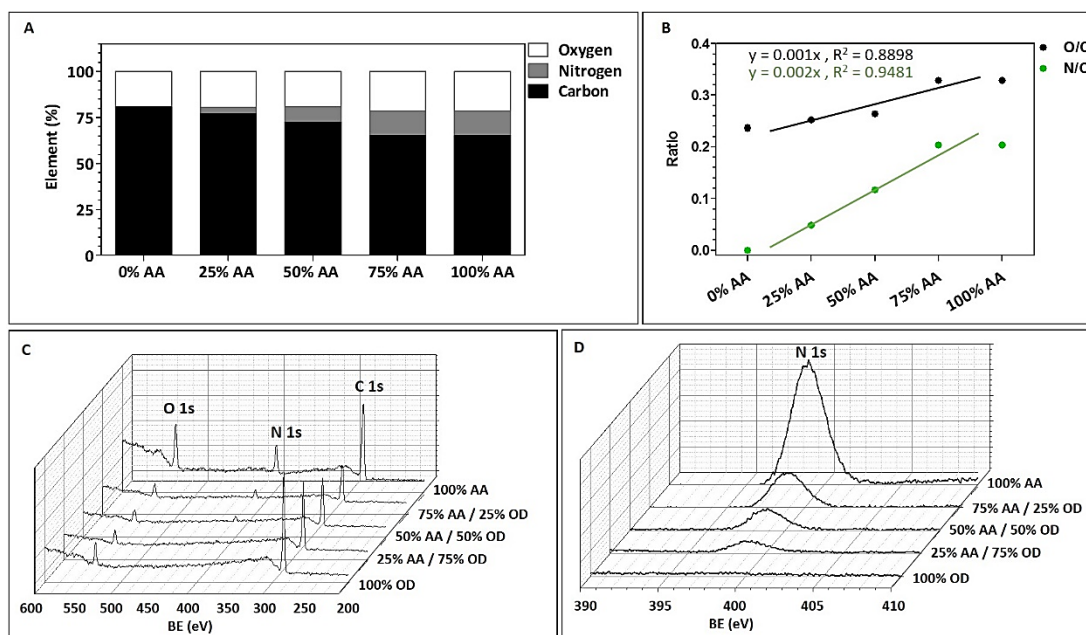


Figure 5.3: (A) Quantification of the elemental composition of plasma polymer coated homo- and copolymers (B) Ratio of oxygen/carbon (O/C) and nitrogen/carbon (N/C). Survey (C) and (D) high resolution N1s peak spectra show changes of the elemental composition with increasing AA content.

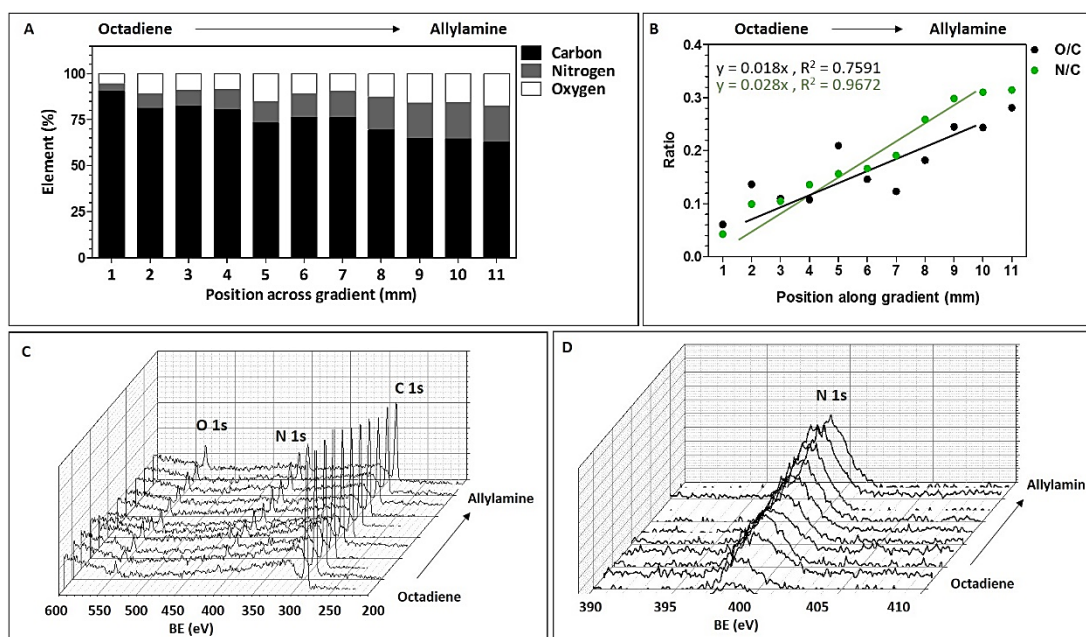


Figure 5.4: (A) Quantification of the elemental composition of plasma polymer gradients (B) Ratio of oxygen/carbon (O/C) and nitrogen/carbon (N/C). Survey (C) and (D) high resolution N1s peak spectra show changes of the elemental composition with increasing AA content.

Table 5.1: Elemental surface composition of homo- and copolymers. Shown is the elemental percentage of carbon, oxygen and nitrogen as well as the O/C and N/C ratios to allow a compare between substrates. All data were obtained via analyses of the survey spectra.

	Element			Ratio	
	Carbon (%)	Nitrogen (%)	Oxygen (%)	N (%) / C (%)	O (%) / C (%)
100% AA	52.61	17.83	29.56	0.34	0.56
75% AA	65.29	13.26	21.45	0.20	0.33
50% AA	72.46	8.427	19.11	0.12	0.26
25% AA	76.91	3.716	19.38	0.05	0.25
100% OD	80.88		19.12		0.68

Table 5.2: Elemental surface composition of plasma polymer gradients. Shown is the elemental percentage of carbon, oxygen and nitrogen as well as the O/C and N/C ratios to allow a compare between substrates. All data were obtained via analyses of the survey spectra.

	Element			Ratio	
	Carbon (%)	Nitrogen (%)	Oxygen (%)	N (%) / C (%)	O (%) / C (%)
1 mm (AA)	62.67	19.72	17.61	0.31	0.28
2 mm	64.34	19.98	15.68	0.31	0.24
3 mm	64.78	19.34	15.88	0.30	0.25
4 mm	69.39	17.98	12.63	0.26	0.18
5 mm	76.10	14.53	9.37	0.19	0.12
6 mm	76.20	12.67	11.13	0.17	0.15
7 mm	73.19	11.46	15.35	0.16	0.21
8 mm	80.40	10.93	8.66	0.14	0.11
9 mm	82.35	8.61	9.04	0.10	0.11
10 mm	80.94	8.02	11.04	0.10	0.14
11 mm (OD)	90.64	3.84	5.52	0.04	0.06

Further analyses of the high resolution C1s peaks allowed quantification of the elemental binding states within the plasma layers. [Figure 5.5](#) shows the C1s peak composition of homo- and copolymers and [Figure 5.6](#) of the gradient. The corresponding values can be found in [Table 5.3](#) and [Table 5.4](#). The results showed an increasing amount of C-N, C-O bonds with increasing AA concentration. The determination of the (C-N, C-O) / (C-C, C-H) bond ratio allowed a compare of the nitrogen concentration between substrates and confirmed an increase of nitrogen (C-N bonds) with an increase of AA ([Figure 5.5](#) and [Figure 5.6](#)). As expected, a linear correlation was found showing R² of 0.833 for homo- and copolymer and

0.9928 for gradients ($p < 0.001$). High resolution O1s and N1s peaks were not further analysed.

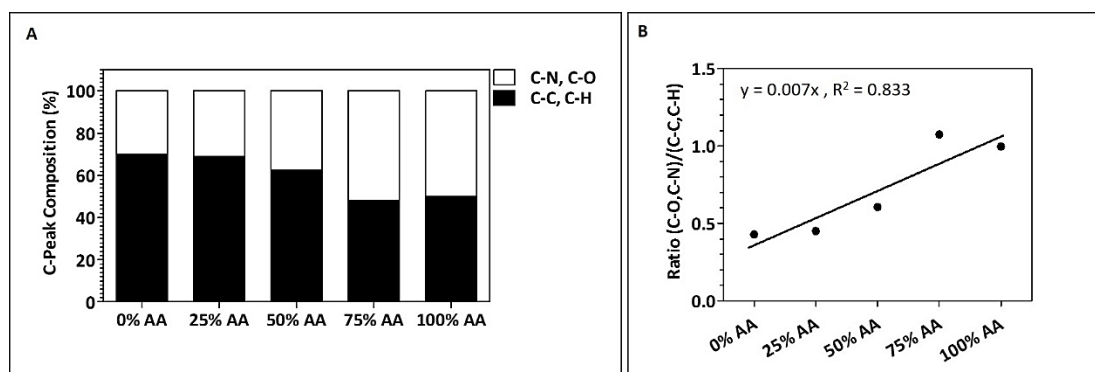


Figure 5.5: (A) C1s peak composition of homo- and copolymers. The proportion of binding states was quantified. All data were obtained by curve fitting analyses of C1s high resolution peaks. (B) Ratio of C-O, C-N / C-C, C-H.

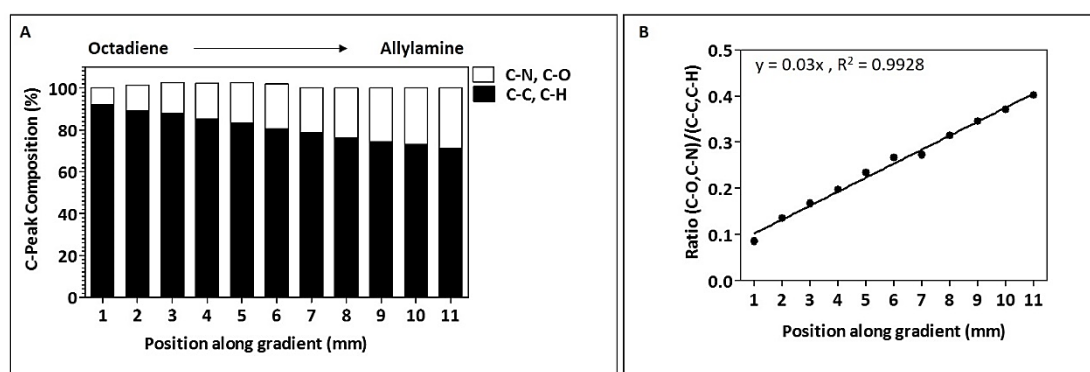


Figure 5.6: C1s peak composition of the gradient. The proportion of binding states was quantified. All data were obtained by curve fitting analyses of C1s high resolution peaks. (B) Ratio of C-O, C-N / C-C, C-H.

Table 5.3: C1s peak composition of homo- and copolymers. All data were obtained by curve fitting analyses of C1s high resolution peaks.

	Carbon C1s		Ratio
	C-C, C-H (%)	C-O, C-N (%)	C-O, C-N / C-C, C-H
100% AA	50.08	49.92	0.99
75% AA	48.23	51.77	1.07
50% AA	62.27	37.63	0.60
25% AA	68.96	31.04	0.45
100% OD	70.02	29.98	0.43

Table 5.4: C1s peak composition on gradients. All data were obtained by curve fitting analyses of C1s high resolution peak.

	Carbon C1s		Ratio
	C-C, C-H (%)	C-O, C-N (%)	C-O, C-N / C-C, C-H
1 mm (AA)	71.28	28.72	0.40
2 mm	72.90	27.10	0.37
3 mm	74.30	25.70	0.35
4 mm	76.08	23.92	0.31
5 mm	78.53	21.47	0.27
6 mm	80.54	19.46	0.24
7 mm	83.15	16.85	0.20
8 mm	85.28	14.72	0.17
9 mm	87.89	12.11	0.14
10 mm	89.09	10.91	0.12
11 mm (OD)	92.13	7.87	0.09

5.2.1.2 Colorimetric quantification of primary amine groups

The primary amine density was quantified via colorimetry using two commonly used dyes: the large, bivalent Coomassie Brilliant Blue (CBB) and the small, monovalent Orange 2 ([chapter 2.2.3.1](#), p 37). The results showed about $1.5 \times 10^4 \pm 0.5 \times 10^4$ primary amine groups / μm^2 on 100% AA coated substrates which was decreasing with increasing OD content. A 25% increase of OD concentration caused a decrease of about 0.5×10^4 primary amine groups / μm^2 . This trend was consistent regardless of the dye used ([Figure 5.7](#)). Interestingly the Orange 2 method showed, compared to the CBB method, a lower amount of primary amines on the 100% OD samples, whereas the CBB method did not show the presence of any amine groups. However, the presence of such small primary amine groups on the OD samples can be treated as a random error which can occur due to inherently unpredictable fluctuations during measurement / instrumental readings.

As expected, the results showed a linear correlation of primary amine increase with an increase of AA concentration. The linear regression ([Figure 5.7](#)) showed a Pearson coefficient of $R^2 = 0.8168$ ($p < 0.001$) for the CBB method and was slightly lower for the Orange 2 method

($R^2 = 0.6471$, $p < 0.001$). As for quantification the entire substrate has to be measured, it was not possible to quantify primary amines/ pm^2 on gradients.

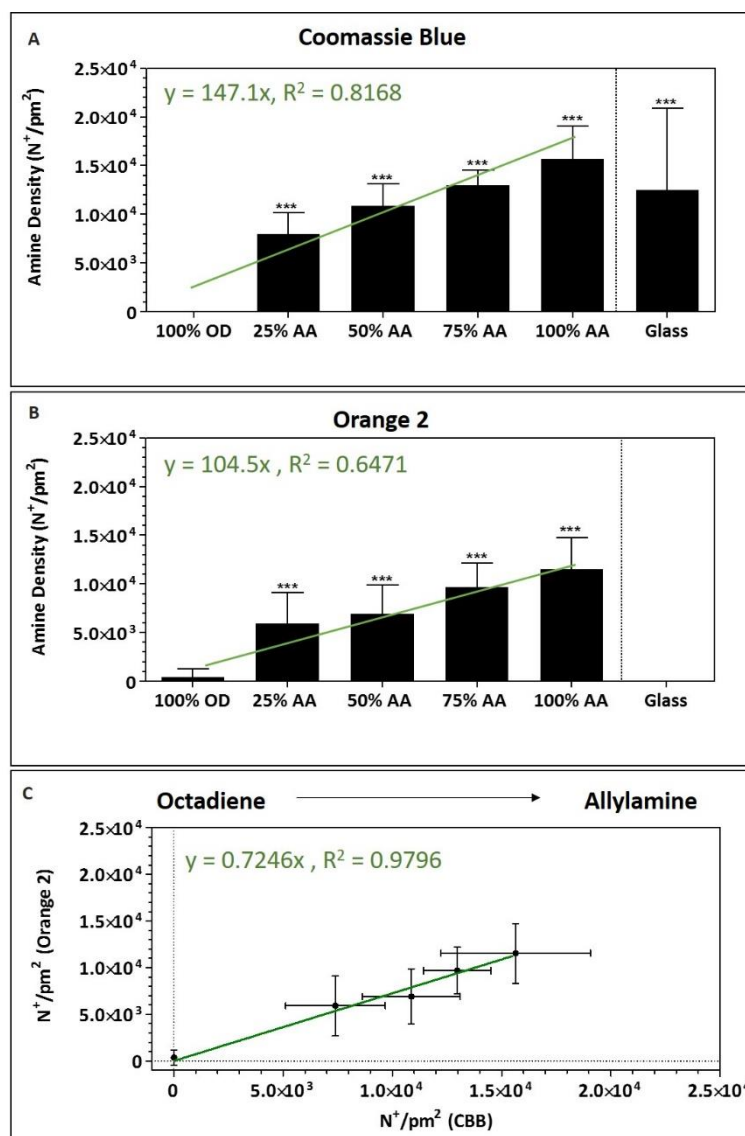


Figure 5.7: Surface primary amine quantification. (A) Coomassie Blue (CBB) method (B) Orange 2 method and (C) Correlation between CBB and Orange 2 method.

The amount of primary amines detected by the CBB and Orange 2 method was then correlated by plotting the amine densities against one another (Figure 5.7 C). Both methods revealed a similar amount of primary amines with a nearly ideal ($R^2 = 1$) Pearson coefficient ($R^2 = 0.9796$, $p < 0.001$).

The colorimetrically determined primary amine densities were also correlated with the amine content that was obtained from XPS analyses (nitrogen / carbon ratio) (Figure 5.8). Both showed a correlation in that, with increasing AA concentration there was an increase in primary amine density ($R^2 = 0.72$, CBB and $R^2 = 0.58$, Orange 2).

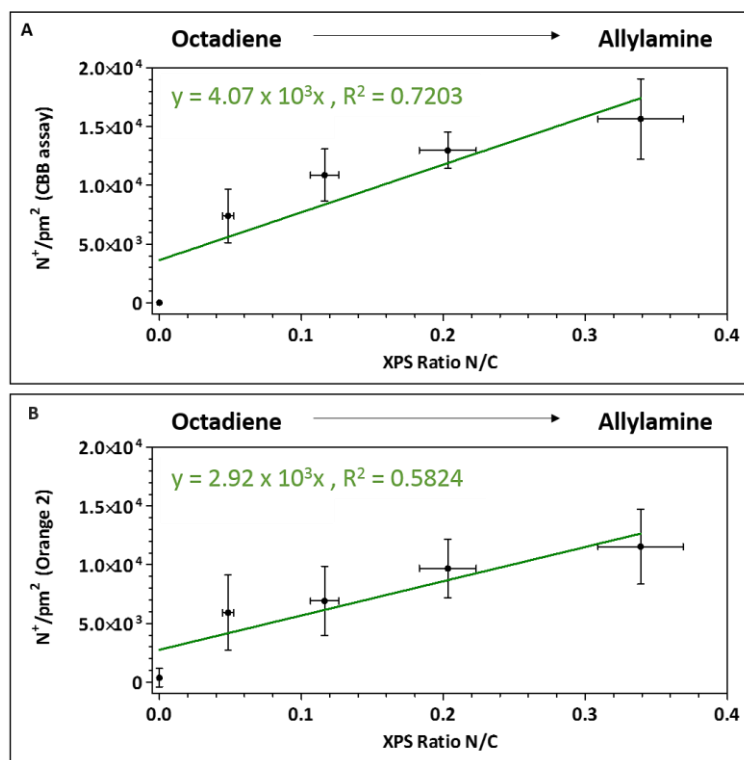


Figure 5.8: Correlation between XPS (N/C ratio) amine group quantification and (A) amine group quantification obtained by CBB method and (B) amine group quantification obtained by Orange 2 method. The XPS error bars correspond to its general 10% error.

Repeated measurements on each sample were not possible as it caused a decrease of primary amine density (Figure 5.9). Although the employed colorimetric approach is a reversible process [287], the rapid change of pH and the high number of washing steps caused a decrease of primary amines, most likely due the loss of plasma coating.

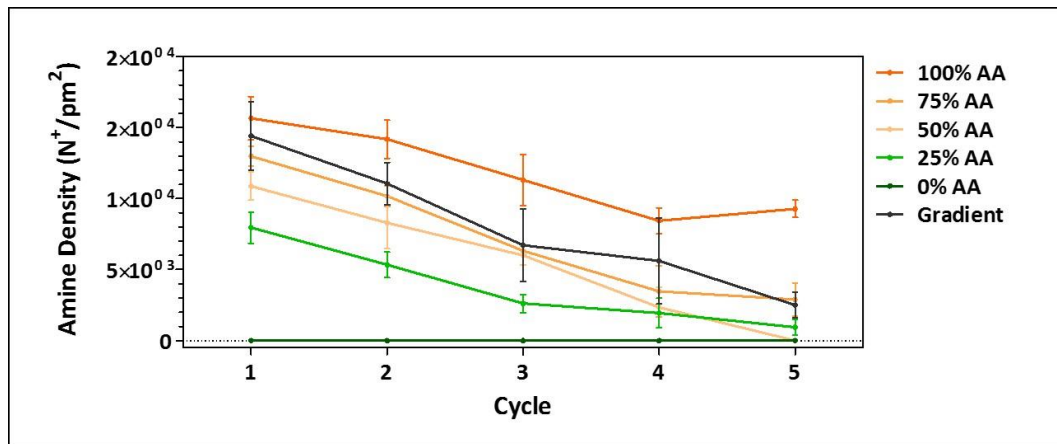


Figure 5.9: Change of primary amine density after repeating the CBB method on the same substrate.

5.2.2 Surface wettability analyses

5.2.2.1 Sessile drop method

Substrate wettability was assessed using the sessile drop technique, in which a droplet of water was placed on the surface. OD rich substrates had high CAs (hydrophobic, 100% OD: $\sim 80^\circ$), whereas an increasing AA concentration caused lower CAs (more hydrophilic, 100% AA: $\sim 60^\circ$) (Figure 5.10). This trend was confirmed throughout the measurements on the gradients, although here only small, insignificant differences were obtained on the AA richer side (position 6 mm to 12 mm). The results also showed a linear correlation of an increase in CA with increasing OD concentration ($R^2 = 0.9447$, $p < 0.001$ for homo- and copolymers and $R^2 = 0.8247$, $p < 0.001$ for gradients). In order to compare homo- and copolymers with corresponding portions of the gradients, the latter ones were divided into 5 sections and the average CA was determined (Table 5.5).

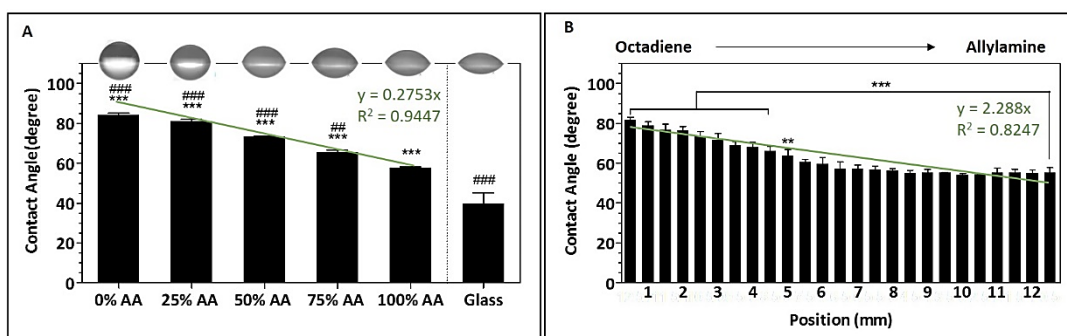


Figure 5.10: Plasma polymer CAs. (A) Homo- and copolymers and (B) CA values obtained across the gradient in steps of 0.5 mm. * Significant difference compared to a glass control. # Significant difference compared to 100% AA. All substrates were significantly different from glass (Tukey model, $p < 0.05$).

Table 5.5: Plasma polymer CAs.

	Contact Angle / ° (homo- and copolymers)	Contact Angle / ° (equivalent area on gradient)
100% AA	57.67 ± 1.38	57.01 ± 2.06
75% AA / 25% OD	65.42 ± 2.78	64.15 ± 1.34
50% AA / 50% OD	73.33 ± 2.78	71.28 ± 1.72
25% AA / 75% OD	81.04 ± 1.48	81.99 ± 2.92
100% OD	84.29 ± 1.19	90.60 ± 3.07

In order to investigate whether there were prominent wettability changes throughout the substrate surface, such as surface contamination or particular patterns caused by an uneven distribution of functional groups, CA maps were collected (Figure 5.11). All CA maps showed an even distribution of CAs across the surfaces with very little variations. The OD substrates were hydrophobic throughout (here indicated by green colour) and with increasing AA concentration the surfaces became more hydrophilic (here indicated by orange colour). A glass substrate was measured as a control and was the most hydrophilic substrate. The gradient substrates showed an even transition (colour change) from the hydrophobic to the hydrophilic side. These maps gave no indication about surface topography, they only represent changes in wettability.

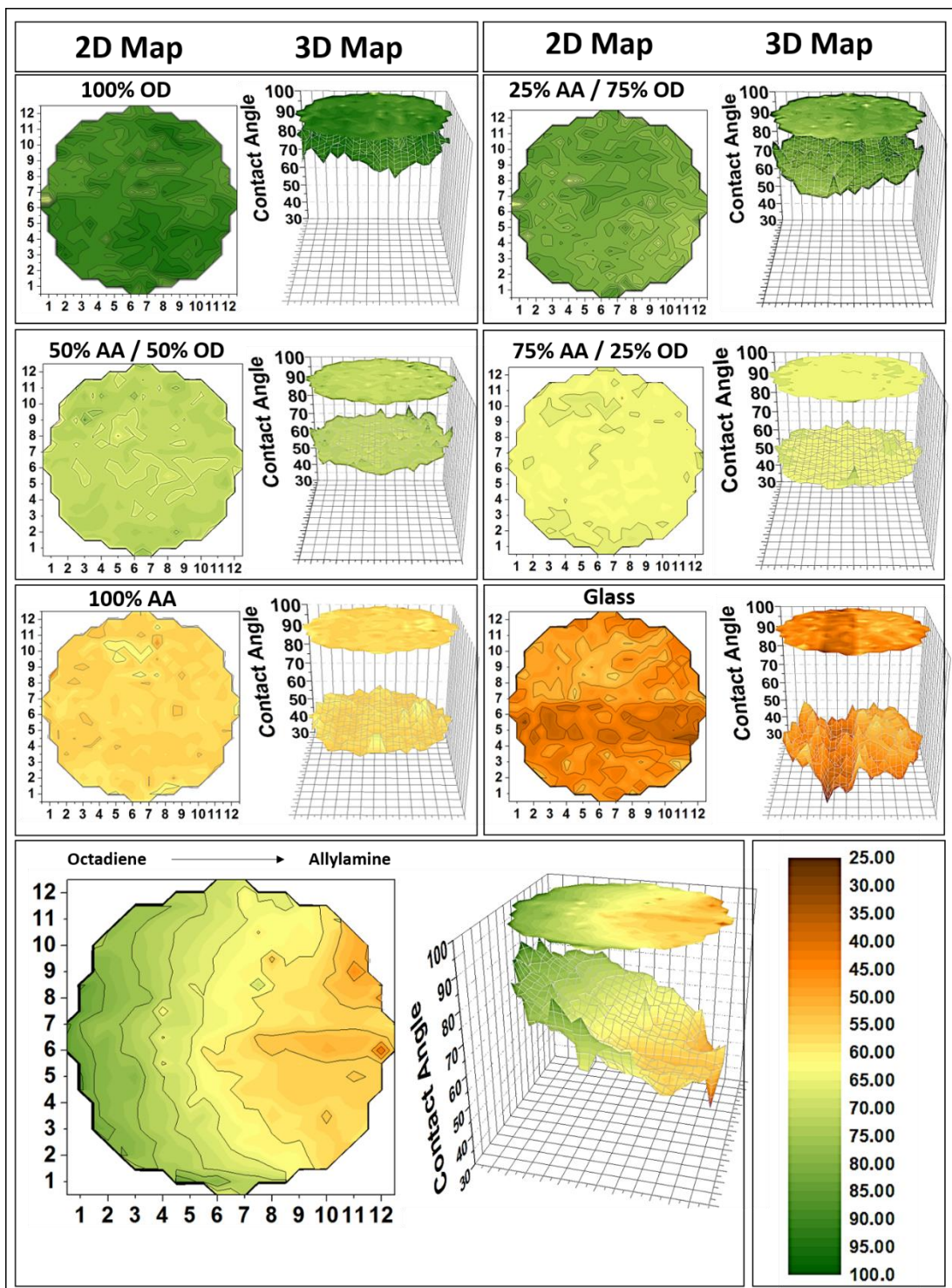


Figure 5.11: 2D (top view) and 3D contact angle maps of plasma polymer coated substrates. 2D maps show the wettability profile across the surface whereas 3D maps show wettability from one point perspective. These maps do not represent topographical features.

5.2.2.2 Captive bubble method

The surface wettability was also investigated using the captive bubble (CB) method where an air bubble was placed on a substrate that was immersed in water. As the air bubble was considerably larger than a water droplet, it was not possible to specify the exact area of measurement for which reason gradient surfaces were not measured. [Figure 5.12](#) shows the CAs obtained for the homo- and copolymers when the substrates were directly immersed and measured in water or 2 h post exposure in FBS.

The CA trend resembled the one observed with the sessile drop method. OD rich substrates were the most hydrophobic (100% OD about 80°) and the CA significantly decreased with increasing AA concentration (100% AA about 40°). Interestingly, the glass CA was higher compared to the one obtained by the sessile drop method. As expected from the results above, a linear correlation was found between increasing AA concentration and a CA decrease ($R^2 = 0.8623$, $p < 0.001$). When substrates were exposed to FBS prior to measurements, the CA of all substrates decreased. This reduction was inconsistent between substrates in that, the higher the AA concentration, the smaller the decrease (delta, white bars). After exposure to FBS all CAs were consistently $36.95 \pm 1.7^\circ$ regardless of the substrate ([Table 5.6](#)) and therefore no linear correlation was detected for delta.

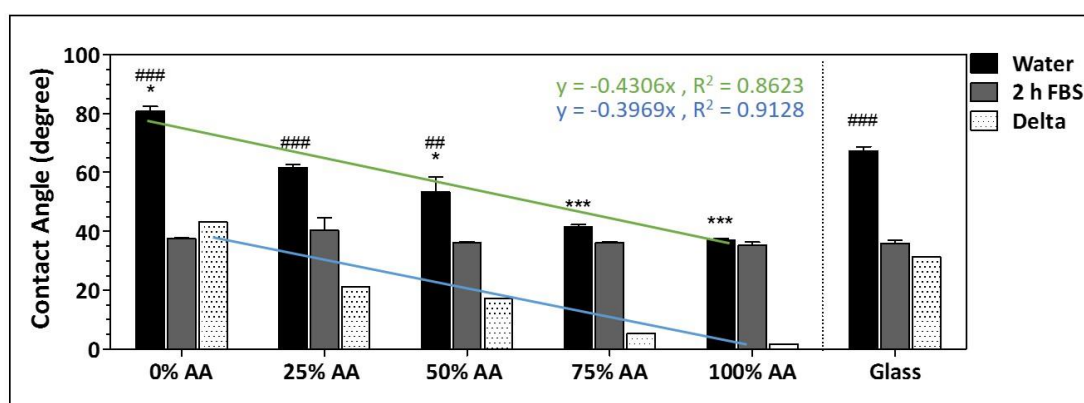


Figure 5.12: CAs obtained by the CB method for plasma homo- and copolymers either directly in water or 2 h post incubation in FBS. Asterisks indicate significant difference compared to a glass control and number signs compared to 100% AA. All substrates were significantly different from glass (Tukey model, $p < 0.05$).

Table 5.6: CB values obtained for homo- and copolymers in distilled water. Samples were either directly in water or 2 h post incubation in FBS.

	Contact Angle (water) / °	Contact Angle (2 h post incubation in FBS) / °
100% AA	36.95 ± 1.62	35.32 ± 0.75
75% AA / 25% OD	41.46 ± 1.87	36.23 ± 1.82
50% AA / 50% OD	53.30 ± 6.36	39.65 ± 2.22
25% AA / 75% OD	61.56 ± 2.72	36.06 ± 0.89
100% OD	80.72 ± 3.83	37.48 ± 1.96

5.2.3 Substrate characterisation using Atomic Force Microscopy

5.2.3.1 Surface topography and roughness

The thickness of the plasma polymers coated on glass coverslips was consistently about 10-15 nm with insignificant variation ($p < 0.05$, Tukey model) (Figure 5.13).

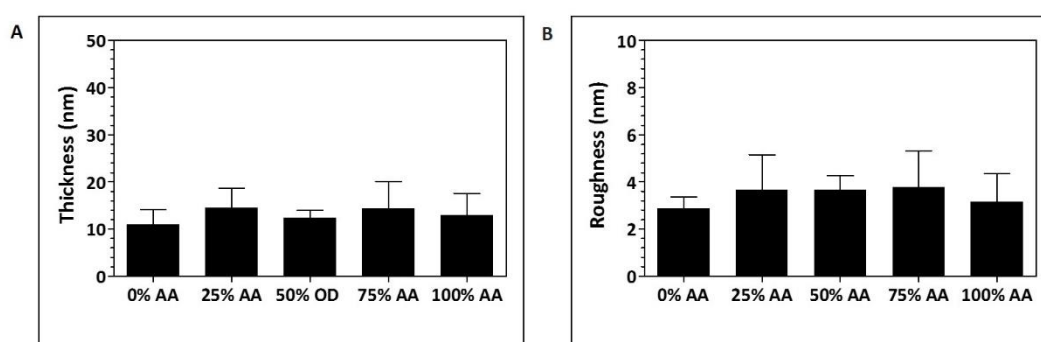


Figure 5.13: (A) Plasma polymer layer thickness after application on glass cover slips. No significant difference was detected ($p < 0.05$, Tukey model). (B) Analyses of the RMS roughness of all homo- and copolymer coated substrates. No significant difference was found ($p < 0.05$, Tukey model).

Figure 5.14 shows 5 μm^2 2D AFM images. All plasma layers were very smooth and showed little topographical differences between substrates ($\pm 2\text{nm}$). Surface root mean square (RMS) roughness quantification did not reveal significant differences between substrates.

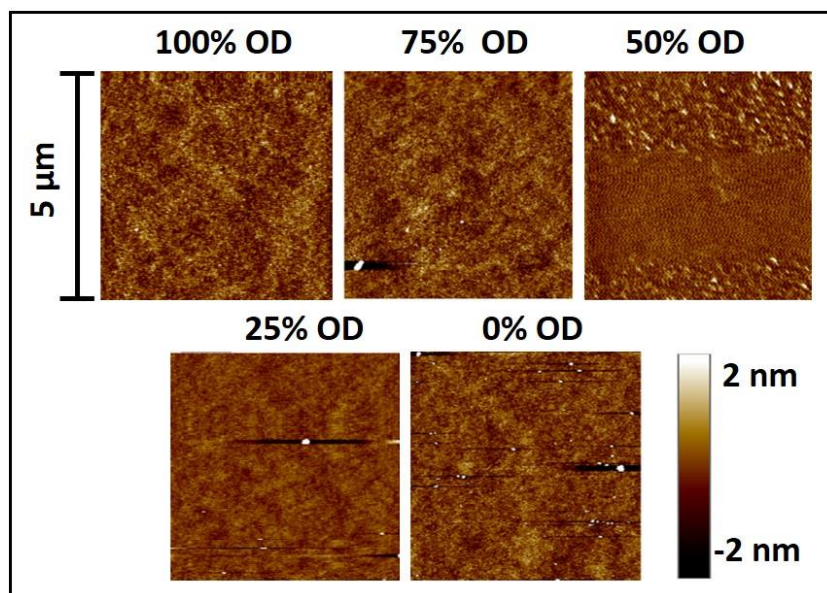


Figure 5.14: 2D AFM 5 μm^2 topographical surface images of homo- and copolymer coated substrates. Brighter colours represent higher areas and darker colours represent lower areas.

5.2.3.2 Surface mechanical properties

Also surface mechanical properties were analysed by AFM using force measurements. [Figure 5.15](#) shows the Young's modulus (elastic modulus) that was obtained for plasma coated homo- and copolymers. All substrates had an elastic modulus of about 1 ± 0.3 GPa with no significant difference between the different plasma coatings.

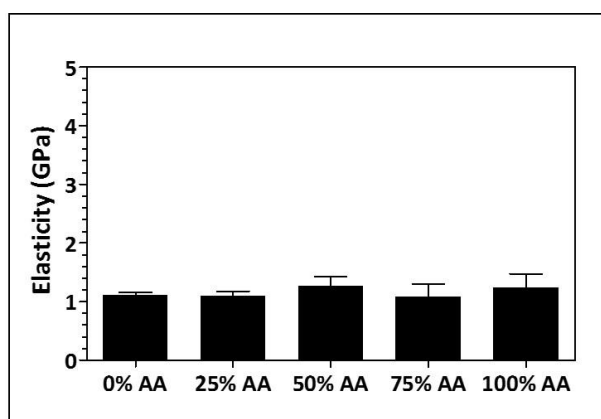


Figure 5.15: Analyses of the Young's modulus (Elastic modulus) of homo- and copolymer plasma coated substrates. No significant difference was found ($p < 0.05$, Tukey model). All substrates show an elastic modulus of about 1 ± 0.3 GPa.

The above analyses did not reveal any significant differences in surface topography, RMS roughness and elasticity between homo- and copolymers. Therefore gradient substrates were assumed to have similar properties and potential changes across the surface with respect to these properties were excluded.

5.3 Discussion

5.3.1 Characterisation of surface chemistry

5.3.1.1 X-Ray Photoelectron Spectroscopy

The XPS analyses from the survey scans showed a high concentration of carbons in all substrates, which originated from the hydrocarbon that AA and OD were composed of. It was also found that an increasing AA concentration caused an increase in surface amines and oxygen functional groups as shown by determination of the N/C and O/C ratio. This trend was maintained on gradients. Interestingly the N/C ratio between the 75% AA and 100% AA substrates was equal which may be related to a maximum possible ratio reached above which the polymer layer would be unstable. Another explanation could be possible surface damage as a result of the transport of substrates which may have caused a decrease of nitrogen [474].

XPS analyses showed that about 20% oxygen species were present on the surface of the 100% OD coated substrates and increased with increasing AA concentration. Surface oxygenation might have been caused by the presence of H₂O and excess oxygen in the reactor during polymerisation, or through exposure to atmospheric air [480-483]. XPS analyses were performed in dry ultra-high vacuum state, which did not reflect a physiological state. *Tarasova et al.* recently investigated the stability of AA and heptylamine films in water and found that already after 24 h a strong ageing occurred that resulted in a high surface oxygen content [470]. They also found, that the AA films were more stable when copolymerised with OD [470]. This could also explain why the AA rich films investigated here have undergone

oxidation rather quickly, whereas copolymerisation with OD lead to an increased stability and decreased surface oxidation.

Although no nitrogen was detected on the 100% OD, a C-N, C-O signal was detected. It has to be noted that the C-N and C-O peak areas were fitted together as their peaks are generally very close (C-N: 285.7 – 286 eV and C-O: 286.2 – 286.7 eV) [468, 484, 485]. The increase of C-O, C-N bonds with increasing AA concentration was probably related to the presence of hydroxyl groups through surface oxidation. However, the C-N, C-O / C-C, C-H ratio increased with increasing AA concentration could be due to an increase of nitrogen functional groups and therefore also primary amines [95].

The AA plasma layer is composed of several different nitrogen based chemical groups, including amines, imines, amides and nitrile groups, whose concentration depends on the experimental conditions [479, 486]. The composition of the AA plasma layer alone, and copolymerised with OD, is highly complex [472, 475, 480, 486-488]. Therefore no further analyses of the oxygen and nitrogen species were performed within this study.

5.3.1.2 Colorimetric quantification of primary amine groups

Several methods have been described to quantify the density of primary amine groups on surfaces including fluorometry [489], spectrometry [490] and chemical derivatisation of functional groups in combination with XPS [491, 492], all of which can be very time consuming, expensive and may lack accuracy.

Here a colorimetric approach was chosen. Two commonly used dyes, Coomassie Brilliant Blue (CBB) and Orange 2, were compared about their ability to support the quantification of primary amines. Their reaction is based on the electrostatic interactions between the negatively charged dye and the positively charged amine groups (protonated in acidic solution) [291, 493]. When exchanging the acidic by an alkaline solution, the dye is released

and its absorbance can be measured and allows the quantification of primary amine groups (chapter 2.2.3.2, p 39) [287, 290].

An increase of primary amine groups with increasing AA concentration was observed using both dyes. However, a comparison of these methods revealed differences in the amount of adsorbed dye onto surfaces. Quantification of primary amines using Orange 2 showed only $\frac{1}{4}$ of the amount detected by the CBB method. The error bars of all measurements were on average $0.4 \pm 0.1 \times 10^4 \text{ N}^+ / \text{pm}^2$ regardless of the dye used. When comparing both methods a linear correlation was found ($R^2 = 0.98$, $p < 0.0001$) and indicated that both methods gave a satisfying (and in one another's range) indication of surface primary amine density.

Noel et al. used both methods to quantify the amount of primary amines on aminated polyethylene terephthalate (PET) films. They found that the CBB method gave higher values than the Orange 2 method on pristine (not aminated) films, suggesting non-specific adsorption of CBB [290]. This would also explain the higher amount of CBB detected on plasma polymers compared to the Orange 2 method. Other experimental conditions, such as pH, temperature and time, were optimised previously by other groups and can therefore be excluded [494, 495]. However, after *Noel et al.* aminated the PET films they found that the CBB method revealed lower values than the Orange 2 method. They suggested that CBB molecules were sterically hindering other CBB molecules and therefore did not reach all amine groups of the surface, whereas the small monovalent Orange 2 would reach the majority [290]. They also suggested that CBB reacts to primary amines stoichiometrically 2:1. However, it has been demonstrated before that one single CBB molecule interacts with only one protonated amine group and binding only occurs to protonated amine groups that are spatially available [287, 289, 291]. These findings demonstrated that primary amine quantification with CBB can be challenging. The argument whether it binds to primary amines 2:1 or 1:1 stoichiometrically can cause large difference when analysing data. Moreover, it is

a large molecule and its steric hindrance towards other CBB molecules as well as the hindrance caused by surfaces itself can easily lead to underestimation of primary amines. Therefore, Orange 2 might be a more suitable for primary amine quantification [290]. However, in contrast to many other methods colorimetry has been found cost efficient, fast and quantitative with the most influential drawback being non-specific adsorption [288, 290]. Also the correlation of primary amine densities obtained by colorimetry and those obtained by XPS (N / C ratio) confirmed the increase of amine groups with increasing AA concentration. In conclusion, both methods were suitable to quantify the amount of primary amine groups on biomaterial surfaces and allowed the detection of primary amine groups sufficiently. Alongside XPS, this colorimetric approach highlighted an increasing presence of primary amine groups with increasing AA concentration. However, due to its characteristic monovalent structure the Orange 2 dye may be the better choice compared to the large bivalent CBB dye for the detection of primary amine groups as it can bind to sterically hindered groups to a higher extent.

5.3.2 Surface wettability analyses

Both, the sessile drop and CB analyses showed a decreasing CA with increasing AA concentration. This can be attributed to the fact that AA contained a large number of hydrophilic nitrogen functional groups such as primary amines, amides and imines [466, 471]. In addition, as discussed above, a higher AA content led to an increased presence of surface oxygen species (surface oxidation) that will contribute to a CA decrease.

As for the CB method it has to be noted that AA films are composed of a complex and flexible network that can rearrange itself and the surface amine groups [496]. Such a rearrangement may occur in a short time and lead to hydrophilic groups sticking out of the surface and therefore making it more hydrophilic.

The interactions between proteins and surfaces of varying wettability are of great interest. In order to investigate whether the substrates differed in their ability to adsorb proteins, they were immersed in FBS for 2 h prior to measurements. Interestingly, the CA decreased on all substrates and reached a value of about 40°, regardless of the coating. This indicated that proteins adsorbed onto all surfaces. An initial protein adsorption occurs within seconds with the main driving force being the cumulative effect of non-covalent interactions, such as electrostatic interactions and van der Waals forces [378, 497]. Proteins in solution will disturb the water molecule organisation on hydrophobic surfaces, which causes an increase in entropy and drives protein adsorption [497]. On the other hand polar groups of proteins and water will compete for interaction with hydrophilic surfaces (repulsive solvation forces) [80, 81, 378]. Although protein adsorption onto hydrophilic surfaces is energetically unfavourable and research has shown that generally more proteins adsorb to hydrophobic surfaces, the CA measurements did not reveal any significant difference between the substrates [82, 498]. However, the CA measurements did not give information about protein identity and conformation and therefore did not allow a direct comparison of substrates with respect to protein adsorption. Moreover, it has to be taken into account that the interactions between proteins themselves, their chemical properties and concentration but also substrate properties influence protein adsorption [497]. Gradient substrates were not analysed using the CB method as the applied air bubbles were too large to be attributed to a particular area of the coverslips. However, protein adsorption on plasma polymer gradients has been studied in the past [32, 474].

Finally it has to be noted that the CAs for the glass control differed between both methods. When analysed by the sessile drop method, the CA was hydrophilic (~35°) as expected whereas determination using the CB approach revealed a rather hydrophobic value (~68°). The CA increase most likely occurred due to surface damage, such as small scratches or was caused by contamination, such as dust particles or air-borne lipids. The glass has not been

specially treated with detergent / surfactant solution, neither has it undergone velocity jet cleaning or any kind of plasma or acid treatment prior measurements [365, 366].

5.3.3 Substrate characterisation using Atomic Force Microscopy

5.3.3.1 Surface thickness and topography

Plasma thickness was found to be in the order of 10 ± 5 nm and this was consistent for all layers. This was expected as plasma films are generally ultrathin films [499].

Surface topographical images were taken from homo- and copolymers and roughness analysis showed that all surfaces were very smooth with an overall distance between lowest points and highest points of about 4 nm. Although no images were collected from gradient surfaces, these results suggested a rather smooth transition from the hydrocarbon rich side to the amine rich side without the formation of particular surface structures or artefacts. Plasma polymer films are generally flat and show only little roughness variations of few nanometres, sometimes even below 1 nm [499].

5.3.3.2 Surface mechanical properties

All coatings had a Young's modulus of 1 ± 0.2 GPa. Therefore it can be assumed that on gradients no significant elasticity changes occurred across the surface. However, the plasma polymer layers were very thin (~ 10 -15 nm) and therefore a contribution of the underlying glass cover slip cannot be excluded. Depending on the method used, the Young's modulus of a glass cover slip was found to be about ~ 72.4 GPa by biaxial flexure [500], 85 GPa using the ultrasonic pulse-echo method [500] and ~ 67 -85.5 by nanoindentation [501, 502].

5.4 Conclusions

The above data showed that the gradients displayed changes in physicochemical properties that resembled, depending on the area, the homo- and copolymers. An increase in AA concentration caused an increase of nitrogen-containing functional groups, but also oxygen

species due to surface oxidation. As both of these functional groups are hydrophilic, this contributed to an increase of wettability with increasing AA concentration. On the other hand, the plasma polymer composition did not influence elasticity, topography and roughness. However, it has to be noted that the latter measurements were employed in air and did not fully reflect a physiological (cell culture conditions, *in vivo*) state. These data also demonstrated that there was no phase separation due to the chemical differences between these two monomers in that no signs of surface formation with amine-rich or hydrocarbon rich areas were found. Although no analyses of topography and elasticity were performed on gradients it was assumed that no such differences would occur across the surfaces.

6 Effect of plasma polymer coatings on mouse kidney-derived stem cells

6.1 Introduction

It is well known that surface physicochemical properties can influence cell behaviour greatly. This has led to the development of a large variety of biomaterials in recent years for various applications, including cell culture, tissues engineering and drug delivery. In this respect, particularly plasma polymer coatings have gained interest as they have many advantages. For instance, they allow the modification of any material, including the chemical functionalisation of surfaces for designing substrates with tailored properties that can improve substrate biocompatibility [457-459, 503-505]. A large range of plasma polymers, including ethanol, hexane, acrylic acid and 1,7-octadiene (OD), have been explored for their effect on cellular behaviour in the past [302, 506]. Also allylamine (AA) is a well-studied plasma precursor. It contains a primary amine group which allows the deposition of a large number of nitrogen-based functional groups on surfaces, particularly primary amine groups. These have been linked to cellular regulation, including enhanced proliferation, adhesion, spreading and differentiation in the past [302, 459, 472, 487, 492, 507].

In addition, plasma polymer coatings can be applied in multilayers or as gradients that allows to develop substrates with changing properties across the length of a substrate and therefore allows high throughput screening of cells on a single substrate [95, 112, 277, 474, 508, 509].

In vivo processes are highly complex. Many of these are guided through the presence of gradients, i.e. chemotaxis, a phenomenon that characterises cell movement in response to chemical stimuli and is responsible for a number of processes in the body, including the immune response to cytokine gradients [510, 511] and cell migration during nervous system development in response to protein gradients [512-516].

Surface gradients have been shown to influence cell behaviour and differentiation in the past [56, 112, 517]. For example, *Wang et al.* studied adhesion, growth and differentiation of MSCs on surface chemical plasma gradients and showed the influence of changing surface chemistry on cell density and osteogenic differentiation [56].

Here, plasma-coated substrates composed of 100% allylamine (AA), 100% 1,7-octadiene (OD) (homopolymers) and copolymers composed of 75% AA / 25% OD, 50% AA / 50% OD and 25% AA / 75% OD (referred to as 75% AA, 50% AA and 25% AA) as well as AA-OD gradients were compared for their effects on cell growth, spreading and differentiation of mouse kidney stem cells (mKSCs) with particular interest in cell differentiation into proximal tubule cells (PTCs) and podocytes, two cell types that are commonly involved in kidney disease.

As plasma polymers can be applied on any type of surface, regardless of its shape, composition and topography, plasma polymerisation is also a useful method to analyse surface topography under exclusion of other physicochemical properties. As part of this study, a range of substrates with different topographies has been additionally investigated². 16 nm and 68 nm gold nanoparticles (AuNPs) have been applied on a AA coated glass substrate (via covalent binding) either with homogeneous density or in form of a density gradient, as previously described [95]. The AuNP density on homogeneous coatings equalled the density of nanoparticles on the densest portion of the gradient substrates. Based on the above introduced ([chapter 5](#)) plasma polymer coatings and their influence on mKSC behaviour and differentiation, these AuNP coated substrates were over coated with one of four plasma coatings: 100% AA, 75%AA, 25%AA or 100% OD ([Figure 6.1](#)). This allowed an analyses of surface topography on mKSC differentiation in combination with different surface chemistries.

² This work has been part of a collaboration with Ass. Prof. Krasimir Vasilev and Dr. Melanie Ramiasa, University of South Australia.

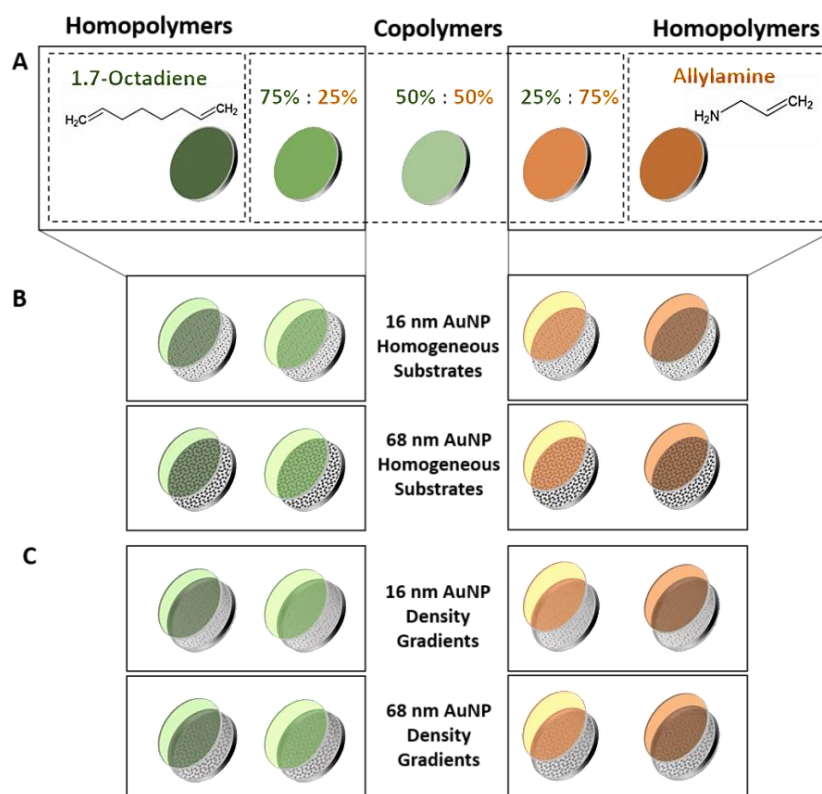


Figure 6.1: Representation of substrates that were investigated for their ability to direct the differentiation of mKSCs during the course of this study. (A) Homo- and copolymer coated substrates (physicochemically analysed in chapter 5). (B) Substrates, coated with a homogeneous layer of 16 nm or 68 nm diameter AuNPs, over-coated with plasma polymers and (C) Substrates, coated with a 16 nm or 68 nm diameter AuNP density gradient layer and coated with plasma polymers.

Aims of this chapter

- (1) Explore the ability of AA and OD composed plasma polymer-coated substrates to influence cell behaviour and promote differentiation of mKSCs.
- (2) Explore the influence of nanotopography size and density in combination with plasma polymer coatings to promote differentiation of mKSCs.

6.2 Results

6.2.1 Effect of surface chemistry on mouse kidney-derived stem cells

6.2.1.1 Effect of surface chemistry on the behaviour of mouse kidney-derived stem cells

Plasma polymer coatings composed of AA and OD were investigated for their influence on mKSC behaviour. mKSCs were seeded on plasma coated substrates and on a glass control at

a density of 1000 cells / well (24 well plate containing a polymer coated 13 mm coverslip). Cell number and viability were analysed at five different time points post seeding and population doubling time (PDT) was determined. [Figure 6.2](#) shows mKSC proliferation over a course of 96 h in culture. At 6 h post seeding about 10 cells / mm² were attached on all substrates and all areas across the gradient. The number of cells on homo- and copolymers increased by a similar extent regardless of the surface. On gradient substrates there was a trend of an increasing cell number 72 and 96 h post seeding towards the middle portion, which was not significant. PDT showed no significant difference between homo- and copolymers as well as when comparing different areas of the gradient ([Figure 6.3](#)). In both cases cells needed on average about 30 ± 5 h to double their population. The cell viability on substrates confirmed an exponential cell growth of viable cells on homo- and copolymers ([Figure 6.4](#)). For viability measurements, mKSCs cultured on the entire substrate were analysed. Therefore, it was not possible to assess cell viability on gradients.

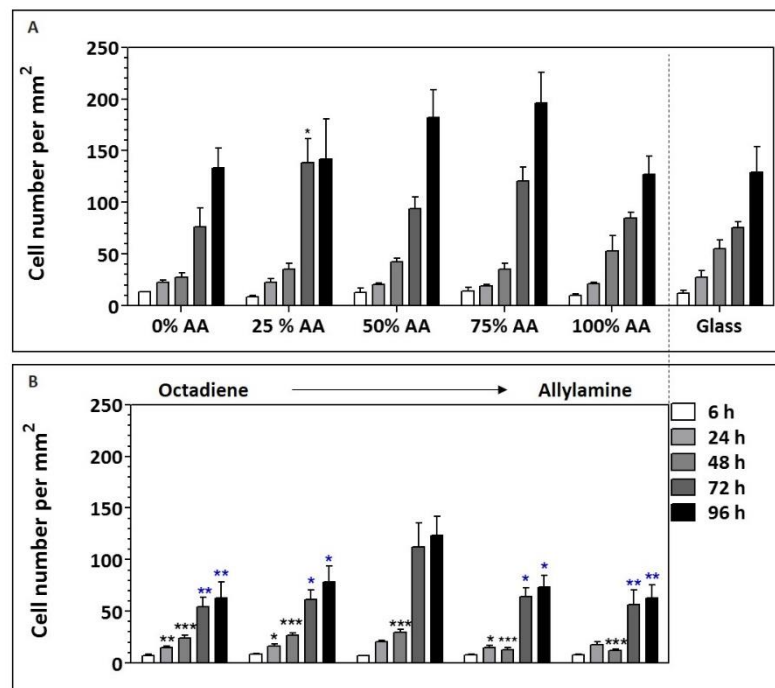


Figure 6.2: mKSC cell proliferation. mKSCs were seeded at a density of 1×10^3 cells / well. Cell number was determined at 5 different time points post seeding on (A) homo- and copolymers and (B) gradient. Results represent the mean of three biological replicates ± SEM. Black asterisks indicate significant difference compared to a glass control. Blue asterisks indicate significant difference compared to the middle portion at the same time point (Tukey model, $p < 0.05$).

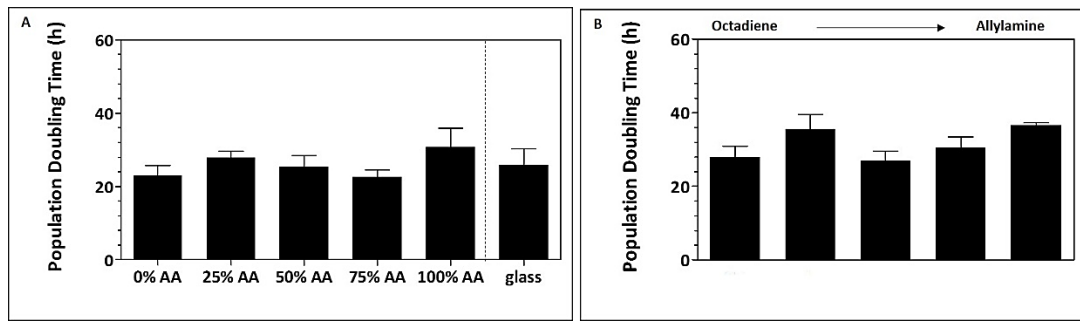


Figure 6.3: Population doubling time. mKSCs were seeded at a density of 1×10^3 cells / well. PDT was quantified from cell proliferation over 96 h in culture on (A) homo- and copolymers and (B) gradients. Results represent the mean of three biological replicates \pm SEM. No significant difference was found (Tukey model, $p < 0.05$).

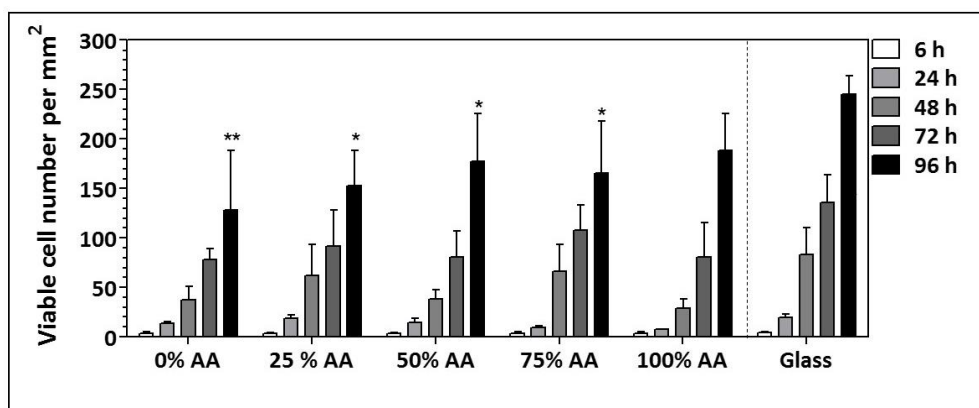


Figure 6.4: mKSC cell viability. mKSCs were seeded at a density of 1×10^3 cells / well. Cell viability was determined at 5 different time points post seeding on homo- and copolymers and a glass. Results represent the mean of three biological replicates \pm SEM. Asterisks indicate significant difference compared to a glass control (Tukey model, $p < 0.05$).

6.2.1.2 Effect of surface chemistry on the differentiation of mouse kidney-derived stem cells into podocytes

Figure 6.5 and Figure 6.6 show phase contrast images and phalloidin labelled mKSCs seeded onto plasma polymers and gradients 24 h and 96 h post seeding. The images show that the cells were homogeneously distributed across the surfaces and the gradients 24 h post seeding with cells displaying a similar morphology on all substrates and portions of the gradients. However, 96 h post seeding cells on AA richer substrates / regions appeared more spread with a podocyte-like morphology, in that, they were large and rounded with a pronounced cytoskeleton at the cell periphery (white arrows).

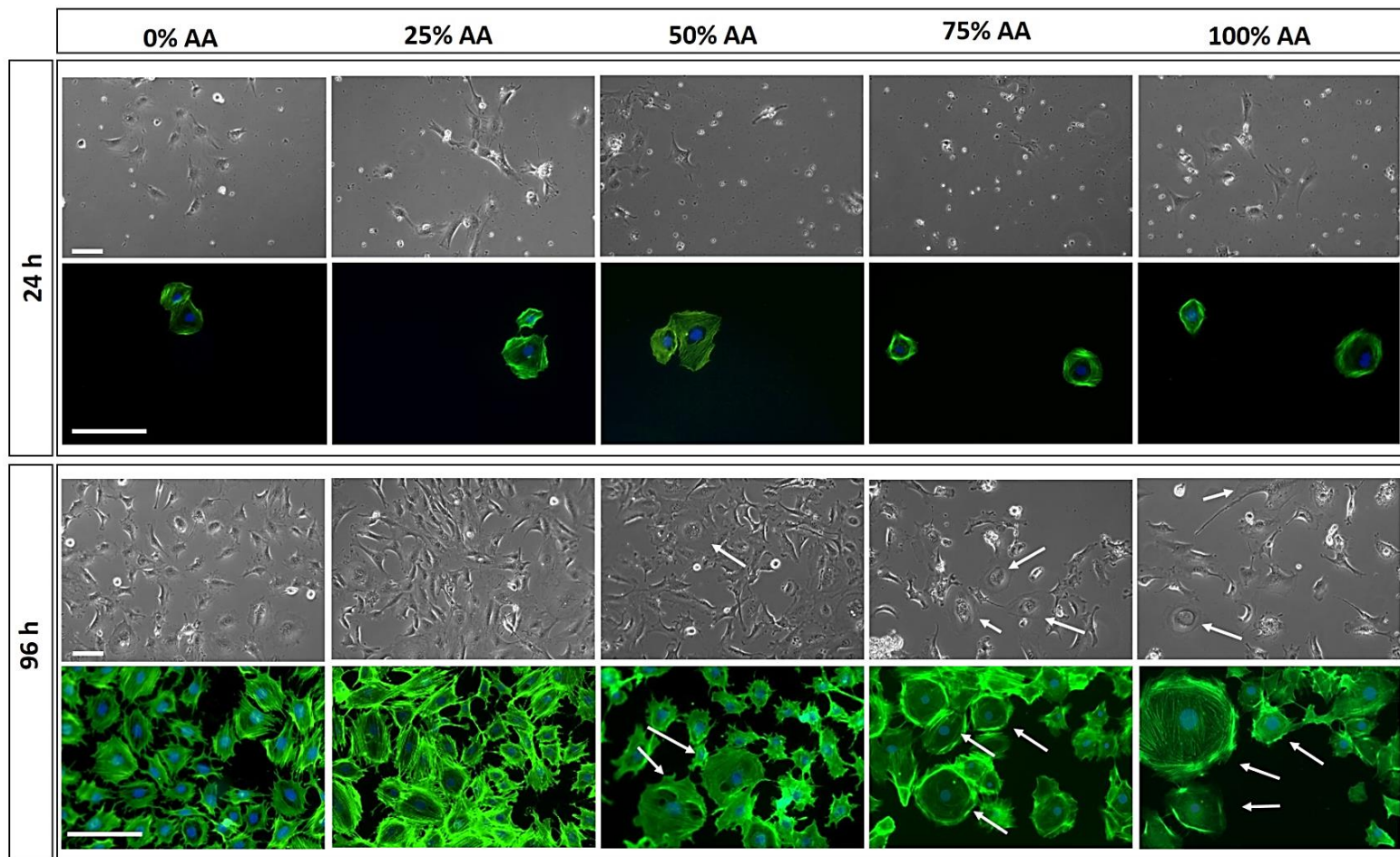


Figure 6.5: mKSCs cultured on homo- and copolymers. The images show phase contrast images and, correspondingly, F-actin and DAPI labelled cells at a higher resolution at two different time points post seeding. mKSCs were seeded at a density of 1×10^3 cells / well. White arrows indicate podocyte-like cells. Scale bar is 100 μm .

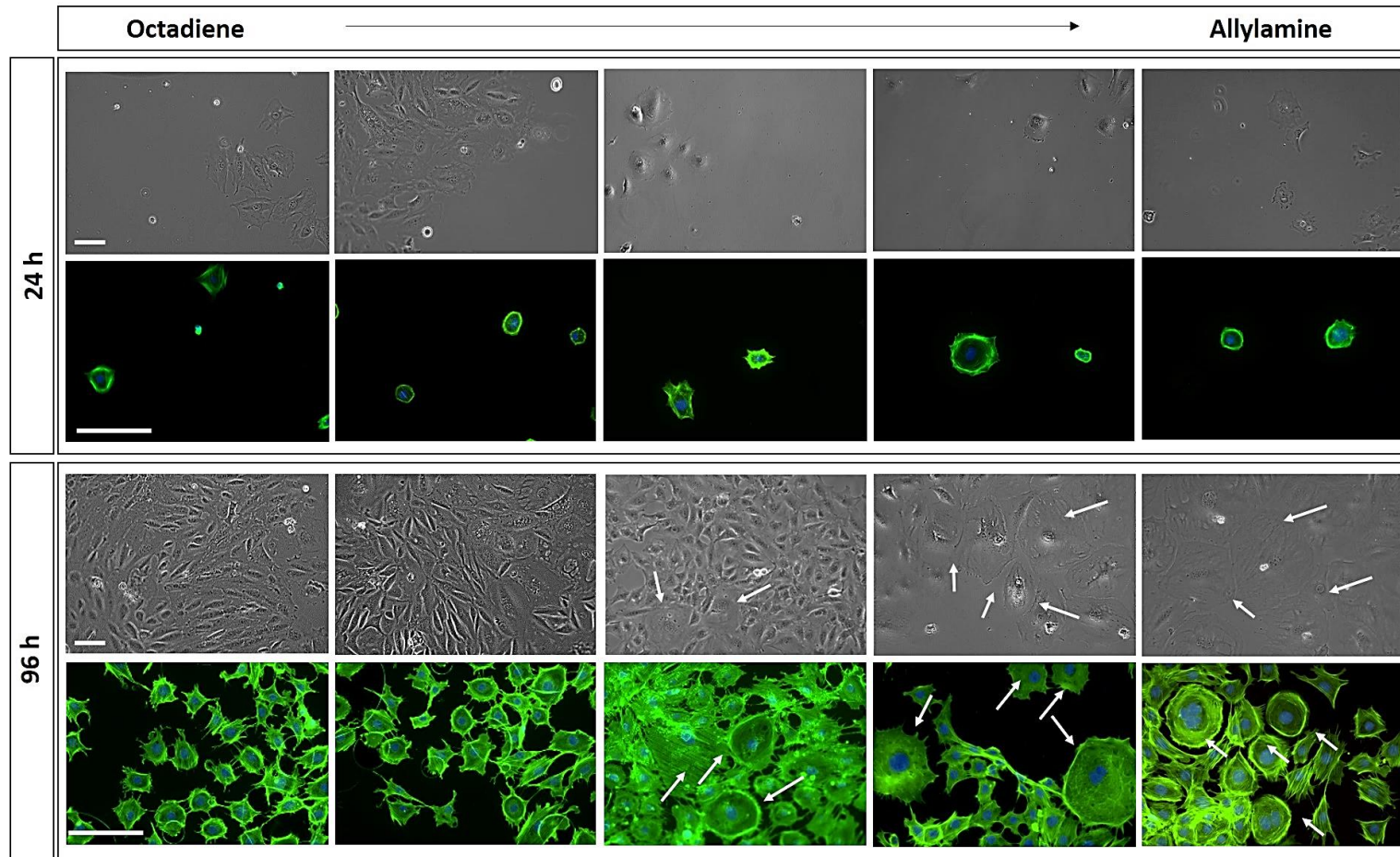


Figure 6.6: mKSCs cultured on gradient surfaces. The images show phase contrast images and, correspondingly, F-actin and DAPI labelled cells at a higher resolution at two different time points post seeding. mKSCs were seeded at a density of 1×10^3 cells / well. White arrows indicate podocyte-like cells. Scale bar is 100 μ m.

Following these observations, mKSC spread was quantified (Figure 6.7). The results showed, that 6 h post seeding the cell spread a very similar on all substrates (about $2000 \pm 500 \mu\text{m}^2$) with no significant difference between homo- and copolymers and between different portions across the gradient. However, with increasing cell culture time the cell spread area on AA richer surfaces / regions increased significantly up to $3500 - 4000 \mu\text{m}^2$ after 72 to 96 h culture. On the contrary, cells on OD richer surfaces were only about $2500 - 3000 \mu\text{m}$ in size.

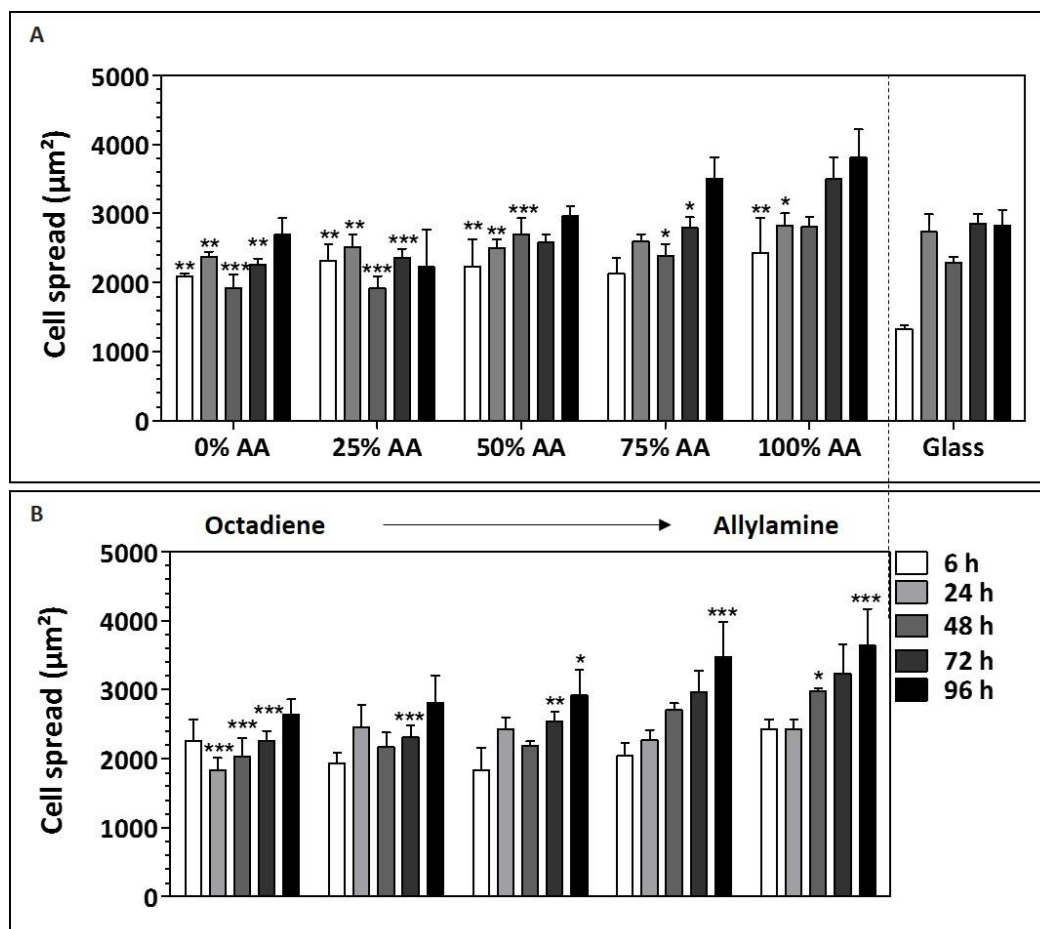


Figure 6.7: mKSCs spread analyses. mKSCs were seeded at a density of 1×10^3 cells / 13 mm polymer coated coverslip. Cell spread was quantified at five different time points post seeding. Asterisks indicate significant difference compared to a glass control (Tukey test, $p < 0.05$). Results represent the mean of three biological replicates \pm SEM.

Subsequently, the number of podocyte-like cells was quantified at two time points: 24 and 96 h post seeding (Figure 6.8). On all substrates, including the gradients, 24 h post seeding about 10-15% of the cells were displaying a podocyte-like morphology, which can be

attributed to spontaneous differentiation. 96 h post seeding a significantly larger number of podocyte-like cells was detected on AA rich surfaces / regions compared to a glass control and OD richer surfaces / regions.

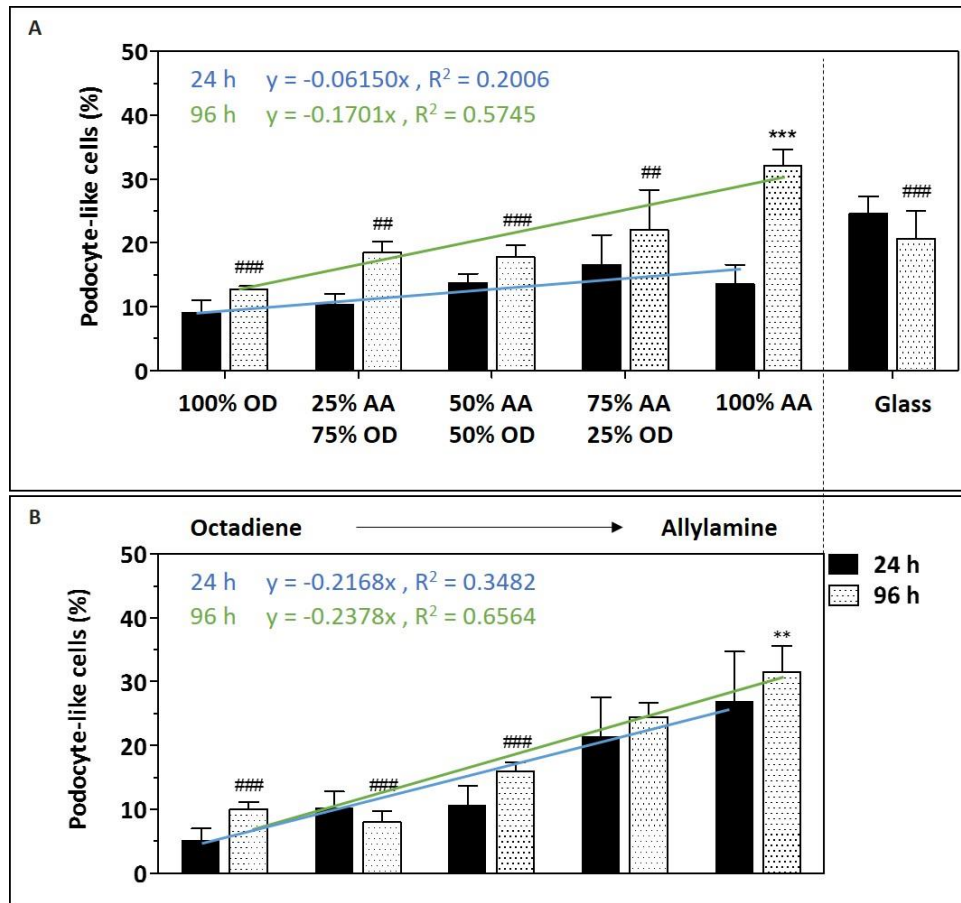


Figure 6.8: Podocyte like cells. mKSCs were seeded at a density of 1×10^3 cells well. The number of podocyte like cells was quantified. Asterisks indicate significant difference compared to a glass control (Tukey model, $p < 0.05$). Results represent the mean of three biological replicates \pm SEM.

These findings were supported by immunostaining. [Figure 6.9](#) shows the staining of mKSC for the podocyte marker nephrin. Towards AA richer surfaces, areas on the gradient respectively, the cells became larger with podocyte-like morphology and were often binuclear (arrows).

Finally, mKSCs were analysed for the expression of three podocyte characteristic genes: *Synaptopodin (Synpo)*, *Podocalyxin (Pdx)* and *Wilms Tumor Gene (WT1)* ([Figure 6.10](#)). The results indicated a trend for higher podocyte gene expression, particularly for *Synpo* and *WT1*, on AA richer surfaces. However, no significant difference was detected. Gradients were

not analysed, as it was not possible to determine which particular area the cells were isolated from.

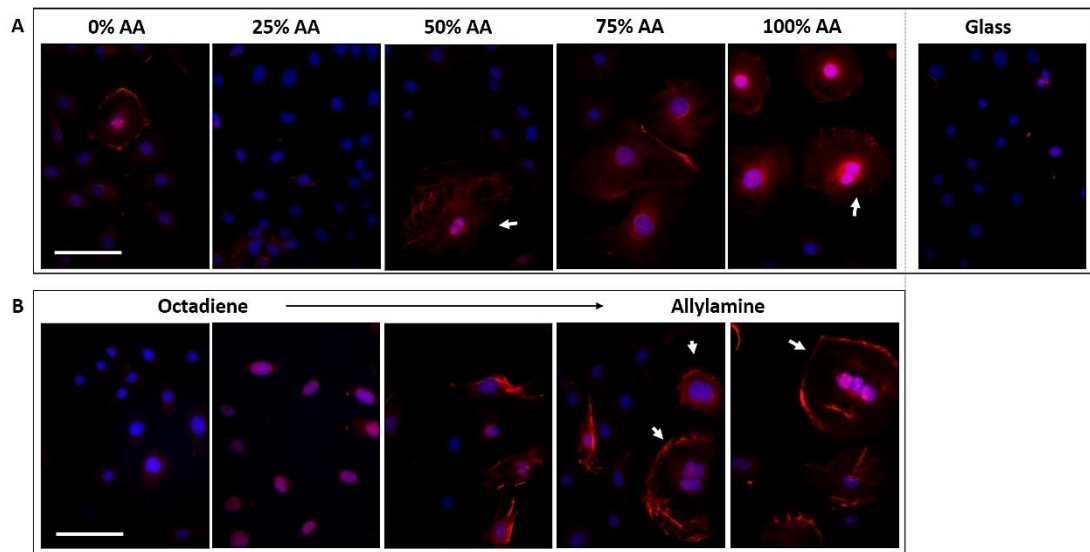


Figure 6.9: Nephrin staining. mKSCs were seeded at a density of 1×10^3 cells / well and cultured on polyacrylates for 96 h. White arrows indicate podocytes. Blue: DAPI. Scale bar: 100 μ m.

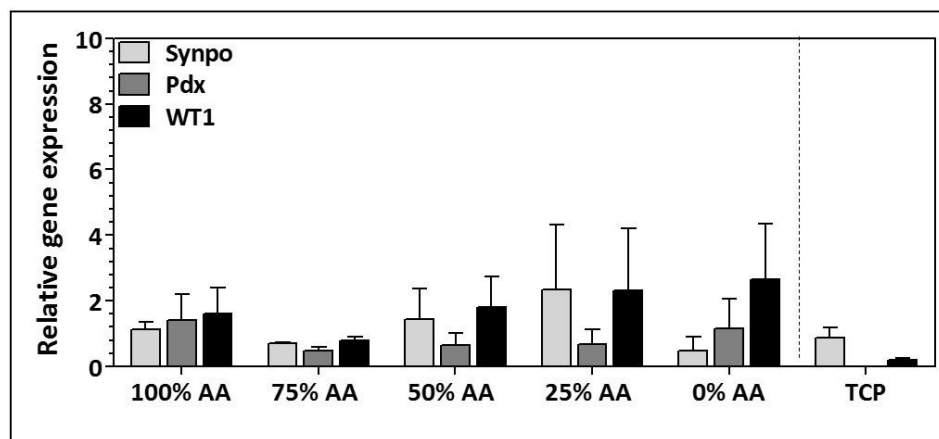


Figure 6.10: qRT-PCR analyses of mKSCs for podocyte characteristic genes as relative expression to mKSCs on a glass control 96 h post seeding on substrates. Seeding density: 1×10^3 cells / well. *Gapdh* and *beta Actin (ACTB)* were used as housekeeping genes. No significant difference was detected. Results represent the mean of three biological replicates \pm SEM.

6.2.1.3 Effect of surface chemistry on the differentiation of mouse kidney-derived stem cells into proximal tubule cells

In order to explore whether mKSCs were differentiating into proximal tubule cells (PTCs), the cells were stained for the presence of megalin. [Figure 6.11](#) shows mKSCs stained for megalin

96 h post seeding on the plasma coated substrates (here co-stained with the glycoprotein marker laminin for improved visualisation of the cells). On homo- and copolymers a larger number of megalin expressing cells were detected on OD richer surfaces / regions. On gradients a higher number of cells were found to be expressing megalin on OD richer regions, but also towards the middle portion of the substrates. Cells on the glass control showed only a small number of megalin expressing cells (spontaneous differentiation).

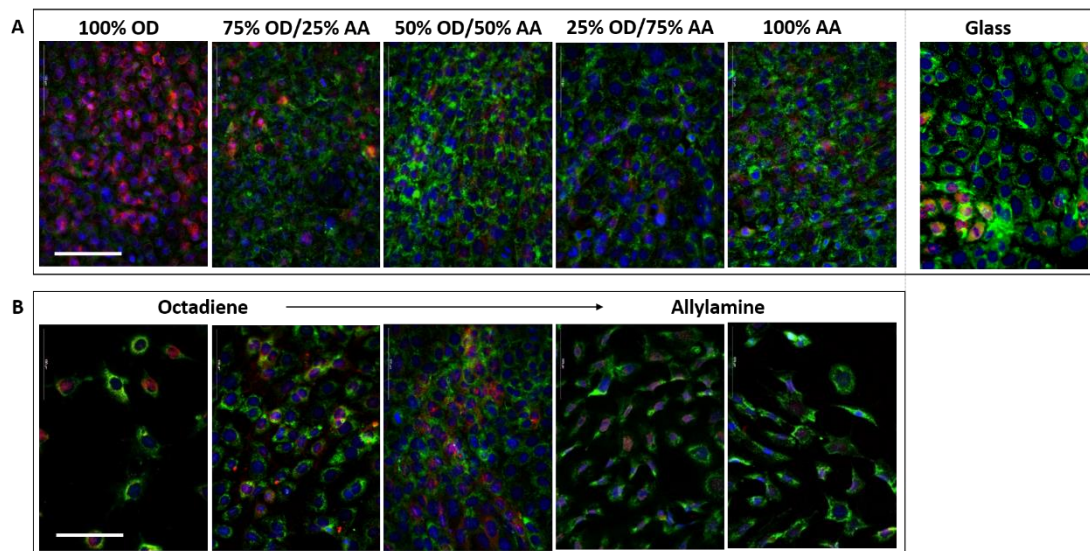


Figure 6.11: Megalin staining 96 h post seeding on polyacrylates. Blue: DAPI and green: Laminin. mKSCs were seeded at a density of 1×10^3 cells / well. Scale bar: 100 μ m.

In order to confirm that the megalin expression in fact resulted from the influence of the plasma substrates, the cell number of megalin expressing cells was quantified at three different time points: 6, 48 and 96 h post seeding. Glass was used as a control (Figure 6.12). The results showed that 6 h post seeding an equal amount of cells (about 10%) were megalin positive on all substrates and areas across the gradient (spontaneous differentiation). The number of positive cells increased over time on all substrates with a trend of higher number of these cells towards OD richer surfaces / regions. In addition, on gradients a larger number of megalin positive cells (about 30%) was detected on the middle portion of the gradient (ideally equivalent in surface chemistry to the 50% AA sample), which confirms above findings.

Moreover, the ability of the mKSCs to endocytotically uptake albumin through the *in vivo* functionality of the transmembrane receptor megalin was assessed. For that, cells were cultured on substrates and 24 h before the end of cell culture, incubated in serum-free medium and subsequently incubated in serum-free medium supplemented with fluorescently labelled albumin (F-BSA) ([chapter 2.4.8.3](#), p 50). The F-BSA uptake of mKSC was then quantified using flow cytometry ([Figure 6.13](#)) [236]. The results showed that the number of cells that did uptake F-BSA was highest on OD rich surfaces and reached values of about 45% on these. The cell number that did uptake F-BSA was decreasing with increasing AA concentration.

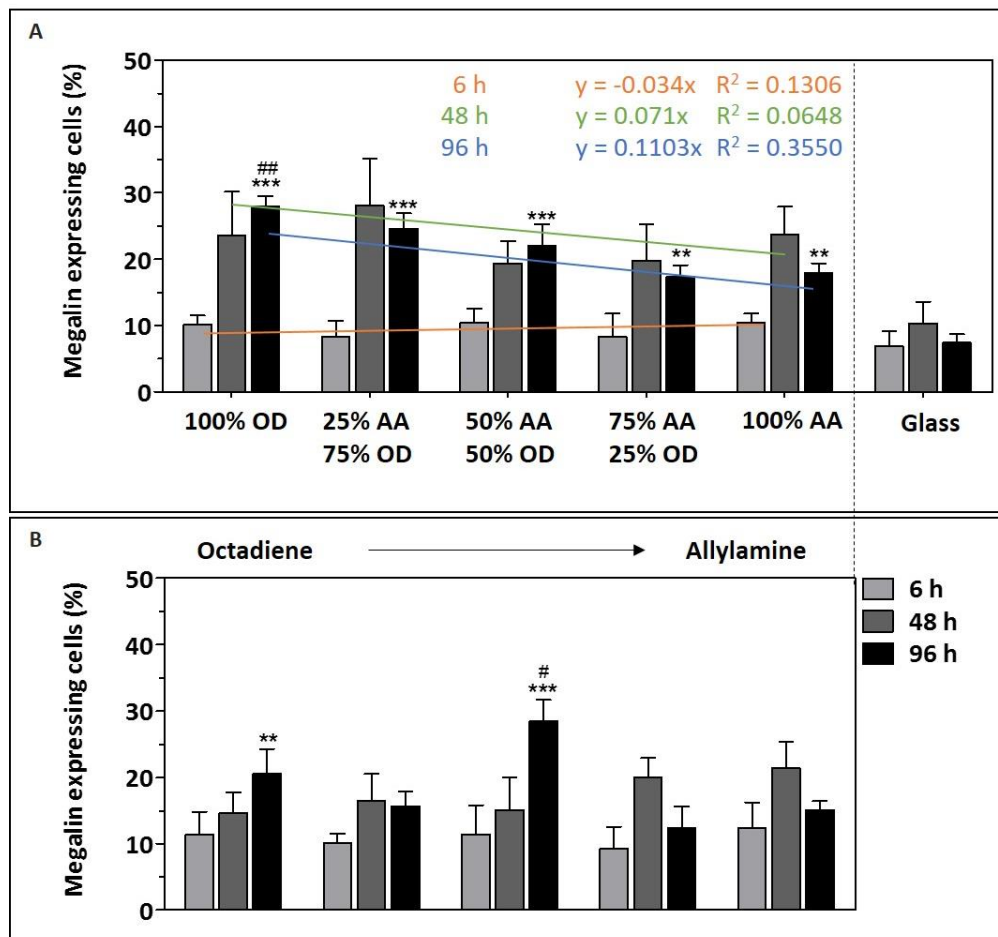


Figure 6.12: Quantification of the number of megalin expressing cells. mKSC were seeded at a density of 1×10^3 cells / well. The number of megalin expressing cells was quantified at 3 different time points post seeding on (A) homo- and copolymers and (B) gradients. Asterisks indicate statistical difference compared to a glass control. Results represent the mean of three biological replicates \pm SEM.

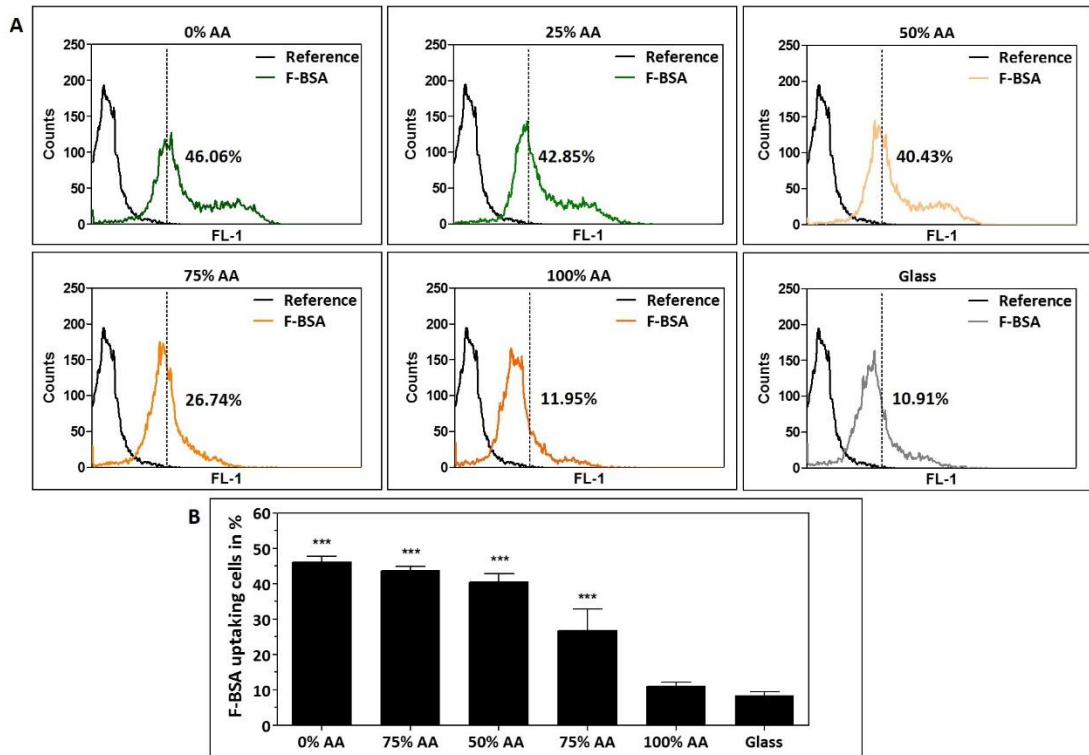


Figure 6.13: Albumin uptake assay. (A) Spectra and (B) Flow cytometric analyses of mKSCs after starvation in serum free medium and subsequent incubation in serum-free medium supplemented with F-BSA. Cells were seeded at a density of 1×10^3 cells/well. Asterisks indicate significant difference compared to a glass control (Tukey model $p < 0.05$). Results represent the mean of three biological replicates \pm SEM.

The gene expression of mKSCs was then analysed for the expression of three PTC characteristic genes: *megalyn (Meg)*, *alkaline phosphatase (AlkPhos)* and *aquaporin 1 (Aqp1)* (Figure 6.14). The results showed a trend of higher expression for all PTC markers on the OD rich surfaces, however, no significant difference was detected. Gradients were not analysed, as it was not possible to determine which substrate portion the cells were isolated from.

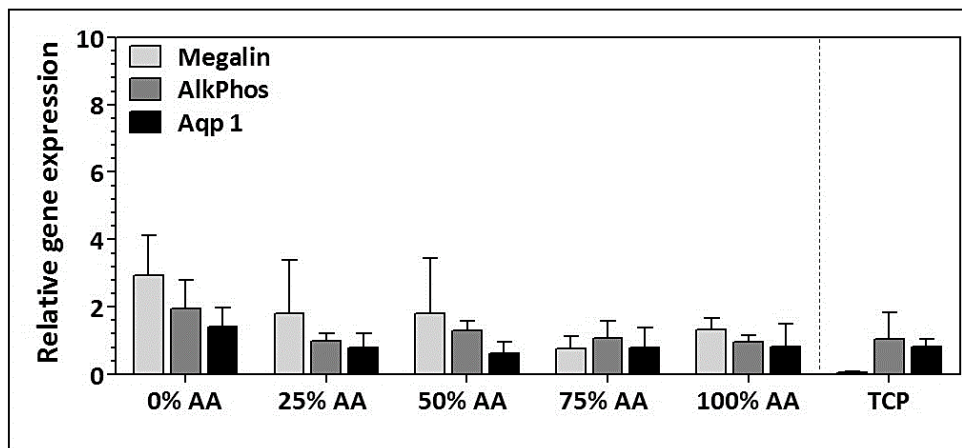


Figure 6.14: qRT-PCR analyses of mKSCs for PTC characteristic genes as relative expression to mKSCs on a glass control. Seeding density: 1×10^3 cells / polymer coated coverslip. *Gapdh* and *beta actin (ACTB)* were used as housekeeping genes. No statistical differences were detected. Results represent the mean of three biological replicates \pm SEM.

6.2.2 Effect of surface nanotopography on mouse kidney-derived stem cells

6.2.2.1 Effect of homogeneous nanotopography on the behaviour and differentiation of mouse kidney-derived stem cells

After evaluation of mKSC behaviour and differentiation on the above described plasma polymer substrates, it was investigated whether changes in topography would have an additional effect on mKSCs behaviour and differentiation³. For that, glass cover slips were coated with gold nanoparticles (AuNPs) of 16 and 68 nm diameter either homogeneously or in form of a density gradient. Four plasma polymer coatings were chosen to overcoat these AuNPs: 100% AA, 75% AA, 25% AA or 100% OD (Figure 6.1, p 176).

Firstly, the effect of AuNPs on mKSC proliferation was analysed. mKSC number was determined 24 and 96 h post seeding on substrates that were homogeneously coated with 16 or 68 nm AuNPs (Figure 6.15). The homogeneity of these AuNP coatings was shown in

³ The following data were obtained as part of a short term collaboration with Ass. Prof. Krasimir Vasilev and Dr. Melanie Ramiasa, University of South Australia.

previous work (unpublished work)⁴. The cell number was similar on all substrates at each time point with no significant differences with respect to AuNP size.

Also the PDT did not reveal any significant difference between substrates and showed that cells took about 25 h to double their population on all substrates.

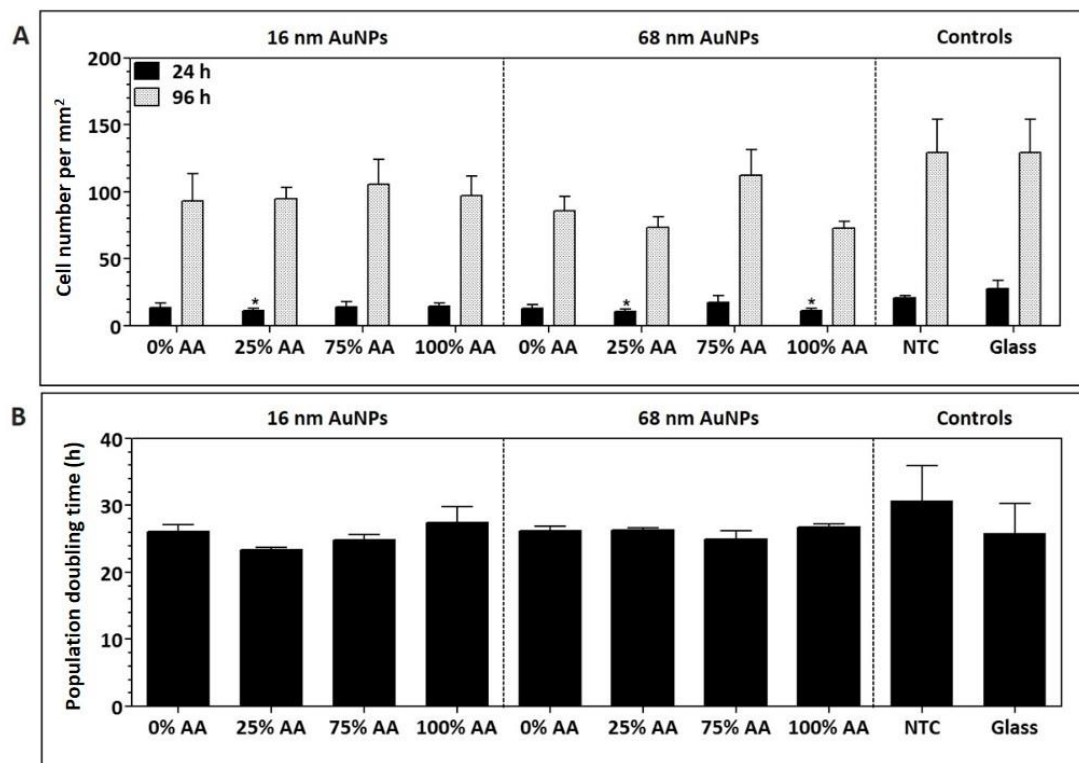


Figure 6.15: mKSC proliferation and PDT on AuNP and plasma coated substrates. Cells were seeded at a density of 1×10^3 cells / well and cultured for 96 h. (A) Cell proliferation and (B) PDT was determined. A glass and a no-topography sample (NTC, 100% AA without AuNPs) were used as controls. No significant differences were found (Tukey model, $p > 0.05$). Results represent the mean of three biological replicates \pm SEM.

Subsequently, mKSC morphology was investigated. [Figure 6.16](#) shows phase contrast images of mKSCs seeded onto substrates homogeneously coated with either 16 nm or 68 nm AuNPs and over coated with plasma polymers. The images showed a higher number of podocyte-like cells on substrates with higher AA content (white arrows), which confirmed previous findings ([chapter 6.2.1.2](#), pp 176-183). However, AuNP size did not appear to have an effect on mKSC differentiation into podocytes.

⁴ Unpublished work by M. Ramiasa et al (2016)

These results were reaffirmed by immunostaining. [Figure 6.18](#) shows mKSCs stained for the podocyte marker nephrin 96 h post seeding on substrates that were homogeneously coated with AuNPs. The images showed a higher number of nephrin expressing cells on substrates with a higher AA concentration on both, 16 nm and 68 nm AuNPs.

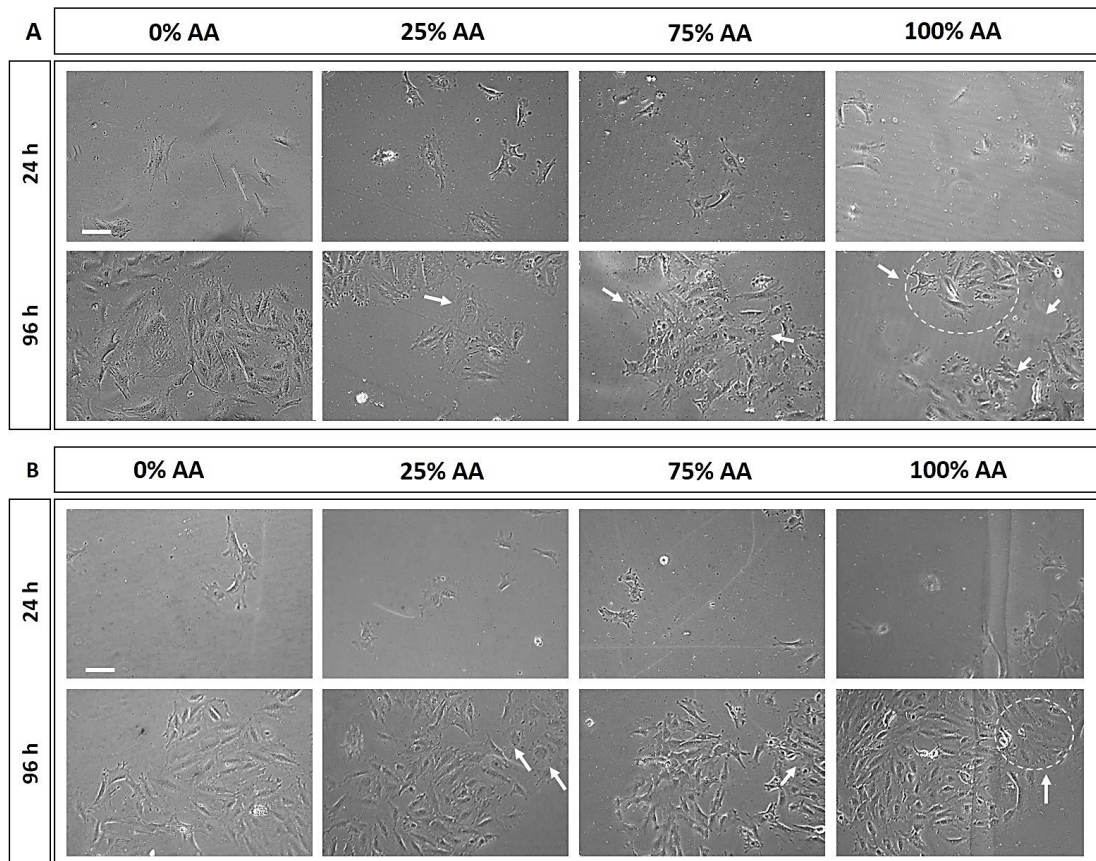


Figure 6.16: Phase contrast of mKSC seeded onto AuNP and AA and OD plasma coated substrates. Cells were seeded at a density of 1×10^3 cells / well and imaged 24 and 96 h post seeding. White arrows and circles indicate podocyte-like cells. (A) 16 nm and (B) 68 nm AuNPs.

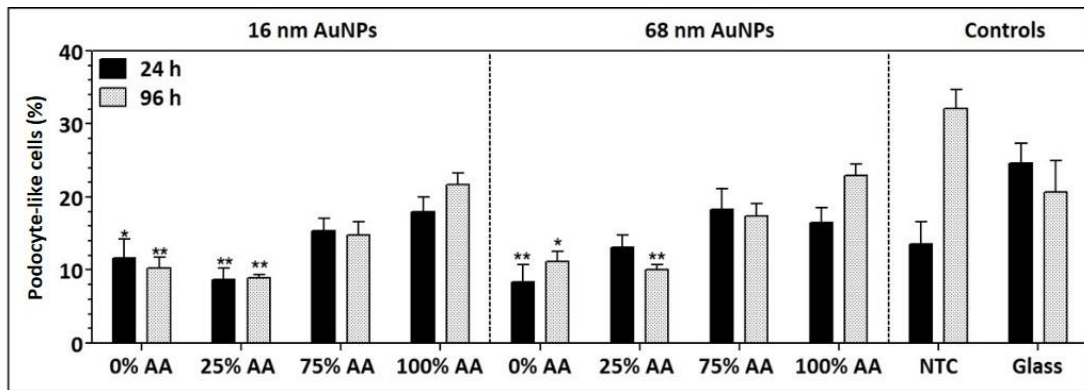


Figure 6.17: Quantification of podocyte-like cells. mKSC were seeded at a density of 1×10^3 cells / well. A glass and a no-topography sample (NTC, 100% AA without AuNPs) were used as controls. Asterisks indicate significant difference compared to a glass control (Tukey model, $p < 0.05$). Results represent the mean of three biological replicates \pm SEM.

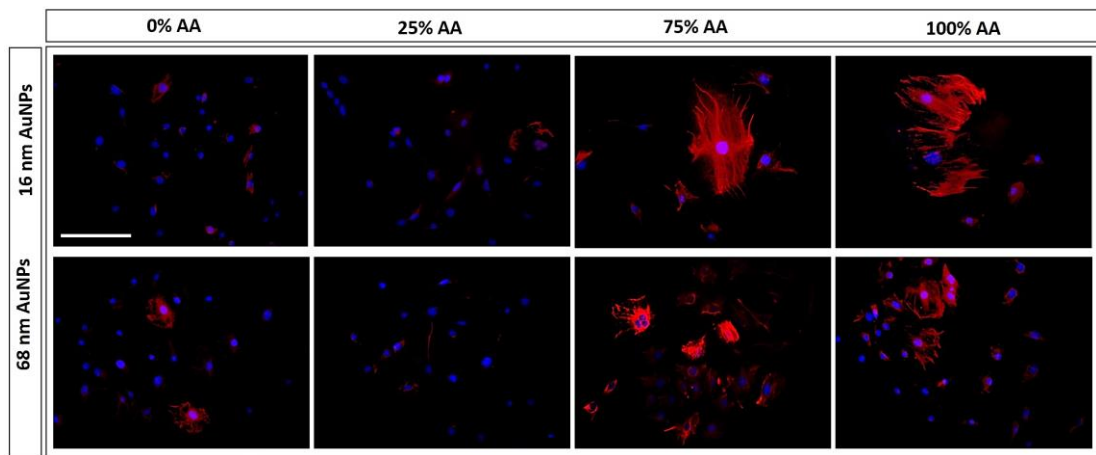


Figure 6.18: Nephtrin staining on mKSCs cultured on AuNP and plasma coated substrates for a period of 96 h. Blue: DAPI. mKSCs were seeded at a density of 1×10^3 cells / well. Scale bar: 100 μ m.

Moreover, it was confirmed that mKSCs differentiated into PTCs on OD rich surfaces. [Figure 6.19](#) shows images of mKSCs, seeded on substrates that were homogeneously coated with 16 or 68 nm AuNPs. Cells were stained for the PTC marker megalin. The results showed a higher number of megalin positive cells on OD rich surfaces and a lower number on AA rich surfaces.

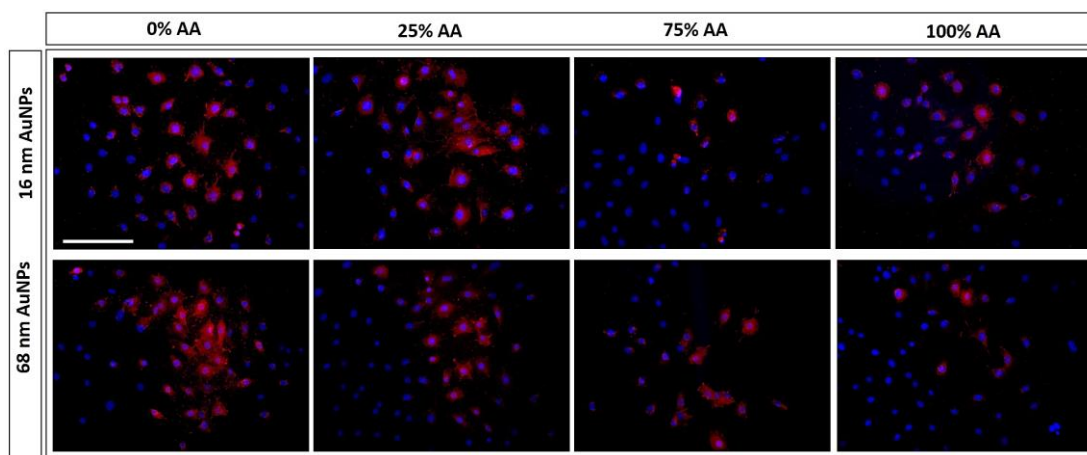


Figure 6.19: Megalin staining on mKSCs cultured on AuNP and plasma coated substrates for a period of 96 h. Blue: DAPI. mKSCs were seeded at a density of 1×10^3 cells / coverslip. Scale bar: 100 μ m.

6.2.2.2 Effect of nanotopographic gradients on behaviour and differentiation of mouse kidney-derived stem cells

To further explore the influence of AuNPs on mKSC behaviour and differentiation, mKSCs were seeded on substrates that displayed an AuNP density gradient that was overcoated with either 100% AA, 75% AA, 25% AA or 0% AA plasma (Figure 6.1, p 176). mKSC number was determined 24 and 96 h post seeding on five separate portions of the substrates (Figure 6.20). mKSC number was similar on all substrates 24 h post seeding and cells were proliferating to a similar extent on all substrates. Therefore, AuNP density did not have a significant impact on cell proliferation.

Figure 6.21 shows phase contrast images of mKSCs cultured on 16 or 68 nm AuNP density gradients that were overcoated with either 100% AA (representative for 75% AA) and 0% AA (100% OD, representative for 25% AA). The images show that mKSCs had the characteristic morphology and proliferated on all substrates. As expected, mKSCs cultured on AA richer substrates (100% AA and 75% AA) showed a podocyte-like morphology (chapter 6.2.1.2, p 178). Moreover, it was observed that with increasing AuNP density a higher number of podocyte-like cells was present (white arrows). This trend was maintained on all substrates, regardless of the AuNP size and plasma coating. The number of podocyte-like cells was then

quantified ([Figure 6.22](#)). As expected, substrates coated with AA rich plasma films showed, compared to OD richer coatings, higher numbers of podocyte-like cells. Moreover, the quantification confirmed that the number of podocyte-like cells was highest at substrate portions with highest AuNP density, regardless of the AuNP size.

As expected, mKSCs cultured on OD rich plasma coatings differentiated into PTCs as indicated by megalin staining ([Figure 6.23](#)). However, mKSC differentiation into PTCs appeared to be independent of nanotopography density gradients.

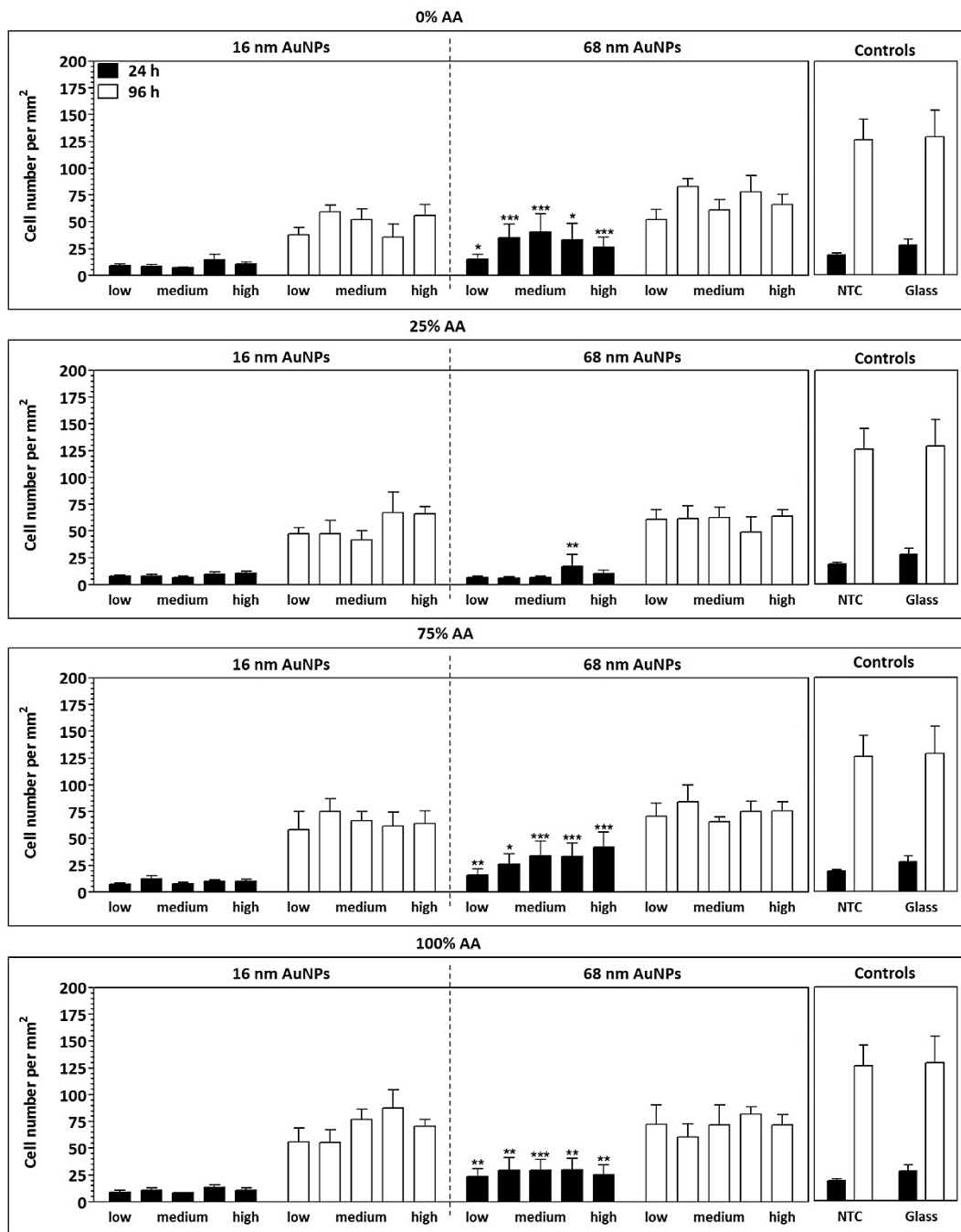


Figure 6.20: mKSC proliferation on AuNP density gradients over coated with plasma. Cells were seeded at a density of 1×10^3 cells / well. Cell number was determined at 24 and 96 h post seeding. Results represent the mean of three biological replicates \pm SEM. A glass and a no-topography sample (NTC, 100% AA without AuNPs) were used as controls. Asterisks indicate significant difference between cells cultured on 68 nm AuNPs compared to the equivalent portion of the gradient coated with 16 nm AuNPs (Tukey model, $p < 0.05$).

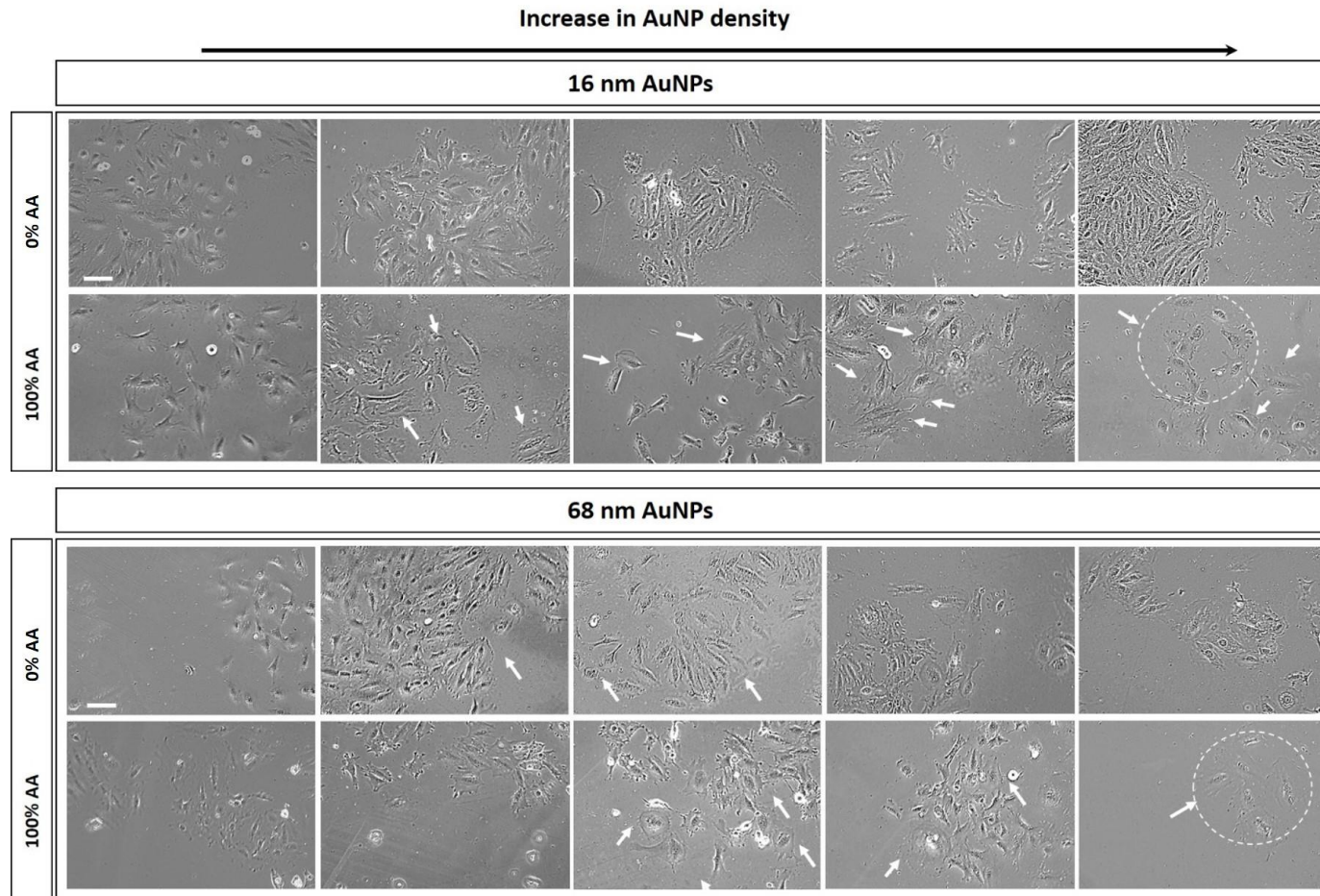


Figure 6.21: Representative phase contrast images of mKSCs cultured for 96 h on AuNP density gradients that were over coated with either 100% AA (representative for 75% AA) and 0% AA (representative for 25% AA) plasma. Cells were seeded at a density of 1×10^3 cells / coverslip. Scale bar is 100 μ m.

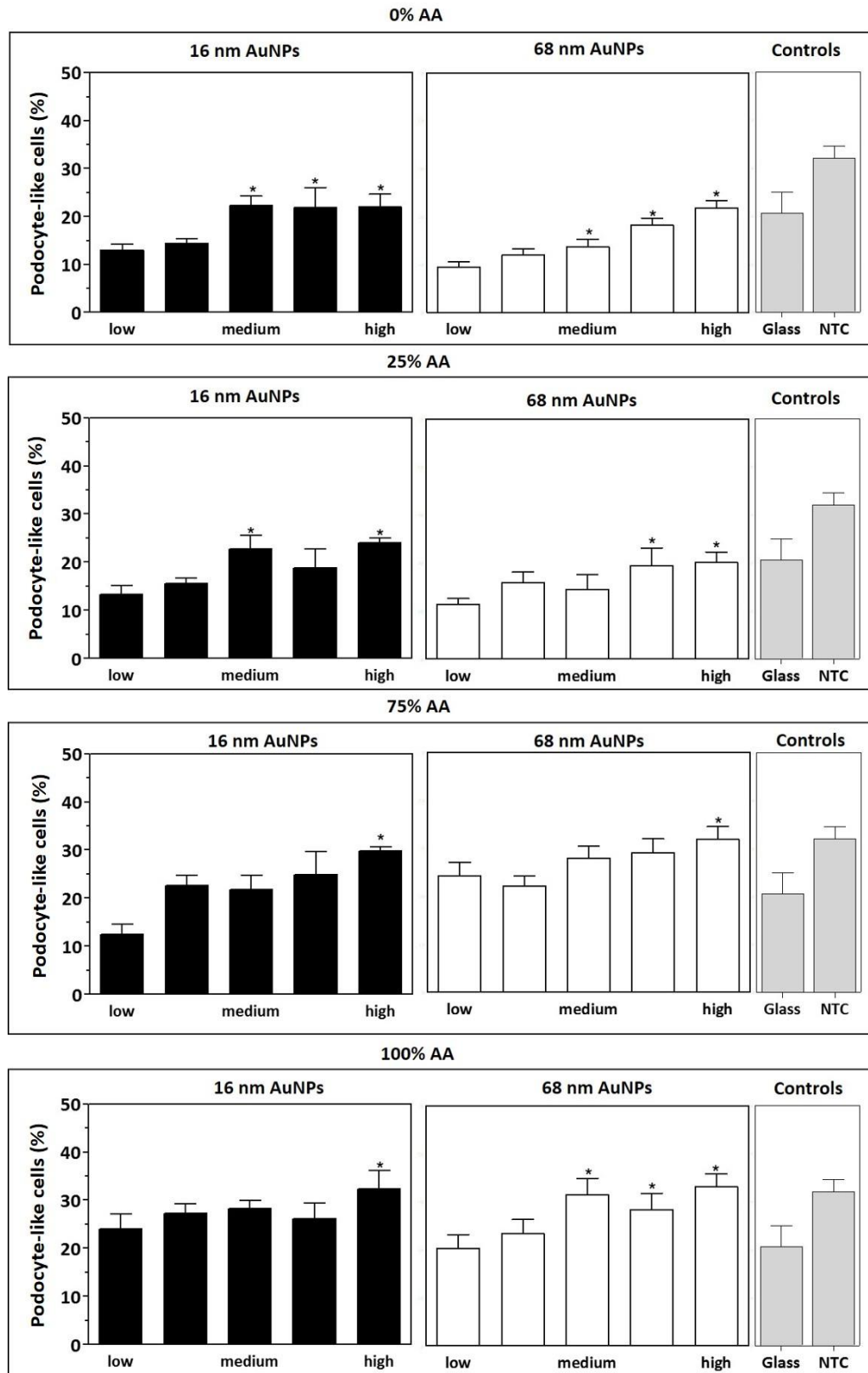


Figure 6.22: Quantification of podocyte-like cells on AuNP density gradient substrates over coated with plasma. mKSCs were seeded at a density of 1×10^3 cells / well. A glass and a no-topography sample (NTC, 100% AA without AuNPs) were used as controls. Asterisks indicate significant difference compared to the portion of the substrates with the lowest AuNP density (Tukey model, $p < 0.05$). Results represent the mean of three biological replicates \pm SEM.

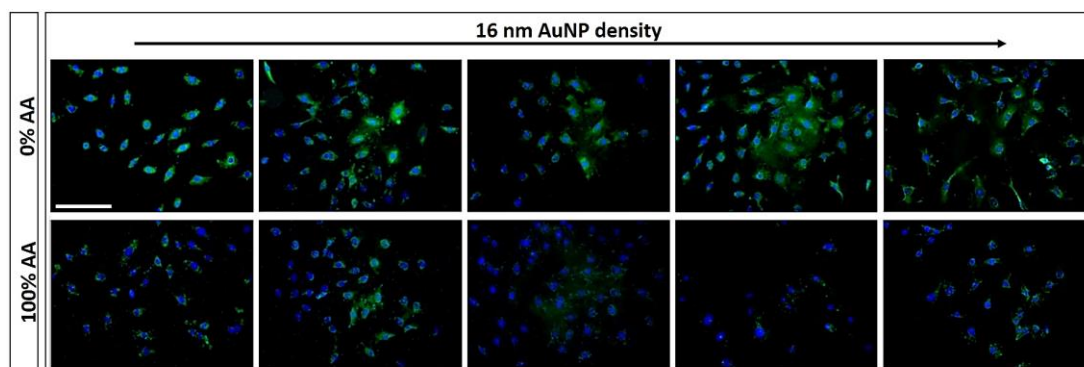


Figure 6.23: Megalin staining. Blue: DAPI. mKSCs were seeded at a density of 1×10^3 cells / coverslip on a 16 nm AuNP density gradient (representative for 68 nm AuNPs). Images display mKSCs that were seeded on 0% AA coated gradients (representative for 25% AA) and 100% AA coated gradients (representative for 75% AA). Scale bar: 100 μ m.

6.3 Discussion

6.3.1 Effect of surface chemistry on mouse kidney-derived stem cells

Firstly isolated from a neonatal mouse kidney, the mKSC line was shown to spontaneously generate podocyte-, mesangial – and proximal tubule like cells *in vitro* [249, 251]. These cells were also capable of differentiating into non-renal cells, such as adipocytes, osteocytes or chondrocytes under appropriate cell culture conditions [7, 13, 250, 271, 345, 408]. This study was aimed on identifying plasma polymer coatings, composed of AA and OD that direct the differentiation of mKSCs into specialised renal cell lines, podocytes or PTCs.

The mKSCs proliferated and showed the characteristic mKSC morphology on all substrates and across the gradient. As the cell number was similar on all substrates 24 h post seeding, an initial homogeneous distribution of cells across the substrates was assumed. However, on gradients the cell number showed a trend to increase towards the middle portion. A reason could be that cells were proliferating faster in this region. However, such a trend was not observed on 50% AA copolymers which should be approximately equal in terms of physicochemical properties. On the other hand, this phenomenon could also be explained with cell migration in response to gradual changes of substrate properties. Cell migration is

a common process in *in vivo* that takes part in a number of physiological and pathological processes, including angiogenesis, tumour metastasis and wound healing [518-522]. Therefore, cells respond to external physicochemical properties and stimuli often with migration that is generally accompanied by cytoskeletal changes, extension of membranes (such as lamellipodia and filopodia) and the formation of protrusions [523]. The resulting counter-forces between cells and substrates allow cell attachment to the surfaces and can promote cell migration [524].

Cells often respond to stimuli gradients *in vivo*, such as biophysical cues that include durotaxis (cell migration in response to surface rigidity gradients), mechanotaxis (the directed cellular movement in response to mechanical cues) and chemotaxis (cell movement in response to chemical stimuli) [514, 525-528]. These processes are often difficult to explore *in vitro* and therefore increase interest in developing biomaterials that mimic gradual changes of surface physicochemical properties for high throughput screening of cells. Particularly substrate stiffness gradients have been increasingly recognised in terms of supporting cell migration and differentiation [529, 530]. However, the physicochemical analyses of plasma substrates did not show any significant differences in terms of elasticity nor topography, which is why this trend of migration was correlated to changes in surface chemistry. Surface chemistry can have striking effects on cellular behaviour. For example, it was shown that human lung cancer cells change their metastatic behaviour and migration in response to different functional groups with preference to migrate towards -COOH and -NH₂ rich areas [531]. Neural stem cells were shown to migrate on -OH rich surfaces [532] and adipose-derived stromal cells migrate reinforced in the presence of -CH₃ functional groups in which their identity also influences the migration speed [533]. These data show that changes in surface chemistry may allow cells to migrate towards a favoured position [534].

Within this study it was also found that mKSCs showed larger spread and a podocyte-like morphology when cultured on AA richer substrates / regions. These cells were often binuclear and voluminous with an arborised well-developed cytoskeleton and large foot processes [214, 215, 250]. This trend was also observed on gradients. This was confirmed by analysing the cellular morphology and quantification of these podocyte-like cells that showed an average of about 30% differentiated cells on AA rich substrates / regions 96 h post seeding compared to about 15% on OD richer substrates. These podocyte-like cells also expressed the characteristic marker nephrin.

On substrates with higher OD content a larger number of proximal tubule cells (PTCs) were identified. About 30% of mKSCs cultured on OD rich substrates were megalin positive, compared to about 10% on the control. These cells were also functional as confirmed by an albumin uptake assay. Although also on gradients significantly more megalin expressing cells were present on the OD rich side there was also a high number of PTCs found towards the middle portions, where about 35% of the cells expressed megalin. This could be related to the cell density.

It has recently been shown that MSC attachment to plasma gradients was highly dependent on surface chemistry and caused the formation of a cell density gradient along the substrate [56]. This effect became negligible during long term cell culture as a result of cell migration and proliferation. It was also found that the cells differentiated into adipocytes and osteocytes, although it was emphasised that this could be a result of increased cell density. Particularly osteogenic differentiation was found in areas with high cell densities [56]. Similar effects have been shown on other cell types before [56, 535-538]. Similar results were obtained within this study. mKSCs showed higher cell density in the middle portion of the gradient. This increased cell density have influenced cell differentiation towards PTCs on gradients, whereas podocyte differentiation was independent of it. During the course of this

study it was generally noticed that the cell density was a contributing factor for mKSC differentiating into PTCs, for which reason mKSCs were initially seeded at low densities and the cell culture period was kept short.

However, surface chemistry that is generally accompanied by changes in wettability, had the largest impact on cell differentiation. A number of groups have shown enhanced cell adhesion on hydrophilic surfaces [65, 66]. For example, fibroblasts were found to display rounded, largely spread morphology, highly organised actin stress fibers and a large number of focal adhesions on hydrophilic surfaces, whereas they were smaller with bipolar morphology, minimal actin fibers and only little focal adhesions on hydrophobic surface [539]. Adipose derived stromal cells spread largely on positively charged amine groups and neutral hydroxyl groups, whereas they were displayed a smaller phenotype and differentiated towards adipocytes on $-CH_3$ functional groups [533]. This resembles the results found in this study. AA rich, hydrophilic surfaces showed a larger number of cells with a voluminous body that displayed increased cell spread and a podocyte-like morphology, whereas cells on the more hydrophobic, carbon rich substrates were rather maintaining their initial phenotype, did not spread as much and expressed PTC markers.

Also protein adsorption to substrates might have had an impact on cell differentiation [539]. The presence of surface functional groups can influence conformation of adsorbed proteins and therefore cell attachment, differentiation and also migration [77, 533, 540, 541].

Gene expression analyses showed a trend for higher podocyte gene expression on AA rich surfaces and, vice versa, PTC gene expression on hydrocarbon richer surfaces. A possible explanation is that, in order to gain enough cDNA for subsequent analyses, we combined cell material from 3 coverslips for each replicate. This could have caused an error and therefore covered significant differences as all protein analyses were accomplished on single coverslip replicates. In addition, it has to be noted that gene expression is controlled by a number of

factors, including transcriptional and post-transcriptional regulation [409-411]. The half-life of various proteins can range from minutes to days and is therefore often larger than the degradation rate of mRNAs. Moreover, the rate of mRNA transcription is lower than the rate of protein translation [412]. Furthermore, protein concentration itself is influenced by various parameters, such as synthesis and cleavage. Therefore it is possible to have low mRNA expression but high concentration of protein, i.e. if a protein directly influences its own expression [413].

6.3.2 Effect of surface topography on mouse kidney-derived stem cells

The above described results have shown that surface chemistry directed mKSC differentiation into specialised renal cell types, namely podocytes and PTCs.

However, it is well-known that cellular response can also be effected by surface topography [86, 542]. In order to investigate whether surface topographical cues have effects on mKSCs behaviour and the extent of differentiation, glass coverslips were coated with gold nanoparticles (AuNPs), 16 or 68 nm in size, either with homogeneous density or in form of density gradients, and overcoated with plasma polymers that were shown to effect mKSC differentiation: AA rich coatings, as these directed mKSC differentiation into podocytes (100% AA and 75% AA / 25% OD) and hydrocarbon rich coatings (100% OD and 75% OD / 25% AA) as these coatings directed mKSC differentiation into PTCs⁵. The AuNP density on the densest portion of the gradients equalled the density on homogeneous coatings.

The results showed that surface topography did not have a significant impact on cell proliferation. In terms of cell differentiation, hydrocarbon rich surfaces were confirmed to direct mKSC differentiation into PTCs, but neither AuNP size nor density had a significant

⁵ This work was part of a collaborative project with Ass. Prof. Krasimir Vasilev and Dr. Melanie Ramiasa, University of South Australia. The physicochemical characterisation of these surface has been accomplished by the collaborators.

effect on mKSC differentiation into PTC. The results also confirmed that AA rich substrates directed mKSC differentiation into podocytes. Nanoparticle size did not appear to influence cell differentiation, as a similar amount of podocyte-like cells was found on 16 nm and 68 nm AuNPs coated substrates. However, it was found that a change in surface topography (AuNP density gradients) resulted in the presence of significantly more podocyte-like cells towards the AuNP denser portions of these gradients. This trend was observed regardless of the plasma overcoating. It has to be noted that the AuNP density on homogeneous substrates equalled the density on the densest portions of the gradients. Therefore we can correlate this increased amount of podocyte-like cells on gradients with the presence of a gradient itself. Nanotopography was shown to effect gene expression and cell differentiation of various cell types in the past [44, 99, 543, 544]. Cells can respond to local variations in topography with morphological and cytoskeletal changes [534]. For example, embryonic stem cells (ESCs) and MSCs differentiated into neuronal lineages when cultured on substrates with nanogratings [99, 545]. MSCs were also shown to differentiate into osteocytes when cultured on topographically irregular substrates, whereas no differentiation was observed on fully ordered nanopits [544]. As discussed before ([chapter 4.3.2](#), p 137) with polyacryales, also here there might have been an effect of the spatial distribution of these AuNPs and the degree of disorder. However, this will not be further discussed as all surface analyses were accomplished by collaborators (unpublished work, *Ramiasa et al.*, 2016).

However, it is interesting that the AuNP density gradients had an impact on mKSC differentiation into podocyte-like cells, whereas homogenous AuNP density did not have a significant impact. This suggests that the presence of a AuNP density gradient was the driving factor for cell differentiation into podocytes in this study. Cells recognise their environment and will responds to the presented features as shown here by introducing topographical cues. For example, fibroblast explore a substrate with filopodia on their cell laminae and,

once a suitable area is found, the cell-substrate contact is stabilised through the recruitment of microtubules and formation of focal adhesions and mature actin fibres [546]. Therefore, the presence of a gradient may allow mKSCs to adapt their morphology in response to these changes, the increase of AuNP density (and therefore topographical cues) and promote the development of the podocyte characteristic morphology.

Lastly, also protein adsorption might have effected these results. Surface topography can critically influence substrate-protein interactions and therefore cell response [547]. This is supported by recent research that has shown that the nanotopography does not necessarily influence cell behaviour in serum free medium [93]. However, this effect was not further investigated.

6.4 Conclusions

In this study plasma polymer coated surfaces composed of AA and OD were investigated for their ability to influence behaviour and differentiation of mKSCs. The results showed that mKSCs cultured on AA richer surfaces were to a high extent largely spread, voluminous, displayed a podocyte-like morphology and expressed characteristic markers. mKSCs on OD differentiated to a higher extent into PTCs as was evidenced by the expression of characteristic PTC markers and *in vitro* functionality. As substrate elasticity and topography did not differ between substrates it was concluded that mKSC differentiation was a result of the surface chemical composition and the accompanied differences in wettability,

The incorporation of gold nanoparticles (AuNPs) underneath promising plasma coatings allowed us to explore whether nanotopographic cues would inhibit or enhance mKSC differentiation additionally. Homogeneous density AuNP coating did not have a significant effect on cell differentiation. However, on AuNP density gradients a higher number of podocyte-like cells was found on substrate portions with higher AuNP density. This trend was consistent for 16 and 68 nm and all plasma coatings. However, the final number of podocyte-

like cells was highest on AA richer substrates. Nanotopography did not have an effect on PTCs differentiation, as we did not find significant evidence of increased differentiation into PTC in response to AuNP size nor density.

7 Concluding remarks and future work

Proximal tubule cells (PTC) and podocytes play a key role in the pathogenesis of kidney glomerular and tubular dysfunction leading to kidney diseases [234, 548, 549]. Currently the only treatment options are dialyses or organ replacement. In addition, present drug therapies cannot prevent further damage but only delay disease progress. A limitation is also that patients often respond to these drugs by developing side effects. Therefore there is a high demand for novel therapeutic options to improve the outcome of patients suffering from renal disease.

Some promising concepts to treat renal pathologies include direct treatment with stem cells [550]. In this respects, therapies using pluripotent stem cells (embryonic stem cells and induced pluripotent stem cells) are encouraging [168].

On the other hand, employing kidney (progenitor) cells derived from kidney tissue may offer an alternative for the treatment of renal disorders [551]. The development of conditionally immortalised cell lines has been a great progress in terms of developing suitable cellular models to study renal disease processes. However, such genetically modified cell lines often do not represent the characteristics that are expected from specialised cells *in vivo*. Moreover, cells that were isolated from kidney tissue have limitations, including limited availability of these mature cells and the difficulty of expanding them in culture. Recently also the potential of urine-derived kidney cells has been highlighted as urine contains various renal cells including specialised and progenitor cells that can be harvested [552]. If tissue or urine derived kidney stem/progenitor cells could be expanded and differentiated *in vitro* into mature and functional kidney cells, many of these impediments could be overcome. This would offer great advances as it would allow the study of renal (patho) physiological

processes, but also assist in the discovery of better drugs to treat renal pathologies and would therefore also be advantageous for the development of personalised medicine.

In this respect biomaterial cell culture substrates can provide further assistance, as their – often tuneable – physicochemical properties are well now to influence cell response [38]. Biomaterials could offer a solution to allow not only long-term culture of renal cells, but also the generation of differentiated cells *in vitro* from kidney-derived progenitor cells. In addition, such advances would assist in the development of novel drug therapies, provide scale-up opportunities for drug screening to predict eventual drug toxicity and, in the future, may support the *ex vivo* treatment of cells for subsequent transplantation.

The wide range of biomaterials and the ease of modifying their physicochemical properties led to a rapid evolution of novel biomaterials in recent years. In the current work, two different types of biomaterials were investigated for their use in overcoming the aforementioned problems: (1) polyacrylates, polymeric substrates that mimic common *in vivo* cell binding motifs stereochemically and (2) plasma polymer substrates composed of allylamine (AA) and octadiene (OD). These substrates were then compared about their ability to influence cell culture and differentiation of kidney-derived stem cells *in vitro*.

7.1 Polyacrylates

7.1.1 Key findings

- (1) Polyacrylates differed in chemical / surface functional group composition. The wettability analyses showed that substrates were generally hydrophobic with exception of ESP 008, ESP 009 ad ESP 010 which were rather hydrophilic. Topographical analyses showed that all substrates differed in micro roughness (hill height) and nano RMS roughness, but not in elasticity.

- (2) Non- direct and direct contact studies using mouse fibroblasts (L929) and bovine endothelial cells (BAE) were performed to investigate substrate cytotoxicity. None of the polyacrylates were cytotoxic. However, cells cultured on ESP 008, ESP 009 and ESP 010 had a rounded morphology and appeared to decrease in cell number over time.
- (3) mKSC behaviour and differentiation was analysed on: ESP 003, ESP 004, ESP 007 and BTL15. All four substrates supported cell proliferation and viability. Moreover, two substrates showed a desirable response: ESP 003 directed mKSC differentiation into podocytes (40%), whereas ESP 007 directed mKSC differentiation into functional PTCs (40%). mKSCs on controls (glass and TCP) were differentiated to an extent of about 10%, which was attributed to spontaneous differentiation. The results suggested that both, surface chemistry and nanotopography, were key factors for mKSC differentiation.
- (4) The culture of conditionally immortalised podocytes (ciPodocytes) and PTCs (ciPTCs) showed similar results as cytotoxicity studies. All polyacrylates supported cell growth and the expression of characteristic markers with exception of ESP 008, ESP 009 and ESP 010, where cells were rounded and decreased in cell number over time.
- (5) Fetal and infant kidney-derived cells were sorted to be either double positive (DP) or double negative (DN) for two putative kidney stem cell markers: CD24 and CD133. Based on previous findings, three polyacrylates, ESP 003, ESP 007 and ESP 011, were investigated for their ability to influence behaviour and differentiation of these four cell types. The results showed that DN and DP cells differed in their cell response to biomaterial substrates. However, no indication of cell differentiation was found regardless of the substrate.

7.1.2 Applications and future work

The use of these polyacrylates has been shown previously in a number of potential biological applications. They were shown to effect cell adhesion and proliferation of human aortic endothelial cells and coronary artery smooth muscle cells and therefore have potential applications for the company's propriety coronary stent coatings [305-307]. In another study a number of polyacrylates was shown to direct MSC differentiation into specialised cells [13, 345]. The here propounded key findings also showed that polyacrylates were very suitable biomaterial substrates to direct mKSC differentiation.

All polyacrylate substrates were individually designed to mimic stereochemically the structure of particular *in vivo* cell attachment motifs. For example, ESP 003, ESP 004, ESP 007 and ESP 011 mimicked RGD, a three amino acid sequence (Arginine-Glycine-Aspartic acid) that is commonly found in proteins such as fibrinogen and laminin [312]. However, all substrates effected cell differentiation differently. For example, ESP 004 mimicked RGD using $-\text{COOH}$ and $-\text{NH}_2$ functional groups, whereas in ESP 007 mimicked RGD using $-\text{OH}$ and $-\text{NH}_2$ functional groups, but both substrates had the exact same (theoretical) stereochemistry and only differed in the identity of a single acrylate monomeric unit. However, one promoted cell differentiation into podocytes and the other one into PTCs. This highlighted the importance of the biomaterial-cell interphase in terms of cell response. Therefore, polyacrylates can assist in developing synthetic substrates in high purity and that mimic the natural cellular environment closely in a novel way. In addition, the unique composition and synthesis of substrates can allow to develop substrates that mimic amino acid sequences of proteins that are particularly common in specific tissues and therefore may improve the outcome of further studies. The advantage of the here described polyacrylates is that their design is precisely tuned theoretically and therefore a large number of biological motifs can be imitated easily and inexpensively. For example, the glomerular basement membrane that

lies between glomerular endothelial cells and podocytes, is composed of four major protein components: laminin, type IV collagen, nidogen, and heparan sulfate proteoglycans (i.e. agrin and perlecan) [553, 554]. If the polyacrylates would be designed to mimic specific signalling sequences from these molecules, this might increase the rate of kidney progenitor/stem cell differentiation and – in the course – for further use in the field of pharmaceutical studies and in regenerative medicine.

However, although the design of polyacrylates is theoretically quite accurate (choice of monomers, theoretical calculation of reaction parameters) it would still be of great interest to see which functional groups are in fact present at the immediate substrate-cell interface as theory and practice may vary. During the course of this study also other surface analytical methods were applied in order to obtain more information about the substrate-cell interphase. These included scanning electron microscopy (further topographical analyses), solid state magnetic resonance spectroscopy (polymer structure, chemical environment of molecules) and Raman spectroscopy (analyses of vibrational, rotational, low-frequency modes). Although these methods were not suitable to give exact information of the substrate-air (or substrate-cell) interface, it would be worth investigating other methods for further and more precisely analyse this interface.

Lastly, a number of studies have investigated the importance of biomaterial dimensions to influence cell behaviour. The use of more complex and *in vivo* – analogue 3D matrices has gained much recognition compared to the rather conventional 2D cell culture systems [555-557]. As polyacrylates were shown to have very encouraging potential for influencing cell behaviour and differentiation *in vitro*, their application in 3D scaffoldings may be very promising and improve the outcome of future studies in terms of developing materials that allow high percentages of differentiated cells to be obtained to further our understanding of pathophysiology's and for future use in drug discovery programmes [558-561].

7.2 Plasma polymer coatings

7.2.1 Key findings

- (1) The physicochemical analyses of plasma polymer coatings composed of allylamine (AA) and octadiene (OD) showed differences in the chemical composition. An increase of AA concentration caused an increase in the presence of nitrogen and oxygen species (surface oxidation). The increasing number of these hydrophilic groups caused in turn an increased wettability. No differences in topography nor elasticity were detected.
- (2) mKSCs showed similar proliferation and viability on all substrates. However, AA richer surfaces directed mKSCs differentiation into podocytes (30%), whereas OD rich surfaces directed cell differentiation into PTCs (30%). mKSCs on controls (glass and TCP) showed about 10% differentiated cells which was attributed to spontaneous differentiation. This trend of differentiation was confirmed on AA-OD plasma gradients.
- (3) mKSC behaviour was additionally analysed on gold nanoparticle (AuNP) coated substrates (diameter 16 or 68 nm) overcoated with promising plasma polymers composed of AA and OD. This allowed to investigate the influence of nanotopography on mKSC behaviour [95]. Homogeneous AuNP density coatings (AuNP density equivalent to portions with highest density on the gradients) did not have significant effects on mKSC differentiation. However, an AuNP density gradient revealed a higher number of podocytes on denser portions of the substrates on both, 16 and 68 nm AuNPs (30 to 40%). These findings suggested that AuNP density (topography) itself enhanced cell differentiation into podocytes, whereas it had no effect on PTC differentiation.

7.2.2 Applications and future work

The use of the here investigated plasma polymers has been shown previously in a number of potential biological applications. In particular, the concept of physicochemical surface gradients has gone a long way, from simple surface modification to cost efficient biomaterial platforms that allow screening of cellular behaviour in large scale on a single substrate (gradients) [562].

The promising results of this study open possibilities to explore systems with other plasma precursors. Within this study it was found that surface chemistry, particularly nitrogen functional groups can influence mKSC differentiation. It would be interesting to investigate whether this effect would be enhanced by using other nitrogen containing plasma polymers such as ethylenediamine, diaminocyclohexane or cyclopropylamine (CPA), an AA isomer that leads to the deposition of a higher number of amine groups than for example AA and has the essential film stability [455, 563-567].

Another interesting approach would be the application of plasma polymers onto other structures, as shown within this study where AuNPs were employed to introduce topographical cues, but surface chemistry was maintained by overcoating these substrates with plasma. In the future, such promising plasma polymers could enable the chemical modification of 3D structures /scaffolds to influence cell behaviour [568-570].

Of particular interest in this study was the cell behaviour on AA-OD gradients. We found that mKSC differentiation followed the same trend on homo- and copolymers as on gradients. Only little is known yet about cell response on surfaces with gradual changing chemistry. Such materials would enable the study of numerous cell types on a single substrate and therefore allow to circumvent the time consuming and expensive production and research on single substrates to find the desired surface properties for a single cell type.

Moreover, it would be interesting to compare the available data to another plasma pattern. i.e. radial or in form of distinct patterns [517, 571].

7.3 Final Remarks

Within this study two constitutional different materials were investigated. Polyacrylates are solid and highly defined polymers that are specifically designed to mimic structurally cell binding motifs. Plasma polymers on the other hand are a different state of matter and display a rather uncontrolled and random occurrence of surface functional groups [505]. During this study both substrates were shown to influence cell behaviour and differentiation. However, it was challenging to relate a particular substrate property to mKSC differentiation. For example, the results of mKSC differentiation on polyacrylates suggested that a combination of surface chemistry and nanoroughness induced cell differentiation. On plasma polymers on the other hand no significant differences in topography were detected, but the density of nitrogen functional groups appeared to effect cellular differentiation into specialised cells.

However, there is a scope of further analyses. The chemical surface investigation of (nano) topography, surface chemistry and elasticity were not performed in aqueous environment. The exposure to such an aqueous environment may have caused the reorganisation of the polymer bulk and surface functional groups at the direct solid-liquid interface. Moreover, the penetration of water molecules into the polymer bulk may have caused topographical and mechanical changes. For example, it has recently been shown that plasma layers composed of hexane and AA undergo topographical changes in aqueous solution which resulted in pore formation almost immediately after immersion in the liquid, which suggested segregation of the material through liquid penetration [96]. Other groups have observed similar surface changes [469, 499]. Such processes process could also occur within the here investigates substrates as well.

In addition, it would be interesting to investigate protein adsorption onto substrates further as a large number of these is present in serum and the interactions between proteins with surfaces and with each other are complex. The affinity of some proteins towards surfaces may vary between substrates which could influence protein conformation and – in turn – cell response [378]. Some proteins, such as fibronectin and fibrinogen have been shown to promote cell adhesion whereas others, such as albumin, rather inhibited it [30, 572]. However, the analyses of proteins and their conformation onto surfaces is challenging and was not investigated within this study [573-576].

Finally it has to be mentioned that mKSCs were only cultured for 96 h on substrates. No experiments were conducted at longer periods of time, but may lead to a larger pool of differentiated cells.

This study emphasised the potential of both, polyacrylates and plasma polymers, as potential platforms for kidney (stem) cell culture and differentiation. A number of substrates within the range of both materials had a significant impact on cell differentiation into specialised renal cells. Therefore they hold great promise for physiologic and pharmacological studies, but also in the field of regenerative medicine in the future.

8 References

1. Harvey, G., et al., *Editor's choice: Improving the identification and management of chronic kidney disease in primary care: lessons from a staged improvement collaborative*. International Journal for Quality in Health Care, 2015. **27**(1): p. 10.
2. Stevens, P., et al., *Chronic kidney disease management in the United Kingdom: NEOERICA project results*. Kidney International, 2007. **72**(1): p. 92-99.
3. Lasagni, L. and P. Romagnani, *Basic research: Podocyte progenitors and ectopic podocytes*. Nature Reviews Nephrology, 2013.
4. Romagnani, P. and G. Remuzzi, *CD133 + renal stem cells always co-express CD24 in adult human kidney tissue*. Stem cell research, 2014. **12**(3): p. 828-829.
5. Angelotti, M.L., et al., *Characterization of Renal Progenitors Committed Toward Tubular Lineage and Their Regenerative Potential in Renal Tubular Injury*. Stem Cells, 2012. **30**(8): p. 1714-1725.
6. Sagrinati, C., et al., *Isolation and characterization of multipotent progenitor cells from the Bowman's capsule of adult human kidneys*. Journal of the American Society of Nephrology : JASN, 2006. **17**(9): p. 2443-2456.
7. Ronconi, E., et al., *Regeneration of Glomerular Podocytes by Human Renal Progenitors*. Journal of the American Society of Nephrology, 2009. **20**(2): p. 322-332.
8. Helsen, J.A. and H. Jürgen Breme, *Metals as biomaterials*. Metals as Biomaterials, by Jef A. Helsen (Editor), H. Jürgen Breme (Editor), pp. 522. ISBN 0-471-96935-4. Wiley-VCH, October 1998., 1998: p. 522.
9. Ohgushi, H. and A.I. Caplan, *Stem cell technology and bioceramics: From cell to gene engineering*. Journal of Biomedical Materials Research, 1999. **48**(6): p. 913-927.
10. Lam, M.T. and J.C. Wu, *Biomaterial applications in cardiovascular tissue repair and regeneration*. Expert review of cardiovascular therapy, 2012. **10**(8): p. 1039-1049.
11. Goda, T. and K. Ishihara, *Soft contact lens biomaterials from bioinspired phospholipid polymers*. Expert review of medical devices, 2006. **3**(2): p. 167-174.
12. Holmes, T.C., *Novel peptide-based biomaterial scaffolds for tissue engineering*. Trends in Biotechnology, 2002. **20**(1): p. 16-21.
13. Glennon-Alty, L.J., *Developing synthetic polymer substrates for stem cell*, 2012, University of Liverpool.
14. Sionkowska, A., *Current research on the blends of natural and synthetic polymers as new biomaterials: Review*. Progress in Polymer Science, 2011. **36**(9): p. 1254-1276.
15. Pérez, R.A., et al., *Naturally and synthetic smart composite biomaterials for tissue regeneration*. Advanced drug delivery reviews, (0).
16. Ha, T.L.B., et al., *Naturally derived biomaterials: Preparation and application*. Regenerative medicine and tissue engineering, 2013: p. 247-274.
17. Singh, A. and J. Elisseff, *Biomaterials for stem cell differentiation*. Journal of Materials Chemistry, 2010. **20**(40): p. 8832.
18. Vasilev, K., et al., *Tunable antibacterial coatings that support mammalian cell growth*. Nano letters, 2009. **10**(1): p. 202-207.
19. Sengupta, D. and S.C. Heilshorn, *Protein-engineered biomaterials: highly tunable tissue engineering scaffolds*. Tissue Engineering Part B: Reviews, 2010. **16**(3): p. 285-293.
20. Brizzi, M.F., G. Tarone, and P. Defilippi, *Extracellular matrix, integrins, and growth factors as tailors of the stem cell niche*. Current Opinion in Cell Biology, 2012.
21. Trappmann, B., et al., *Extracellular-matrix tethering regulates stem-cell fate*. Nature materials, 2012. **11**(7): p. 642-649.

22. Walters, N.J. and E. Gentleman, *Evolving insights in cell–matrix interactions: Elucidating how non-soluble properties of the extracellular niche direct stem cell fate*. *Acta Biomaterialia*, 2015. **11**: p. 3-16.
23. Cabodi, S., et al., *Integrins and signal transduction*, in *Integrins and Ion Channels* 2010, Springer. p. 43-54.
24. Gittens, R.A., et al., *The effects of combined micron-/submicron-scale surface roughness and nanoscale features on cell proliferation and differentiation*. *Biomaterials*, 2011. **32**(13): p. 3395-3403.
25. Romano, N.H., et al., *Protein-engineered biomaterials: nanoscale mimics of the extracellular matrix*. *Biochimica et Biophysica Acta (BBA)-General Subjects*, 2011. **1810**(3): p. 339-349.
26. Engler, A.J., et al., *Matrix Elasticity Directs Stem Cell Lineage Specification*. *Cell*, 2006. **126**(4): p. 677-689.
27. Discher, D.E., P. Janmey, and Y. Wang, *Tissue cells feel and respond to the stiffness of their substrate*. *Science*, 2005. **310**(5751): p. 1139-1143.
28. Gobin, A.S. and J.L. West, *Cell migration through defined, synthetic ECM analogs*. *The FASEB journal*, 2002. **16**(7): p. 751-753.
29. Kalaskar, D.M., et al., *Characterization of the interface between adsorbed fibronectin and human embryonic stem cells*. *Journal of The Royal Society Interface*, 2013. **10**(83): p. 20130139.
30. Koenig, A.L., V. Gambillara, and D.W. Grainger, *Correlating fibronectin adsorption with endothelial cell adhesion and signaling on polymer substrates*. *Journal of Biomedical Materials Research Part A*, 2003. **64**(1): p. 20-37.
31. Gomes, R.R., Jr., M.C. Farach-Carson, and D.D. Carson, *Perlecan functions in chondrogenesis: insights from in vitro and in vivo models*. *Cells Tissues Organs*, 2004. **176**(1-3): p. 79-86.
32. Robinson, D.E., et al., *Surface gradient of functional heparin*.
33. Iwamoto, Y., et al., *YIGSR, a synthetic laminin pentapeptide, inhibits experimental metastasis formation*. *Science (Classic)*, 1987. **238**(4830): p. 1132.
34. Kleinman, H.K., et al., *Identification of a second active site in laminin for promotion of cell adhesion and migration and inhibition of in vivo melanoma lung colonization*. *Arch Biochem Biophys*, 1989. **272**(1): p. 39-45.
35. Li, Z., et al., *Effects of RGD nanospacing on chondrogenic differentiation of mesenchymal stem cells*. *Journal of Materials Chemistry B*, 2015.
36. Wang, X., et al., *Fabrication of RGD Micro/Nanopattern and Corresponding Study of Stem Cell Differentiation*. *Nano letters*, 2015. **15**(3): p. 1457-1467.
37. Wang, X., et al., *Effect of RGD nanospacing on differentiation of stem cells*. *Biomaterials*, 2013. **34**(12): p. 2865-2874.
38. Murphy, W.L., T.C. McDevitt, and A.J. Engler, *Materials as stem cell regulators*. *Nature materials*, 2014. **13**(6): p. 547-557.
39. O'Neill, J.D., et al., *The regulation of growth and metabolism of kidney stem cells with regional specificity using extracellular matrix derived from kidney*. *Biomaterials*, 2013. **34**(38): p. 9830-9841.
40. Kim, D.H., et al., *Matrix nanotopography as a regulator of cell function*. *J Cell Biol*, 2012. **197**(3): p. 351-60.
41. Ross, A.M., et al., *Physical Aspects of Cell Culture Substrates: Topography, Roughness, and Elasticity*. *Small*, 2012. **8**(3): p. 336-355.
42. Dalby, M.J., et al., *The control of human mesenchymal cell differentiation using nanoscale symmetry and disorder*. *Nature materials*, 2007. **6**(12): p. 997-1003.
43. Dalby, M.J., et al., *Osteoprogenitor response to defined topographies with nanoscale depths*. *Biomaterials*, 2006. **27**(8): p. 1306-1315.
44. McNamara, L.E., et al., *Nanotopographical Control of Stem Cell Differentiation*. *Journal of Tissue Engineering*, 2010. **1**(1).

45. Benoit, D.S.W., et al., *Small functional groups for controlled differentiation of hydrogel-encapsulated human mesenchymal stem cells*. *Nature materials*, 2008. **7**(10): p. 816-823.
46. Curran, J.M., R. Chen, and J.A. Hunt, *The guidance of human mesenchymal stem cell differentiation in vitro by controlled modifications to the cell substrate*. *Biomaterials*, 2006. **27**(27): p. 4783-4793.
47. Holst, J., et al., *Substrate elasticity provides mechanical signals for the expansion of hemopoietic stem and progenitor cells*. *Nature Biotechnology*, 2010. **28**(10): p. 1123-1128.
48. Williams, D.F., *On the mechanisms of biocompatibility*. *Biomaterials*, 2008. **29**(20): p. 2941-2953.
49. Zheng, W., W. Zhang, and X. Jiang, *Precise Control of Cell Adhesion by Combination of Surface Chemistry and Soft Lithography*. *Adv Healthc Mater*, 2012. **13**(10): p. 201200104.
50. Chen, C.S., X. Jiang, and G.M. Whitesides, *Microengineering the environment of mammalian cells in culture*. *Mrs Bulletin*, 2005. **30**(03): p. 194-201.
51. Gandavarapu, N.R., et al., *Extracellular matrix protein adsorption to phosphate-functionalized gels from serum promotes osteogenic differentiation of human mesenchymal stem cells*. *Acta Biomaterialia*, 2013. **9**(1): p. 4525-4534.
52. Uygun, B.E., S.E. Stojich, and H.W. Matthew, *Effects of immobilized glycosaminoglycans on the proliferation and differentiation of mesenchymal stem cells*. *Tissue Engineering Part A*, 2009. **15**(11): p. 3499-3512.
53. NIKITOVIC, D., et al., *Effects of Glycosaminoglycans on Cell Proliferation of Normal Osteoblasts and Human Osteosarcoma Cells Depend on their Type and Fine Chemical Compositions*. *Anticancer Research*, 2005. **25**(4): p. 2851-2856.
54. Tsutsumi, S., et al., *Retention of multilineage differentiation potential of mesenchymal cells during proliferation in response to FGF*. *Biochemical and biophysical research communications*, 2001. **288**(2): p. 413-419.
55. Mei, Y., et al., *Combinatorial development of biomaterials for clonal growth of human pluripotent stem cells*. *Nature materials*, 2010. **9**(9): p. 768-778.
56. Wang, P.-Y., et al., *Screening rat mesenchymal stem cell attachment and differentiation on surface chemistries using plasma polymer gradients*. *Acta Biomaterialia*, 2015. **11**: p. 58-67.
57. Yang, J., et al., *Polymer surface functionalities that control human embryoid body cell adhesion revealed by high throughput surface characterization of combinatorial material microarrays*. *Biomaterials*, 2010. **31**(34): p. 8827-8838.
58. Whittle, J.D., et al., *A method for the deposition of controllable chemical gradients*. *Chemical Communications*, 2003(14): p. 1766-1767.
59. Hallab, N., et al., *Cell adhesion to biomaterials: correlations between surface charge, surface roughness, adsorbed protein, and cell morphology*. *Journal of long-term effects of medical implants*, 1994. **5**(3): p. 209-231.
60. Arcangeli, A., et al., *Polar/apolar compounds induce leukemia cell differentiation by modulating cell-surface potential*. *Proceedings of the National Academy of Sciences*, 1993. **90**(12): p. 5858-5862.
61. Schneider, G.B., et al., *The effect of hydrogel charge density on cell attachment*. *Biomaterials*, 2004. **25**(15): p. 3023-3028.
62. Makohliso, S.A., R.F. Valentini, and P. Aebischer, *Magnitude and polarity of a fluoroethylene propylene electret substrate charge influences neurite outgrowth in vitro*. *Journal of Biomedical Materials Research*, 1993. **27**(8): p. 1075-1085.
63. Goddard, J.M. and J. Hotchkiss, *Polymer surface modification for the attachment of bioactive compounds*. *Progress in Polymer Science*, 2007. **32**(7): p. 698-725.
64. Xu, L.-C. and C.A. Siedlecki, *Effects of surface wettability and contact time on protein adhesion to biomaterial surfaces*. *Biomaterials*, 2007. **28**(22): p. 3273-3283.
65. Groth, T. and G. Altankov, *Cell-surface interactions and the tissue compatibility of biomedical materials*. DC: ISO Press, Wasington, 1998: p. 12.

66. Satriano, C., E. Conte, and G. Marletta, *Surface chemical structure and cell adhesion onto ion beam modified polysiloxane*. *Langmuir*, 2001. **17**(7): p. 2243-2250.
67. Tamada, Y. and Y. Ikada, *Effect of preadsorbed proteins on cell adhesion to polymer surfaces*. *Journal of colloid and interface science*, 1993. **155**(2): p. 334-339.
68. Wei, J., et al., *Influence of surface wettability on competitive protein adsorption and initial attachment of osteoblasts*. *Biomedical Materials*, 2009. **4**(4): p. 045002.
69. Yildirim, E.D., et al., *Accelerated differentiation of osteoblast cells on polycaprolactone scaffolds driven by a combined effect of protein coating and plasma modification*. *Biofabrication*, 2010. **2**(1): p. 014109.
70. Redey, S.A., et al., *Behavior of human osteoblastic cells on stoichiometric hydroxyapatite and type A carbonate apatite: Role of surface energy*. *Journal of Biomedical Materials Research*, 2000. **50**(3): p. 353-364.
71. Gittens, R.A., et al., *The roles of titanium surface micro/nanotopography and wettability on the differential response of human osteoblast lineage cells*. *Acta Biomaterialia*, 2013. **9**(4): p. 6268-6277.
72. Ayala, R., et al., *Engineering the cell-material interface for controlling stem cell adhesion, migration, and differentiation*. *Biomaterials*, 2011. **32**(15): p. 3700-11.
73. Thian, E., et al., *The role of surface wettability and surface charge of electrosprayed nanoapatites on the behaviour of osteoblasts*. *Acta Biomaterialia*, 2010. **6**(3): p. 750-755.
74. Moller, K., et al., *The influence of zeta-potential and interfacial-tension on osteoblast-like cells*. *Cells and Materials*, 1994. **4**(3): p. 263-274.
75. Khorasani, M., H. Mirzadeh, and S. Irani, *Plasma surface modification of poly (L-lactic acid) and poly (lactic-co-glycolic acid) films for improvement of nerve cells adhesion*. *Radiation Physics and Chemistry*, 2008. **77**(3): p. 280-287.
76. Lee, S.J., et al., *The effect of surface wettability on induction and growth of neurites from the PC-12 cell on a polymer surface*. *Journal of colloid and interface science*, 2003. **259**(2): p. 228-235.
77. Arima, Y. and H. Iwata, *Effect of wettability and surface functional groups on protein adsorption and cell adhesion using well-defined mixed self-assembled monolayers*. *Biomaterials*, 2007. **28**(20): p. 3074-3082.
78. Bumgardner, J., et al., *Contact angle, protein adsorption and osteoblast precursor cell attachment to chitosan coatings bonded to titanium*. *Journal of Biomaterials Science, Polymer Edition*, 2003. **14**(12): p. 1401-1409.
79. Van Oss, C.J., R.J. Good, and M.K. Chaudhury, *The role of van der Waals forces and hydrogen bonds in "hydrophobic interactions" between biopolymers and low energy surfaces*. *Journal of colloid and interface science*, 1986. **111**(2): p. 378-390.
80. Noh, H. and E.A. Vogler, *Volumetric interpretation of protein adsorption: mass and energy balance for albumin adsorption to particulate adsorbents with incrementally increasing hydrophilicity*. *Biomaterials*, 2006. **27**(34): p. 5801-5812.
81. Israelachvili, J. and H. Wennerström, *Role of hydration and water structure in biological and colloidal interactions*. 1996.
82. Vogler, E.A., *Structure and reactivity of water at biomaterial surfaces*. *Advances in Colloid and Interface Science*, 1998. **74**(1-3): p. 69-117.
83. Almaawi, A., et al., *Effect of acetaminophen and nonsteroidal anti-inflammatory drugs on gene expression of mesenchymal stem cells*. *Tissue Engineering Part A*, 2013. **19**(7-8): p. 1039-1046.
84. Stevens, M.M. and J.H. George, *Exploring and engineering the cell surface interface*. *Science*, 2005. **310**(5751): p. 1135-1138.
85. Engel, E., et al., *Mesenchymal stem cell differentiation on microstructured poly (methyl methacrylate) substrates*. *Annals of Anatomy*, 2009. **191**(1): p. 136-144.
86. Park, J., et al., *TiO₂ nanotube surfaces: 15 nm—an optimal length scale of surface topography for cell adhesion and differentiation*. *Small*, 2009. **5**(6): p. 666-671.

87. Chaubey, A., et al., *Surface patterning: tool to modulate stem cell differentiation in an adipose system*. J Biomed Mater Res B Appl Biomater, 2008. **84**(1): p. 70-8.
88. Vagaská, B., et al., *Osteogenic cells on bio-inspired materials for bone tissue engineering*. Physiological Research, 2010. **59**(3): p. 309.
89. De Bartolo, L., et al., *Influence of membrane surface properties on the growth of neuronal cells isolated from hippocampus*. Journal of Membrane Science, 2008. **325**(1): p. 139-149.
90. Zinger, O., et al., *Differential regulation of osteoblasts by substrate microstructural features*. Biomaterials, 2005. **26**(14): p. 1837-1847.
91. Lee, S.J., et al., *Response of MG63 osteoblast-like cells onto polycarbonate membrane surfaces with different micropore sizes*. Biomaterials, 2004. **25**(19): p. 4699-4707.
92. Hatano, K., et al., *Effect of surface roughness on proliferation and alkaline phosphatase expression of rat calvarial cells cultured on polystyrene*. Bone, 1999. **25**(4): p. 439-445.
93. Lim, J.Y., et al., *Human foetal osteoblastic cell response to polymer-demixed nanotopographic interfaces*. Journal of The Royal Society Interface, 2005. **2**(2): p. 97-108.
94. Bettinger, C.J., *Synthesis and microfabrication of biomaterials for soft-tissue engineering*. Pure and Applied Chemistry, 2009. **81**(12): p. 2183-2201.
95. Goreham, R.V., R.D. Short, and K. Vasilev, *Method for the generation of surface-bound nanoparticle density gradients*. The Journal of Physical Chemistry C, 2011. **115**(8): p. 3429-3433.
96. Zelzer, M. and M.R. Alexander, *Nanopores in single-and double-layer plasma polymers used for cell guidance in water and protein containing buffer solutions*. The Journal of Physical Chemistry B, 2009. **114**(1): p. 569-576.
97. Wang, C. and M. Wang, *Electrospun multifunctional tissue engineering scaffolds*. Frontiers of Materials Science, 2014. **8**(1): p. 3-19.
98. Venugopal, J., et al., *Interaction of cells and nanofiber scaffolds in tissue engineering*. Journal of Biomedical Materials Research Part B: Applied Biomaterials, 2008. **84**(1): p. 34-48.
99. Yim, E.K., S.W. Pang, and K.W. Leong, *Synthetic nanostructures inducing differentiation of human mesenchymal stem cells into neuronal lineage*. Experimental Cell Research, 2007. **313**(9): p. 1820-1829.
100. Yim, E.K., et al., *Nanotopography-induced changes in focal adhesions, cytoskeletal organization, and mechanical properties of human mesenchymal stem cells*. Biomaterials, 2010. **31**(6): p. 1299-1306.
101. Bettinger, C.J., et al., *Enhancement of in vitro capillary tube formation by substrate nanotopography*. Advanced Materials, 2008. **20**(1): p. 99-103.
102. Kaivosoja, E., et al., *Chemical and physical properties of regenerative medicine materials controlling stem cell fate*. Annals of Medicine, 2011(0): p. 1-16.
103. Kong, Y.P., et al., *Expression of Oct4 in human embryonic stem cells is dependent on nanotopographical configuration*. Acta Biomaterialia, 2013. **9**(5): p. 6369-6380.
104. Luo, W., S.R. Jones, and M.N. Yousaf, *Geometric Control of Stem Cell Differentiation Rate on Surfaces*. Langmuir, 2008. **24**(21): p. 12129-12133.
105. Flemming, R.G., et al., *Effects of synthetic micro- and nano-structured surfaces on cell behavior*. Biomaterials, 1999. **20**(6): p. 573-88.
106. Carlberg, B., et al., *Electrospun polyurethane scaffolds for proliferation and neuronal differentiation of human embryonic stem cells*. Biomedical Materials, 2009. **4**(4): p. 045004.
107. Nava, M.M., M.T. Raimondi, and R. Pietrabissa, *Controlling Self-Renewal and Differentiation of Stem Cells via Mechanical Cues*. Journal of Biomedicine and Biotechnology, 2012. **2012**.
108. Evans, N.D., et al., *Substrate stiffness affects early differentiation events in embryonic stem cells*. Eur Cell Mater, 2009. **18**(1-13): p. 13-14.
109. Zajac, A.L. and D.E. Discher, *Cell differentiation through tissue elasticity-coupled, myosin-driven remodeling*. Curr Opin Cell Biol, 2008. **20**(6): p. 609-15.

110. Dawson, E., et al., *Biomaterials for stem cell differentiation*. Advanced drug delivery reviews, 2008. **60**(2): p. 215-228.
111. Grinnell, F. and W.M. Petroll, *Cell motility and mechanics in three-dimensional collagen matrices*. Annual Review of Cell and Developmental Biology, 2010. **26**: p. 335-361.
112. Hopp, I., et al., *The influence of substrate stiffness gradients on primary human dermal fibroblasts*. Biomaterials, 2013.
113. Chia, H., M. Vigen, and A. Kasko, *Effect of substrate stiffness on pulmonary fibroblast activation by TGF- β* . Acta Biomaterialia, 2012. **8**(7): p. 2602-2611.
114. Till, J. and E. McCulloch, *A Direct Measurement of the Radiation Sensitivity of Normal Mouse Bone Marrow Cells 1*. Radiation research, 2011. **175**(2): p. 145-149.
115. Odorico, J.S., D.S. Kaufman, and J.A. Thomson, *Multilineage differentiation from human embryonic stem cell lines*. Stem Cells, 2001. **19**(3): p. 193-204.
116. Chamberlain, G., et al., *Concise Review: Mesenchymal Stem Cells: Their Phenotype, Differentiation Capacity, Immunological Features, and Potential for Homing*. Stem Cells, 2007. **25**(11): p. 2739-2749.
117. Lodish, H.F., *Molecular cell biology* 2003, New York: W.H. Freeman and Company.
118. Konstantinov, I.E., *In search of Alexander A. Maximow: the man behind the unitarian theory of hematopoiesis*. Perspectives in biology and medicine, 2000. **43**(2): p. 269-276.
119. Maximow, A., *The lymphocyte as a stem cell, common to different blood elements in embryonic development and during the post-fetal life of mammals*. Folia Haematologica, 1909. **8**: p. 123-134.
120. Becker, A.J., E.A. McCulloch, and J.E. Till, *Cytological demonstration of the clonal nature of spleen colonies derived from transplanted mouse marrow cells*. 1963.
121. Altman, J. and G.D. Das, *Autoradiographic and histological evidence of postnatal hippocampal neurogenesis in rats*. The Journal of Comparative Neurology, 1965. **124**(3): p. 319-335.
122. Martin, G.R., *Isolation of a pluripotent cell line from early mouse embryos cultured in medium conditioned by teratocarcinoma stem cells*. Proceedings of the National Academy of Sciences, 1981. **78**(12): p. 7634-7638.
123. Evans, M.J. and M.H. Kaufman, *Establishment in culture of pluripotential cells from mouse embryos*. Nature, 1981. **292**(5819): p. 154-156.
124. Thomson, J.A., et al., *Isolation of a primate embryonic stem cell line*. Proceedings of the National Academy of Sciences, 1995. **92**(17): p. 7844-7848.
125. Czyz, J., et al., *Potential of embryonic and adult stem cells in vitro*. Biological chemistry, 2003. **384**(10-11): p. 1391-1409.
126. Shroff, G. and R. Gupta, *Human embryonic stem cells in the treatment of patients with spinal cord injury*. Annals of Neurosciences, 2015. **22**(4).
127. Agulnick, A.D., et al., *Insulin-producing endocrine cells differentiated in vitro from human embryonic stem cells function in macroencapsulation devices in vivo*. Stem cells translational medicine, 2015: p. sctm. 2015-0079.
128. Menasché, P., et al., *Human embryonic stem cell-derived cardiac progenitors for severe heart failure treatment: first clinical case report*. European heart journal, 2015. **36**(30): p. 2011-2017.
129. Körbling, M. and Z. Estrov, *Adult Stem Cells for Tissue Repair — A New Therapeutic Concept?* New England Journal of Medicine, 2003. **349**(6): p. 570-582.
130. Caplan, A.I., *Mesenchymal stem cells*. Journal of Orthopaedic Research, 1991. **9**(5): p. 641-650.
131. Caplan, A.I., *Adult mesenchymal stem cells for tissue engineering versus regenerative medicine*. Journal of cellular physiology, 2007. **213**(2): p. 341-347.
132. Smith, C. and B. Storms, *Hematopoietic stem cells*. Clinical orthopaedics and related research, 2000. **379**: p. S91-S97.
133. Seita, J. and I.L. Weissman, *Hematopoietic stem cell: self-renewal versus differentiation*. Wiley Interdisciplinary Reviews: Systems Biology and Medicine, 2010. **2**(6): p. 640-653.

134. Jaiswal, N., et al., *Osteogenic differentiation of purified, culture-expanded human mesenchymal stem cells in vitro*. Journal of cellular biochemistry, 1997. **64**(2): p. 295-312.
135. Barry, F., et al., *Chondrogenic Differentiation of Mesenchymal Stem Cells from Bone Marrow: Differentiation-Dependent Gene Expression of Matrix Components*. Experimental Cell Research, 2001. **268**(2): p. 189-200.
136. Mackay, A.M., et al., *Chondrogenic differentiation of cultured human mesenchymal stem cells from marrow*. Tissue engineering, 1998. **4**(4): p. 415-428.
137. Pittenger, M., et al., *Mesenchymal stem cells*. Human cell culture, 2002: p. 189-207.
138. Pittenger, M.F., et al., *Multilineage potential of adult human mesenchymal stem cells*. Science, 1999. **284**(5411): p. 143-147.
139. Richardson, S.M., et al., *Mesenchymal stem cells in regenerative medicine: focus on articular cartilage and intervertebral disc regeneration*. Methods, 2015.
140. Rookmaaker, M.B., et al., *Development and application of human adult stem or progenitor cell organoids*. Nature Reviews Nephrology, 2015. **11**(9): p. 546-554.
141. Broughton, K.M. and M.A. Sussman, *Empowering Adult Stem Cells for Myocardial Regeneration V2. O Success in Small Steps*. Circulation Research, 2016. **118**(5): p. 867-880.
142. Scadden, D.T., *The stem-cell niche as an entity of action*. Nature, 2006. **441**(7097): p. 1075-1079.
143. Morrison, S.J. and A.C. Spradling, *Stem cells and niches: mechanisms that promote stem cell maintenance throughout life*. Cell, 2008. **132**(4): p. 598-611.
144. Walker, M., K. Patel, and T. Stappenbeck, *The stem cell niche*. The Journal of pathology, 2009. **217**(2): p. 169-180.
145. Discher, D.E., D.J. Mooney, and P.W. Zandstra, *Growth factors, matrices, and forces combine and control stem cells*. Science, 2009. **324**(5935): p. 1673-1677.
146. Zhang, J., et al., *Identification of the haematopoietic stem cell niche and control of the niche size*. Nature, 2003. **425**(6960): p. 836-841.
147. Tumber, T., et al., *Defining the epithelial stem cell niche in skin*. Science, 2004. **303**(5656): p. 359-363.
148. Tavazoie, M., et al., *A specialized vascular niche for adult neural stem cells*. Cell Stem Cell, 2008. **3**(3): p. 279-288.
149. Collins, C.A., et al., *Stem cell function, self-renewal, and behavioral heterogeneity of cells from the adult muscle satellite cell niche*. Cell, 2005. **122**(2): p. 289-301.
150. Enam, S. and S. Jin, *Substrates for clinical applicability of stem cells*. World Journal of Stem Cells, 2015. **7**(2): p. 243-252.
151. Frith, J.E., B. Thomson, and P.G. Genever, *Dynamic three-dimensional culture methods enhance mesenchymal stem cell properties and increase therapeutic potential*. Tissue Engineering Part C: Methods, 2009. **16**(4): p. 735-749.
152. Dykstra, B., et al., *High-resolution video monitoring of hematopoietic stem cells cultured in single-cell arrays identifies new features of self-renewal*. Proceedings of the National Academy of Sciences, 2006. **103**(21): p. 8185-8190.
153. Shim, J.H., T.R. Lee, and D.W. Shin, *Novel In Vitro Culture Condition Improves the Stemness of Human Dermal Stem/Progenitor Cells*. Molecules and Cells, 2013. **36**(6): p. 556-563.
154. Driskell, R.R., et al., *Clonal growth of dermal papilla cells in hydrogels reveals intrinsic differences between Sox2-positive and-negative cells in vitro and in vivo*. Journal of Investigative Dermatology, 2012. **132**(4): p. 1084-1093.
155. Kuroda, Y., et al., *Unique multipotent cells in adult human mesenchymal cell populations*. Proceedings of the National Academy of Sciences, 2010. **107**(19): p. 8639-8643.
156. Lutolf, M.P., P.M. Gilbert, and H.M. Blau, *Designing materials to direct stem-cell fate*. Nature, 2009. **462**(7272): p. 433-441.
157. Guilak, F., et al., *Control of Stem Cell Fate by Physical Interactions with the Extracellular Matrix*. Cell Stem Cell, 2009. **5**(1): p. 17-26.

158. Potten, C.S. and M. Loeffler, *Stem cells: attributes, cycles, spirals, pitfalls and uncertainties. Lessons for and from the crypt*. Development, 1990. **110**(4): p. 1001-1020.
159. Blanpain, C., V. Horsley, and E. Fuchs, *Epithelial stem cells: turning over new leaves*. Cell, 2007. **128**(3): p. 445-458.
160. Hong, K.U., et al., *In vivo differentiation potential of tracheal basal cells: evidence for multipotent and unipotent subpopulations*. American Journal of Physiology-Lung Cellular and Molecular Physiology, 2004. **286**(4): p. L643-L649.
161. Reule, S. and S. Gupta, *Kidney regeneration and resident stem cells*. Organogenesis, 2011. **7**(2): p. 135-139.
162. Seaberg, R.M. and D. van der Kooy, *Stem and progenitor cells: the premature desertion of rigorous definitions*. Trends in neurosciences, 2003. **26**(3): p. 125-131.
163. Kamiya, A. and Y. Inagaki, *Stem and progenitor cell systems in liver development and regeneration*. Hepatology Research, 2015. **45**(1): p. 29-37.
164. Pleniceanu, O., O. Harari-Steinberg, and B. Dekel, *Concise review: Kidney stem/progenitor cells: differentiate, sort out, or reprogram?* Stem Cells, 2010. **28**(9): p. 1649-60.
165. Miyajima, A., M. Tanaka, and T. Itoh, *Stem/progenitor cells in liver development, homeostasis, regeneration, and reprogramming*. Cell Stem Cell, 2014. **14**(5): p. 561-574.
166. Gaetani, R., et al., *Cardiac tissue engineering using tissue printing technology and human cardiac progenitor cells*. Biomaterials, 2012. **33**(6): p. 1782-1790.
167. Takahashi, K. and S. Yamanaka, *Induction of pluripotent stem cells from mouse embryonic and adult fibroblast cultures by defined factors*. Cell, 2006. **126**(4): p. 663-676.
168. Takahashi, K., et al., *Induction of Pluripotent Stem Cells from Adult Human Fibroblasts by Defined Factors*. Cell, 2007. **131**(5): p. 861-872.
169. Vanslambrouck, J.M. and M.H. Little, *Direct transcriptional reprogramming to nephron progenitors*. Current opinion in genetics & development, 2015. **34**: p. 10-16.
170. Lam, A.Q. and J.V. Bonventre, *Regenerating the nephron with human pluripotent stem cells*. Current Opinion in Organ Transplantation, 2015. **20**(2): p. 187-192.
171. Inoue, H., et al., *iPS cells: a game changer for future medicine*. The EMBO journal, 2014. **33**(5): p. 409-417.
172. Rao, M.S., *Multipotent and restricted precursors in the central nervous system*. Anat Rec, 1999. **257**(4): p. 137-48.
173. Kassem, M., M. Kristiansen, and B.M. Abdallah, *Mesenchymal Stem Cells: Cell Biology and Potential Use in Therapy*. Basic & Clinical Pharmacology & Toxicology, 2004. **95**(5): p. 209-214.
174. Lo, B. and L. Parham, *Ethical Issues in Stem Cell Research*. Endocrine Reviews, 2009. **30**(3): p. 204-213.
175. Yamada, M., et al., *Human oocytes reprogram adult somatic nuclei of a type 1 diabetic to diploid pluripotent stem cells*. Nature, 2014. **510**(7506): p. 533-536.
176. Murphy, M.B., K. Moncivais, and A.I. Caplan, *Mesenchymal stem cells: environmentally responsive therapeutics for regenerative medicine*. Experimental & molecular medicine, 2013. **45**(11): p. e54.
177. Wilson, A. and A. Trumpp, *Bone-marrow haematopoietic-stem-cell niches*. Nature reviews. Immunology, 2006. **6**(2): p. 93-106.
178. Gunsilius, E., G. Gastl, and A.L. Petzer, *Hematopoietic stem cells*. Biomedicine & Pharmacotherapy, 2001. **55**(4): p. 186-194.
179. Ogawa, M., *Differentiation and proliferation of hematopoietic stem cells*. Blood, 1993. **81**(11): p. 2844.
180. Spangrude, G.J., S. Heimfeld, and I.L. Weissman, *Purification and characterization of mouse hematopoietic stem cells*. Science, 1988. **241**(4861): p. 58-62.
181. Wayne, A.S., K. Baird, and R.M. Egeler, *Hematopoietic stem cell transplantation for leukemia*. Pediatric clinics of North America, 2010. **57**(1): p. 1-25.

182. Gribben, J.G., *Stem cell transplantation in chronic lymphocytic leukemia*. *Biology of blood and marrow transplantation : journal of the American Society for Blood and Marrow Transplantation*, 2008. **15**(1 Suppl): p. 53-58.
183. Johnson, P.W., et al., *Bone marrow and peripheral blood stem cell transplantation for malignancy*. *Health Technol Assess*, 1998. **2**(8): p. 1-187.
184. Parkman, R., *The application of bone marrow transplantation to the treatment of genetic diseases*. *Science (New York, N.Y.)*, 1986. **232**(4756): p. 1373-1378.
185. Hanna, J., et al., *Treatment of Sickle Cell Anemia Mouse Model with iPS Cells Generated from Autologous Skin*. *Science*, 2007. **318**(5858): p. 1920-1923.
186. Santarone, S., et al., *Bone marrow transplantation in patients with thalassemia*. *Biology of Blood and Marrow Transplantation*, 2006. **12**(2): p. 20-20.
187. Abbott, A., *Gene therapy. Italians first to use stem cells*. *Nature*, 1992. **356**(6369): p. 465.
188. Kiem, H.P., et al., *Hematopoietic-stem-cell-based gene therapy for HIV disease*. *Cell Stem Cell*, 2012. **10**(2): p. 137-47.
189. Schatteman, G.C., M. Dunnwald, and C. Jiao, *Biology of bone marrow-derived endothelial cell precursors*. *American journal of physiology. Heart and circulatory physiology*, 2007. **292**(1): p. H1-18.
190. Zannettino, A., et al., *Multipotential human adipose-derived stromal stem cells exhibit a perivascular phenotype in vitro and in vivo*. *Journal of cellular physiology*, 2008. **214**(2): p. 413-421.
191. Ferrari, G., et al., *Muscle regeneration by bone marrow-derived myogenic progenitors*. *Science*, 1998. **279**(5356): p. 1528-1530.
192. Nakahara, H., et al., *Bone and cartilage formation in diffusion chambers by subcultured cells derived from the periosteum*. *Bone*, 1990. **11**(3): p. 181-188.
193. da Silva Meirelles, L., P.C. Chagastelles, and N.B. Nardi, *Mesenchymal stem cells reside in virtually all post-natal organs and tissues*. *Journal of cell science*, 2006. **119**(11): p. 2204-2213.
194. Rojas, M., et al., *Bone marrow-derived mesenchymal stem cells in repair of the injured lung*. *Am J Respir Cell Mol Biol*, 2005. **33**(2): p. 145-52.
195. Togel, F., et al., *Administered mesenchymal stem cells protect against ischemic acute renal failure through differentiation-independent mechanisms*. *Am J Physiol Renal Physiol*, 2005. **289**(1): p. 15.
196. Togel, F., et al., *Vasculotropic, paracrine actions of infused mesenchymal stem cells are important to the recovery from acute kidney injury*. *Am J Physiol Renal Physiol*, 2007. **292**(5): p. 9.
197. Aggarwal, S. and M.F. Pittenger, *Human mesenchymal stem cells modulate allogeneic immune cell responses*. *Blood*, 2005. **105**(4): p. 1815-1822.
198. Glenn, J.D. and K.A. Whartenby, *Mesenchymal stem cells: emerging mechanisms of immunomodulation and therapy*. *World J Stem Cells*, 2014. **6**(5): p. 526-539.
199. Trounson, A. and N.D. DeWitt, *Pluripotent stem cells progressing to the clinic*. *Nature Reviews Molecular Cell Biology*, 2016. **17**(3): p. 194-200.
200. Trounson, A., et al., *Clinical trials for stem cell therapies*. *BMC medicine*, 2011. **9**(1): p. 52.
201. Murphy, J.M., et al., *Reduced chondrogenic and adipogenic activity of mesenchymal stem cells from patients with advanced osteoarthritis*. *Arthritis & Rheumatism*, 2002. **46**(3): p. 704-713.
202. O'Connor, T.P. and R.G. Crystal, *Genetic medicines: treatment strategies for hereditary disorders*. *Nature Reviews Genetics*, 2006. **7**(4): p. 261-276.
203. Tisher, C.C. and K.M. Madsen, *Anatomy of the kidney*. *The kidney*, 1991. **1**: p. 3-75.
204. Gilbert, S.F., *Developmental biology* 2010, Sunderland, Mass: Sinauer Associates.
205. Eknoyan, G., et al., *The burden of kidney disease: Improving global outcomes*. *Kidney International*, 2004. **66**(4): p. 1310-1314.
206. Martínez-Castelao, A., et al., *Consensus document for the detection and management of chronic kidney disease*. *Nefrologia*, 2014. **34**(2): p. 243-62.

207. Levey, A.S. and J. Coresh, *Chronic kidney disease*. Lancet, 2012. **379**(9811): p. 165.
208. Hogg, R.J., et al., *National Kidney Foundation's Kidney Disease Outcomes Quality Initiative clinical practice guidelines for chronic kidney disease in children and adolescents: evaluation, classification, and stratification*. Pediatrics, 2003. **111**(6 Pt 1): p. 1416-1421.
209. Kerr, M., et al., *Estimating the financial cost of chronic kidney disease to the NHS in England*. Nephrology Dialysis Transplantation, 2012: p. gfs269.
210. Toyoda, K. and T. Ninomiya, *Stroke and cerebrovascular diseases in patients with chronic kidney disease*. The Lancet Neurology, 2014. **13**(8): p. 823-833.
211. Stevens, P.E. and A. Levin, *Evaluation and management of chronic kidney disease: synopsis of the kidney disease: improving global outcomes 2012 clinical practice guideline*. Annals of internal medicine, 2013. **158**(11): p. 825-830.
212. Dudley, C. and P. Harden, *Assessment of the potential kidney transplant recipient*. Renal Association clinical practice guideline, 2014.
213. Baer, P.C., et al., *Isolation of proximal and distal tubule cells from human kidney by immunomagnetic separation: technical note*. Kidney International, 1997. **52**(5): p. 1321-1331.
214. Hermann, P., et al., *Cell Biology of the Glomerular Podocyte*. Physiological Reviews, 2003. **83**(1): p. 253-261.
215. Abe, Y., et al., *Bioenergetic characterization of mouse podocytes*. American Journal of Physiology-Cell Physiology, 2010. **299**(2): p. C464-C476.
216. Mathieson, P.W., *Update on the podocyte*. Curr Opin Nephrol Hypertens, 2009. **18**(3): p. 206-11.
217. Asanuma, K. and P. Mundel, *The role of podocytes in glomerular pathobiology*. Journal of Clinical and Experimental Nephrology, 2003. **7**(4): p. 255-259.
218. Kerjaschki, D., *Caught flat-footed: podocyte damage and the molecular bases of focal glomerulosclerosis*. The Journal of Clinical Investigation, 2001. **108**(11): p. 1583-1587.
219. Wiggins, R., *The spectrum of podocytopathies: a unifying view of glomerular diseases*. Kidney International, 2007. **71**(12): p. 1205-1214.
220. Kalluri, R., *Proteinuria with and without renal glomerular podocyte effacement*. Journal of the American Society of Nephrology, 2006. **17**(9): p. 2383-2389.
221. Kriz, W., et al., *The podocyte's response to stress: the enigma of foot process effacement*. American Journal of Physiology-Renal Physiology, 2013. **304**(4): p. F333-F347.
222. D'Agati, V.D., *Podocyte injury in focal segmental glomerulosclerosis: Lessons from animal models (a play in five acts)*. Kidney International, 2008. **73**(4): p. 399-406.
223. Matsusaka, T., et al., *Podocyte injury damages other podocytes*. Journal of the American Society of Nephrology, 2011. **22**(7): p. 1275-1285.
224. Asanuma, K., et al., *Synaptopodin orchestrates actin organization and cell motility via regulation of RhoA signalling*. Nature cell biology, 2006. **8**(5): p. 485-491.
225. Mundel, P., et al., *Synaptopodin: an actin-associated protein in telencephalic dendrites and renal podocytes*. The Journal of Cell Biology, 1997. **139**(1): p. 193-204.
226. Asanuma, K., et al., *Synaptopodin regulates the actin-bundling activity of α -actinin in an isoform-specific manner*. The Journal of Clinical Investigation, 2005. **115**(5): p. 1188-1198.
227. Saleem, M.A., et al., *A conditionally immortalized human podocyte cell line demonstrating nephrin and podocin expression*. Journal of the American Society of Nephrology, 2002. **13**(3): p. 630-638.
228. Saleem, M.A., et al., *Co-localization of nephrin, podocin, and the actin cytoskeleton: evidence for a role in podocyte foot process formation*. The American Journal of Pathology, 2002. **161**(4): p. 1459-1466.
229. Ryan, G., et al., *Repression of Pax-2 by WT1 during normal kidney development*. Development, 1995. **121**(3): p. 867-875.

230. Wagner, N., et al., *The major podocyte protein nephrin is transcriptionally activated by the Wilms' tumor suppressor WT1*. Journal of the American Society of Nephrology, 2004. **15**(12): p. 3044-3051.
231. Nakhoul, N. and V. Batuman, *Role of proximal tubules in the pathogenesis of kidney disease*. 2011.
232. Qi, W., et al., *Isolation, propagation and characterization of primary tubule cell culture from human kidney*. Nephrology, 2007. **12**(2): p. 155-9.
233. Brown, C.D., et al., *Characterisation of human tubular cell monolayers as a model of proximal tubular xenobiotic handling*. Toxicology and applied pharmacology, 2008. **233**(3): p. 428-438.
234. *Diabetic nephropathy: The central role of renal proximal tubular cells in tubulointerstitial injury*. Histology and Histopathology, 2002. **17**(1): p. 247.
235. Christensen, E.I. and H. Birn, *Megalin and cubilin: synergistic endocytic receptors in renal proximal tubule*. American Journal of Physiology-Renal Physiology, 2001. **280**(4): p. F562-F573.
236. Zhai, X.Y., et al., *Cubilin-and megalin-mediated uptake of albumin in cultured proximal tubule cells of opossum kidney*. Kidney International, 2000. **58**(4): p. 1523-1533.
237. Ilsø Christensen, E., et al., *Membrane receptors for endocytosis in the renal proximal tubule*. International review of cytology, 1998. **180**: p. 237-284.
238. Cui, S., et al., *Megalin/gp330 mediates uptake of albumin in renal proximal tubule*. American Journal of Physiology - Renal Physiology, 1996. **271**(4): p. F900-F907.
239. Storm, T., et al., *Renal phenotypic investigations of megalin-deficient patients: novel insights into tubular proteinuria and albumin filtration*. Nephrology Dialysis Transplantation, 2013. **28**(3): p. 585-591.
240. Arany, I. and R.L. Safirstein. *Cisplatin nephrotoxicity*. in *Seminars in nephrology*. 2003. Elsevier.
241. Lieberthal, W., V. Triaca, and J. Levine, *Mechanisms of death induced by cisplatin in proximal tubular epithelial cells: apoptosis vs. necrosis*. American Journal of Physiology-Renal Physiology, 1996. **270**(4): p. F700-F708.
242. Miller, R.P., et al., *Mechanisms of cisplatin nephrotoxicity*. Toxins, 2010. **2**(11): p. 2490-2518.
243. Ryan, M.J., et al., *HK-2: an immortalized proximal tubule epithelial cell line from normal adult human kidney*. Kidney International, 1994. **45**(1): p. 48-57.
244. Racusen, L.C., et al., *Cell lines with extended in vitro growth potential from human renal proximal tubule: characterization, response to inducers, and comparison with established cell lines*. Journal of Laboratory and Clinical Medicine, 1997. **129**(3): p. 318-329.
245. Terry, S., et al., *A primary culture of mouse proximal tubular cells, established on collagen-coated membranes*. American Journal of Physiology-Renal Physiology, 2007. **293**(2): p. F476-F485.
246. Wilmer, M.J., et al., *Novel conditionally immortalized human proximal tubule cell line expressing functional influx and efflux transporters*. Cell and tissue research, 2010. **339**(2): p. 449-457.
247. Oliver, J.A., et al., *The renal papilla is a niche for adult kidney stem cells*. J Clin Invest, 2004. **114**(6): p. 795-804.
248. Osafune, K., et al., *Identification of multipotent progenitors in the embryonic mouse kidney by a novel colony-forming assay*. Development, 2006. **133**(1): p. 151-61.
249. Fuente-Mora, C., *Isolation and characterisation of a novel population of potential kidney stem cells from postnatal mouse kidney*. School of Biomedical Science, University of Liverpool, PhD-Thesis, 2009.
250. Fuente Mora, C., et al., *Differentiation of podocyte and proximal tubule-like cells from a mouse kidney-derived stem cell line*. Stem Cells Dev, 2012. **21**(2): p. 296-307.
251. Ranghini, E., et al., *Stem cells derived from neonatal mouse kidney generate functional proximal tubule-like cells and integrate into developing nephrons in vitro*. 2013.
252. Humphreys, B.D. and J.V. Bonventre, *Mesenchymal stem cells in acute kidney injury*. Annual review of medicine, 2008. **59**(1): p. 311-325.

253. Hopkins, C., et al., *Stem cell options for kidney disease*. The Journal of pathology, 2009. **217**(2): p. 265-281.
254. Bruno, S., et al., *Isolation and characterization of resident mesenchymal stem cells in human glomeruli*. Stem Cells Dev, 2009. **18**(6): p. 867-80.
255. Lasagni, L., et al., *Notch activation differentially regulates renal progenitors proliferation and differentiation toward the podocyte lineage in glomerular disorders*. Stem Cells, 2010. **28**(9): p. 1674-1685.
256. Curtis, L.M., et al., *Contribution of intrarenal cells to cellular repair after acute kidney injury: subcapsular implantation technique*. American Journal of Physiology-Renal Physiology, 2008. **295**(1): p. F310-F314.
257. Lin, F., A. Moran, and P. Igarashi, *Intrarenal cells, not bone marrow–derived cells, are the major source for regeneration in postischemic kidney*. The Journal of Clinical Investigation. **115**(7): p. 1756-1764.
258. McCampbell, K.K. and R.A. Wingert, *Renal stem cells: fact or science fiction?* Biochemical Journal, 2012. **444**(2): p. 153-168.
259. Pierres, M., et al., *Evidence that murine hematopoietic cell subset marker J11d is attached to a glycosyl-phosphatidylinositol membrane anchor*. European journal of immunology, 1987. **17**(12): p. 1781-1785.
260. Corbeil, D., et al., *The human AC133 hematopoietic stem cell antigen is also expressed in epithelial cells and targeted to plasma membrane protrusions*. Journal of Biological Chemistry, 2000. **275**(8): p. 5512-5520.
261. Lazzeri, E., et al., *Regenerative potential of embryonic renal multipotent progenitors in acute renal failure*. Journal of the American Society of Nephrology, 2007. **18**(12): p. 3128-3138.
262. Duffield, J.S., et al., *Restoration of tubular epithelial cells during repair of the postischemic kidney occurs independently of bone marrow-derived stem cells*. The Journal of Clinical Investigation. **115**(7): p. 1743-1755.
263. Humphreys, B.D., et al., *Intrinsic epithelial cells repair the kidney after injury*. Cell Stem Cell, 2008. **2**(3): p. 284-291.
264. Bonventre, J.V., *Dedifferentiation and proliferation of surviving epithelial cells in acute renal failure*. Journal of the American Society of Nephrology, 2003. **14**(suppl 1): p. S55-S61.
265. Chou, Y.-H., et al., *Stem cells and kidney regeneration*. Journal of the Formosan Medical Association, 2014. **113**(4): p. 201-209.
266. Lindgren, D., et al., *Isolation and characterization of progenitor-like cells from human renal proximal tubules*. The American Journal of Pathology, 2011. **178**(2): p. 828-837.
267. Metsuyanin, S., et al., *Expression of stem cell markers in the human fetal kidney*. PLoS One, 2009. **4**(8): p. e6709.
268. Harari-Steinberg, O., et al., *Identification of human nephron progenitors capable of generation of kidney structures and functional repair of chronic renal disease*. EMBO molecular medicine, 2013. **5**(10): p. 1556-1568.
269. Buzhor, E., et al., *Reactivation of NCAM1 defines a subpopulation of human adult kidney epithelial cells with clonogenic and stem/progenitor properties*. The American Journal of Pathology, 2013. **183**(5): p. 1621-1633.
270. Bussolati, B. and G. Camussi, *Therapeutic use of human renal progenitor cells for kidney regeneration*. Nature Reviews Nephrology, 2015. **11**(12): p. 695-706.
271. Bussolati, B., et al., *Isolation of Renal Progenitor Cells from Adult Human Kidney*. The American Journal of Pathology, 2005. **166**(2): p. 545-555.
272. Murray, P., et al., *The potential of small chemical functional groups for directing the differentiation of kidney stem cells*. Biochem Soc Trans, 2010. **38**(4): p. 1062-6.
273. *British Standards BS EN ISO 10993-5:2009. Biological Evaluation of Medical Devices. Part 5: Tests for in vitro cytotoxicity.*

274. *BS EN ISO 10993-5:2009 Biological evaluation of medical devices. Tests for in vitro cytotoxicity. Évaluation biologique des dispositifs médicaux. Essais concernant la cytotoxicité in vitro*2009: BSI Standards Limited.
275. Harding, F., et al., *Surface bound amine functional group density influences embryonic stem cell maintenance*. *Advanced Healthcare Materials*, 2013. **2**(4): p. 585-590.
276. Griesser, H.J., *Small scale reactor for plasma processing of moving substrate web*. *Vacuum*, 1989. **39**(5): p. 485-488.
277. Michelmore, A., et al., *Versatile gradients of chemistry, bound ligands and nanoparticles on alumina nanopore arrays*. *Nanotechnology*, 2011. **22**(41): p. 415601.
278. Zhu, T., et al., *Surface modification of citrate-reduced colloidal gold nanoparticles with 2-mercaptosuccinic acid*. *Langmuir*, 2003. **19**(22): p. 9518-9525.
279. Kwok, D. and A. Neumann, *Contact angle measurement and contact angle interpretation*. *Advances in Colloid and Interface Science*, 1999. **81**(3): p. 167-249.
280. Lotfi, M., M. Naceur, and M. Nejib, *Cell Adhesion to Biomaterials: Concept of Biocompatibility*2013: INTECH Open Access Publisher.
281. Adamcik, J., A. Berquand, and R. Mezzenga, *Single-step direct measurement of amyloid fibrils stiffness by peak force quantitative nanomechanical atomic force microscopy*. *Applied Physics Letters*, 2011. **98**(19): p. 3701.
282. Giessibl, F.J., *Advances in atomic force microscopy*. *Reviews of modern physics*, 2003. **75**(3): p. 949.
283. Briggs, D., *Surface analysis of polymers by XPS and static SIMS*1998: Cambridge University Press.
284. Chung, Y.-W., *Practical guide to surface science and spectroscopy*. Vol. 1. 2001: Academic Press.
285. Briggs, D. and G. Beamson, *XPS studies of the oxygen 1s and 2s levels in a wide range of functional polymers*. *Analytical chemistry*, 1993. **65**(11): p. 1517-1523.
286. Beamson, G. and D. Briggs, *High resolution XPS of organic polymers: the Scienta ESCA300 database*. 1992. There is no corresponding record for this reference.
287. Coussot, G., et al., *A rapid and reversible colorimetric assay for the characterization of aminated solid surfaces*. *Analytical and bioanalytical chemistry*, 2011. **399**(3): p. 1061-1069.
288. Zemljič, L.F., Strnad, S., Šauperl, O., & Stana-Kleinschek, K, *Characterization of amino groups for cotton fibers coated with chitosan*. *Textile Research Journal*, 2009. **79**(3), **219-226**.
289. Coussot, G., et al., *Aminated dendritic surfaces characterization: a rapid and versatile colorimetric assay for estimating the amine density and coating stability*. *Analytical and bioanalytical chemistry*, 2011. **399**(6): p. 2295-2302.
290. Noel, S., et al., *Quantification of primary amine groups available for subsequent biofunctionalization of polymer surfaces*. *Bioconjugate chemistry*, 2011. **22**(8): p. 1690-1699.
291. Coussot, G., et al., *Colorimetric quantification of amino groups in linear and dendritic structures*. *Polymer International*, 2009. **58**(5): p. 511-518.
292. Winyard, P.J. and K.L. Price, *Experimental renal progenitor cells: Repairing and recreating kidneys?* *Pediatric Nephrology*, 2014. **29**(4): p. 665-672.
293. Schneider, C.A., W.S. Rasband, and K.W. Eliceiri, *NIH Image to ImageJ: 25 years of image analysis*. *Nat Methods*, 2012. **9**(7): p. 671-675.
294. WS., R., *ImageJ, U.S. National Institutes of Health, Bethesda Maryland, USA*. imagej.nih.gov/ij/, 1997-2012.
295. Ye, J., et al., *Primer-BLAST: a tool to design target-specific primers for polymerase chain reaction*. *BMC bioinformatics*, 2012. **13**(1): p. 134.
296. Udvardi, M.K., T. Czechowski, and W.-R. Scheible, *Eleven golden rules of quantitative RT-PCR*. *The Plant Cell Online*, 2008. **20**(7): p. 1736-1737.
297. Pfaffl, M.W., *A new mathematical model for relative quantification in real-time RT-PCR*. *Nucleic Acids Research*, 2001. **29**(9): p. e45-e45.

298. Rustad, K.C., et al., *Strategies for organ level tissue engineering*. *Organogenesis*, 2010. **6**(3): p. 151-157.
299. Lutolf, M. and J. Hubbell, *Synthetic biomaterials as instructive extracellular microenvironments for morphogenesis in tissue engineering*. *Nature Biotechnology*, 2005. **23**(1): p. 47-55.
300. Graeter, S.V., et al., *Mimicking cellular environments by nanostructured soft interfaces*. *Nano letters*, 2007. **7**(5): p. 1413-1418.
301. Saha, K., et al., *Designing synthetic materials to control stem cell phenotype*. *Current Opinion in Chemical Biology*, 2007. **11**(4): p. 381-387.
302. Liu, X., et al., *Surface modification by allylamine plasma polymerization promotes osteogenic differentiation of human adipose-derived stem cells*. *ACS applied materials & interfaces*, 2014. **6**(12): p. 9733-9741.
303. Higuchi, A., et al., *Physical cues of biomaterials guide stem cell differentiation fate*. *Chemical reviews*, 2013. **113**(5): p. 3297-3328.
304. Morelli, C., et al., *Cell morphology, markers, spreading, and proliferation on orthopaedic biomaterials. An innovative cellular model for the "in vitro" study*. *Journal of Biomedical Materials Research Part A*, 2007. **83**(1): p. 178-183.
305. Nickson, C.M., P.J. Doherty, and R.L. Williams, *Novel Polymeric Coatings with the Potential to Control In-stent Restenosis — An In Vitro Study*. *Journal of Biomaterials Applications*, 2010. **24**(5): p. 437-452.
306. McNulty, M., *Memry, Biomer to develop stent coatings*. *Plastics news*, 2004. **16**(28): p. 13.
307. *Joint program to develop drug-loadable coatings for stents, medical devices*, 2004. p. 339.
308. Janović, Z., A. Jukić, and O. Vogl, *Spacer groups in macromolecular structures*. *Polimeri: časopis za plastiku i gumu*, 2010. **31**(1): p. 14-21.
309. Nel, A.E., et al., *Understanding biophysicochemical interactions at the nano–bio interface*. *Nature materials*, 2009. **8**(7): p. 543-557.
310. Salinas, C.N. and K.S. Anseth, *The influence of the RGD peptide motif and its contextual presentation in PEG gels on human mesenchymal stem cell viability*. *Journal of tissue engineering and regenerative medicine*, 2008. **2**(5): p. 296-304.
311. Sharon, J. and D. Puleo, *Immobilization of glycoproteins, such as VEGF, on biodegradable substrates*. *Acta Biomaterialia*, 2008. **4**(4): p. 1016-1023.
312. Pierschbacher, M.D. and E. Ruoslahti, *Cell attachment activity of fibronectin can be duplicated by small synthetic fragments of the molecule*. *Nature*, 1983. **309**(5963): p. 30-33.
313. Dsouza, S.E., M.H. Ginsberg, and E.F. Plow, *ARGINYL-GLYCYL-ASPARTIC ACID (RGD) - A CELL-ADHESION MOTIF*. *Trends in Biochemical Sciences*, 1991. **16**(7): p. 246-250.
314. Ruoslahti, E., *RGD and other recognition sequences for integrins*. *Annual Review of Cell and Developmental Biology*, 1996. **12**(1): p. 697-715.
315. Cao, F.-Y., et al., *Evaluating the Effects of Charged Oligopeptide Motifs Coupled with RGD on Osteogenic Differentiation of Mesenchymal Stem Cells*. *ACS applied materials & interfaces*, 2015. **7**(12): p. 6698-6705.
316. Ruoslahti, E. and M.D. Pierschbacher, *Arg-Gly-Asp: a versatile cell recognition signal*. *Cell*, 1986. **44**(4): p. 517-518.
317. Hersel, U., C. Dahmen, and H. Kessler, *RGD modified polymers: biomaterials for stimulated cell adhesion and beyond*. *Biomaterials*, 2003. **24**(24): p. 4385-4415.
318. Cavalcanti-Adam, E.A., et al., *Cell Spreading and Focal Adhesion Dynamics Are Regulated by Spacing of Integrin Ligands*. *Biophysical Journal*, 2007. **92**(8): p. 2964-2974.
319. Dillow, A.K. and M. Tirrell, *Targeted cellular adhesion at biomaterial interfaces*. *Current Opinion in Solid State and Materials Science*, 1998. **3**(3): p. 252-259.
320. VandeVondele, S., J. Vörös, and J.A. Hubbell, *RGD-grafted poly-l-lysine-graft-(polyethylene glycol) copolymers block non-specific protein adsorption while promoting cell adhesion*. *Biotechnology and bioengineering*, 2003. **82**(7): p. 784-790.

321. Grzesik, W.J. and P.G. Robey, *Bone matrix RGD glycoproteins: immunolocalization and interaction with human primary osteoblastic bone cells in vitro*. Journal of Bone and Mineral Research, 1994. **9**(4): p. 487-496.
322. Puleo, D. and R. Bizios, *RGDS tetrapeptide binds to osteoblasts and inhibits fibronectin-mediated adhesion*. Bone, 1991. **12**(4): p. 271-276.
323. Lin, H.-B. and S.L. Cooper. *Synthesis, surface and cell-adhesion properties of polyurethanes containing covalently grafted RGD-peptides*. in *MRS Proceedings*. 1993. Cambridge Univ Press.
324. Rowley, J.A. and D.J. Mooney, *Alginate type and RGD density control myoblast phenotype*. Journal of Biomedical Materials Research, 2002. **60**(2): p. 217-223.
325. Wang, X., et al., *Adhesion, proliferation, and differentiation of mesenchymal stem cells on RGD nanopatterns of varied nanopacings*. Organogenesis, 2013. **9**(4): p. 280-286.
326. Ochsenhirt, S.E., et al., *Effect of RGD secondary structure and the synergy site PHSRN on cell adhesion, spreading and specific integrin engagement*. Biomaterials, 2006. **27**(20): p. 3863-3874.
327. Aota, S.-i., M. Nomizu, and K.M. Yamada, *The short amino acid sequence Pro-His-Ser-Arg-Asn in human fibronectin enhances cell-adhesive function*. Journal of Biological Chemistry, 1994. **269**(40): p. 24756-24761.
328. Hojo, K., et al., *Amino acids and peptides. Part 39: A bivalent poly (ethylene glycol) hybrid containing an active site (RGD) and its synergistic site (PHSRN) of fibronectin*. Bioorganic & medicinal chemistry letters, 2001. **11**(11): p. 1429-1432.
329. Redick, S.D., *Defining Fibronectin's Cell Adhesion Synergy Site by Site-directed Mutagenesis*. Journal of Cell Biology, 2000. **149**(2): p. 521.
330. Lai, Y., et al., *Design and synthesis of a potent peptide containing both specific and non-specific cell-adhesion motifs*. Biomaterials, 2010. **31**(18): p. 4809-4817.
331. Furth, M.E., A. Atala, and M.E. Van Dyke, *Smart biomaterials design for tissue engineering and regenerative medicine*. Biomaterials, 2007. **28**(34): p. 5068-5073.
332. Petit, A., et al., *Effect of nitrogen-rich cell culture surfaces on type X collagen expression by bovine growth plate chondrocytes*. Biomedical engineering online, 2011. **10**(1): p. 4.
333. Hautanen, A., et al., *Effects of modifications of the RGD sequence and its context on recognition by the fibronectin receptor*. Journal of Biological Chemistry, 1989. **264**(3): p. 1437-1442.
334. Pierschbacher, M.D. and E. Ruoslahti, *Influence of stereochemistry of the sequence Arg-Gly-Asp-Xaa on binding specificity in cell adhesion*. Journal of Biological Chemistry, 1987. **262**(36): p. 17294-17298.
335. Hynes, R.O., *Integrins: versatility, modulation, and signaling in cell adhesion*. Cell, 1992. **69**(1): p. 11-25.
336. Vandenberg, P., et al., *Characterization of a type IV collagen major cell binding site with affinity to the alpha 1 beta 1 and the alpha 2 beta 1 integrins*. The Journal of Cell Biology, 1991. **113**(6): p. 1475-1483.
337. Senger, D.R., et al., *Adhesive properties of osteopontin: regulation by a naturally occurring thrombin-cleavage in close proximity to the GRGDS cell-binding domain*. Molecular Biology of the Cell, 1994. **5**(5): p. 565-574.
338. Mann, K., et al., *Amino acid sequence of mouse nidogen, a multidomain basement membrane protein with binding activity for laminin, collagen IV and cells*. The EMBO journal, 1989. **8**(1): p. 65.
339. Minoux, H., et al., *Structural analysis of the KGD sequence loop of barbourin, an α IIb β 3-specific disintegrin*. Journal of Computer-Aided Molecular Design, 2000. **14**(4): p. 317.
340. Ghiso, J., et al., *A 109-amino-acid C-terminal fragment of Alzheimer's-disease amyloid precursor protein contains a sequence, -RHDS-, that promotes cell adhesion*. The Biochemical Journal, 1992. **288**(3): p. 1053.

341. Matter, M.L., et al., *The $\alpha 5 \beta 1$ Integrin Mediates Elimination of Amyloid- β Peptide and Protects Against Apoptosis*. The Journal of Cell Biology, 1998. **141**(4): p. 1019-1030.
342. Di Matteo, P., et al., *Immunogenic and structural properties of the Asn-Gly-Arg (NGR) tumor neovasculature-homing motif*. Molecular Immunology, 2006. **43**(10): p. 1509-1518.
343. Curnis, F., et al., *Spontaneous formation of L-isoaspartate and gain of function in fibronectin*. Journal of Biological Chemistry, 2006. **281**(47): p. 36466-36476.
344. Yamada, K.M. and D.W. Kennedy, *Peptide inhibitors of fibronectin, laminin, and other adhesion molecules: Unique and shared features*. Journal of cellular physiology, 1987. **130**(1): p. 21-28.
345. Glennon-Alty, L., et al., *Induction of mesenchymal stem cell chondrogenesis by polyacrylate substrates*. Acta Biomaterialia, 2012.
346. Benoit, D.S., et al., *Small molecule functional groups for the controlled differentiation of human mesenchymal stem cells encapsulated in poly (ethylene glycol) hydrogels*. Nature materials, 2008. **7**(10): p. 816.
347. Lee, J.H., et al., *Cell behaviour on polymer surfaces with different functional groups*. Biomaterials, 1994. **15**(9): p. 705-711.
348. Moulder, J.F., J. Chastain, and R.C. King, *Handbook of X-ray photoelectron spectroscopy: a reference book of standard spectra for identification and interpretation of XPS data*1992: Perkin-Elmer Eden Prairie, MN.
349. Milling, A.J., *Surface characterization methods: principles, techniques, and applications*. Vol. 87. 1999: CRC Press.
350. Kowalewska, A., et al., *Novel polymer systems with very bulky organosilicon side chain substituents*. Polymer, 1999. **40**(3): p. 813-818.
351. Safa, K.D., et al., *Synthesis and characterization of new polymer systems containing very bulky tris(trimethylsilyl)methyl substituents as side chains*. European Polymer Journal, 2004. **40**(3): p. 459-466.
352. Tabei, J., R. Nomura, and T. Masuda, *Conformational study of poly (N-propargylamides) having bulky pendant groups*. Macromolecules, 2002. **35**(14): p. 5405-5409.
353. Marmur, A., *Solid-Surface Characterization by Wetting*. Annual review of materials research, 2009. **39**(1): p. 473.
354. Carraher, C.E. and J.A. Moore, *Modification of polymers*. Vol. 21. 2012: Springer Science & Business Media.
355. Chandler, D., *Interfaces and the driving force of hydrophobic assembly*. Nature, 2005. **437**(7059): p. 640-647.
356. Tanford, C., *The Hydrophobic Effect: Formation of Micelles & Biological Membranes*, 1980. p. 8.
357. Chaudhury, M.K., *Interfacial interaction between low-energy surfaces*. Materials Science and Engineering: R: Reports, 1996. **16**(3): p. 97-159.
358. Pace, C.N., et al., *Protein structure, stability and solubility in water and other solvents*. Philosophical Transactions of the Royal Society of London B: Biological Sciences, 2004. **359**(1448): p. 1225-1235.
359. Mather, N., *Polymers as aids in organic chemistry*2012: Elsevier.
360. Chen, Y.L., C.A. Helm, and J.N. Israelachvili, *Molecular mechanisms associated with adhesion and contact angle hysteresis of monolayer surfaces*. The Journal of Physical Chemistry, 1991. **95**(26): p. 10736.
361. Herminghaus, S., *Roughness-induced non-wetting*. EPL (Europhysics Letters), 2000. **52**(2): p. 165.
362. Meiron, T.S., A. Marmur, and I.S. Saguy, *Contact angle measurement on rough surfaces*. Journal of colloid and interface science, 2004. **274**(2): p. 637-644.
363. Berg, J.C., *Wettability*, Surfactant Science Series, Marcel Dekker, 1993. **49**(76).

364. Dowling, D.P., et al., *Effect of surface wettability and topography on the adhesion of osteosarcoma cells on plasma-modified polystyrene*. Journal of Biomaterials Applications, 2010.
365. Guha, A., R.M. Barron, and R. Balachandar, *An experimental and numerical study of water jet cleaning process*. Journal of Materials Processing Technology, 2011. **211**(4): p. 610-618.
366. Aegerter, M.A. and M. Mennig, *Sol-gel technologies for glass producers and users*2013: Springer Science & Business Media.
367. Takeda, S., et al., *Surface OH group governing wettability of commercial glasses*. Journal of Non-Crystalline Solids, 1999. **249**(1): p. 41-46.
368. Stout, K.J., *Development of methods for the characterisation of roughness in three dimensions*2000.
369. Dalby, M.J., N. Gadegaard, and R.O. Oreffo, *Harnessing nanotopography and integrin-matrix interactions to influence stem cell fate*. Nature materials, 2014. **13**(6): p. 558-569.
370. Chen, W., et al., *Nanotopography Influences Adhesion, Spreading, and Self-Renewal of Human Embryonic Stem Cells*. ACS nano, 2012. **6**(5): p. 4094.
371. Lafuma, A. and D. Quéré, *Superhydrophobic states*. Nature materials, 2003. **2**(7): p. 457-460.
372. Wenzel, R.N., *Resistance of solid surfaces to wetting by water*. Industrial & Engineering Chemistry, 1936. **28**(8): p. 988-994.
373. Bhushan, B. and Y.C. Jung, *Natural and biomimetic artificial surfaces for superhydrophobicity, self-cleaning, low adhesion, and drag reduction*. Progress in Materials Science, 2011. **56**(1): p. 1-108.
374. Bettinger, C.J., R. Langer, and J.T. Borenstein, *Engineering Substrate Topography at the Micro- and Nanoscale to Control Cell Function*. Angewandte Chemie International Edition, 2009. **48**(30): p. 5406-5415.
375. Xu, C., et al., *In vitro study of human vascular endothelial cell function on materials with various surface roughness*. Journal of Biomedical Materials Research Part A, 2004. **71**(1): p. 154-161.
376. Chanphai, P., et al., *Effect of synthetic polymers on polymer–protein interaction*. Polymer, 2014. **55**(2): p. 572-582.
377. Györgyey, Á., et al., *Attachment and proliferation of human osteoblast-like cells (MG-63) on laser-ablated titanium implant material*. Materials Science and Engineering: C, 2013. **33**(7): p. 4251-4259.
378. Wilson, C.J., et al., *Mediation of biomaterial-cell interactions by adsorbed proteins: a review*. Tissue engineering, 2005. **11**(1-2): p. 1-18.
379. Tse, J.R. and A.J. Engler, *Stiffness gradients mimicking in vivo tissue variation regulate mesenchymal stem cell fate*. PLoS One, 2011. **6**(1): p. 0015978.
380. Ayala, R., et al., *Engineering the cell–material interface for controlling stem cell adhesion, migration, and differentiation*. Biomaterials, 2011. **32**(15): p. 3700-3711.
381. Chai, C. and K.W. Leong, *Biomaterials approach to expand and direct differentiation of stem cells*. Molecular Therapy: The Journal Of The American Society Of Gene Therapy, 2007. **15**(3): p. 467-480.
382. Fu, R.-H., et al., *Differentiation of stem cells: strategies for modifying surface biomaterials*. Cell Transplantation, 2011. **20**(1): p. 37-47.
383. Roy, K. and SpringerLink, *Biomaterials as Stem Cell Niche*. Vol. 2. 2010, Berlin, Heidelberg: Springer Berlin Heidelberg.
384. Guvendiren, M. and J.A. Burdick, *The control of stem cell morphology and differentiation by hydrogel surface wrinkles*. Biomaterials, 2010. **31**(25): p. 6511-6518.
385. Liu, S.Q., et al., *Synthetic hydrogels for controlled stem cell differentiation*. Soft Matter, 2010. **6**(1): p. 67.
386. Awad, H.A., et al., *Chondrogenic differentiation of adipose-derived adult stem cells in agarose, alginate, and gelatin scaffolds*. Biomaterials, 2004. **25**(16): p. 3211-3222.

387. Kroupová, J., et al., *Functional polymer hydrogels for embryonic stem cell support*. Journal of Biomedical Materials Research Part B: Applied Biomaterials, 2006. **76**(2): p. 315-325.
388. Horák, D., et al., *Poly(2-hydroxyethyl methacrylate)-based slabs as a mouse embryonic stem cell support*. Biomaterials, 2004. **25**(22): p. 5249-5260.
389. Melkounian, Z., et al., *Synthetic peptide-acrylate surfaces for long-term self-renewal and cardiomyocyte differentiation of human embryonic stem cells*. Nature Biotechnology, 2010. **28**(6): p. 606-610.
390. Lesny, et al., *Polymer hydrogels usable for nervous tissue repair*. Journal of chemical neuroanatomy, 2002. **23**(4): p. 243.
391. Mabilletau, G., et al., *Biodegradability of poly (2-hydroxyethyl methacrylate) in the presence of the J774.2 macrophage cell line*. Biomaterials, 2004. **25**(21): p. 5155-5162.
392. Štol, M., M. Tolar, and M. Adam, *Poly(2-hydroxyethyl methacrylate)—collagen composites which promote muscle cell differentiation in vitro*. Biomaterials, 1985. **6**(3): p. 193-197.
393. Filmon, R., et al., *Adherence of osteoblast-like cells on calcospherites developed on a biomaterial combining poly (2-hydroxyethyl) methacrylate and alkaline phosphatase*. Bone, 2002. **30**(1): p. 152-158.
394. Filmon, R., et al., *Poly (2-hydroxy ethyl methacrylate)-alkaline phosphatase: A composite biomaterial allowing in vitro studies of bisphosphonates on the mineralization process*. Journal of Biomaterials Science, Polymer Edition, 2000. **11**(8): p. 849-868.
395. *BS EN ISO 10993-1:October 2009 Biological evaluation of medical devices. Evaluation and testing within a risk management process. Évaluation biologique des dispositifs médicaux. Évaluation et essais au sein d'un processus de gestion du risque*2010: BSI Standards Limited.
396. Serrano, M.C., et al., *In vitro biocompatibility assessment of poly(ε-caprolactone) films using L929 mouse fibroblasts*. Biomaterials, 2004. **25**(25): p. 5603-5611.
397. Jung, O., et al., *Optimized in vitro procedure for assessing the cytocompatibility of magnesium-based biomaterials*. Acta Biomaterialia, 2015. **23**: p. 354-363.
398. Little, M.H., *Regrow or Repair: Potential Regenerative Therapies for the Kidney*. Journal of the American Society of Nephrology, 2006. **17**(9): p. 2390-2401.
399. Yadav, N., et al., *Bone marrow cells contribute to tubular epithelium regeneration following acute kidney injury induced by mercuric chloride*. The Indian journal of medical research, 2012. **136**(2): p. 211.
400. Ward, H.H., et al., *Adult human CD133/1⁺ kidney cells isolated from papilla integrate into developing kidney tubules*. Biochimica et Biophysica Acta (BBA)-Molecular Basis of Disease, 2011. **1812**(10): p. 1344-1357.
401. Maeshima, A., S. Yamashita, and Y. Nojima, *Identification of renal progenitor-like tubular cells that participate in the regeneration processes of the kidney*. J Am Soc Nephrol, 2003. **14**(12): p. 3138-46.
402. Maeshima, A., et al., *Involvement of Pax-2 in the action of activin A on tubular cell regeneration*. Journal of the American Society of Nephrology, 2002. **13**(12): p. 2850-2859.
403. Smeets, B., et al., *Proximal tubular cells contain a phenotypically distinct, scattered cell population involved in tubular regeneration*. The Journal of pathology, 2013. **229**(5): p. 645-659.
404. Zia, S., et al., *Amniotic Fluid Derived Stem Cells with a Renal Progenitor Phenotype Inhibit Interstitial Fibrosis in Renal Ischemia and Reperfusion Injury in Rats*. PLoS One, 2015. **10**(8): p. e0136145.
405. Di Silvio, L., *Cellular response to biomaterials*2008: Elsevier.
406. Rampersad, S.N., *Multiple Applications of Alamar Blue as an Indicator of Metabolic Function and Cellular Health in Cell Viability Bioassays*. Sensors (Basel, Switzerland), 2012. **12**(9): p. 12347-12360.
407. von Recum, A.F., *Handbook of biomaterials evaluation: scientific, technical and clinical testing of implant materials*1998: CRC Press.

408. Gupta, S., et al., *Isolation and characterization of kidney-derived stem cells*. Journal of the American Society of Nephrology : JASN, 2006. **17**(11): p. 3028-3040.
409. Wu, J., *Post-Transcriptional Gene Regulation : RNA Processing in Eukaryotes*, 2013, Wiley: Somerset.
410. Filipowicz, W., S.N. Bhattacharyya, and N. Sonenberg, *Mechanisms of post-transcriptional regulation by microRNAs: are the answers in sight?* Nat Rev Genet, 2008. **9**(2): p. 102-114.
411. Keene, J.D., *RNA regulons: coordination of post-transcriptional events*. Nature Reviews Genetics, 2007. **8**(7): p. 533-543.
412. Vogel, C. and E.M. Marcotte, *Insights into the regulation of protein abundance from proteomic and transcriptomic analyses*. Nature reviews. Genetics, 2012. **13**(4): p. 227-232.
413. Greenbaum, D., et al., *Comparing protein abundance and mRNA expression levels on a genomic scale*. Genome Biol, 2003. **4**(9): p. 117.
414. Turner, L.-A. and M.J. Dalby, *Nanotopography–potential relevance in the stem cell niche*. Biomaterials Science, 2014. **2**(11): p. 1574-1594.
415. Gallagher, J., et al., *Interaction of animal cells with ordered nanotopography*. IEEE transactions on nanobioscience, 2002. **1**(1): p. 24-28.
416. Das, R.K., et al., *Influence of nanohelical shape and periodicity on stem cell fate*. ACS nano, 2013. **7**(4): p. 3351-3361.
417. Fisher, O.Z., et al., *Bioinspired Materials for Controlling Stem Cell Fate*. Accounts of Chemical Research, 2009. **43**(3): p. 419-428.
418. Bettinger, C.J., et al., *Microfabrication of poly (glycerol–sebacate) for contact guidance applications*. Biomaterials, 2006. **27**(12): p. 2558-2565.
419. Meyle, J., K. Gültig, and W. Nisch, *Variation in contact guidance by human cells on a microstructured surface*. Journal of Biomedical Materials Research, 1995. **29**(1): p. 81-88.
420. Anderson, D.G., S. Levenberg, and R. Langer, *Nanoliter-scale synthesis of arrayed biomaterials and application to human embryonic stem cells*. Nature Biotechnology, 2004. **22**(7): p. 863-866.
421. Anderson, D.G., et al., *Biomaterial microarrays: rapid, microscale screening of polymer–cell interaction*. Biomaterials, 2005. **26**(23): p. 4892-4897.
422. Satchell, S., et al., *Conditionally immortalized human glomerular endothelial cells expressing fenestrations in response to VEGF*. Kidney International, 2006. **69**(9): p. 1633-1640.
423. Jansen, J., et al., *A morphological and functional comparison of proximal tubule cell lines established from human urine and kidney tissue*. Experimental Cell Research, 2014. **323**(1): p. 87-99.
424. Buck, M.E., et al., *Chemical modification of reactive multilayered films fabricated from poly (2-alkenyl azlactone) s: design of surfaces that prevent or promote mammalian cell adhesion and bacterial biofilm growth*. Biomacromolecules, 2009. **10**(6): p. 1564-1574.
425. Buck, M.E., J. Zhang, and D.M. Lynn, *Layer-by-Layer Assembly of Reactive Ultrathin Films Mediated by Click-Type Reactions of Poly (2-Alkenyl Azlactone) s*. Advanced Materials, 2007. **19**(22): p. 3951-3955.
426. Abouna, G.M., et al., *REVERSAL OF DIABETIC NEPHROPATHY IN HUMAN CADAVERIC KIDNEYS AFTER TRANSPLANTATION INTO NON-DIABETIC RECIPIENTS*. The Lancet. **322**(8362): p. 1274-1276.
427. Shmelkov, S.V., et al., *CD133 expression is not restricted to stem cells, and both CD133+ and CD133–metastatic colon cancer cells initiate tumors*. The Journal of Clinical Investigation, 2008. **118**(6): p. 2111.
428. Uchida, N., et al., *Direct isolation of human central nervous system stem cells*. Proceedings of the National Academy of Sciences, 2000. **97**(26): p. 14720-14725.
429. Bakondi, B., et al., *CD133 identifies a human bone marrow stem/progenitor cell sub-population with a repertoire of secreted factors that protect against stroke*. Molecular Therapy, 2009. **17**(11): p. 1938-1947.

430. Shirasawa, T., et al., *Gene expression of CD24 core peptide molecule in developing brain and developing non-neural tissues*. *Developmental Dynamics*, 1993. **198**(1): p. 1-13.
431. Challen, G.A., et al., *Identifying the molecular phenotype of renal progenitor cells*. *Journal of the American Society of Nephrology : JASN*, 2004. **15**(9): p. 2344-2357.
432. Eyre, J., et al., *Statin-sensitive endocytosis of albumin by glomerular podocytes*. *American Journal of Physiology-Renal Physiology*, 2007. **292**(2): p. F674-F681.
433. Okamura, K., et al., *Endocytosis of albumin by podocytes elicits an inflammatory response and induces apoptotic cell death*. *PLoS One*, 2013. **8**(1): p. e54817.
434. Arcolino, F.O., et al. *Preterm neonatal urine as a novel source of highly potent kidney progenitor cells*. in *Pediatric Nephrology*. 2015. Springer International.
435. Lam, A.Q., et al., *Rapid and efficient differentiation of human pluripotent stem cells into intermediate mesoderm that forms tubules expressing kidney proximal tubular markers*. *Journal of the American Society of Nephrology*, 2013: p. ASN. 2013080831.
436. Takasato, M., et al., *Directing human embryonic stem cell differentiation towards a renal lineage generates a self-organizing kidney*. *Nature cell biology*, 2014. **16**(1): p. 118-126.
437. Taguchi, A. and R. Nishinakamura, *Nephron reconstitution from pluripotent stem cells*. *Kidney International*, 2015. **87**(5): p. 894-900.
438. Shen, M. and A.T. Bell. *Plasma polymerization*. in *ACS Symposium Series*. 1979.
439. Shi, F.F., *Recent advances in polymer thin films prepared by plasma polymerization synthesis, structural characterization, properties and applications*. *Surface and Coatings Technology*, 1996. **82**(1): p. 1-15.
440. Kersten, H., et al., *Plasma–powder interaction: trends in applications and diagnostics*. *International Journal of Mass Spectrometry*, 2003. **223**: p. 313-325.
441. Keidar, M. and I.I. Beilis, *Chapter 1 - Plasma Concepts*, in *Plasma Engineering*, M. Keidar and I.I. Beilis, Editors. 2013, Academic Press: Boston. p. 1-81.
442. Michelmore, A., et al., *Nanoscale deposition of chemically functionalised films via plasma polymerisation*. *RSC Advances*, 2013. **3**(33): p. 13540-13557.
443. Friedrich, J., *Mechanisms of plasma polymerization—reviewed from a chemical point of view*. *Plasma Processes and Polymers*, 2011. **8**(9): p. 783-802.
444. Yasuda, H. and T. Hirotsu, *Distribution of polymer deposition in plasma polymerization. III. Effect of discharge power*. *Journal of Polymer Science: Polymer Chemistry Edition*, 1978. **16**(10): p. 2587-2592.
445. Yasuda, H., *Plasma polymerization*2012: Academic press.
446. Morita, S., A. Bell, and M. Shen, *The effect of frequency on the plasma polymerization of ethane*. *Journal of Polymer Science: Polymer Chemistry Edition*, 1979. **17**(9): p. 2775-2782.
447. Rossnagel, S.M., J.J. Cuomo, and W.D. Westwood, *Handbook of plasma processing technology: fundamentals, etching, deposition, and surface interactions*1990: William Andrew.
448. Chan, C.-M., *Polymer surface modification and characterization*1993: Carl Hanser, GmbH & Co.
449. Michelmore, A., et al., *Role of positive ions in determining the deposition rate and film chemistry of continuous wave hexamethyl disiloxane plasmas*. *Langmuir*, 2011. **27**(19): p. 11943-11950.
450. Yasuda, H., *Glow discharge polymerization*. *Thin Film Processes*, 1978: p. 361-396.
451. Boenig, H.V., *Fundamentals of plasma chemistry and technology*1988: CRC.
452. Liston, E., L. Martinu, and M. Wertheimer, *Plasma surface modification of polymers for improved adhesion: a critical review*. *Journal of Adhesion Science and Technology*, 1993. **7**(10): p. 1091-1127.
453. Chu, P.K., et al., *Plasma-surface modification of biomaterials*. *Materials Science and Engineering: R: Reports*, 2002. **36**(5): p. 143-206.
454. Inagaki, N., *Plasma surface modification and plasma polymerization*1996: CRC Press.
455. Zajíčková, L., et al., *Plasma Polymerization of Amine-Rich Films Aimed at Their Bioapplications*.

456. Hamerli, P., et al., *Surface properties of and cell adhesion onto allylamine-plasma-coated polyethyleneterephthalat membranes*. *Biomaterials*, 2003. **24**(22): p. 3989-3999.
457. Detomaso, L., et al., *Plasma deposited acrylic acid coatings: Surface characterization and attachment of 3T3 murine fibroblast cell lines*. *Surface and Coatings Technology*, 2005. **200**(1): p. 1022-1025.
458. Detomaso, L., et al., *Stable plasma-deposited acrylic acid surfaces for cell culture applications*. *Biomaterials*, 2005. **26**(18): p. 3831-3841.
459. Siow, K.S., et al., *Plasma Methods for the Generation of Chemically Reactive Surfaces for Biomolecule Immobilization and Cell Colonization-A Review*. *Plasma Processes and Polymers*, 2006. **3**(6-7): p. 392-418.
460. Han, L.M., et al., *Pulsed plasma polymerization of pentafluorostyrene: synthesis of low dielectric constant films*. *Journal of applied physics*, 1998. **84**(1): p. 439-444.
461. Chang, T.C., *Plasma surface treatment in composites manufacturing*. *Journal of Industrial Technology*, 1999. **15**(1): p. 1-7.
462. Ulbricht, M. and G. Belfort, *Surface modification of ultrafiltration membranes by low temperature plasma II. Graft polymerization onto polyacrylonitrile and polysulfone*. *Journal of Membrane Science*, 1996. **111**(2): p. 193-215.
463. Silva, S.S., et al., *Plasma surface modification of chitosan membranes: characterization and preliminary cell response studies*. *Macromolecular bioscience*, 2008. **8**(6): p. 568-576.
464. Favia, P. and R. d'Agostino, *Plasma treatments and plasma deposition of polymers for biomedical applications*. *Surface and Coatings Technology*, 1998. **98**(1): p. 1102-1106.
465. St-Georges-Robillard, A., et al., *Adhesion of U-937 Monocytes on Different Amine-functionalised Polymer Surfaces*. *Plasma Processes and Polymers*, 2012. **9**(3): p. 243-252.
466. Truica-Marasescu, F. and M.R. Wertheimer, *Nitrogen-Rich Plasma-Polymer Films for Biomedical Applications*. *Plasma Processes and Polymers*, 2008. **5**(1): p. 44-57.
467. Wertheimer, M.R., et al., *Amine-Rich Organic Thin Films for Cell Culture: Possible Electrostatic Effects in Cell-Surface Interactions*. *Japanese Journal of Applied Physics*, 2012. **51**(11S): p. 11PJ04.
468. Shard, A.G., et al., *A NEXAFS examination of unsaturation in plasma polymers of allylamine and propylamine*. *The Journal of Physical Chemistry B*, 2004. **108**(33): p. 12472-12480.
469. Vasilev, K., et al., *Solvent-Induced Porosity in Ultrathin Amine Plasma Polymer Coatings*. *The Journal of Physical Chemistry B*, 2008. **112**(35): p. 10915-10921.
470. Tarasova, A., et al., *Colloid Probe AFM and XPS Study of Time-Dependent Aging of Amine Plasma Polymer Coatings in Aqueous Media*. *Plasma Processes and Polymers*, 2008. **5**(2): p. 175-185.
471. Girard-Lauriault, P.-L., et al., *Atmospheric Pressure Deposition of Micropatterned Nitrogen-Rich Plasma-Polymer Films for Tissue Engineering*. *Plasma Processes and Polymers*, 2005. **2**(3): p. 263-270.
472. Fally, F., et al., *Quantification of the functional groups present at the surface of plasma polymers deposited from propylamine, allylamine, and propargylamine*. *Journal of applied polymer science*, 1995. **56**(5): p. 597-614.
473. Beck, A.J., et al., *Plasma co-polymerisation of two strongly interacting monomers: Acrylic acid and allylamine*. *Plasma Processes and Polymers*, 2005. **2**(8): p. 641-649.
474. Vasilev, K., et al., *Creating gradients of two proteins by differential passive adsorption onto a PEG-density gradient*. *Biomaterials*, 2010. **31**(3): p. 392-397.
475. Robinson, D.E., et al., *The substrate and composition dependence of plasma polymer stability*. *Plasma Processes and Polymers*, 2010. **7**(2): p. 102-106.
476. Munro, H. and C. Till, *A preliminary electron spectroscopy for chemical analysis investigation of the plasma copolymerization of tetramethyltin and perfluorobenzene*. *Thin solid films*, 1985. **131**(3): p. 255-260.

477. Beck, A.J., F.R. Jones, and R.D. Short, *Plasma copolymerization as a route to the fabrication of new surfaces with controlled amounts of specific chemical functionality*. *Polymer*, 1996. **37**(24): p. 5537-5539.
478. Alexander, M.R., et al., *Plasma polymer chemical gradients for evaluation of surface reactivity: epoxide reaction with carboxylic acid surface groups*. *Journal of Materials Chemistry*, 2004. **14**(3): p. 408-412.
479. Choukourov, A., et al., *Mechanistic studies of plasma polymerization of allylamine*. *The Journal of Physical Chemistry B*, 2005. **109**(48): p. 23086-23095.
480. Whittle, J.D., et al., *Differences in the aging of allyl alcohol, acrylic acid, allylamine, and octa-1, 7-diene plasma polymers as studied by X-ray photoelectron spectroscopy*. *Chemistry of materials*, 2000. **12**(9): p. 2664-2671.
481. Gengenbach, T.R., R.C. Chatelier, and H.J. Griesser, *Characterization of the Ageing of Plasma-deposited Polymer Films: Global Analysis of X-ray Photoelectron Spectroscopy Data*. *Surface and interface analysis*, 1996. **24**(4): p. 271-281.
482. Gengenbach, T.R. and H.J. Griesser, *Deposition conditions influence the postdeposition oxidation of methyl methacrylate plasma polymer films*. *Journal of Polymer Science Part A: Polymer Chemistry*, 1998. **36**(6): p. 985-1000.
483. Gengenbach, T.R. and H.J. Griesser, *Aging of 1, 3-diaminopropane plasma-deposited polymer films: Mechanisms and reaction pathways*. *Journal of Polymer Science Part A: Polymer Chemistry*, 1999. **37**(13): p. 2191-2206.
484. Truica-Marasescu, F. and M.R. Wertheimer, *Nitrogen-Rich Plasma-Polymer Films for Biomedical Applications*. *Plasma Processes and Polymers*, 2008. **5**(1): p. 44-57.
485. Briggs, D., et al., *Analysis of the surface chemistry of oxidized polyethylene: comparison of XPS and ToF-SIMS*. *Surface and interface analysis*, 2003. **35**(2): p. 156-167.
486. Krishnamurthy, V., I.L. Kamel, and Y. Wei, *Analysis of plasma polymerization of allylamine by FTIR*. *Journal of Polymer Science Part A: Polymer Chemistry*, 1989. **27**(4): p. 1211-1224.
487. Myung, S.W. and H.S. Choi, *Chemical structure and surface morphology of plasma polymerized-allylamine film*.
488. Montes Ruiz-Cabello, F., et al., *Comparison of sessile drop and captive bubble methods on rough homogeneous surfaces: a numerical study*. *Langmuir*, 2011. **27**(15): p. 9638-9643.
489. Chen, Y. and Y. Zhang, *Fluorescent quantification of amino groups on silica nanoparticle surfaces*. *Analytical and bioanalytical chemistry*, 2011. **399**(7): p. 2503-2509.
490. Janolino, V.G. and H.E. Swaisgood, *A spectrophotometric assay for solid phase primary amino groups*. *Applied biochemistry and biotechnology*, 1992. **36**(2): p. 81-85.
491. Ruiz, J.C., et al., *Approaches to Quantify Amine Groups in the Presence of Hydroxyl Functional Groups in Plasma Polymerized Thin Films*. *Plasma Processes and Polymers*, 2014. **11**(9): p. 888-896.
492. Tatouliau, M., et al., *Plasma deposition of allylamine on polymer powders in a fluidized bed reactor*. *Plasma Processes and Polymers*, 2005. **2**(1): p. 38-44.
493. Albrecht, W., et al., *Amination of Poly (ether imide) Membranes Using Di-and Multivalent Amines*. *Macromolecular Chemistry and Physics*, 2003. **204**(3): p. 510-521.
494. Uchida, E., Y. Uyama, and Y. Ikada, *Sorption of low-molecular-weight anions into thin polycation layers grafted onto a film*. *Langmuir*, 1993. **9**(4): p. 1121-1124.
495. Kakabakos, S.E., et al., *Colorimetric determination of reactive solid-supported primary and secondary amino groups*. *Biomaterials*, 1994. **15**(4): p. 289-297.
496. Gengenbach, T.R., et al., *Contributions of restructuring and oxidation to the aging of the surface of plasma polymers containing heteroatoms*. *Plasmas and polymers*, 1997. **2**(2): p. 91-114.
497. Norde, W., *Adsorption of proteins from solution at the solid-liquid interface*. *Advances in Colloid and Interface Science*, 1986. **25**: p. 267-340.

498. Absolom, D., W. Zingg, and A. Neumann, *Protein adsorption to polymer particles: role of surface properties*. Journal of Biomedical Materials Research, 1987. **21**(2): p. 161-171.
499. Förch, R., Z. Zhang, and W. Knoll, *Soft plasma treated surfaces: tailoring of structure and properties for biomaterial applications*. Plasma Processes and Polymers, 2005. **2**(5): p. 351-372.
500. Seal, A., et al., *Mechanical properties of very thin cover slip glass disk*. Bulletin of Materials Science, 2001. **24**(2): p. 151-155.
501. Kese, K., Z.-C. Li, and B. Bergman, *Method to account for true contact area in soda-lime glass during nanoindentation with the Berkovich tip*. Materials Science and Engineering: A, 2005. **404**(1): p. 1-8.
502. Yoshida, S., J.-C. Sanglebœuf, and T. Rouxel, *Quantitative evaluation of indentation-induced densification in glass*. Journal of materials research, 2005. **20**(12): p. 3404-3412.
503. Wang, H., et al., *Tailoring of Mesenchymal Stem Cells Behavior on Plasma-Modified Polytetrafluoroethylene*. Advanced Materials, 2012. **24**(25): p. 3315-3324.
504. Zhao, J.H., et al., *Controlling cell growth on titanium by surface functionalization of heptylamine using a novel combined plasma polymerization mode*. Journal of Biomedical Materials Research Part A, 2011. **97**(2): p. 127-134.
505. Attri, P., B. Arora, and E.H. Choi, *Utility of plasma: a new road from physics to chemistry*. RSC Advances, 2013. **3**(31): p. 12540-12567.
506. Choukourov, A., et al., *Plasma Polymerization on Mesoporous Surfaces: N-Hexane on Titanium Nano-Particles*. The Journal of Physical Chemistry C, 2015.
507. Mwale, F., et al., *Suppression of genes related to hypertrophy and osteogenesis in committed human mesenchymal stem cells cultured on novel nitrogen-rich plasma polymer coatings*. Tissue engineering, 2006. **12**(9): p. 2639-2647.
508. Yang, J., et al., *A high-throughput assay of cell-surface interactions using topographical and chemical gradients*. Advanced Materials, 2009. **21**(3): p. 300-304.
509. Schuh, C., et al., *Polymer brushes with nanometer-scale gradients*. Advanced Materials, 2009. **21**(46): p. 4706.
510. Parkin, J. and B. Cohen, *An overview of the immune system*. The Lancet, 2001. **357**(9270): p. 1777-1789.
511. Rot, A. and U.H. von Andrian, *Chemokines in innate and adaptive host defense: basic chemokinese grammar for immune cells*. Annu. Rev. Immunol., 2004. **22**: p. 891-928.
512. Nguyen, L., et al., *Neurotransmitters as early signals for central nervous system development*. Cell and tissue research, 2001. **305**(2): p. 187-202.
513. Sanes, D.H., T.A. Reh, and W.A. Harris, *Development of the nervous system* 2011: Academic Press.
514. Cardona, A.E., et al., *Chemokines in and out of the central nervous system: much more than chemotaxis and inflammation*. Journal of leukocyte biology, 2008. **84**(3): p. 587-594.
515. Roussos, E.T., J.S. Condeelis, and A. Patsialou, *Chemotaxis in cancer*. Nature Reviews Cancer, 2011. **11**(8): p. 573-587.
516. Ellis, L.M. and D.J. Hicklin, *VEGF-targeted therapy: mechanisms of anti-tumour activity*. Nature Reviews Cancer, 2008. **8**(8): p. 579-591.
517. Zelzer, M., M.R. Alexander, and N.A. Russell, *Hippocampal cell response to substrates with surface chemistry gradients*. Acta Biomaterialia, 2011. **7**(12): p. 4120-4130.
518. Lamalice, L., F. Le Boeuf, and J. Huot, *Endothelial cell migration during angiogenesis*. Circulation Research, 2007. **100**(6): p. 782-794.
519. Yamaguchi, H., J. Wyckoff, and J. Condeelis, *Cell migration in tumors*. Current Opinion in Cell Biology, 2005. **17**(5): p. 559-564.
520. Rørth, P., *Collective cell migration*. Annual Review of Cell and Developmental, 2009. **25**: p. 407-429.

521. Martin, P., *Wound healing--aiming for perfect skin regeneration*. *Science*, 1997. **276**(5309): p. 75-81.
522. Bernstein, L.R. and L.A. Liotta, *Molecular mediators of interactions with extracellular matrix components in metastasis and angiogenesis*. *Current opinion in oncology*, 1994. **6**(1): p. 106.
523. Raftopoulou, M. and A. Hall, *Cell migration: Rho GTPases lead the way*. *Developmental Biology*, 2004. **265**(1): p. 23-32.
524. Mitchison, T. and L. Cramer, *Actin-based cell motility and cell locomotion*. *Cell*, 1996. **84**(3): p. 371-379.
525. Schneider, L., et al., *Directional cell migration and chemotaxis in wound healing response to PDGF-AA are coordinated by the primary cilium in fibroblasts*. *Cellular physiology and Biochemistry*, 2010. **25**(2-3): p. 279-292.
526. Ricoult, S.G., et al., *Large Dynamic Range Digital Nanodot Gradients of Biomolecules Made by Low-Cost Nanocontact Printing for Cell Haptotaxis*. *Small*, 2013. **9**(19): p. 3308-3313.
527. Recho, P., T. Putelat, and L. Truskinovsky, *Mechanotaxis and cell motility*. arXiv preprint arXiv:1302.3999, 2013.
528. Singh, M., C. Berkland, and M.S. Detamore, *Strategies and applications for incorporating physical and chemical signal gradients in tissue engineering*. *Tissue Eng Part B Rev*, 2008. **14**(4): p. 341-66.
529. Zaari, N., et al., *Photopolymerization in microfluidic gradient generators: microscale control of substrate compliance to manipulate cell response*. *Advanced Materials*, 2004. **16**(23-24): p. 2133-2137.
530. Pelham, R.J. and Y.-L. Wang, *Cell locomotion and focal adhesions are regulated by substrate flexibility*. 1998.
531. Zheng, G., et al., *Effects of different functional groups on metastatic behavior of SPC-A-1/human lung cancer cells in self-assembled monolayers*. *RSC Advances*, 2015. **5**(52): p. 41412-41419.
532. Yao, S., et al., *Ordered self-assembled monolayers terminated with different chemical functional groups direct neural stem cell lineage behaviours*. *Biomedical Materials (Bristol, England)*, 2015. **11**(1): p. 014107-014107.
533. Chieh, H.-F., et al., *Migration patterns and cell functions of adipose-derived stromal cells on self-assembled monolayers with different functional groups*. *Journal of Biomaterials Science, Polymer Edition*, 2013. **24**(1): p. 94-117.
534. Wu, J., et al., *Gradient biomaterials and their influences on cell migration*. *Interface focus*, 2012: p. rsfs20110124.
535. Zhou, H., M.D. Weir, and H.H. Xu, *Effect of cell seeding density on proliferation and osteodifferentiation of umbilical cord stem cells on calcium phosphate cement-fiber scaffold*. *Tissue Engineering Part A*, 2011. **17**(21-22): p. 2603-2613.
536. Bitar, M., et al., *Effect of cell density on osteoblastic differentiation and matrix degradation of biomimetic dense collagen scaffolds*. *Biomacromolecules*, 2007. **9**(1): p. 129-135.
537. Wilson, C., et al., *Evaluating 3D bone tissue engineered constructs with different seeding densities using the alamarBlue™ assay and the effect on in vivo bone formation*. *Journal of Materials Science: Materials in Medicine*, 2002. **13**(12): p. 1265-1269.
538. Hui, T., et al., *In vitro chondrogenic differentiation of human mesenchymal stem cells in collagen microspheres: influence of cell seeding density and collagen concentration*. *Biomaterials*, 2008. **29**(22): p. 3201-3212.
539. Webb, K., V. Hlady, and P.A. Tresco, *Relative importance of surface wettability and charged functional groups on NIH 3T3 fibroblast attachment, spreading, and cytoskeletal organization*. *Journal of Biomedical Materials Research*, 1998. **41**(3): p. 422-430.
540. García, A.J., M.a.D. Vega, and D. Boettiger, *Modulation of Cell Proliferation and Differentiation through Substrate-dependent Changes in Fibronectin Conformation*. *Molecular Biology of the Cell*, 1999. **10**(3): p. 785-798.

541. Shelton, R., A. Rasmussen, and J. Davies, *Protein adsorption at the interface between charged polymer substrata and migrating osteoblasts*. *Biomaterials*, 1988. **9**(1): p. 24-29.
542. Craighead, H., C. James, and A. Turner, *Chemical and topographical patterning for directed cell attachment*. *Current Opinion in Solid State and Materials Science*, 2001. **5**(2): p. 177-184.
543. Chou, L., et al., *Substratum surface topography alters cell shape and regulates fibronectin mRNA level, mRNA stability, secretion and assembly in human fibroblasts*. *Journal of cell science*, 1995. **108**(4): p. 1563-1573.
544. Dalby, M.J., et al., *The control of human mesenchymal cell differentiation using nanoscale symmetry and disorder*. *Nature materials*, 2007. **6**(12): p. 997-1003.
545. Lee, M.R., et al., *Direct differentiation of human embryonic stem cells into selective neurons on nanoscale ridge/groove pattern arrays*. *Biomaterials*, 2010. **31**(15): p. 4360-4366.
546. O'Connor, T.P. and D. Bentley, *Accumulation of actin in subsets of pioneer growth cone filopodia in response to neural and epithelial guidance cues in situ*. *The Journal of Cell Biology*, 1993. **123**(4): p. 935-948.
547. Lord, M.S., M. Foss, and F. Besenbacher, *Influence of nanoscale surface topography on protein adsorption and cellular response*. *Nano today*, 2010. **5**(1): p. 66-78.
548. Kretzler, M., *Role of podocytes in focal sclerosis: defining the point of no return*. *Journal of the American Society of Nephrology*, 2005. **16**(10): p. 2830-2832.
549. Carney, E.F., *Glomerular disease: Albuminuria inhibits podocyte regeneration*. *Nat Rev Nephrol*, 2013. **9**(10): p. 554-554.
550. Zhang, Z., et al., *WNT/ β -Catenin Signaling Is Required for Integration of CD24*. *Stem cells international*, 2015. **2015**.
551. Dekel, B. and Y. Reisner, *Engraftment of human early kidney precursors*. *Transplant Immunology*, 2004. **12**(3): p. 241-247.
552. Oliveira Arcolino, F., et al., *Human urine as a noninvasive source of kidney cells*. *Stem cells international*, 2015. **2015**.
553. Timpl, R., *Structure and biological activity of basement membrane proteins*. *European Journal of Biochemistry*, 1989. **180**(3): p. 487-502.
554. Miner, J.H., *The glomerular basement membrane*. *Experimental Cell Research*, 2012. **318**(9): p. 973-978.
555. Ribeiro, A., E. Powell, and J. Leach. *Neural Stem Cell Differentiation in 2D and 3D Microenvironments*. in *26th Southern Biomedical Engineering Conference SBEC 2010, April 30-May 2, 2010, College Park, Maryland, USA*. 2010. Springer.
556. Garreta, E., et al., *Osteogenic differentiation of mouse embryonic stem cells and mouse embryonic fibroblasts in a three-dimensional self-assembling peptide scaffold*. *Tissue engineering*, 2006. **12**(8): p. 2215-2227.
557. Hosseinkhani, H., et al., *DNA nanoparticles encapsulated in 3D tissue-engineered scaffolds enhance osteogenic differentiation of mesenchymal stem cells*. *Journal of Biomedical Materials Research Part A*, 2008. **85**(1): p. 47-60.
558. Chia, H.N. and B.M. Wu, *Recent advances in 3D printing of biomaterials*. *Journal of biological engineering*, 2015. **9**(1): p. 1.
559. Zein, I., et al., *Fused deposition modeling of novel scaffold architectures for tissue engineering applications*. *Biomaterials*, 2002. **23**(4): p. 1169-1185.
560. Williams, J.M., et al., *Bone tissue engineering using polycaprolactone scaffolds fabricated via selective laser sintering*. *Biomaterials*, 2005. **26**(23): p. 4817-4827.
561. Leong, K., C. Cheah, and C. Chua, *Solid freeform fabrication of three-dimensional scaffolds for engineering replacement tissues and organs*. *Biomaterials*, 2003. **24**(13): p. 2363-2378.
562. Khang, G., *Evolution of gradient concept for the application of regenerative medicine*. *Biosurface and Biotribology*, 2015. **1**(3): p. 202-213.
563. Kim, J., et al., *Protein immobilization on plasma-polymerized ethylenediamine-coated glass slides*. *Anal Biochem*, 2003. **313**(1): p. 41-5.

564. Jarvis, K.L. and P. Majewski, *Optimization of Plasma Polymerized Ethylenediamine Film Chemistry on Quartz Particles*. Plasma Processes and Polymers, 2013. **10**(7): p. 619-626.
565. Müller, M. and C. Oehr, *Plasma aminofunctionalisation of PVDF microfiltration membranes: comparison of the in plasma modifications with a grafting method using ESCA and an amino-selective fluorescent probe*. Surface and Coatings Technology, 1999. **116**: p. 802-807.
566. Denis, L., et al., *Deposition of functional organic thin films by pulsed plasma polymerization: a joint theoretical and experimental study*. Plasma Processes and Polymers, 2010. **7**(2): p. 172-181.
567. Manakhov, A., et al., *Optimization of Cyclopropylamine Plasma Polymerization toward Enhanced Layer Stability in Contact with Water*. Plasma Processes and Polymers, 2014. **11**(6): p. 532-544.
568. Rigogliuso, S., et al., *Use of Modified 3D Scaffolds to Improve Cell Adhesion and Drive Desired Cell Responses*. CHEMICAL ENGINEERING TRANSACTIONS, 2012. **27**(27).
569. Domingos, M., et al., *Improved osteoblast cell affinity on plasma-modified 3-D extruded PCL scaffolds*. Acta Biomaterialia, 2013. **9**(4): p. 5997-6005.
570. Barry, J.J., et al., *Using Plasma Deposits to Promote Cell Population of the Porous Interior of Three-Dimensional Poly (D, L-Lactic Acid) Tissue-Engineering Scaffolds*. Advanced functional materials, 2005. **15**(7): p. 1134-1140.
571. Leclair, A.M., S.S. Ferguson, and F. Lagugné-Labarthe, *Surface patterning using plasma-deposited fluorocarbon thin films for single-cell positioning and neural circuit arrangement*. Biomaterials, 2011. **32**(5): p. 1351-1360.
572. Barrias, C.C., et al., *The correlation between the adsorption of adhesive proteins and cell behaviour on hydroxyl-methyl mixed self-assembled monolayers*. Biomaterials, 2009. **30**(3): p. 307-316.
573. Roach, P., D. Farrar, and C.C. Perry, *Interpretation of protein adsorption: surface-induced conformational changes*. Journal of the American Chemical Society, 2005. **127**(22): p. 8168-8173.
574. Chittur, K.K., *FTIR/ATR for protein adsorption to biomaterial surfaces*. Biomaterials, 1998. **19**(4-5): p. 357-369.
575. Baneyx, G., L. Baugh, and V. Vogel, *Coexisting conformations of fibronectin in cell culture imaged using fluorescence resonance energy transfer*. Proceedings of the National Academy of Sciences, 2001. **98**(25): p. 14464-14468.
576. Baugh, L. and V. Vogel, *Structural changes of fibronectin adsorbed to model surfaces probed by fluorescence resonance energy transfer*. Journal of Biomedical Materials Research Part A, 2004. **69**(3): p. 525-534.

Appendix I Cell culture

Cell culture components	Manufacturer, Catalogue No.
Albumin from Bovine Serum	Sigma, A2058
Cell Counting Kit-8 Solution	Sigma, 96992
Corning 15ml Centrifuge Tubes (sterile)	Appleton Woods, BC031
Corning 50ml tubes (sterile)	Appleton Woods, BC034
Counting Slides, TC 10	BioRAD, 145-0011
Cell culture plates, 6 well, Corning®	Appleton Woods, BC010
Cell culture plates, 12 well, Corning®	Appleton Woods, BC011
Cell culture plates, 24 well, Corning®	Appleton Woods, BC012
Cell culture plates, 96 well, Corning®	Appleton Woods, BC015
Cell culture plates, 60 mm, Corning®	Greiner Bio-One, 628160
Cell culture plates, 100 mm, Corning®	Greiner Bio-One, 664160
Dexamethasone	Sigma, D8893
Dulbecco's Modified Eagle Medium (DMEM)	Sigma, D6546
DMEM: F12 (1:1) medium	Lonza, 12-719
Dulbecco's Phosphate Buffered Saline	Sigma, D8537
Foetal Bovine Serum Albumin	Sigma, 16000044
Formaldehyde Solution	Thermo Scientific, 28908
Holo-Transferrin	Sigma, T0665
Hydrocortisone	Sigma, H0135
Insulin-Transferrin-Selenium (ITS) supplement	Gibco, 41400-045
L-glutamine 200mM	Sigma, G7513
MEM non-essential amino acids (100x)	Life Technologies, 11140035
Penicillin / Streptomycin	Life Technologies, 15140122
PES filter (0.22µm)	MILLEX-GP, SLGP033RS
Prostaglandin E1	Sigma, P8908
Recovery™ Cell Culture Freezing Medium	Invitrogen, 12648010
RPMI-1640 Medium	Sigma, R8758
3,3',5'-triiodo-L-thyronine sodium salt (T3)	Sigma, T5516
Triton X-100	Sigma, T-8787
Trypan Blue Solution	Sigma, T8154
Trypsin-EDTA solution	Sigma, T3924
Vacuum Filter System, bottle top, Corning®	Sigma, CLS430767 and CLS430769

Cell culture medium composition

Cell culture medium A

DMEM	
foetal Bovine Serum	10%
L-glutamine	1%
Penicillin / Streptomycin	1%
MEM non-essential amino acids	1%

Cell culture medium B

RPMI-1640	
foetal Bovine Serum	10%
Penicillin / Streptomycin	1%

Cell culture medium C

DMEM/F12	
foetal Bovine Serum	10%
ITS supplement	1%
Penicillin / Streptomycin	1%
Hydrocortisone	36 ng / mL
Triiodothyronin (T3)	4 µg / mL
hEGF	10 ng / mL

Cell culture medium D

DMEM/F12	
foetal Bovine Serum	5%
ITS supplement	1%
Penicillin / Streptomycin	1%
Prostaglandin E1	100 ng / mL
Dexamethasone	40 ng / mL
Holo-Transferrin	20 ng / mL
Triiodo-L-Thyronine	4 ng / mL

Components filtered with Corning® bottle-top vacuum filter system

Appendix II Immunofluorescence and cell staining

Immunofluorescence Analyses	Host	Isotype	Concentration	Manufacturer, Catalogue No.
Primary Antibody				
Aquaporin 1	gt	IgG	1 : 200	Santa Cruz, sc-9878
Collagen IV	rb	IgG	1 : 200	Millipore, AB756P
Laminin	rb	IgG	1 : 500	Abcam, ab11575
LRP2 antibody (Megalin)	m	IgG1	1 : 200	Acris, DM3613P
Nephrin	rb	IgG	1 : 200	Abcam, ab58968
Podocin	rb	IgG	1 : 200	Abcam, ab50339
Synaptopodin	m	IgG1	1 : 2	Progen, 65194
Secondary Antibody				
Alexa Fluor® 594 gt anti m	gt	IgG1	1 :1000	Invitrogen, A-21125
Alexa Fluor® 488 gt anti rb	gt	IgG	1 : 1000	Invitrogen, A-11008
Alexa Fluor® 594 gt anti rb	gt	IgG	1 : 1000	Invitrogen, A-11012
Alexa Fluor® 594 ck anti gt	ck	IgG1	1 : 1000	Invitrogen, A-21468
Cytofluorimetric Analyses				
CD24-FITC, human (32D12)	m	IgG1	1 : 50	Miltenyibiotec, 130-095-952
CD13-APC, human (REA263)	h	IgG1	1 : 50	Miltenyibiotec, 130-103-734
CD133/2 (293C3)-APC, human	m	IgG2b	1 : 50	Miltenyibiotec, 130-090-854

(m) mouse, (h) human, (gt) goat, (ck) chicken, (rb) rabbit

Other fluorescent markers used	Concentration	Manufacturer, Catalogue No.
Alexa Fluor® 488 Phalloidin	5 : 200 in PBS	Life Technologies, A12379
DAPI	1 : 1000 in PBS	Sigma, D9542
BSA, FITC conjugate	40 µg /mL in medium	Invitrogen, A23015

Alkaline phosphatase staining solution	Concentration	Manufacturer, Catalogue No.
Tris-HCl pH 9.2		
Naphtol AS-MX phosphate	0.2 mg / mL	Sigma, 855
Fast Red TR Salt hemi(zinc chloride) salt	1 mg / mL	Sigma, F8764

Others	Concentration	Manufacturer, Catalogue No.
Dako Florescent Mounting Medium		Dako, S3023
Glycerol	80% in dH ₂ O	Sigma, 536407
Triton-X 100		Sigma, X100

Appendix III Buffers and solutions

4% (v/v) Formaldehyde	
16% Formaldehyde Solution	4 mL
10x PBS	26 mL
dH ₂ O	10 mL

PBS (1x)	
NaCl	8 g
KCl	0.2 g
Na ₂ HPO ₄ dibasic	1.15 g
KH ₄ PO ₄ monobasic	0.2 g
dH ₂ O	1 L
adjust to pH 7.2 with NaOH	

FACS buffer	
PBS	
Foetal Bovine Serum	2%
Penicillin / Streptomycin	2%

10x TAE Buffer	
NaCl	48.4 g
Glacial Acetic Acid (17.4M)	11.4 mL
EDTA	3.7 g
dH ₂ O	1 L

Tris-HCl (pH 9.2)	
dH ₂ O	500 mL
6 Trizma base	6 g
adjust pH with conc. HCl	1%

Appendix IV Molecular biology

Components for molecular biology	Manufacturer, Catalogue No.
2-propanol	Sigma, I9516
Agarose	Biosciences, 8201-07
Chloroform	Sigma, C2432
dNTP Set	Bioline, BIO-39025
Counting Slides, TC 10	BioRAD, 145-0011
Ethanol	Sigma, E7023
Ethidium bromide	Sigma, 1239-45-8
Glycogen	Sigma, G1767
Hard-Shell 96-Well PCR	BioRAD, HSP-9645
HyperLadder™ I	Bioline, BIO-33026
HyperLadder™ IV	Bioline, BIO-33030
5x DNA Loading Buffer Blue	Bioline, BIO-37045
2.0ml Microcentrifuge Tube	Elkay, 021-4204-500
Microseal adhesives for PCR HSPs	BioRAD, MSB-1001
Nuclease free water	Promega, P1197
Random hexamers	QIAGEN, 79236
RQ1 DNase 10x reaction buffer	Promega, M198A
RQ1 DNase Stop Solution	Promega, M199A
RQ1 RNase-Free DNase	Promega, M6101A
SuperScript™III Reverse Transcriptase	Invitrogen, 18080-044
SYBR® Green Jumpstart™	Sigma, S4438-500RXN
TRIzol® Reagent	Invitrogen, 15596-026

Primers

Organism: mouse

Denomination	Oligo Name	Sequence 5' to 3'	Product Length / bp
Alkaline Phosphatase	mF_AlkPhos	CTGCAGGATCGGAACGTCAA	106
	mR_AlkPhos	GGTGTACCCTGAGATTCTGTCC	
Aquaporin 1	mF_Aqp 1	ACAATTCACCTGGCCGCAAT	139
	mR_Aqp 1	GAGCCACCTAAGTCTCGGC	
beta Actin	mF_ACTB	GTACCCAGGCATTGCTGACA	145
	mF_ACTB	CTGGAAGGTGGACAGTGAGG	
Glycerinaldehyd-3-phosphat Dehydrogenase	mF_Gapdh	TGAAGCAGGCATCTGAGGG	102
	mR_Gapdh	CGAAGGTGGAAGAGTGGGAG	
Megalin	mF_Meg	AGTGCAGGGACCGTCAGTAA	140
	mR_Meg	TGCCCTGAGTTTCATCAGCTC	
Podocalyxyn	mF_Pdx	AAGCCCTGTGTAGAACAGCC	109
	mR_Px	AACAGAAAGGCCCCACAAA	
Synaptopodin	mF_Synpo	GTACACTGCCCCAGTCCAAG	146
	mR_Synpo	CAGCATTCCGGGTGGAGAAG	
Wilms tumor 1	mF_WT1	CACGGCACAGGGTATGAGAG	128
	mR_WT1	GTTGGGGCCACTCCAGATAC	

(m) mouse

Appendix V Polymer analyses

Glass cover slips	Manufacturer, Catalogue No.
13 mm glass coverslips (rd)	Appleton Woods, GWN041
13 mm plastic cover slips (sq)	Thermo Scientific, 174950
19 mm glass cover slips (rd)	Appleton Woods, GWN041
22 mm ² glass cover slips (sq)	VWR, 470019-004
25 mm ² glass cover slips (rd)	EMS, 72223-10
(rd) round (sq) square	

Atomic Force Microscopy	Manufacturer, Catalogue No.
SCANASYST-AIR Cantilevers	Bruker AFM Probe TAP150A, MPP-12120-10
AFM mounting disk	Bruker, SPM sample mounting disks, 15mm, SD-102

Plasma chemical components	Manufacturer, Catalogue No.
Allylamine	Sigma, 145831
1,7-Octadiene	Sigma, O2501

Colorimetry	Manufacturer, Catalogue No.
Coomassie Brilliant Blue	Sigma, B0770
Orange 2 sodium salt	Sigma, 69143

